যাদবপুর বিশ্ববিদ্যালয়
কলকাতা - ৭০০০৩২, ভারত

JADAVPUR UNIVERSITY
KOLKATA -700 032, INDIA

FACULTY OF SCIENCE : DEPARTMENT OF GEOLOGICAL SCIENCES

CERTIFICATE FROM SUPERVISORS

This is to certify that the thesis entitled "Petrology and Geochemistry of the granitoid rocks from parts of North Purulia Shear Zone, Chotanagpur Granite Gneissic Complex, India.", submitted by Smt. Kuhu Chakraborty who got her name registered on 17th August 2016, for the award of Ph.D. (Science) degree of Jadavpur University, is absolutely based upon her own work under the supervision of Dr. Subir Mukhopadhyay of Jadavpur University and Dr. Arijit Ray of Presidency University and neither this thesis nor any part of it has been submitted for either any degree or diploma or any other academic award anywhere before.

S. Mukhopadhyay 12/12/2022

Dr. Subir Mukhopadhyay
Professor
Dept. of Geological Sciences
Jadavpur University
Kolkata - 700032

Arijit Ray 12/12/2022

(Signature of the Supervisors, date with official seal)

Dr. Arijit Ray
Professor of Geology
Presidency University, Kolkata

Petrology and Geochemistry of the granitoid rocks from parts of North Purulia Shear Zone, Chotanagpur Granite Gneissic Complex, India

Thesis submitted for attainment of the Degree of Doctor of Philosophy (Science) in Geology

Thesis Submitted

by

KUHU CHAKRABORTY

Department of Geological Sciences

Jadavpur University, Kolkata

2022

ACKNOWLEDGEMENTS

First and foremost, I would like to convey my heartfelt gratitude to Prof. Subir Mukhopadhyay of the Department of Geological Sciences, Jadavpur University and Prof. Arijit Ray of the Department of Geology, Presidency University for their tremendous support and assistance in the completion of my work. The completion of the work would not have been possible without their help and insights.

I would like to thank the Head of the Department, Department of Geological Sciences, Jadavpur University, Kolkata and Head of the Department, Department of Geology, Presidency University, Kolkata, for providing me with infrastructural support.

Special thanks to all the research scholars and lab mates of the Department of Geology, Presidency University, Kolkata, for their moral support and help in various instances.

I am thankful to Department of Science and Technology for providing fellowship throughout my work tenure.

Last but not the least, I would like to dedicate this work to my parents, whose unending support and belief encouraged me to complete my work. I would also like to express gratitude towards my family members, husband, sweet little daughter and friends for their continuous support and adjustments which helped me to reach my goal.

ABSTRACT

The granitoid rocks exposed along the NPSZ of Chotanagpur Granite Gneissic Complex, West Bengal, are the focus of the present study. The granitoid rocks of the Raghunathpur-Bero area located to the north-eastern sector of Puruliya and Jhalda region located in the western part of Puruliya are mainly emphasized in the present study. Three granitoid varieties are observed in the north-eastern sector: garnetiferous granite gneiss (GGG), megacrystic granite gneiss (MGG) and pink granite (PG) while the western sector is mainly dominated by the megacrystic granite gneiss similar to that of north eastern sector with mounds of aegirine-ribeckite granite (ARG). Geochemically the granites of the Raghunathpur area are classified as ferroan, per-aluminous, S-type granites which were generated from the anatexis of meta-sedimentary protolith (khondalite) in a volcanic-arc to syn-collisional setting. On the other hand, the AR granites are ferroan, peralkaline granitoid rocks which shows similarities with A-type granites. They were supposed to be emplaced in a post orogenic setting during orogeny-anorogeny transition at the time of waning stage of orogenic activity. REE modeling of S-type granites of Raghunathpur area shows that 20-30% partial melting of khondalites under limited H_2O content condition at around 5kbar pressure give rise to the anatectic melt which may be considered as the parent melt of GGG. On the other hand, trace element modeling of the AR granitoids indicates that a moderate degree partial melting (5% to 20%) of charnockite+khondalite source rock followed by ~ 30% fractional crystallization of plagioclase feldspar is responsible to generate parent magma of alkali granite. Age data of the granitoids of Raghunathpur area and Jhalda area shows overlapping ages around 1000Ma. Occurrences of post orogenic / anorogenic granites in association with the orogenic I-type (megacrystic granite in Jhalda area) and S-type granites (Raghunathpur area) of similar or overlapping ages (1000 Ma) represents contrasting granite magmatism during orogeny-anorogeny transition in a Proterozoic orogenic belt of eastern India. Thus the 970 Ma Jhalda anorogenic granite of NPSZ confirm India's active participation in Rodinia event.

CONTENTS

LIST OF FIGURES

CHAPTER-1: INTRODUCTION

CHAPTER-2: GEOLOGICAL SETTING

CHAPTER-4: FIELD OCCURRENCE, PETROGRAPHY AND MINERAL CHEMISTRY OF THE GRANITOID ROCKS OF RAGHUNATHPUR-BERO AREA AND JHALDA AREA OF CGGC

CHAPTER-5: GEOCHEMISTRY OF THE GRANITOID ROCKS OF RAGHUNATHPUR-BERO AREA AND JHALDA AREA OF CGGC

LIST OF TABLES

CHAPTER-2: GEOLOGICAL SETTING

CHAPTER-3: PREVIOUS WORK

CHAPTER-4: FIELD OCCURRENCE, PETROGRAPHY AND MINERAL CHEMISTRY OF GRANITOID ROCKS OF CGGC

CHAPTER-5: GEOCHEMISTRY OF THE GRANITOID ROCKS OF RAGHUNATHPUR-BERO AREA AND JHALDA AREA OF CGGC

CHAPTER-6: GEOCHRONOLOGY OF THE GRANITOID ROCKS OF RAGHUNATHPUR-BERO AREA AND JHALDA AREA OF CGGC

CHAPTER- 7: PETROGENESIS OF THE GRANITOID ROCKS OF RAGHUNATHPUR-BERO AREA AND JHALDA AREA OF CGGC

CHAPTER-8: DISCUSSION AND CONCLUSION

CHAPTER-1

INTRODUCTION

1.1.INTRODUCTION

1.2.OBJECTIVES

1.3.METHODOLOGY

FIGURES

1.1.Introduction:

Granites (*sensustricto*) and 'granite looking rocks' are the most abundant rock type in the upper continental crust. The continents are dominated mainly by granite. It forms the oldest core of the long-eroded continent and the tall peaks of the youngest mountain range (Myers, 1997). The term Granite has been loosely used to describe a group of rock which consists of quartz and feldspar. Granite (*sensustricto*) refers to a group of silicic plutonic rocks consisting of quartz-plagioclase feldspar-alkali feldspar, with >20% quartz and 10-65 volume % plagioclase feldspar among total feldspar. A still broader term, 'Granitoid' is a generic term defined for a diverse category of coarse grained leucocratic to mesocratic igneous rock that consists of quartz-plagioclase feldspar-alkali feldspar with varied proportions of the felsic components. The other common minerals are biotite, muscovite, hornblende etc, though alkali granites contain sodic pyroxene and amphibole also. The accessory minerals in granitoids include apatite, zircon, tourmaline etc. They embrace a group of rocks, from plagioclase rich tonalities (58% quartz) to alkali rich syenites (78% quartz) and from quartz poor monzonites to quartz rich quartzolites.

Granitoids are coarse to medium grained, leucocratic rocks, consisting of quartz, alkali feldspar and plagioclase feldspar as predominant phases. Grain size of these rock type indicates role of volatiles mainly H_2O during its crystallization. Hornblende and biotite are the dominant mafic phases. Muscovite is common in aluminous granites. Fayalites can be present in some alkali granitoids and orthopyroxene occurs in charnockites (high temperature anhydrous variety of granitoid). The plagioclase feldspars are subhedral in nature whereas quartz and alkali feldspars occur late in the crystallization sequence and are anhedral in nature. The colour of majority of granites ranges from cream to pink, grey to white, which depends on the composition of dominant feldspars. In general granitoids are devoid of any prominent foliation, but some mafic

rich granitoids shows foliation defined by mafic rocks like biotite, amphibole etc. Minor (or accessory) minerals in granitoids include apatite, zircon, magnetite, ilmenite, monazite, titanite, allanite, tourmaline, pyrite, and fluorite, and a host of others, depending on the concentration of incompatible trace elements (that generally concentrate in silicic magmas).

Granitoids are the most abundant rocks in the continental crust, but no single classification scheme has been widely applied. Despite similarity in mineral assemblage, granites varieties may differ in mineral composition, geochemical composition, genesis and mode of occurrence. It was recognized earlier that the granitoids can be formed by different processes, solely from crustal components, or evolved mantle-derived melts, or may be a mixture of crustal and mantle-derived melts (Clarke 1992; Pitcher 1993; Clemens 2012; Brown 2013).Because of this varied complexities, no single classification scheme can describe the granitoids. The traditional IUGS classification scheme for granitoids was based on the modal abundances of quartz, alkali feldspar and plagioclase feldspar. Advantages of this classification scheme are that it is inexpensive, easy to use and truly non-genetic. However, the problem with this classification scheme is that it ignores compositional changes other than feldspar. The granitic rocks can be chemically classified as peraluminous-metaluminous-peralkaline based on the alumina saturation (Shand, 1927; Maniar and Piccoli, 1987). Peraluminous granites have Al_2O_3> ($CaO + Na_2O + K_2O$); Metaluminous: $Al_2O_3 = Na_2O + K_2O$ and peralkaline ($Na_2O + K_2O$)> Al_2O_3.

Harris et al. (1986) recognized four groups for granites of collisional zones: (1) Pre-collisional calc-alkaline granites (volcanic-arc granites) that are mostly derived from mantle modified by a subduction component and are characterized by selective enrichments in LILE; (2) Syn-collision peraluminous granites (leucogranites) that may originate from hydrated bases of continental thrust sheets and are characterized by high Rb/Zr and Ta/Nb and low K/Rb ratios; (3) Late or

post-collision calc-alkaline granites that may be derived from a mantle source and which undergoes extensive crustal contamination, which can only be distinguished from volcanic-arc intrusions by higher ratios of Ta/Hf and Ta/Zr and (4) Post-collision alkaline granites that may originate from mantle lithosphere under the collision zones and which carry high concentrations of both LILE and HFSE.

Sources of granitic magma include two proposed processes: (i) fractional crystallization of mantle - derived basic magma; and (ii) partial melting of old sialic continental crust, leading either to the formation of anatectic plutons or to the contamination of mantle - derived magmas. According to Frost et al., (2001), the Cordilleran-type granites form in arc environments and are characterized by magnesian compositions. In contrast, ferroan granites are the characteristic rock type of extensional environments, where they form by partial melting or extreme differentiation of basaltic magma. Island arc granitoids or the I-type granites are produced above subduction zones. I- type granites are metaluminous, calc alkaline with small to high K contents (Nedelec et al., 2015), relatively sodic, have a wide range of silica content (56-74%) and formed from a mafic, meta-igneous source. S-type granites in continental collision span compositions from granodiorites to granite, peraluminous granites without magnetite. They are peraluminous, relatively potassic with restricted silica range (64-77%) and formed from melting of metasediments. Granite emplacements can be classified with respect to time relation with orogenesis or regional deformation. A-type granites are emplaced in post-orogenic or late-orogenic environment and in rifted continental block. They are mostly hypersolvus granites with alkaline affinity. Mainly A-type granites are peralkaline or metaluminous with enriched silica content and having high contents of LILE, HFSE (Zr, Ce, Nb, Hf, Ta, etc.), REE, K and Zr, but low in trace elements compatible in mafic silicates (Co, Sc, Cr, Ni) and feldspars (Ba, Sr, Eu)

relative to the I-type ones. In general, they intrude during waning phase of deformation of mobile belts or in continental rift zones associated with extensional tectonics. Granites are reported to form in a variety of tectonic settings around the world, either at plate margins or intraplate. Intraplate (within plate) granites can be subdivided based on tectonic criteria into intra-oceanic, intra-continental and attenuated continental lithosphere. Intraplate A-type granitoids have significantly higher Fe/Mg ratios (Fe – number) than typical Cordilleran granitoids and accordingly fall in the "ferroan" granitoid category. Eby (1992) divided A-type granites into two categories according to their Y/ Nb ratios: a group have low Y/Nb ratios and generally low initial $^{87}Sr/ ^{86}Sr$ ratios that formed by differentiation of basaltic magmas of OIB – like (plume) mantle sources; the second group of A-type granitoids characterized by higher Y/Nb ratios (1.2–7) and highly variable initial $^{87}Sr/ ^{86}Sr$ ratios. This group shows a complex petrogenetic history as having a significant mantle component or may be totally of crustal origin. On the other hand, M-type granites are plagiogranites that are localized in oceanic island arcs and represent volcanic arc granites (VAG). They contain a variable amount of pyroxene besides other mafic minerals like hornblende and biotite. M-type granites (plagiogranites) can be subdivided tectonically into subduction-related and subduction-unrelated on the basis of the chemistry of their associated basalts. Plagiogranites are characterized by primitive mantle normalized trace element spider-diagram and chodrite normailized REE patterns with a notable depletion in the most highly incompatible large-ion lithophile (LIL) elements Rb, Ba and K, greater enrichment in Th, Nb and prominent negative anomalies in P and Ti.

Pearce et al., (1984) discriminated tectonic setting of granites based on the trace element composition: ocean ridge granite (ORG), volcanic arc granite (VAG), within plate granite (WPG) and syn-collision granite (COLG). Based on this, Hyndman, (1985) divided granites into

A-type and M-type. Whalen et al. (1987) discriminated the granitoid based on the selective trace elements like Zr, Ce, Y and Nb (normalized to Ga/Al) to discriminate between A-type granites and I- and S- type granites. A more comprehensive basis for chemically subdividing granitoids was given by Frost et al. (2001), in which they subdivided granitic rocks based on the so - called Fe - number (whole– rock Σ FeO/[Σ FeO + MgO] into ferroan and magnesian rocks.

The igneous rock record across the Archean–Proterozoic transition is characterized by sudden changes in mineralogy and chemistry (Condie, 1989; Condie & O'Neill, 2010; Keller & Schoene, 2012; Keller & Schoene, 2018). Archean time was characterized by much higher heat production than today and, as a consequence, higher geothermal gradients, which resulted in the genesis of unique lithologies such as komatiites and massive volumes of tonalite–trondhjemite–granodiorite (TTG) magmas (Condie, 1981; Taylor & McLennan, 1985; Martin, 1986, 1987; Nisbet, 1987), which underwent a transition to reflect a more K-rich granite–granodiorite series in the Neoarchean (2.5–2.8 Ga) and Proterozoic (Barker, 1979; Hillet al.,1992; Smithies & Champion, 2000; Champion & Smithies, 2001; Moyen 2003; Martin et al., 2009; Condie & O'Neill, 2010; Laurent et al., 2014; Halla et al., 2017; Joshi et al.,2017). The maximum values of oxygen isotope ratios (as expressed as $\delta^{18}O=[(^{18}O/^{16}O)_{sample}/(^{18}O/^{16}O)_{VSMOW} - 1]\times1000]$, where VSMOW is the Vienna Standard Mean Ocean Water) in igneous and detrital zircon during the Archean time remained relatively low (~7.5 ‰), which dramatically increased by >10‰ (by ~2.0 Ga) during the Proterozoic (Valley et al., 2005; Dhuime et al., 2012; Spencer et al., 2014, 2019; Payne et al., 2015).

The mineralogical and geochemical changes in igneous rocks during the Archean–Proterozoic transition have been the focus of extensive and long-standing research. This task is challenging as the Archean–Proterozoic transition was one of the most dynamic one in the Earth's

history, because fundamental changes occurred across the geophysical, tectonic, and atmospheric realms. The character of the continental crust changed from being dominantly below sea level (occurrence of pillow basalts in Archean green-stone belts) to subaerial (thick sequences of clastic sediments in the early Proterozoic) (Windley, 1977; Thurston, 1990; Condie, 1994; Arndt, 1999; Kump & Barley, 2007; Flament et al., 2008; Campbell & Davies, 2017). The Earth's atmosphere experienced an increase in oxygen concentrations by about five orders of magnitude during the Archean-Proterozoic transition period (2.3–2.4 Ga) [i.e. the Great Oxidation Event (GOE); Holland, 1984, 2002, 2006; Canfield et al., 2000; Kasting, 2001; Kump et al., 2001; Bekker et al., 2004; Catling & Claire, 2005; Guo et al., 2009; Lyons et al., 2014; Gumsley et al., 2017]. The sudden increase in atmospheric oxygen profoundly affected redox-sensitive elements at the surface of the Earth (e.g. Fe, S, Mo, U; Scott et al., 2008; Partin et al., 2013; Reinhard et al., 2013; Planavsky et al., 2014), which in turn destabilized some minerals during weathering (e.g. pyrite, uraninite, molybdenite; Rasmussen & Buick,1999), while stabilizing new classes of Fe^{3+} bearing clays, phosphorites/ates, and sulfates (Hazen et al., 2008, 2013; Sverjensky & Lee, 2010).

The major granitoid types encountered in the Archean time includes (i) TTG's: they are the most common Archaean granitoid type. They are characterised by sodium-enrichment (K/Na < 0.3) and strongly fractionated REE patterns ($[Ce/Yb]_N$ = 10–40) with no significant Eu anomaly (Martin, 1994). (ii) Biotite-bearing granites: Most of the "Late Archaean, K-rich plutons" belong to this type (Sylvester, 1994). They are biotite- (and rarely hornblende-) bearing monzo- to syenogranites to granodiorites, with high K/Na ratios (>1), moderately fractionated REE patterns ($[Ce/Yb]_N$ < 30) and a significant negative Eu anomaly. These granites have been demonstrated to be products of partial melting of pre-existing TTG gneisses (Querré, 1985; Jahn

et al., 1988; Collins, 1993; Champion and Sheraton, 1997; Frost et al., 1998; Champion and Smithies, 1999). (iii) Sanukitoids: They are defined as diorites to granodiorites with high Mg# (>70), associated with high Ni and Cr contents; they are also alkali and LILE-rich ($Na_2O + K_2O$ > 3% for SiO2 = 50%; Ba > 800 ppm; Sr > 800 ppm). REE patterns are strongly fractionated ($[Ce/Yb]_N$ = 10–50) with high LREE contents (Ce_N > 100) and no, or slightly negative, Eu anomalies. (iv) Peraluminous granites: they are occasionally reported. They are muscovite-bearing (and rarely garnet-bearing) leucogranites with high K/Na ratios (up to 2.5), moderately fractionated REE patterns ($[Ce/Yb]_N$ < 30), with a strong negative Eu anomaly, and Rb- and Th-rich. (v) Peralkaline granites: Minor amount of this type have also been reported from the Superior Province (Laflèche et al., 1991; Bourne and L'Heureux, 1991), Yilgarn Craton (Champion and Sheraton, 1997) and Pilbara Craton (Champion and Smithies, 1999) and Eastern Dharwar Craton (EDC), in South India (Jayananda et al., 2000).

It is during the late Paleoproterozoic to Meso-Proterozoic ages (1.9-0.9 Ga) that the anorthosite-mangearite-charnockite-granite (AMCG) assemblages are commonly observed. Granites of this association are often A-types and display a typical texture named as rapakivi texture. It is in the Proterozoic granites that muscovite and tourmaline become important phases. High-K granites from the Proterozoic terrain shows higher concentrations of Zr, Hf, Th, Ba, Sr, K and ΣREE than their late Archaean counterparts. The key trace element ratios used to distinguish between the magmas of high-K granites from both the ages, involve an incompatible element and middle to heavy REE (i.e. Zr/Sm, Zr/Y, Zr/Nb, Ba/Nb, Th/Ta) as well as the K_2O/Na_2O ratio. Partial melting of the juvenile igneous rocks including the TTG's and the greenstones were prerequisite for the generation of the high-K granites in the Archaean ages, while partial melting of the more evolved crustal rocks including the Archaean rocks were needed for the

generation of those in the Proterozoic time. At the Archaean-Proterozoic boundary, the production of high-K granitic magmas signalled a change from the intra-crustal recycling of pre-existing material to the formation of the Neoarchaean continental crust with the addition of juvenile mantle derived material. Additionally, it signalled the completion of the global stabilisation of the Archaean Cratons.

Proterozoic period witnessed a series of orogenic events related to assembly and breakup of the supercontinents. During 1.8-1.7 Ga, the continents coalesced together to form a giant supercontinent Columbia, and then regrouped to form Rodinia (1.0-0.9 Ga) supercontinent (Hoffman 1991; Li 1999, 2004, Li et al., 2008; Rogers and Santosh 2002, 2003, 2004; Meert and Santosh 2017; Nance et al., 2014; Zhao et al., 2004a, 2004b). These Proterozoic tectonic events are well preserved in the form of distinct orogenic belts from different continents and discrete Proterozoic terrains. An overall apparent clockwise rotation of the continents after the Columbia phase gives the configuration of the Rodinia supercontinent in ~1.0-0.9 Ga. Imprints of Rodinia tectonics are well documented from the CITZ (Lippolt and Hautmann, 1995), ADFB (Buick et al., 2006; Bhowmik et al., 2010; Deb et al., 2001), EGMB (Chatterjee et al., 2010), CGGC (Maji et al., 2008; Sanyal and Sengupta, 2012; Chatterjee et al., 2010; Chakraborty et al., 2018) and SMGC (Chatterjee, et al., 2007) of India; Albany-Fraser hills of Australia; Bunger Hills of East Antarctica (both referred in Harris 1995); Yangtze block of South China (Zhou et al., 2002); Grenville province of Laurentia (Kalsbeek, et al., 2008); Sunsas orogen and Putumayo orogen of Amazonia (Rizzotto et al., 2014). Magmatic rocks during Rodinia Supercontinent cycle, having both alkaline-anorogenic and calc-alkaline-orogenic affinity can be observed from India, Australia, Antarctica, South China, and South Africa. Reports on the alkaline magmatism from different parts of the world during Neoproterozoic age are well documented by the works of Li et

al.,(2002); Upadhyay et al., (2008); Wang et al., (2003a) etc. The alkaline rocks of Neoproterozoic age from India can be correlated with that of the alkaline rocks of Australia, Lauretia, Madagascar, South Africa, South China etc.

Occurrences of alkaline rocks of Proterozoic age in India are well reported from the works of Santosh et al., 1989; Natarajan et al., 1994; Kumar et al., 1998; Upadhyay et al., 2006a, b; Upadhyay 2008; Mukhopadhyay et al., 2011a; Renjith et al., 2014; Chakraborty et al., 2016; Hippe et al., 2016; Ackerman et al., 2017; Das et al., 2018; Ranjan et al., 2018; Paul et al., 2020 etc. alkaline rocks are mainly reported from the western part (Rajasthan), eastern part (West Bengal and Odisha) and southern part (Tamil Nadu and Kerala) in India. Alkaline granites having ages similar to or slightly younger than orogenic granites are common in many orogenic belts all over the world (Bonin, 1990, 2004, 2007; Litivinovsky et al., 2011). Typical examples of association of orogenic-anorogenic granitoid are observed in Variscan orogenic belt (Bonin, 2004, 2007), late Paleozoic felsic magmatism of Transbaikalia, Russia (Litvinovsky et al., 2011), Neoproterozoic Tuareg belt of Africa (Liegeois et al., 1998), Nagarparker belt in Pakistan (Rehman et al., 2018) and Eastern Ghats Mobile belt in South India.

Similar observation has also been noticed in the NPSZ where S-type granitoid rocks of Raghunathpur-Bero area shows similar crystallization age (1000Ma; Chakraborty et al., 2018) with that of the alkaline AR granites of Jhalda area (966.7 ± 7.0Ma; this study). They present a unique example of contrasting granitoid magmatism during orogeny to orogeny-anorogeny transition.

Granitoid rocks of varied types can be encountered along the entire stretch of North Puruliya Shear Zone (NPSZ) of Chhotanagpur Granite Gneissic Complex (CGGC) (Fig. 1.1). This NPSZ has a roughly E-W trend but more precisely it is WNW in the western sector, E-W in the central

sector near Jaipur and ENE in the eastern sector near Para-Anara area (Ray 2008). According to the early workers like Dasgupta et al., (2000), publication of GSI (1977), this shear zone appears to die out towards W of Jhalda region, but the WNW continuation of this shear zone can be traced further west as the porphyritic granite gneiss to the south of Brajapur and aegirine-riebeckite granite of Perehandopahar and Dimra (Das et al., 2007). The Shear Zone is characterised by occurrence of the following rock types such as: i) sheared alkali granite and syenite (PerhandoPahar, Dimra; Das et al., 2007); ii) sheared and brecciated quartzite (Jaipur); iii) barite and Uranium-Thorium mineral-bearing pegmatite (Nawahatu; Das, 1977; Sarkar, 1977; Baidya and Chakravarty, 1988; Baidya, 1992; Sarkar et al., 1993; Sarkar et al., 2001; Som et al., 2002) ; iv) carbonatite (Gandhudih, Das and Nandi, 1995); v) apatite-magnetite chert rock (Panrkidih and Lanka, Das, 1977) and vi) ultramafic rocks having different modes of occurrence and mineralogical character having the effect of shearing on microscopic scale (Das et al.,2009). The non-foliated quartzite of Jabar hill (23°28'05" N &85°59'48" E) is the finest example of pure quartzite rock which consists of quartz entirely, with few trace elements like zircon, rutile, magnetite etc and represents the oldest rock group in the area. The occurrences of Calc-silicate rock of the Archean era is also reported from the south-eastern part of Jabar range (Baidya, 1981). Belamu hill (located just 1.2 km east of Jabar) primarily consists of intrusive granite rock of the Proterozoic period. The granitic rocks consist mainly of quartz, microcline, biotite, Na-rich plagioclase, garnet, sphene and magnetite (Baidya, 1981). Muscovite rich granite variety is also observed in this hill area.

The area of the present research work is mainly concentrated in two sectors along the North Puruliya shear zone of CGGC (Fig. 1.1) in Puruliya district, West Bengal: Raghunathpur-Bero area in the north-eastern part of the Puruliya town and Perehando Pahar and Dimra region to the

west of Jhalda in the north-west part of the Puruliya town. These two areas are about 58 km apart. They are the representative of two contrasting granitoid types exposed along the shear zone. The Raghunathpur-Bero area comprises of megacrystic granite granite, garnetiferous granite gneiss and pink granite while Perhando Pahar and Dimra represents the aegirine-riebeckite granite variety.

1.2.Objectives:

- Detailed geological mapping of Raghunathpur and Jhalda areas to understand the actual disposition of different types of granitoid rocks, their field relationship with adjoining meta-sedimentary and meta-igneous country rocks and their relative ages.
- Field and petrographic studies of the granitoid rocks of Raghunathpur and Jhalda area to characterize different petrographic types and to correlate them with same rock groups in other parts of India
- Geochemical data analysis and interpretation of the samples in order to understand the source of the parent magma, its nature and magma generation process
- Geochronological study of the granitoids of CGGC to determine the absolute age of formation of the rocks
- Comparative study and correlation of the granites of Jhalda, Raghunathpur area with other Proterozoic terrains of India and abroad
- Attempt will be made to develop a petro-tectonic model using field and laboratory information for the generation of CGGC granitoids

1.3.Methodology:

- Geological maps on 1:50,000 scale was prepared, which indicates the exposure of different types of granitoid rocks and their relationship with adjoining country rocks and other mafic intrusives. For this purpose, GPS was used for precise location and conventional compass-measuring tape was used for geological mapping.

- The fresh rocks were preferred for sampling purpose. The outcrops were thoroughly mapped, and representative samples were collected systematically from each variety of granitoid types.

- Thin sections of rocks were selected from different granitoid types. Detailed studies of the thin sections were carried out in order to know the mineralogical and textural variations within the granitoid rocks. The important characters (shape, size, zoning, and twinning) of minerals were studied in detail in order to have an idea about the nature of deformation and metamorphism.

- Polished thin sections were prepared for petrographical and mineralogical studies in PLM (Polarizing Light Microscope) and Scanning Electron Microscope/X-ray Microanalysis.

- Thin sections were carbon coated for analysis in Electron Microprobe analysis (EPMA) in order to get high precision mineral compositional data.

- The point counter and NIS software were used for micrometric analysis of minerals in selected specimens in order to get a reliable estimate in volume percent of major minerals in a slide.

- Rock samples were crushed and grinded into powder form for whole rock geochemical analysis using X-ray Fluorescence (XRF) spectrometry and Inductively Coupled Plasma-Mass Spectrometry (ICP-MS).

- U-Pb zircon dating will be carried out by LA-ICP-MS at Department of Earth and Planetary Systems Science, Hiroshima University.

- U-Th-total Pb monazite dating will be carried out at Natural Science Center for Basic Research and Development, Hiroshima University using EPMA.

- All the above stated data were interpreted and co-related with the other similar granitoid types of India and abroad to create a petro-tectonic model on the generation of these granitoids in the prevailing tectonic setting.

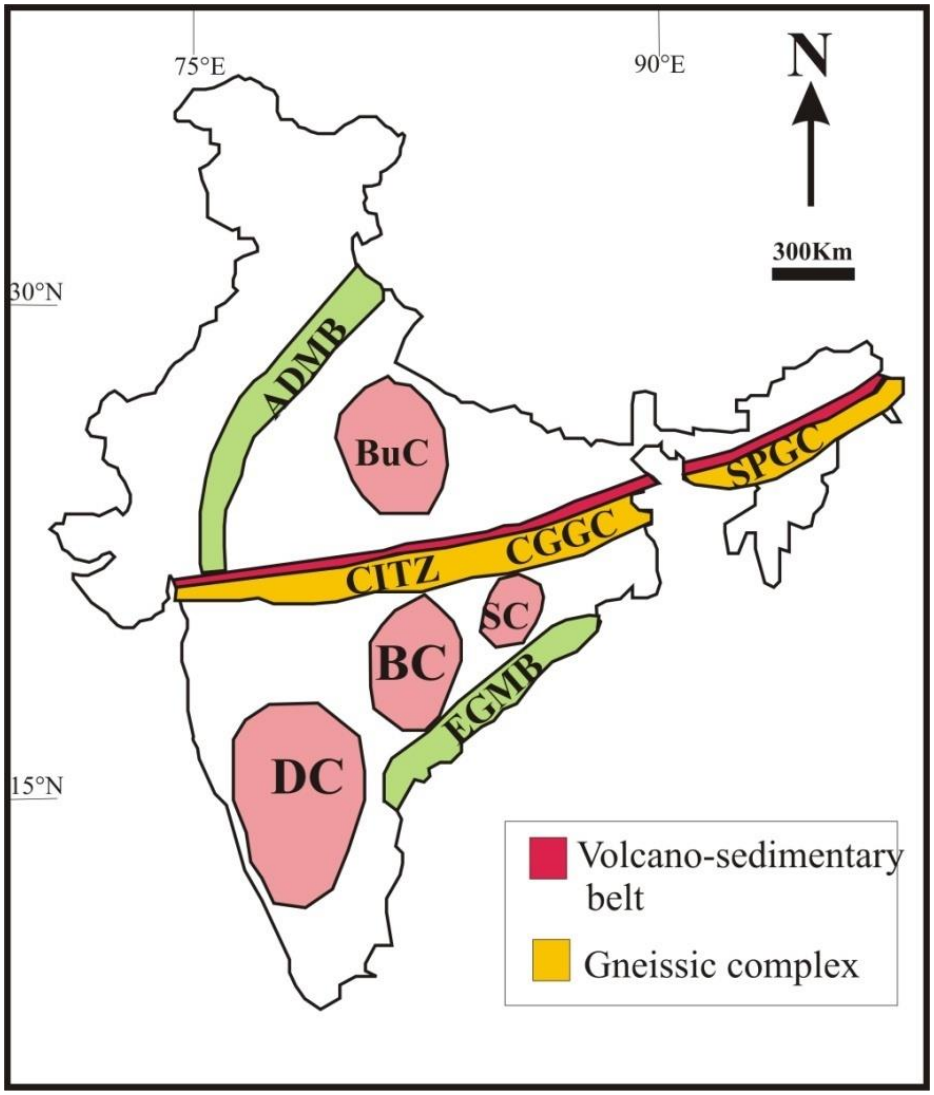

Figure 1.1 Map of India showing the approximately 1500 km-long ENE–WSW-trending orogenic belt consisting of Central Indian Tectonic Zone (CITZ), Chotanagpur Granite Gneiss Complex (CGGC) and Shillong Plateau Gneissic Complex (SPGC). Northern part of it comprises the North Indian Block with Bundelkhand Craton (BuC) as its nucleus and bordered by Aravalli Delhi Mobile Belt (ADMB) to the west. The southern part of it comprises the South Indian Block which consists of Dharwar Craton (DC), Bastar Craton (BC) and Singhbhum Craton (SC).

CHAPTER-2

GEOLOGICAL SETTING

2.1. EXTENSION AND DISPOSITION OF CGGC

2.2. CLASSIFICATION OF CGGC ROCKS

2.3. METAMORPHIC AND DEFORMATION EVENT IN CGGC

FIGURES

TABLES

The Chhotanagpur Granite Gneiss Complex (CGGC) is a Proterozoic orogenic belt located in the eastern part of India (Fig. 2.1 and Fig. 2.2). It has suffered multiple phases of deformation, metamorphism and magmatic activity since the Paleoproterozoic age. This high grade gneissic terrain is sandwiched between two low-grade mobile belts i.e. the North Singhbhum Mobile Belt (NSMB) at south and the Mahakoshal Mobile Belt (MMB) at north (Saha, 1994; Roy and Devrajan, 2000). It is composed of supracrustal metasedimentary enclaves bearing basement gneisses and multiple intrusives of varying ages and varying compositions ranging from ultramafic to acidic and sodic alkaline to ultrapotassic. In most parts, the pervasive gneissic foliation of the CGGC has a general trend that varies from an E-W to an ENE-WSW direction with moderate to steep dip towards the north.

2.1. Extension and Disposition of CGGC:

The Chotanagpur Gneissic Complex (also known as Chhotanagpur Granitic Gneiss Complex) is a vast (1,00,000 square kilometer area: around 500 km in length and 200 km in width of the belt), ENE–WSW high grade terrane in the eastern part of the CITZ (Dunn, 1929; Ghose, 1983, 1992; Sarkar, 1988; Mazumdar, 1988; Mahadevan, 2002).CGGC is dispersed along the states of Jharkhand, Chhattisgarh, Orissa, Bihar and West Bengal (Acharyya, 2003; Mahadevan, 2002; Sharma, 2009). It is bounded in the north by Gangetic alluvium and in the northeast by Rajmahal basalt. In the south it is separated from the Eastern Ghat Mobile Belt by the Singhbhum mobile belt and the Archean Singhbhum craton (Saha, 1994). The east-west trending crustal scale shear zone i.e. the South Purulia Shear Zone (SPSZ) or the Tamar-Porapahar-Khatra Shear zone marks the contact between CGGC and Proterozoic rocks of the North Singhbhum Fold Belt (NSFB) in the southern part (Mazumdar, 1988). The eastern edge of the CGGC is covered in Ganges Brahmaputra alluvial deposits, which separate it from the Shillong-Meghalaya gneissic complex

(SMGC) (Chatterjee et al., 2007). The younger Gondwana sediments separate the CGGC in the western part from the central Indian tectonic zone (CITZ). The foliation trends in the CGGC and CITZ are approximately ENE-WSW to E-W and both complexes abut a common rift zone in the north (Acharyya, 2003). The south-eastern boundary is covered by tertiary deposits of West Bengal. The western part is bordered by younger Gondwana sediments of the Son-Mahanadi Valley, and supracrustal rocks and granitoids of the Palaeoproterozoic Mahakoshal Group of the Central Indian Tectonic Zone (CITZ), which seperates CGGC from central CITZ and the northwestern margin is covered by Vindhyan sediments. Recent studies have discovered that the eastern boundary of the CGGC can be extended further beneath the thick cover of the Gangetic alluvium in the Maddhapara of Bangladesh (Hossain et al., 2007). This observation leads to the fact that boundaries of the CGGC originally can be extended further beneath the younger unmetamorphosed sediments cover and extrusive. The structural tendency of the CGGC is similar to the CITZ of central India and about ENE-WSW to E-W except in the northeastern part (Acharyya, 2003).

2.2. Classification of CGGC rocks

Ghose (1983) and Banerjee (1991) classified CGGC into three distinct lithostratigraphic units: crystalline basement, older metasediments and late intrusive. They considered that these units are the products of three major orogenic phases- Chhotanagpur orogeny (1.6-1.5 Ga), the Satpura orogeny (0.90 – 0.85 Ga) and Munger Orogeny (0.42 – 0.35 Ga). Singh (1998) opined that the rocks of the CGGC can only be classified on the basis of lithodemic groups, rather than lithostratigraphic groups. According to him, the rocks do not follow the law of superposition. He proposed a three-fold classification where the CGGC group is the oldest followed by Koderma and Rajgir groups. They further sub-divided CGGC into three main suites: (a) the enclave suite

comprising the granulit pockets of the Dumka, Puruliya and Palamau areas, along with low to medium grade schist, BIF, marble and mafics of Chakrabanda, Sua and other areas; (b) the Chatra Gneiss suite comprising several granite and tonalitic gneisses and migmatites and (c) the intrusive rocks comprising haplogranite, pegmatite and quartz veins.

Mahadevan (2002) sub-divided the rocks of CGGC into five divisions running E-W direction: (a) the south Palamau-Gumla-Ranchi-Puruliya belt south of the Damodar Valley Basin, (b) the Daltonganj-Hazaribag-Dumka belt between the Damodar and Koel river basin, (c) the north Garhwa-Chatra-Giridi-Deoghar belt north of the Koel river basin, (d) the Bihar Mica Belt, north of the Chhotanagpur plateau and (e) the Rajgir-Kharagpur belt north of the Bihar Mica Belt.

Later, Sanyal and Sengupta (2012) divided CGGC into following sectors for the convenience of description:

(i) the Bero–Saltora–Santuri (BSS) sector near Bankura, West Bengal

(ii) the Murguma–Purulia–Raghunathpur(MPR) sector, West Bengal;

(iii) the Jabarban–Belamu–Nawahatu (JBN) sector, West Bengal;

(iv) the Garu–Baresanr (GB) sector, Jharkhand;

(v) the Massanjor–Baglan–Rangaliya (MBR) sector, Jharkhand;

(vi) the Deoghar–Josidihi–Rohini (DJR) sector,Jharkhand;

(vii) the Dumka–Jamua–Ghormara (DJG) sector, Jharkhand;

(viii) the Ramanujganj–Tatapani (RT) sector, Chattisgarh;

(ix) the Raikera – Kunkuri (RK) sector, Chattisgarh;

(x) the Bihar Mica Belt (BMB), Bihar

Sector 1: The Bero–Saltora–Santuri (BSS) sector:

This sector lies in the SE part of the CGGC and many researches have been done in this sector since the early 1970s (Manna & Sen 1974; Roy, 1977; Bhattacharyya & Mukherjee, 1987; Sen & Bhattacharya, 1993; Mukherjee et al., 2005; Ghose & Chatterjee, 2008; Maji et al., 2008). The country rock of this part includes migmatitic quartzo-feldspathic gneiss (quartz+ K-feldspar+ plagioclase+ garnet + biotite + hornblende + orthopyroxene) containing enclaves of metapelitic gneiss (almandine rich garnet + sillimanite + K-feldspar + quartz + hercynite + ilmenite + biotite) which are successively intruded by massif type anorthosite (plagioclase + orthopyroxene+ clinopyroxene+ ilmenite+ hornblende+ biotite+ chlorite + quartz+ garnet) and porphyritic granitoids (quartz + K-feldspar + plagioclase + hornblende + garnet + biotite). The subsequent magmatic rocks include lenses of mafic granulite (orthopyroxene + clinopyroxene+ plagioclase + hornblende+ garnet+ quartz) and calc-silicate gneiss (clinopyroxene + scapolite + wollastonite + plagioclase + K-feldspar + calcite + quartz) (Sanyal and Sengupta, 2012). This sector suffered at least three phases of deformation (D1–D3) and four phases of metamorphism (M1– M4) (Maji et al., 2008). Alignments of the granulite-facies minerals (garnet + orthopyroxene in quartzofeldspathic rock and garnet + sillimanite + spinel in metapelite) define the S1 foliation planes which were developed along the axial planes of D1 folds found in calcsilicate rocks and hardly in metapelites (Sanyal and Sengupta, 2012). The S1 planes were coaxially deformed by D2-D3 folds. The most prominent foliation plane in this sector is the S2 plane which developed parallel to the axial plane of the D2 fold. D3 folds locally have a sheath-like geometry (Sanyal and Sengupta, 2012). The massif-type anorthosite or the Bengal anorthosite is reported to be emplaced during the interlude period of the D1 and D2 deformations (Bhattacharya & Mukherjee, 1987; Maji et al., 2008), whereas the protolith of a suite of

granitoids to fayalite-bearing syenitic gneisses are reported to be intruded during the interlude period of the D2 and D3 deformations (Maji et al., 2008). The recent U–Pb date of zircon in anorthosite shows that the Bengal anorthosite was crystallized at around 1.55 Ga (Chatterjee et al. 2008). Therefore, the maximum age of D2 deformational events is implied to be 1.55 Ga. Both D2 and D3 deformations are associated with amphibolite-facies mineralogy (M2-M3) that replaces the granulite-facies minerals of M1 (Maji et al., 2008). M4 metamorphism resulted into the formation of coronal garnet, which generally occurs as a symplectic intergrowth with ilmenite and/or quartz. M1 metamorphism is considered to be occurred during 1.70 Ga which is estimated from the Rb–Sr whole-rock isochron ages of the high-grade gneisses and the calculated ages of monazite inclusions present in M1 garnet (Chatterjee et al., 2010; Sanyal and Sengupta, 2012). The development of the S2 fabric along with the hydration of M1 assemblages (M2-M3) are suggested to be occurred between 1.3 and 1.1 Ga by monazite dating (Maji et al., 2008). The M4 metamorphism occurred at around 650±50°C temperature and 4–5 kbar pressure between 1.0 and 0.95 Ga as estimated from the chemical date of monazite in the M4 garnet corona (Maji et al., 2008).

Sector 2: The Murguma-Purulia- Raghunathpur (MPR) sector:

This sector represents the southernmost part of the CGGC and adjoins the Palaeoproterozoic Singhbhum Mobile Belt and has been studied by many research workers (Dunn, 1929; Sen, 1956, 1959; Baidya et al., 1987, 1989; Ray Barman et al., 1994). Migmatitic quartzofeldspathic gneiss with stromatic leucosomes (locally with garnet) and well-foliated mesosome consisting of biotite and hornblende are the most dominant rock types in this area. The gneissic banding in the quartzo-feldspathic rock has an east–west trend similar to the trend of axial planes of a set of fold demarcated by calc-silicate bands. The gneissic bandings are folded by two generations of

coaxial folds (D2- D3). These deformations are followed by D3 deformation which resulted into broad warping of the east–west-trending gneissosity. Field features show that intrusion of porphyritic charnockite (plagioclase + microcline + quartz + hornblende + biotite+ orthopyroxene + garnet) occurred between the D1 and D2 folding events (Ray Barman et al. 1994). Rb-Sr whole-rock dating of porphyritic charnockite and migmatitic gneiss gave an age of 1.07 and 1.17 Ga respectively (Ray Barman et al., 1994) which are interpreted as the ages of the protolith formation of these rock types (Ray Barman et al., 1994).

Sector 3: The Jabarban-Belamu-Nawahatu- (JBN) sector:

This sector lies in the NE part of Puruliya, West Bengal. The country rocks include migmatitic to non-migmatitic granite gneisses containing enclaves of metapelite and calc-gneisses. The protoliths of composite gneiss is intruded by amphibolite and biotite-bearing porphyritic granite (locally pegmatite) respectively (Baidya et al., 1989). The east–west trending gneissic banding defines S1 plane which is axial planar to D1 folds present in the mafic bands. S1 foliation plane is again folded by D2 deformation resulting into a fold with east–west trending axial plane. This D1 and D2 folds were superposed by D3 folds and developed north-south-closing open warps. Structural features suggest that the biotite-bearing porphyritic granite was emplaced during the interlude period of the D1 and D2 deformations (Baidya et al., 1989). K-Ar dates from the composite gneiss and biotite-bearing porphyritic granites provide an age range between 1.08 and 0.80 Ga (Sarkar, 1980; Baidya et al., 1987).

Sector 4: The Garu-Baresanr (GB) sector:

This sector occurs in the north of the Damodar Valley Gondwana basins and in the central part of the CGGC. The country rock includes migmatitic to non-migmatitic composite gneisses which

is intruded by porphyritic granite (Mazumder, 1988). Bands and lenses of graphite-bearing khondalite and calc-silicate rocks occur within the host gneiss. Mafic intrusive like dismembered bodies of amphibolite are also reported (Mazumder, 1988). In southern areas of Daltonganj, base–metal deposits hosted in ultramafic rock are reported (Ghose, 1992). No detail petrological or geochronological information is available from this sector.

Sector 5: The Massanjor-Baglan-Rangalia (MBR) sector:

This sector is situated near the eastern edge of the CGGC, north of the Damodar Valley Gondwana Basin. The principal rock type of this sector is migmatitic charnockite which is in places retrogressed to hornblende+ biotite-bearing quartzofeldspathic gneiss. These migmatitic charnockite contains bands of khondalite, Mg-Al granulites, calc-silicates and mafic granulites and was intruded by porphyritic charnockite. This sector has also suffered three deformation phases (D1-D3) (Sanyal and Sengupta, 2012). D1 deformation resulted into the formation of east–west trending migmatitic banding in the charnockites. The intrusion of porphyritic charnockite occurred between D1 and D2 and a crude foliation plane parallel to the axial plane of D2, developed in the porphyritic charnockite (Sanyal and Sengupta, 2012). Geothermobarometric calculation (Lee & Ganguly, 1988; Bhattacharya et al., 1991) involving garnet, pyroxene and plagioclase mineral phases gave results of 700±50°C, 6.5±1 kbar, which depicts the metamorphic condition during D2 deformation. The mineral assemblage in the mafic dykes indicates that the D3 deformation was accompanied with amphibolite-facies conditions (Sanyal and Sengupta, 2012). The protolith ages of migmatitic and porphyritic charnockite are reported to be 1.62±0.05 and 1.51± 0.05 Ga, respectively (Acharyya, 2003).

Sector 6: The Deoghar–Josidihi–Rohini (DJR) sector:

The country rocks of this sector (Migmatitic quartzofeldspathic gneiss and augen gneiss) are intruded by a swarm of mafic dykes (Ghosh & Sengupta, 1999; Ray et al., 2011) and several generations of pegmatite veins (Ghosh & Sengupta, 1999; Mahmoud et al., 2008; Ray et al., 2011). This kind of mafic dykes and pegmatite veins of different generations are also reported from other sectors of the CGGC, and these intrusive phenomenons are considered to be the result of regional extension under brittle–ductile regimes (Ghosh et al., 2008; Mahmoud et al., 2008). From the preserved structural elements three sets of folds (D4-D6) in the mafic dykes are identified which involved and succeeded the development of the gneissic banding in the host felsic gneiss (pre-D4) (Sanyal et al., 2007; Ray et al., 2011). D4 and D5 are coaxial folds and resulted into north–south- to NNE–SSW-trending regional foliations parallel to the axial planes of D4 (and rarely D5) folds (Sanyal and Sengupta, 2012). The third generation folds (D6) are east– west open warps. This sector bears evidence of two stages of metamorphism M1 and M2. The M1 granulite-facies metamorphic event caused the formation of stromatic leucosomes in the quartzofeldspathic gneiss. The next amphibolite-facies metamorphic event (M2) was accompanied with the D4-D6 folding and caused partial to complete replacement of the magmatic mineralogy of mafic dykes by hornblende-bearing assemblages (Sanyal and Sengupta, 2012). Quantitative geothermobarometry and numerical analyses of appropriate bulk compositions by Ray et al (2011) suggest a P–T range of 7±1 kbar and 600–750°C which is considered as the peak metamorphic condition during M2.

Sector 7: The Dumka-Jamua-Ghormara (DJG) sector:

This sector is situated at the NE part of the CGGC between the DJR sector and the Mesozoic Rajmahal volcanics. The country rock in this sector is migmatitic quartzo-feldspathic gneiss containing enclaves of khondalite, mafic rocks and calc-silicate rocks. Coaxial folds D2-D3 with

general east-west trending axial planes are reported to be present in the quartzo-feldspathic gneiss in the eastern domain whereas folds with general north-south axial planes are reported in the mafic dykes in the western domain (Sanyal and Sengupta, 2012). It has been also reported that intrusive bodies of syenite and anorthosite were emplaced during the interlude period of D1 (S1) and D2 deformation events (Bhattacharya 1976; Sanyal et al. 2007). Mainly two phases of high grade metamorphism and multiple phases of amphibolite-facies metamorphism have been reported from this sector (Sanyal and Sengupta, 2012). The high grade metamorphism resulted into the formation of migmatitic bandings in khondalite and charnockite which was followed by retrogression of charnockites into quartzofeldspathic gneisses (Sanyal et al., 2007). The P-T condition of first high grade event, which caused the formation of migmatitic bandings in khondalite, is reported to be 930–950 °C and 5–6 kbar by Sanyal et al., (2007). The P-T condition of second high grade event is not clear. However, the crystallizing P-T condition of orthopyroxene in quartzo-feldspathic gneisses is calculated by Pattison et al., (2003) and reported to be 700–800 °C at 5–6 kbar which can give an idea about the P-T condition during the formation of migmatitic charnockite. Ray Barman et al. (1994) reported a similar P-T condition for the nearby syenitic gneisses i.e. 750– 780 °C and 4–6 kbar. The oldest U-Th-Pb chemical dates of the monazite grains from the cores of porphyroblastic garnet in felsic (charnockite) gneisses and khondalites (Chatterjee et al., 2010) showed that the age of first ultrahigh-temperature metamorphism in the khondalite enclaves is approximately 1.87 Ga. Similarly, the maximum age of the second high-grade metamorphism that developed the gneissic banding in charnockites is reported to be approximately 1.66 Ga from the U-Th-Pb chemical dates of monazite present in the rim of garnet porphyroblasts, as well as in the quartzo-feldspathic matrix of the charnockite gneiss and khondalite (Sanyal et al., 2007; Chatterjee et al., 2010). U-Th-Pb

chemical dates of monazite from felsic gneisses and metapelite (khondalite) enclaves are also reported to give another two age ranges i.e. c. 1.1–0.93 Ga and c. 0.85– 0.75 Ga (Chatterjee et al., 2007, 2010; Sanyal et al., 2007), among which the second age range (0.88– 0.83 Ga) is considered to be accompanied with the high-pressure event having regional east–west compression (Chatterjee et al., 2010).

Sector 8: The Ramanujganj–Tatapani (RT) Sector:

The westernmost part of the CGGC and adjoining Mesozoic Gondwana rocks of the Mahanadi Basin constitute this sector. This sector is characterized by presence of a NW–SE trending domal structure near Ramanujganj area and an alternate sequence of metapelite and psammopelite rocks (Patel, 2007; Patel et al., 2007). The overall metasedimentary sequence including the metapelites, psammopelites and quartzite is intruded by granitic to grano-dioritic rocks in the western and northern part of the domal structure. Three sets of folds viz. D1-D3 have been identified in this sector among which coaxial D1-D2 folds form NW–SE-trending axial-planer schistosity. Interference of D2 and D3 folds is presumed to be the cause of formation of the regional domal structure. Calc-silicate rocks having a mineral assemblage of vesuvianite + grossular garnet + diopside + wollastonite + quartz are also reported to occur in the south of Ramanujganj area.

Sector 9: the Raikera–Kunkuri (RK) sector:

The Raikera–Kunkuri sector occurs in the southern part of RT sector of the CGGC. This area consists of an inter-banded sequence of pelitic schist (with chlorite, biotite and hornblende schist), pebbly quartzite and dolerite dykes/sills which are intruded by voluminous suites of biotite- and muscovite + biotite-bearing granitoids (reviewed in Singh & Krishna, 2009). Rb–Sr

whole-rock isochron ages by earlier workers, show an approximately 1.0±0.05 Ga age for the older granitoids and an approximately 0.81±0.05 Ga age for the younger granitoids of this sector (Singh & Krishna, 2009). The pink granitoids are characterized by Y mineralization. The grey granitoids of this sector is reported to be intruded syn-tectonically with respect to the D3 folds (Singh & Krishna 2009). Singh & Krishna (2009) has correlated the granitoid intrusives of this area with the heavy-metal-bearing granitoids to pegmatoids of the Bihar Mica Belt.

Sector 10: The Bihar Mica Belt (BMB) sector:

The BMB sector lies in the north of the Hazaribagh Plateau at the northern extremity of the CGGC and is famous for the occurrence of one of the world's best industrial grade mica deposits within it. This belt gets obscured in the northern part because of the cover of thick Gangatic alluvium (reviewed in Mahadevan, 2002). This belt is characterized by a group of metamorphosed arenaceous and argillaceous rocks interbanded with hornblende schist, ortho-amphibolite and calc-silicate rocks which were intruded by granitoid rocks, dolerite dykes, gabbro-anorthosite and mica pegmatites. The mica pegmatites act as a host of rare earth elements (REEs) and rare metal deposits (Mahadevan, 2002; Singh & Krishna, 2009). A conglomerate horizon occurs at the base of the BMB belt (Ghose & Chatterjee, 2008). Three phases of deformation has been reported in this area. Emplacement of granitoids occurs during syn- to post- D2 folding, whereas emplacement of mica-bearing granite and pegmatite of different generations occur during pre-D2 to post-D3 folding (Mahadevan, 2002). In case of metamorphic evolution in this sector, Mahadevan (2002) reported an amphibolite grade metamorphism of the metasedimentary rocks and the mafic intrusions based on petrographic studies. Whole-rock and Rb–Sr mineral isochron ages from granitic rocks of the BMB provide the oldest age (~1.6 Ga) for the granite that intruded the sediments of the BMB as well as relatively younger age range of

1.3–1.1 Ga for younger granite intrusives (Pandey et al., 1986a, b). Sedimentation age in the BMB is suggested to be confined in the time span of 1.70–1.65 Ga, based on the Pb/Pb age of galena from base-metal deposits (Singh et al., 2001). This age range matches with the Rb–Sr whole-rock age of older intrusive granite (Pandey et al., 1986a, b). The oldest REE-rare metal-bearing mica pegmatites of the BMB were emplaced at around 0.96±0.05 Ga (Pb/Pb age; Vinogradov et al., 1964). A similar U–Pb and Pb/Pb age range (0.91±0.02 Ga) is also reported from the Columbite–Tantalite minerals of pegmatite (Krishna et al., 2003).

2.3. Metamorphic and deformation events in CGGC

The migmatites, granitoid gneiss, nepheline syenite, granulites and metapelites of CGGC recorded polyphase (D1, D2 and D3) deformation history (Ghose, 1971; Sengupta et al., 1964; Ghose, 1983; Roy, 1977; Chatterjee, and Sengupta, 1980; Sarkar, and Jha, 1985; Ray Burman et al., 1994; Maji et al., 2008; Karmakar et al., 2011), where the peak granulite facies metamorphism being attained during the early phase of deformation. The shape of the early folds (D1) on the bedding surface of the metapelite and of the D2 folds on schistosity/foliation structures is described as tight, isoclinic, mostly receding folds. The attendant foliations including mylonitic foliation and schistosity are parallel, indicating their repetitive generation with gradual progress in deformation from first phase to second. Although it is not very clear in the field, the superposition of D2 folds on D1 folds in the Type 3 pattern is indicated. The D1-D2 composite is folded (during D3) into a series of east-west closing upright, non-cylindrical, asymmetric, slip-related folds. The overall granoblastic texture, undulose texture, subgrain formation in feldspar, and the evolution of the core and mantle structure by feldspar and quartz grains suggest that the evolution of the textures and microstructures of metasedimentary and meta-igneous rocks suggesting that it was caused by abrupt recrystallization at deep crustal

levels, i.e. regions of granulite facies metamorphism. Moreover, the development of small-scale shear bands in conjugate set points to the role of N-S regional compression across the foliation, during the D3 phase. Moreover, the grain size distribution of the porphyroclasts of MGG is self-similar to self-affine, as the size range is recorded over four orders of magnitude. From this, we can conclude that grain refinement during shearing occurred through the process of mylonitization. The metamorphic evolution of CGGC is divided into four stages. M1 metamorphic event is marked as an ultra-high temperature metamorphism (> 900°C) at about 5-8 Kbar pressure (Sanyal et al., 2007; Sanyal and Sengupta, 2012). The minimum age of the first phase of metamorphism (M1) is approximately 1.87 Ga (Chatterjee et al., 2010). Migmatization of the granitoid protoliths and the development of migmatitic charnockite gneiss are associated with a high degree of metamorphism (700-800 °C and 5-7 kbar pressure) called M2 metamorphism (1.66-1.55 Ga). According to Sengupta (2012), CGGC was intruded by a series of felsic igneous rocks after the M2 metamorphism. This magmatic activity was associated with third phase of metamorphism (M3) accompanied by a second stage of folding (D2). M3 occurred at a P-T range of 6.5 ± 1 kbar and 700 ± 50 °C (Maji et al., 2008; Sanyal and Sengupta, 2012). U-Th-Pb chemistry dates of monazite showed that M3 occurred between ~1.2 and 0.93 Ga (Acharyya, 2003; Sanyal et al., 2007; Chatterjee et al., 2010). The last phase of metamorphic event M4 was associated with incipient migmatization and pegmatite emplacement along the D3 axial plane. The M4 metamorphism took place at around 750 – 600 °C temperature (Ray et al., 2011) and 9-12 kbar pressure (Chatterjee et al., 2010). The U-Th-Pb chemical age of monazite indicates that the metamorphism occurred around 0.87 – 0.78 Ga (Sanyal et al., 2007; Chatterjee et al., 2010). Deformation and metamorphism in CGGC were associated with granitoid magmatism (Ghose,1983). Ages obtained from granitoid rocks from different parts of the CGGC

indicates mid-Proterozoic age; western part (U-Pb zircon ages of 1.7 Ga Chatterjee et al., 2008; Sanyal and Sengupta, 2012); central and northern part (Rb-Sr ages of around 1.5+ 0.03 Ga, Pandey et al., 1986; 1.5-1.6 Ga, Chatterjee et al., 2008); eastern part (K-Ar dates around 1.08 and 0.80 Ga, Sarkar, 1988, Baidya et al., 1987). Newer dates by Rb-Sr method on granitic rocks from the Bihar Mica belt and charnockitic rocks from Dumka region yielded ages in the range of 1.0-1.6 Ga, pointing to the impact of the Satpura Orogeny (Mahadevan, 2002).

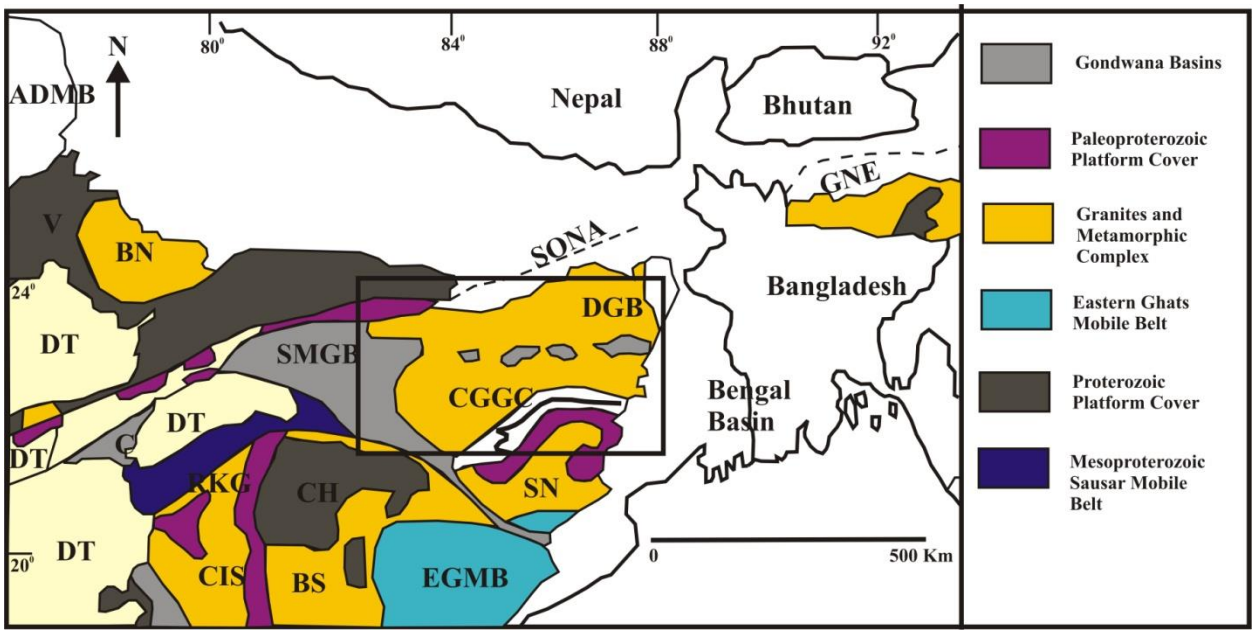

Figure. 2.1. Geological map of the central and eastern parts of India (modified after Acharya, 2003). ADMB: Aravalli–Delhi Mobile Belt; BN: Bundelkhand massif; BS: Bastar Craton; CH: Chattisgarh Basin; CIS: Central Indian Shear; CITZ: Central Indian Tectonic Zone; DGB: Damodar Gondwana Basin; DT: Decan Trap; EGMB: Eastern Ghats Mobile Belt; GNE: Gneissic Complex of NE India; SMGB: Son–Mahanadi Gondwana Basin; SN: Singhbhum Craton; SONA: Son– Narmada lineament; RKG: Ramakona-Katangi Granulite belt; V: Vindhyan Basin.

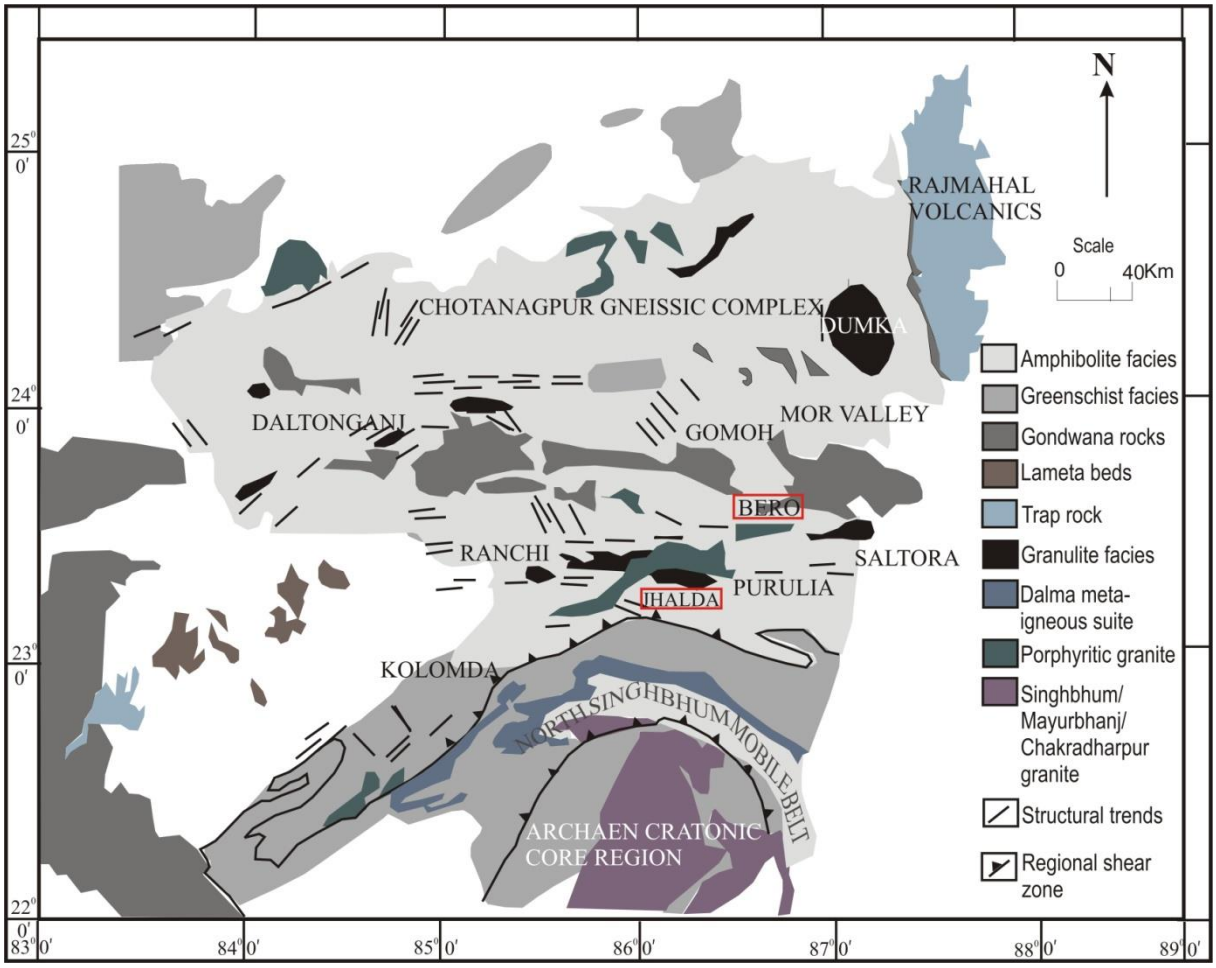

Figure. 2.2. Generalized geological map of the CGGC, modified after Mahadevan (2002). The metamorphic grades indicated in the legend are not exclusive, but are dominant in the zones indicated. The study areas are marked as boxes. The North Singhbhum Mobile Belt is separated from the Archean Singhbhum Craton in the south and the Proterozoic CGC to the north by regional shear zones (bold lines with filled triangles).

Table. 2.1. Stratigraphic relationship of the basement and the magmatic rocks of the Chotanagpur Granite Gneiss Complex (modified after Ghose and Chatterjee, 2008)

Time	**Magmatic rock**	**Lithological relation**	**Age relative to deformation**
Early Tertiary Lower Cretaceous	Dolerite (tholeiite)	Salma dyke cross-cutting entire CGGC section	Post-D2/D3
	Dolerite, lamproite and lamprophyre dykes; flood basalt	Intrusions in Damodar Graben, Gondwana sediments and eruption in Rajmahal Basin	Post-D2/D3
Permo-Carboniferous (Lower Gondwana)		Sandstone with shale partings and coal seams with lower Creatceous intrusive dolerite, lamproite and lamprophyric rocks	Post-D2
	----------*Unconformity*----------		
Meso-Neoproterozoic (1400-540Ma)	Pegmatite, aplite and quartz vein	Intrusions in Bengal Anorthosite massif and country rocks	Post-D2
	Alkali granite (hypersolvus)-A-type	Intrusion in basement and massif anorthosite	Post-D2
	Peraluminous biotite granite (S-type)	Intrusion basement	Post-D2
	Intrusion of mafic rocks and porphyritic granite	Intrusion within poly-metamorphosed high-grade rocks	Syn-to post-D2 (~0.93Ga)
	Rapakivi granite dyke	Intrusion in amphibolite and granulite facies rocks of BMB	pre- to syn-D2
Mesoproterozoic (1600-1400 Ma)	Intrusion of ferroan alkaline granite batholiths	Intrusion in basement gneiss in north-eastern part of the CGGC	Pre-D2/ post-D1 (~1.47-1.45 Ga)
	Syenite and nepheline syenite	Intrusions in basement and Bengal Anorthosite massif	Pre-D2 / post-D1 (~1.47 Ga)
	Bengal Anorthosite massif and anorthosite dyke	Intrusion in basement	Pre-D2 / post-D1 (1.55-1.51 Ga)

	Syn-tectonic mafic-ultramafics: Gabbroids, metabasic granulite, amphibolites and Hornblendite	Intrusive into the basement gneiss and metasediments, bands in and outside Bengal Anorthosite massif, concordant with regional E-W foliation	Pre-D2 / post D1
Paleoproterozoic (>1600 Ma)		Supracrustal enclaves of metapelite (mica schist, sillimanite schists and khondalite), meta-arenite (quartzite and quartz-magnetite rock) and calc-silicate gneiss in basement gneiss (tonalitic to granitic), migmatite, augen gneiss, biotite/hornblende gneiss, charnockite, leptynite and schistose ultramafics	Syn-D1 (~1.6 Ga)

CHAPTER-3

PREVIOUS WORK

3.1. GENERAL ASPECTS

3.2. AGE

3.3. METAMORPHISM

3.4. STRUCTURE

3.5. PREVIOUS WORKS ON THE STUDY AREA

TABLES

3.1. General Aspects:

Ball (1881) was the first to publish a preliminary but comprehensive geological account of Puruliya (erstwhile Manbhum) and Singbhum districts in eastern India. They considered CGGC as the 'Fundamental Gneiss' over which the "Transition Series" and related metamorphic rocks were laid. He proposed a general geological succession for Puruliya district in which the oldest rock formation was called 'metamorphic series' followed upward by 'submetamorphic series' (rocks of lesser degree of metamorphism than the gneisses and schists). Apart from these, comprehensive reviews on the geology of the entire Chhotanagpur gneissic complex have been made by Ghosh (1983, 1992), Mazumder (1988), Sarkar (1988), Banerji (1991) and Singh (1998). Mazumder (1996, 1998) published a very short review on the general geology of the Puruliya district and an abstract on the Chhotanagpur granite gneiss belt respectively. Bhattacharya (1976) and Barman et. al., (1994) have given preliminary report on the occurrence of high grade metamorphic rocks. Early regional studies on the CGGC were by Ghose (1983), Mazumder (1979, 1988), Banerji (1991) and Singh (1998).

3.2. Age:

In a vast and diversified Precambrian terrain like CGGC, which suffered a series of magmatic and metamorphic activities, it is quite difficult to ascertain the actual ages of the varied events. Earlier workers dated the gneisses, amphibolites and granites of CGGC, which give a consistent age range of 900 ±200 Ma (Holmes, 1950, 1955; Vinogradov et al., 1964; Sarkar 1968; Ghose et al., 1973). All these ages denotes a fair relation of these magmatic and metamorphic events with the Satpura Orogeny. Sarkar (1968) reported the metamorphism age of the amphibolites from Gomoh-Dhanbad area to be 1086-893 Ma. Ghose et al (1973) reported amphibolites of 970 Ma from Richughuta of Palamau district. Pegmatites (960 ±50 Ma) (Vinogradov et al., 1964) and

intrusive granites of CGGC yields age range of 1600-700 Ma (Ghose et al., 1973; Pandey et al., 1986; Mazumdar 1988). Age of metamorphism of basic intrusive rocks has been dated between 1400-1000 Ma (Sarkar 1988; Ghose et al., 1973). Clustering of ages of granites around 1000 Ma from all over CGGC indicates a major thermal event during this time which is responsible for resetting the then geological clock. Baidya et al., (1987) reported K-Ar ages of porphyritic granitoid gneiss and leuco-granitoid from the central CGGC to be 840±40 Ma and 810±40 Ma respectively. Intrusive granites from Bihar mica belt (BMB) yielded ages of 1590±30 Ma (Pandey et al 1986a) and gneisses from south of BMB yielded 1717±102 Ma (Mallik et al., 1991). Migmatites, hypersthene granites and granite gneiss from north-eastern part near Dumka yields meso-proterozoic ages (1580±33 Ma, 1699±33 Ma, 1522±71 Ma respectively) (Mallik et al., 1991). Ray Barman and Bishui (1994) reported whole rock Rb-Sr isochron ages of 1741±65 Ma from granites of western CGGC. All these above ages indicates a major tectono-thermal event at about 1.7-1.6 Ga in CGGC. Ray Barman and Bishui (1994) reported Rb-SR date of syenite near Dumka (1475±63 Ma). Migmatites and hypersthene granites, 80 km west of Saltora yielded Rb-Sr ages of 1071-1178 Ma (Ray Barman and Bishui 1994). The significant pegmatitic and granitic activity as indicated by Rb-Sr dates is between 950 Ma and 800 Ma respectively (Mahadevan 2002). Maji et al., (2008) reported that the Pan African dates from CGGC are lacking; the only evidences include: the 500 Ma date obtained from K-rich alkali syenite porphyry and granite aplite (K-Ar mineral age, Ghose et al., 1973; Ghose 1983) and 481±18 Ma in a migmatite from Hazaribagh belt (whole rock Rb-Sr isochron date, Pandey et al, 1986). Zircon in nepheline bearing syenite fixes the crystallization age of alkaline magma at 0.92 Ga (Reddy et al 2008). Chatterjee et al., (2008) reported the emplacement age of anorthosite from U-Pb date of zircon at around 1.55 Ga. Singh and Krishna (2009) reported age of high grade

metamorphism, anatexis and intrusion of grey granite at 1005±51 Ma and pink granite at 815±47 Ma. Wanjari et al., (2012) have reported an Rb-Sr whole rock isochron age of 1337±26 Ma for the granites near Paharpur of Gaya. Pb-Pb dates obtained from the zircon cores, presumed to date the magmatic crystallization of protoliths of charnockitic gneiss define an age of 1447±11 Ma (Mukherjee et al., 2017). LA-ICPMS U-Pb zircon age of pelitic granulites suggest two distinct metamorphic events. The earliest event M1 occurred during the 1680-1580 Ma. Major pulse of the M2 event recorded at ~970-950 Ma. The geochronological ages reported so far from different parts of CGGC are given in Table.3.1.

3.3. Metamorphism:

The first attempt to synthesize the available metamorphic data of CGGC has been made by Ray and Gangopadhyay (1971). They present an isograd map which covers only a small portion of southern CGGC. Earlier workers unanimously suggest three episodes of metamorphism starting with a major phase of regional metamorphism followed by contact metamorphism and lastly by cataclastic metamorphism. Prasad (1975) reported occurrence of andalusite-mica schist at Nagar-Untari and in BMB. Bhattacharya (1976) reported an increase in the grade of metamorphic facies from amphibolites to granulite facies from W to E of CGGC. Baidya (1981) reported a progressive rise in the metamorphic facies from greenschist to amphibolites from SE to NW in southern parts of Puruliya district. Sarkar and Jha (1985) delineated an E-W trending isograd pattern in Ranchi area, where granulite facies rocks are flanked by greenschist facies rocks. Ghose (1973) thus concluded in a general sense that amphibolites facies rocks occur in the central CGGC, greenschist facies in the northern and southern end and granulite facies in the eastern and western ends. Absence or rare presence of staurolite and kyanite and presence of cordierite in metamorphic rocks of CGGC is suggestive of presence of high thermal gradient

during the regional metamorphism of CGGC. Physical conditions of metamorphism from granulites near the Bengal anorthosite was carried out by Sen and Manna (1976), Manna and Sen (1974), Sen and Bhattacharya (1985, 1993) and Bhattacharya and Mukherjee (1987). Ghose (1983) suggested that the widespread metamorphic event that affected the major part of CGGC (as evidenced from the mineral assemblages) was the almandine-amphibolite facies metamorphism. The peak metamorphism was followed by a retrogressive phase essentially marked by unmixing of feldspar phase, crystallization of calcite along the plagioclase-microcline contact, formation of intergranular albite, biotite to chlorite alteration, forsterite to serpentinite alteration and many more such mineralogical changes. Lastly a feldspathization phase resulting into a rapakivi like structure in amphiolites and granites were reported by Sharma and Agarwal (1950). Maji et al (2008) suggested four phases of metamorphic events that affected the rocks of CGGC. M1 stage in mafic granulites is represented by the plagioclase + orthopyroxene + clinopyroxene + ilmenite + hornblende assemblage.M1 metamorphic assemblage in migmatitic-quartzofeldspathic gneisses is defined by almandine-grossular rich garnet $\pm$ orthopyroxene bearing leucocratic layers and biotite $\pm$ hornblende rich melanocratic layers. Cpx-scapolite-plag-K-flds-calcite-qtz in calc-silicate gneisses and gt-silimanite-K-flds-qtz-spinel-il- in metapelites defines the M1 metamorphic stage. M2 and M3 metamorphic stages can be indicated by the following mineralogical characteristics in the common rock types: stabilization of biotite in quartzo-feldspathic gneisses, biotite$\pm$ silimanite in metapelites and hornblende in mafic granulites at the expense of M1 minerals. M4 metamorphic stage is marked by growth of garnet as double layered corona, discrete porphyroblasts and overgrowths on pre-S3 porphyroblasts. Petrogenetic considerations and textural relations suggest that the M1 (750-880 °C, and 4-6 Kbar) and M4 (650 $\pm$50 °C, 4.5 $\pm$ 0.5 Kbar) represents prograde metamorphic episodes while M2

and M3 represent retrograde metamorphic episode. Later Sanyal and Sengupta (2012) classified the geologic events of CGGC into four stages and corresponding four metamorphic phases. The first phase of metamorphism designated as M_I is an ultrahigh temperature metamorphism (>900 °C), documented at 5-8 Kbar pressure as interpreted from the mineral assemblages of Khondalite and quartzofeldspathic rock in the DJG sector (Sanyal et al., 2007) and Mg-Al granulites of MBR sector (Sanyal and Sengupta 2012). U-Th-Pb chemical dates of monazites from cores of garnet porphyroblasts yielded ~1.87 Ga as the minimum age of M1 metamorphic phase. $Stage_{II}$ was marked by the intrusion of the protoliths of granitoids which later deformed and migmatized to produce charnokitic gneiss through M_{II} metamorphic stage. Conventional geothermobarometry yielded 700-800°C temperature and 5-7 Kbar pressure for MII metamorphic stage. Published ages from U-Th-Pb age of monazite (from felsic gneiss and khondalite) and U-Pb zircon ages (from anorthosite) indicate the age of MII within 1.66-1.55 Ga. Early mesoproterozoic magmatic rocks that intruded after MII metamorphic event were subjected to a high grade metamorphic event designated as MIII. P-T range of MIII as calculated by Maji et al., (2008) and Sanyal and Sengupta (2012) shows 6.5 $\pm$ 1 Kbar pressure and 700+ 50 0C temperature and occurred during the age range of 1.2- 0.93 Ga (Acharyya 2003, Sanyal et al 2007, Chatterjee et al 2010). Dey et al., (2019) for the first time, documents the evidence of ~1680–1580 Ma-old granulite facies metamorphic event from the CGGC. Mukherjee et al., (2019) documented late Paleoproterozoic (1710 Ma and 1635 Ma) U–Pb ages of the magmatic zircon grains of the granitic intrusion from Deoghar-Jasidih area. This late Paleoproterozoic felsic magmatism overlaps with the duration of the high-to-ultrahigh-temperature granulite facies metamorphism in CGGC. The interpretation of the geochronological datas along with metamorphic events of CGGC is given in Table 3.2.

3.4. Structure:

The ENE- WSW Satpura trend defines the regional trend of the Chhotanagpur craton and the Shillong plateau of Assam (Krishnan, 1953). This northeasterly trend changes to northerly trend in the central part of the Santhal parganas (Bhattacharyya, 1975). Ghose (1992) reported that structural studies of several isolated areas of CGGC by various workers (Sengupta and Sarkar, 1964; Ghose, 1971, 1974; Chattopadhyay and Saha, 1974; Bhattacharyya. 1975, 1982; Prasad, 1976; Sarkar, 1977; Sarkar and Jha, 1985; Chatterjee and Sengupta, 1980) suggest episodes of polyphase deformation.

Maji et al. (2008) reported four phases of metamorphism (M1–M4) and three phases of deformation (D1–D3) which ultimately resulted into the formation and successive deformation of the gneissic bandings in the migmatitic country rocks. On the other hand, Sanyal and Sengupta (2012) has proposed geological evolution of the CGGC into four stages involving four phases of metamorphism and six phases of deformation. The sequence numbers of metamorphism and deformation in both classifications may not be similar but overall depict a similar sequence of geological evolution in the CGGC.

First folding episode (isoclinals type, F1) on the S0 bedding planes gave rise to the east-west stretching axial plane marked as S1. This S1 fabric can be observed in the calc-silicate rocks and rarely in metapelites (Maji et al., 2008, Sanyal and Sengupta 2012). The S1 fabric is defined by alignment of granulite-facies mineralogy of garnet and orthopyroxene in quartzofeldspathic rock and garnet, sillimanite and spinel in metapelite rock. F2 folding phase was marked as an open and disharmonic folding phase on S0 and S1 which gave rise to S2 axial planar crenulation in the incompetent metapelites and fracture cleavage in the competent quartzites. Sarkar (1988)

reported that F2 plunges steeply in the Ranchi-Hazaribagh area while plunges gently in other areas. A chain of basic igneous rocks were found in the granite-gneiss complex during the second phase of deformation. Mild natured F3 folding gave rise to large scale crenulation of S2. The S2 schistosity shows high angle relationship with S1 near the fold hinges and remains parallel otherwise. The granitic intrusions were of syn- to late kinematic which follows the axial plane of antiformal-synformal structures. In the next major geological event (fourth stage) in the CGGC, emplacement of a set of mafic dykes/swarms is reported that cut across the S1-S2 fabrics (Sanyal and Sengupta, 2012). The dykes and the S1–S2 foliations were successively folded (F4-F5) by a strong east-west compression, which resulted into a north-south-trending foliation that cut across the S1–S2 fabric (Sanyal and Sengupta, 2012).

Summing up the observations of Sanyal and Sengupta (2012) and the U-Pb zircon dates obtained by recent workers (Dey et al., 2017; Mukherjee et al., 2017; Rekha et al., 2011; Saikia et al., 2017), four distinct events have been identified during the Paleoproterozoic to Neoproterozoic, which seemed to have shaped the CGGC into its current form. (i) The basement of the CGGC formed during the Paleoproterozoic at ~1750-1660 Ma and has been identified mainly from the porphyritic granites from northern part of CGGC (Chatterjee and Ghose, 2011; Mallik et al., 1991; Ray Barman and Bishui, 1994; Saikia et al., 2017). Chatterjee and Ghose, (2011), Saikia et al., (2017) have identified these granites as the extension of the Mahakoshal Belt along the northern edge of the CGGC. (ii) The protolith of migmatitic felsic orthogneiss intruded the north-eastern part of CGGC at ~1450 Ma and presently forms the country rock of the area and thereby entrapping all the earlier components as enclaves (Mukherjee et al., 2018, 2017). (iii) Later, the enclaves and host felsic gneiss was metamorphosed under granulite facies condition at ~1000-900 Ma (Chatterjee et al., 2010, 2008; Chatterjee and Ghose, 2011; Dey et

al., 2017; Karmakar et al., 2011; Maji et al., 2008; Mukherjee et al., 2017; Rekha et al., 2011) which give rise to the pervasive migmatitic foliation (Mukherjee et al., 2017). (iv) Afterwards, mafic dyke swarms and the alkaline rocks intruded the country rock (~930-920 Ma; Reddy et al., 2009; Sanyal and Sengupta, 2012), which were deformed and metamorphosed at amphibolite facies at 870-780 Ma (Ray et al., 2011; Sanyal and Sengupta, 2012).

3.5. Previous works on the study area:

Several studies have been conducted in the area around Raghunathpur (West Bengal) situated west of Bero. The area is composed of rocks of different generations, including felsic orthogneisses (porphyritic and deformed granitic rocks), metapelitic and calcareous enclaves (Dunn 1929; Baidya et al. 1987, 1989; Ray Barman and Bishui 1994; Goswami and Bhattacharyya 2010, 2014; Karmakar et al. 2011). In this area, three major deformational events (D1-D3) associated with two major metamorphic phases (M1-M2) are identified. In this area, non-porphyritic granite intrusion is reported at ~1.18 Ga (Rb–Sr whole rock isochron, Ray Barman and Bishui 1994) which was accompanied with the D1 deformation and S1 fabric development event (Goswami and Bhattacharyya, 2010). Ray Barman and Bishui (1994) and Goswami and Bhattacharya (2010) reported an Rb-Sr total rock age of 1071 ± 64 Ma for pre-D2 intercalated porphyritic charnokites. Goswami and Bhattacharyya (2014) reported that these porphyritic granite intrusions are of shoshonite to high-K calcalkaline in composition, which formed by mixing of mantle-derived mafic magma crustal melts in continental-continental collision environments. South-east of Raghunathpur, near Adra (West Bengal), the country rocks are composed of quartzo-feldspaathic migmatitic gneiss containing enclaves of Mg-Al granulite and mafic granulite. Karmakar et al. (2011) provided the chemical age of this Mg-Al-Pelite and monazite from migmatitic gneisses, suggesting that the most prominent and ubiquitous

tectonothermic event in the region occurred between 990 and 940 Ma, which occurred at about 870 °C and a pressure of 11 kbar following a steep decompression path. Goswami and Bhattacharyya (2010) estimated a similar temperature (~800 °C) but a lower Karmakar et al. (2011) provided the chemical ages of monazite from these Mg– Al pelite and migmatitic gneiss and concluded that the most prominent and pervasive tectonothermal event of the area occurred between 990–940 Ma that culminated at ~870 °C and 11 kbar pressure followed by a steeply decompressive path. A similar temperature (~800 °C) but lower pressure (6.5–7.5 kbar) is estimated by Goswami and Bhattacharyya (2010). According to them, M1 occurred during both D1 and D2. Youngest monazite age population of 850–775 Ma reported by Karmakar et al. (2011) matches well with the Neoproterozoic dates of ca. 870 ± 40 Ma of porphyritic granite (K–Ar biotite) and 810 ± 40 Ma age of leucogranite (K–Ar muscovite) reported by Baidya et al. (1987) from the western part of the area near Jaipur, West Bengal. This youngest age clusters are presumably indicative of the third tectonothermal event (D3).

Several studies on the petrology and geochemistry of alkaline rocks along NPSZ have been carried out by different workers over the past decades. Das et al., (2007) reported occurrences of aegirine-riebeckite granite from Perhando Pahar (Lat. 23°27′30″N, Long. 85°50′ E) of Jhalda region and salite granites from Pankridih (Lat. 23°25′N, Long. 85°50′ E). Bhaumik et al., (1990) provided the geochemistry and mineralogy of nepheline syenite of Kankarkiari and Kusumda areas, lying on the eastern extremity of NPSZ. Later, Goswami and Bhattacharyya (2008) reported the metamorphic events suffered by these nepheline syenites. Verma and Barla (Progress Report, Geol. Surv. India, 1994-1995) reported briefly the petrographic description of aegirine - arfvedsonite syenite from southern part of Dimra. Any details of geochemistry, mineral chemistry and geochronology were not provided by them. Later, Goswami et al., (2015)

provided elaborate description of these aegirine - arfvedsonite syenite along with their mineral chemistry, geochemistry and petrogenetic evolution. The aegirine - arfvedsonite syenite was reported to occur at temperatures between 1071ºC and 801ºC at 1.5 kbar pressure (Goswami et al., 2015). They suggested that these syenites were formed by Ca fractionation of basaltic parent magma or very low degree partial melting of mantle rocks. Chakraborty et al., (2022, in press) reported the geochemistry, petrogenetic evolution and geochronology of the aegirine-riebeckite granites of the Perehando Pahar.

Table. 3.1. List of published ages from different sectors of CGGC.

Location	**Rock type**	**method**	**Age**	**Reference**
Bihar mica belt	pegmatites	Pb isochron	960±50	Vinogradov et al., 1964
Muri-Silli region, Ranchi	Biotite schist	K-Ar	970	Sengupta and Sarkar 1968
Richughuta, Palamau district	amphibolites		970	Ghose et al., 1973
	Mica pegmatite	Fission track age dating	830	Lal et al 1976
	Mica pegmatite	Fission track age dating	760	Lal et al 1976
	Mica pegmatite	Fission track age dating	595	Lal et al 1976
	Mica pegmatite	Fission track age dating	590	Lal et al 1976
	Migmatitic granite gneiss	K-Ar	1416-1246	Sarkar 1980

Bihar mica belt	granites	Rb-Sr	1590±30	Pandey et al 1986a
Jhalda	Porphyritic granitoid gneiss	K-Ar	870±40	Baidya et al 1987
Central CGGC	leuco granitoid	K-Ar	810±40	Baidya et al 1987
South of Bihar mica belt	gneisses	Rb-Sr	1717±102	Mallik et al 1991
NE CGGC, near Dumka	migmaties		1580±33	Mallik et al 1991
NE CGGC, near Dumka	Hypersthenes granite		1599±33	Mallik et al 1991
NE CGGC, near Dumka	Granite gneiss		1522±71	Mallik et al 1991
western	granites	Rb-Sr	1741±65	Ray Barman and Bishui 1994
near Dumka	syenite	Rb-Sr	1475±63	Ray Barman and Bishui 1994
Bero	Migmatites and hypersthenes granite	Rb-Sr	1071±64	Ray Barman and Bishui 1994
murguma			1178±61	Ray Barman and Bishui 1994
Muruguma-Puruliya-Raghunathpur	Hy-granite gneiss	U-Pb	1624±5	Ray Barman et al 1994
Muruguma-Puruliya-Raghunathpur	Massive charnockite	U-Pb	1515±5	Ray Barman et al 1994
Muruguma-Puruliya-Raghunathpur	Basic granulite	U-Pb	1515	Ray Barman et al 1994
	charnockite	Rb-Sr	1331±125	Ray Barman et al 1994
Bihar Mica Belt	metasediments	Pb-Pb	1700-1650	Singh et al 2001
Deoghar-Joshidih-Rohini	Quartzo-feldspathic granulite and khondalite	U-Th-Pb	1628	Sanyal et al 2007
Deoghar-Joshidih-Rohini	Quartzo-feldspathic granulite and khondalite	U-Th-Pb	1518	Sanyal et al 2007
Deoghar-Joshidih-Rohini	Quartzo-feldspathic	U-Th-Pb	1118	Sanyal et al 2007

	granulite and khondalite			
Deoghar-Joshidih-Rohini	Quartzo-feldspathic granulite and khondalite	U-Th-Pb	1088	Sanyal et al 2007
Deoghar-Joshidih-Rohini	Quartzo-feldspathic granulite and khondalite	U-Th-Pb	979	Sanyal et al 2007
Deoghar-Joshidih-Rohini	Quartzo-feldspathic granulite and khondalite	U-Th-Pb	942	Sanyal et al 2007
Deoghar-Joshidih-Rohini	Quartzo-feldspathic granulite and khondalite	U-Th-Pb	862	Sanyal et al 2007
Deoghar-Joshidih-Rohini	Quartzo-feldspathic granulite and khondalite	U-Th-Pb	842	Sanyal et al 2007
Deoghar-Joshidih-Rohini	Quartzo-feldspathic granulite and khondalite	U-Th-Pb	788	Sanyal et al 2007
	Nepheline syenite	U-Pb	920	Reddy et al 2008
Saltora	Anorthosite	U-Pb	1550	Chatterjee et al 2008
Bero-Saltora-Santuri	Garnetiferrous metapelitic gneiss	U-Th-Pb	1176±9	Maji et al 2008
Bero-Saltora-Santuri	Garnetiferrous metapelitic gneiss	U-Th-Pb	1082±14	Maji et al 2008
Bero-Saltora-Santuri	Garnetiferrous metapelitic gneiss	U-Th-Pb	1041±20	Maji et al 2008
Bero-Saltora-Santuri	Garnetiferrous metapelitic gneiss	U-Th-Pb	981±26	Maji et al 2008
Bero-Saltora-Santuri	Garnetiferrous metapelitic gneiss	U-Th-Pb	825±26	Maji et al 2008
Bero-Saltora-Santuri	Garnetiferrous metapelitic gneiss	U-Th-Pb	818±11	Maji et al 2008
Bero-Saltora-Santuri	Foliated granite	U-Th-Pb	1021±26	Maji et al 2008

Bero-Saltora-Santuri	Foliated granite	U-Th-Pb	992±11	Maji et al 2008
Bero-Saltora-Santuri	Foliated granite	U-Th-Pb	997±15	Maji et al 2008
Bero-Saltora-Santuri	Foliated granite	U-Th-Pb	967±11	Maji et al 2008
Bero-Saltora-Santuri	Gabbroic anorthosite	U-Pb	1550±12	Chatterjee et al 2008
Bero-Saltora-Santuri	Gabbroic anorthosite	U-Pb	947±21	Chatterjee et al 2008
Dumka-Jamua-Ghormara	Metapelitic granulite	U-Th-Pb	1190±26	Chatterjee et al 2008
Dumka-Jamua-Ghormara	Metapelitic granulite	U-Th-Pb	995±24	Chatterjee et al 2008
Dumka-Jamua-Ghormara	Metapelitic granulite	U-Th-Pb	950±20	Chatterjee et al 2008
Dumka-Jamua-Ghormara	Grey granite		1005±51	Singh and Krishna 2009
Dumka-Jamua-Ghormara	Pink granite		815±47	Singh and Krishna 2009
Bero-Saltora-Santuri	Granite gneiss	U-Th-Pb	1442-1305	Chatterjee et al 2010
Bero-Saltora-Santuri	Granite gneiss	U-Th-Pb	939-967	Chatterjee et al 2010
Bero-Saltora-Santuri Bero-Saltora-Santuri	Granite gneiss	U-Th-Pb	859±87	Chatterjee et al 2010
Bero-Saltora-Santuri	Foliated porphyritic granite	U-Th-Pb	1870-1691	Chatterjee et al 2010
Bero-Saltora-Santuri	Foliated porphyritic granite	U-Th-Pb	965±51	Chatterjee et al 2010
Bero-Saltora-Santuri	Porphyritic granite	U-Th-Pb	1272±35	Chatterjee et al 2010
Bero-Saltora-Santuri	Porphyritic granite	U-Th-Pb	954±32	Chatterjee et al 2010
Bero-Saltora-Santuri	Metapelitic granulite	U-Th-Pb	1720±31	Chatterjee et al 2010
Bero-Saltora-Santuri	Metapelitic granulite	U-Th-Pb	1298-1070	Chatterjee et al 2010
Bero-Saltora-Santuri	Metapelitic granulite	U-Th-Pb	940-924	Chatterjee et al 2010
E CGGC	Quartzofeldspathic gneiss, migmatite	Th-U-Pb	650-600	Chatterjee 2010

NE CGGC	Biotite granodiorite gneiss	U-Pb	560	Chatterjee et al 2011
Paharpur, Gaya	granite	Rb-Sr	1337±26	Wanjari et al 2012
E CGGC	Migmatite, granite, metapelite, biotite granodiorite gneiss	Th-U-Pb, U-Pb	880-750	Chatterjee 2010, Sanyal et al 2007, Karmakar et al 2011, Maji et al 2008, Chatterjee et al 2011
NE CGGC	Metapelite, migmatitic felsic gneiss	Th-U-Pb, U-Pb	910-900	Rekha 2011, Mukherjee et al 2017, 2018

Table.3.2. List of published geochronological information and its relation with tectonothermal events of CGGC.

Age (Ma)	**Methods/Mineral**	**Area**	**Rock type**	**Interpretaion**	**Reference**
~560	U-total Pb xenotime	NE CGGC	Biotite-granodiorite gneiss	?	Chatterjee and Ghose 2011
~650-600	Th-U-total Pb monazite	E CGGC	Quatrzo-feldspathic gneiss, metapelite	Metamorphism, Hydrothermal event	Chatterjee et al., 2010
~880-750	Th-U-total Pb monazite, U-Pb uraninite	E CGGC	Quatrzo-feldspathic gneiss, granite, migmatitic gneiss, Biotite-granodiorite gneiss	Metamorphism, deformation	Chatterjee et al., 2010; Sanyal et al., 2007; Karmakar et al 2011; Maji et al., 2008; Chatterjee

					and Ghose 2011
~910-900	Th-U-total Pb monazite, U-Pb zircon	NE CGGC	Metapelite, migmatitic felsic gneiss	Metamorphism	Rekha et al., 2011; Mukherjee et al., 2017; Mukherjee et al., 2018
~1045	U-Pb zircon	N CGGC	Granite	Magmatism	Wanjari, Chaturvedi and Mahanta 2012
~1100-920	Th-U-total Pb monazite, U-total Pb xenotime, U-Pb zircon	NE CGGC, S CGGC, NW CGGC	Metapelite, quartzo-feldspathic gneiss, granite, granitic gneiss, anorthosite	Metamorphism	Chatterjee et al., 2010; Sanyal et al., 2007; Maji et al., 2008; Chatterjee, Crowley and Ghose 2008; Chatterjee and Ghose 2011; Mukherjee et al., 2017; Karmakar et al 2011
~1280-1190	Th-U-total Pb monazite, U-Pb zircon	NE CGGC, S CGGC	Metapelite, granite, migmatitic gneiss	Thermal event/ Metamorphism	Chatterjee et al., 2010; Rekha et al., 2011; Chatterjee, Crowley and Ghose 2008; Karmakar et al 2011; Maji et al., 2008

~1470-1450	U-Pb zircon	NE CGGC	Charnockitic gneiss	Magmatism	Mukherjee et al., 2017; Mukherjee et al., 2018
~1480-1305	Th-U-total Pb monazite, U-Pb zircon	NE SE CGGC	metapelite	Older thermal event?	Chatterjee et al., 2010; Rekha et al., 2011;
~1550	U-Pb zircon	SE CGGC	anorthosite	Magmatism	Chatterjee, Crowley and Ghose 2008;
~1625-1515	U-total Pb xenotime, U-Pb zircon	N/NE CGGC	Porphyritic granite, charnockites	Magmatism	Acharyya, 2003; Chatterjee and Ghose 2011
~1684-1520	Th-U-total Pb monazite, U-Pb zircon	NE SE CGGC	Quartzo-feldspathic gneiss, metapelite	Older thermal event?/ Metamorphism	Chatterjee et al., 2010; Rekha et al., 2011; Sanyal et al., 2007
~1700-1650	U-Pb zircon, Pb/Pb age of galena	N/NE CGGC	Metasediments, pelitic gneiss	Sedimentation age	Singh et al., 2001; Dey et al., 2017
~1740-1660	U-Pb zircon, Th-U-total Pb monazite	N CGGC	Granite, migmatitic granite gneiss, porphyritic granite	Magmatism	Saikia et al., 2017; Chatterjee and Ghose 2011; Chatterjee et al., 2010
~1870-1824	U-total Pb monazite	NE, SE CGGC	Quartzo-feldspathic gneiss, metapelite, granite	Detrital/older thermal event??	Chatterjee et al., 2010

CHAPTER-4

FIELD OCCURRENCE, PETROGRAPHY AND MINERAL CHEMISTRY OF GRANITOID ROCKS OF RAGHUNATHPUR-BERO AND JHALDA AREA OF CGGC

4.1. ANALYTICAL PROCEDURE

4.2. PETROGRAPHY

4.2.1. GRANITOIDS OF RAGHUNATHPUR AREA

4.2.1.1. MEGACRYSTIC GRANITE GNEISS

4.2.1.2. PINK GRANITE

4.2.1.3. GARNETIFEROUS GRANITE GNEISS

4.2.2. JHALDA AREA

4.3. MINERAL CHEMISTRY

4.3.1. ANALYTICAL PROCEDURE

4.3.2. COMPOSITION OF CONSTITUENT MINERALS OF RAGHUNATHPUR AREA

4.3.3. COMPOSITION OF CONSTITUENT MINERALS OF JHALDA AREA

FIGURES

TABLES

Petrographic study and study of mineral chemistry helps to understand the mineral constituents, optical properties and textural characteristics of the rocks. Selected granitoid samples from both the studied localities are carefully observed under microscope to get aware of their emplacement history and evolutionary history. Modal abundances of minerals, modes of occurrences, nature of mutual contacts, textures are specially emphasized. The microscopic features of the granitoid rocks are ultimately correlated with their macroscopic textures/structures observed in outcrop scale in order to understand the emplacement time.

4.1. Analytical Procedure:

All the rocks for the present study are collected from the different areas of CGGC along the shear zones. The target areas are present within the toposheet numbers 73I/3, 73I/7, 73I/15 etc. Detailed fieldwork and systematic sample collection was carried out from all the target locations. The less weathered rocks are preferred for sampling purpose. The outcrops were thoroughly mapped, and representative samples were collected systematically from each variety of granitoid types. The shear zone present here is roughly trending E-W. Multiple traverses were taken, along the shear zone, to observe and study the granitoids along the shear zone and the effects of shearing on the granitoids. For optical microscopy, a Nikon Eclipse LV100 research model polarizing microscope fitted with digital camera was used and images were processed with Nikon NIS-Elements image processing software. For detailed and advanced microscopic study, scanning electron microscopy was carried out. For that, a TESCAN Vega LSU scanning electron microscope fitted with Oxford Instruments X-act EDS facility was used at the Presidency University.

4.2.Petrography:

4.2.1. Granitoid rocks of Raghunathpur area

Three types of granite have been observed in the Raghunathpur-Bero area. Megacrystalline granite gneiss (MGG) was the most abundant variety in the Raghunathpur-Bero area that was found intrusive in garnetiferous granite gneiss (GGG). Garnet-bearing granite gneiss (GGG) was found in close association with migmatite. Extensive outcrops of the MGG have been observed along the western part of the migmatite quarry. At several locations, MGGs occurred as intrusive veins within migmatite bodies (Fig.4.1a). Megacrystic granites and pink feldspar granites or pink granites (PGs) are oriented east-west parallel to the NPSZ, showing evidence of severe shearing. Pink granite (PG) appeared as thin (2–5 mm) to thick (~24 cm) lenses.

4.2.1.1. Megacrystic granite gneiss (MGG)

Field Occurrences:

MGG was the predominant rock type in the study area. They were exposed as a series of low lying mounds forming bald-headed mounds to low lying chattans around Raghunathpur and Bero areas. They were crudely foliated, with foliation roughly trending E-W direction and dipping northerly. At places traces of prominent shear zones were exposed (Fig. 4.1d). Fine grained aplites were present at many places as thin bands, lens shaped bodies and veins within the MGG. They often contain bands and lenses of biotite rich mafic enclaves. Neither the mafic enclaves nor the granite body show any chilled margin along their contact.

Petrography:

MGG was strongly porphyritic/megacrystic (Fig. 4.1e) and consists of alkali feldspar, quartz, plagioclase feldspar with minor biotite, amphibole and opaque (Fig. 4.2a). Plagioclase and quartz phenocrysts are common (Fig. 4.2b). Gneissosity of the rock is mainly defined by the clusters of biotite laths. They warp around the phenocyrsts and run parallel to the elongated grains of the groundmass. Alkali feldspar occurred both as phenocryst/megacryst and as groundmass (Fig. 4.2c). Large, rectangular, elliptical, rounded (sometimes altered) phenocrysts of alkali feldspar occurred within the fine-medium grained groundmass consisting of quartz, alkali feldspar, plagioclase feldspar, biotite, amphibole and opaque minerals. Foliation was defined by alignment of biotite and also by alignment of extremely stretched alkali feldspar grains. Exolution lamellae in feldspars were common. The alkali feldspar megacrysts are commonly bordered by narrow, anhedral rim of very-fine-grained quartz, microcline, sericitized and turbid plagioclase, and lobate myrmekite. They may contain patches of microperthite and inclusions of quartz, opaque, tiny biotite and occasionally irregular patches of partly altered plagioclase. Marginal granulation and replacement of microcline megacryst by plagioclase-quartz-biotite aggregates along the fractures developed within the above megacryst are common features in the samples from the Shear Zones. Quartz occurs commonly as coarse anhedral megacrysts which sometimes occur as elongate, lenticular grains and deformed or warped crystals around microcline grains. Quartz occurs also as tiny (medium to fine grained) xenomorphs intimately associated with feldspar-biotite-rich groundmass. The elongation of the quartz grains is parallel to the gneissosity of the rock. The quartz augens are invariably composed of aggregates of coarse quartz grains most of which show strain effect. The clusters of biotite laths, mostly oriented along the shearing and define the gneissosity, show warping around quartz augens. At places quartz grains occur as stretched thin lenticles interlayered with the lenticular aggregates of altered feldspars. Plagioclase feldspar was much less abundant than alkali feldspar and occurred as small medium

sized tabular, subhedral, subidiomorphic grains forming aggregates with other groundmass minerals, mainly quartz and biotite, occasionally hornblende. At places, they contain vermicular intergrowth of quartz defining myrmekitic texture (Fig. 4.2e). Megacrysts may show bending of twin lamellae (Fig. 4.2d). Biotite (pleochroic from straw yellow to greenish brown) occurred as elongate, small to medium sized grain laths and clusters in the groundmass. They mostly occurred as clusters around the alkali feldspar phenocrysts defining foliation (Fig. 4.2f). They are intimately associated with the amphibole grains. Amphibole (yellowish green to brownish green to dark green) was relatively rare and occurred as small, sometimes fish-like appearance (Fig. 4.1g), subhedral grains associated with biotite forming clusters. Alteration to clay minerals along the fractures within alkali feldspar, deformed twin lamellae in plagioclase feldspar, ribbon structure of quartz, stretched/ elongated biotite and amphibole were thought to be the result of intense shearing. The accessory minerals like Sphene (weakly pleochroic from pale brown to reddish brown), apatite, opaque (commonly ilmenite), epidote, allanite, zircon, rutile, muscovite and chlorite are intimately associated with biotite-hornblende-rich layers. Zircon when present, occur in trace amount as subidiomorphic to idiomorphic grains within the quartzo-feldspathic mass. Exsolution of magnetite in ilmenite is not uncommon. Often magnetite and ilmenite coexist intimately as discrete grains.

4.2.1.2. Pink Granite

Field Occurrences:

Pink granite occurs mainly as thin to thick lenses and sometimes bands (Fig. 4.1j) within the granetiferous granitoid gneiss. Presence of profuse amount of alkali feldspar in this rock type is responsible for its pinkish appearance (Fig. 4.1h, i). Presence of highly elongated quartz grains (ribbon quartz) appears as translucent markers within this granite variety.

Petrography:

Pink granites are leucocratic, equigranular, medium grained rock which consists of alkali feldspar, quartz, plagioclase feldspar, biotite as major mineral constituents and apatite and opaques as minor constituents. Alkali feldspar grains occurred mainly as coarse grained phenocrysts and were also present in the fine-medium grained groundmass (Fig. 4.2g). Alkali feldspar was the most abundant mineral in this variety. The phenocrysts were very coarse in nature, subhedral in shape, slightly elongated, showed deformed twin lamellae (Fig. 4.2h). The alkali feldspar grains in the groundmass were very fine, rounded and subhedral. The abundance of the alkali feldspar grains in the groundmass was typically high. Quartz occurred less in abundance than alkali feldspar. They were typically elongated – lenticular in shape (ribbon like) due to shearing, had subhedral appearance and were present as phenocrysts (Fig. 4.2i). Fine grained rounded to angular quartz grains were present in the groundmass. Undulose extinction was common in quartz grains. Plagioclase feldspars were relatively less abundant and were medium sized, rounded – sub-rounded in nature. They were also present in the groundmass as small, irregular grains. They showed prominent twinning, and at places deformed twin lamellae. Biotite grains were small, elongated, subhedral to euhedral in nature. They were present along the boundaries of the phenocrysts and sometimes within the groundmass also. At some places they occurred in cluster but reduced to a few in numbers at other places. They were well aligned to define a prominent foliation. Apatite grains were rounded, somewhat drop like appearance and were present in a significant number.

Typical igneous texture includes porphyritic texture defined by phenocrysts of alkali feldspar and quartz which shows preferred orientation.

4.2.1.3. Garnetiferous granite gneiss (GGG)

Field Occurrences:

GGG were typically found in low lying areas, exposed at quarry faces in Bero-Ledason areas (Fig. 4.1b). Garnet grains are present as coarse, rounded, subhedral grains that are present sometimes as discrete grains and sometimes as clusters (Fig. 4.1c) within the felsic groundmass.

Petrography:

This granitoid rock is leuco-mesocratic in nature; medium grained which composed of quartz, alkali-feldspar, plagioclase feldspar, garnet and biotite as major minerals and opaque minerals and zircons as accessory phases (Fig. 4.2j). Quartz grains occurred as medium to coarse grained subhedral phenocrysts. At places they occur as small, anhedral grains in the groundmass. Alkali feldspar grains occurred mostly as large, subhedral grains (phenocrysts) and as small, anhedral grains in the groundmass. They showed undulose extinction. Plagioclase feldspar grains of GGG were medium sized, anhedral and relatively rounded. At places, bending in the twin lamellae of plagioclase feldspars was noticed. Fine to medium flakes of biotite grains were found wrapping the boundaries of quartz and feldspar phenocrysts, defining the foliation. Biotite grains in GGG were of two generations. The first set defined the foliation around larger grains and the other set occurred as inclusions within the garnet (Fig. 4.2k). Garnet occurred as medium to large sized, subhedral, rounded, fractured grains (Fig. 4.2l) within the groundmass made up of small sized quartz grains, alkali feldspar, plagioclase feldspar, biotite and opaques. Some garnet grains were found within phenocrysts of alkali feldspar also.

4.3.3. Granitoid rocks of Jhalda area

Field Occurrences:

Field studies indicate that the aegirine-riebeckite-arfvedsonite granite occurs as E-W elongated isolated lensoid mounds within the migmatitic country rock in the Dimra region and Perehandopahar region of Jhalda. They frequently show brecciation, silicification and limonitisation which gives rise to the reddish-brown hue of the rock. Perehando Pahar is composed totally of the aegirine-riebeckite granite gneiss and is flanked by mica schists to the northwest, calc-silicate geiss to the east, and brecciated-limonitised-silicified quartzite to the south. In the western and central part of the Dimra peralkaline body which typically strikes NE-SW, enclaves of mica schist and quartz schists can be observed.

Petrography:

These peralkaline granites are light coloured and medium grained rock showing gneissic texture. The gneissic texture is defined by alternate bands of thinner ferro-magnesian minerals and relatively thicker quartzo-feldspathic minerals. They show a general hypidiomorphic granular texture and the primary minerals present are quartz, alkali feldspar, alkali pyroxene (aegirine), alkali amphibole (riebeckite, arfvedsonite) and biotite (Fig. 4.2m). The accessory minerals are zircon, plagioclase, sphene, ilmenite, and allanite. Quartz is the major mineral component of these granitoid rocks (modal value varies from 45% to 47%). They occur as medium sized, irregular, lensoidal, unaltered grains and appear at some places next to perthite grains. Undulose extinctions are common. Alkali feldspar (modal value varies from 42% to 44%) is the second most abundant mineral and occurs as elongated, medium sized subhedral grains present in association with quartz and other mafic minerals. Grain boundaries are irregular; perthitic

intergrowth is common in larger alkali feldspar grains while myrmekitic intergrowths occur in the groundmass of alkali feldspar grains. Plagioclase (modal value up to 3%) occurs as occasional phases in this granitoid variety. Some sections are devoid of any plagioclase grains. Pyroxene grains (modal value up to 4%) occur as large elongated prismatic grains showing pleochroism in shades of green and brown and identified as aegirine (Fig. 4.2n). They show embayed boundaries at places and prominent one set of cleavage (extinction angle of pyroxene is around 35^{o}). They are oriented parallel to the gneissosity. The amphiboles (modal value up to 2%) are dark blue to opaque in colour, exhibiting blue to dark blue pleochroism, which is characteristic of sodic amphibole (identified as riebeckite and arfvedsonite) (Fig. 4.2n). The grains are typically long prismatic and occasionally occur as thin laths with euhedral boundaries and they are sometimes associated with pyroxene. Pyroxene, amphibole grains are intimately associated and strongly oriented defining a weak gneissosity. Biotites (modal value up to 2%) are characterized by green to brown pleochroism. Both biotite and amphibole are observed as anhedral and euhedral crystals and are found as interstitial grains between alkali feldspar and quartz, either individually, or as mineral aggregates (Fig. 4.2o, p). Sphene (modal value up to 1%) and opaque mineral occur as fine to medium-sized sub-idiomorphic grains, zircon (modal value up to 0.6%) occur as rounded and sometimes euhedral elongated grains, apatite (modal value up to 0.8%) gains are equidimensional, rounded and rutile as blood red needles — all accessory mineral phases are generally associated with the amphibole-pyroxene rich mineral cluster.

4.3.Mineral chemistry:

4.3.1. Analytical Procedure:

Detailed mineralogical study and Back Scattered Electron (BSE) images of the CGGC granitoid rocks were taken at the optical microscopy and the Scanning Electron Microscope (SEM) facility (Model: Vega Tescan) of Presidency University, Kolkata. Accelerating voltage of 20 Kv and probe currents of 10 nA were used. Electron Micro Probe (EPM) analysis was performed on selected thin sections from CGGC (Sample no.: K9, L10, L21and L24). The EPM facilities (Model: CAMECA SX100) of the Department of Geology and Geophysics, Indian Institute of Technology (IIT) Kharagpur were used. The thin sections were polished and carbon coated prior to analysis at accelerating voltage of 15 Kv and 20 nA current.

4.3.2. Composition of constituent minerals of Raghunathpur area:

The chemical composition of major minerals of Raghunathpur-Bero area granitoids are discussion below:

Feldspar: Alkali feldspar grains are the dominant feldspar types in all the three varieties of granitoid rocks of CGGC. Compositional range of alkali feldspar and plagioclase feldspar grains of GGG, MGG and PG are given in Table 4.1 and 4.2. Plagioclase feldspar grains shows oligoclase-andesine affinity and alkali feldspar shows orthoclase affinity when plotted in feldspar classification triangle (Or-Ab-An triangle; after Deer et. al., 1963, Fig.4.3a). Overall, the alkali feldspar grains and plagioclase feldspar grains have low F, Cl and ZnO abundance. Alkali feldspar has moderate BaO concentration.

Biotite: The biotite grains of CGGC are iron-rich in nature with Fe/ (Fe+Mg) values of 0.43-0.47 (PG), 0.53-0.81(GGG) and 0.54-0.92 (MGG) (Table 4.3). They plot close to the siderophyllite

end of the Siderophyllite-Annite line in the biotite composition quadrilateral (Fig. 4.3b) with half of the MGG biotites plot in the middle of the siderophyllite-annite line. Al2O3 values of GGG, MGG and PG ranged from 13- 21 wt%, 11-13 wt% and 10-18 wt%, respectively. Biotites of GGG and majority of MGG are sub-alkaline in nature while that of PG are subalkaline-alkaline in nature as observed from the plot of Mg versus Al_{total} (Nachit et al., 1985) (Fig. 4.3c). Cl contents of all three varieties are relatively low with a range of 0.002- 0.415wt%. Biotite grains of all the three varieties are of magmatic origin as revealed from the FeOt-MgO-Al2O3 plots (Nockolds, 1947). Majority of GGG and MGG biotite grains plot in the ferrous-biotite field whereas two of GGG, four of MGG and all of the PG biotite grains plot in the magnesio-biotite field in the Mg–(Al VI + Fe 3+ + Ti)– (Fe 2+ + Mn) ternary diagram (Foster, 1960)

Garnet: Garnet is found only in the sample L10, which is the representative of the GGG. The end-member compositions of the garnet are given in Table 4.4. All the analysed garnet grains fall in the Almandine field in the classification diagram based on the end-member component proportions (Fig. 4.3d). These garnet grains are extremely iron rich with Fe / (Fe+Mg) values of (0.423-0.814) which plotted in the (Fe+Mn) field of the plot. They have high Al_2O_3 contents (18-21wt %), low K_2O (0.016-0.7 wt %), TiO_2 (0.015-0.082 wt %) and MnO (0.014- 0.86 wt %) concentrations. Cl contents are relatively low in these garnet grains with a range of (0.016-0.026) wt %.

Calcite: Calcite is found as accessory phase in GGG and PG. The calcite grains are rich in iron content with FeO / (FeO+MgO) value about 0.87. F and Cl contents of these calcite grains are relatively low (0.006-0.016 wt %). They have low Al_2O_3, MnO, and TiO_2 concentration and relatively devoid of any K_2O, Na_2O component.

4.3.3. Composition of constituent minerals of Jhalda area:

Biotite: The biotite grains of the alkali granites of Jhalda area are iron-rich in nature with Fe/ (Fe+Mg) value ranging from 0.3614 to 0.4607 (Table 4.5). They plot close to the siderophyllite end of the Siderophyllite-Annite line in the biotite composition quadrilateral (Fig. 4.4a). Al2O3 values of ARG ranges from 10.7 – 17.8 wt%. Biotites of ARG are subalkaline in nature as observed from the plot of Mg versus Al_{total} (Nachit et al., 1985) (Fig. 4.4b). Cl contents of all three varieties are relatively low with a range of 0.24-0.3 wt%.

Feldspar: Alkali feldspar grains are the dominant feldspar types in the alkali granites of Jhalda. Compositional range of alkali feldspar is given in Table 4.6. Alkali feldspar shows orthoclase affinity when plotted in feldspar classification triangle (Or-Ab-An triangle; after Deer et. al., 1963, Fig.4.4c). Overall, the alkali feldspar grains grains have low F, Cl and ZnO abundance. Alkali feldspar has relatively high BaO concentration.

Pyroxene: The representative composition of the pyroxenes of the alkali granites of Jhalda area is given in Table 4.7. The pyroxenes of this rock type are sodic in nature. They plot in the aegirine field of the triangular classification diagram of pyroxene.

Apatite: The CaO content of the apatite grains of the ARG ranges from 54.9 wt% to 55.9 wt%. The P_2O_5 content of the apatite grains ranges from 39.4 wt% to 41.8 wt%. The representative analysis of the apatite grains of ARG are given in Table 4.8.

Sphene: The representative analysis of the sphene grains of ARG are given in Table 4.8.The CaO content of sphene in ARG ranges from 26.9 wt% to 27.5wt%. The average TiO_2 content of the sphene grains in ARG is 34%.

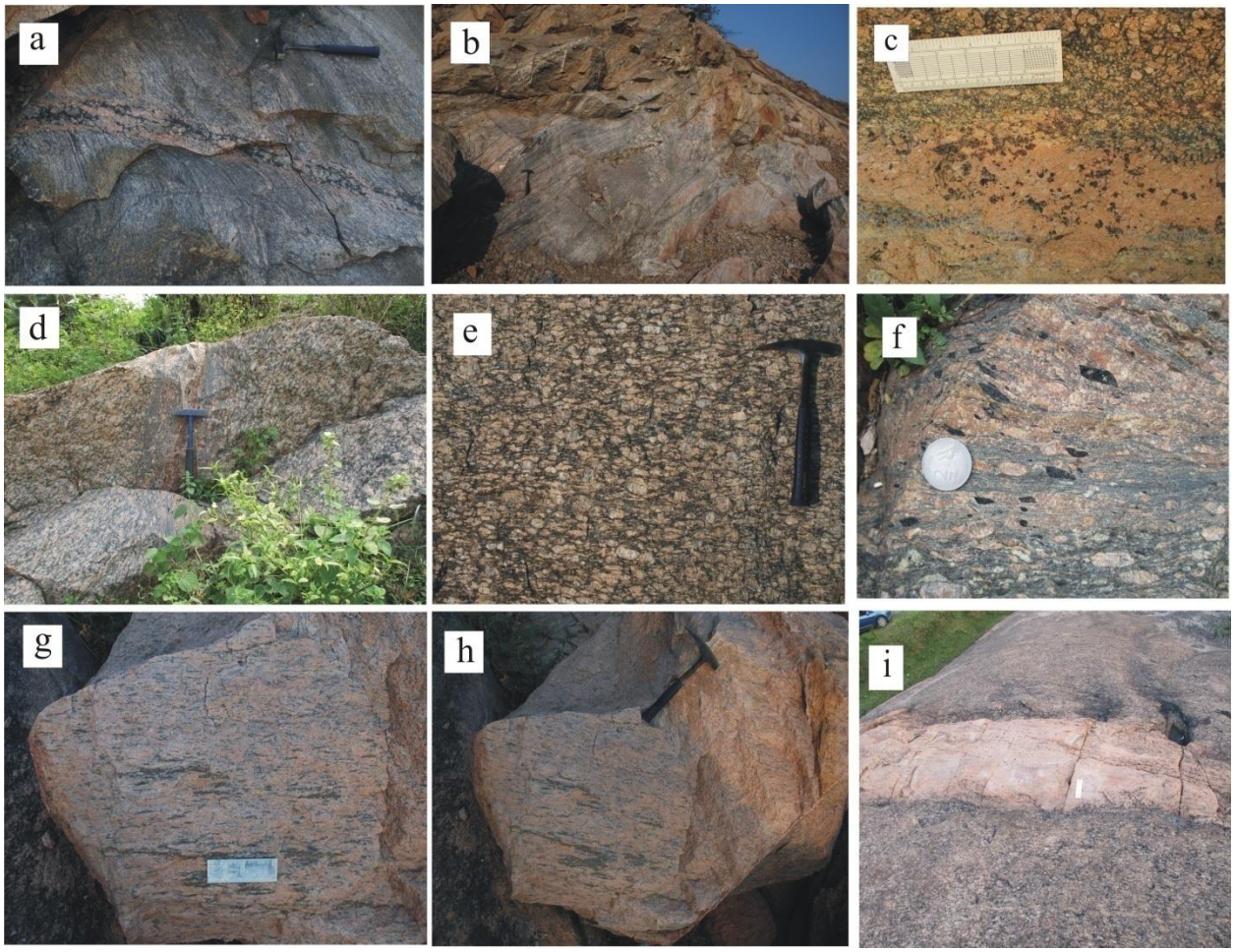

Figure 4.1. Field photographs of different granitoid types of CGGC. (a). Intrusion of MGG in migmatite. (b) Exposure of Garnetiferous Granite Gneiss (GGG). (c) Concentration of garnet grains of GGG within the felsic groundmass. (d) Presence of a regional shear zone within MGG. (e) Overall appearance of megacrysts within MGG (f) Presence of amphibole fish within MGG. (g) and (h) Overall appearance of PG with abundance of stretched quartz grains within feldspar (i) Thick band of PG within GGG.

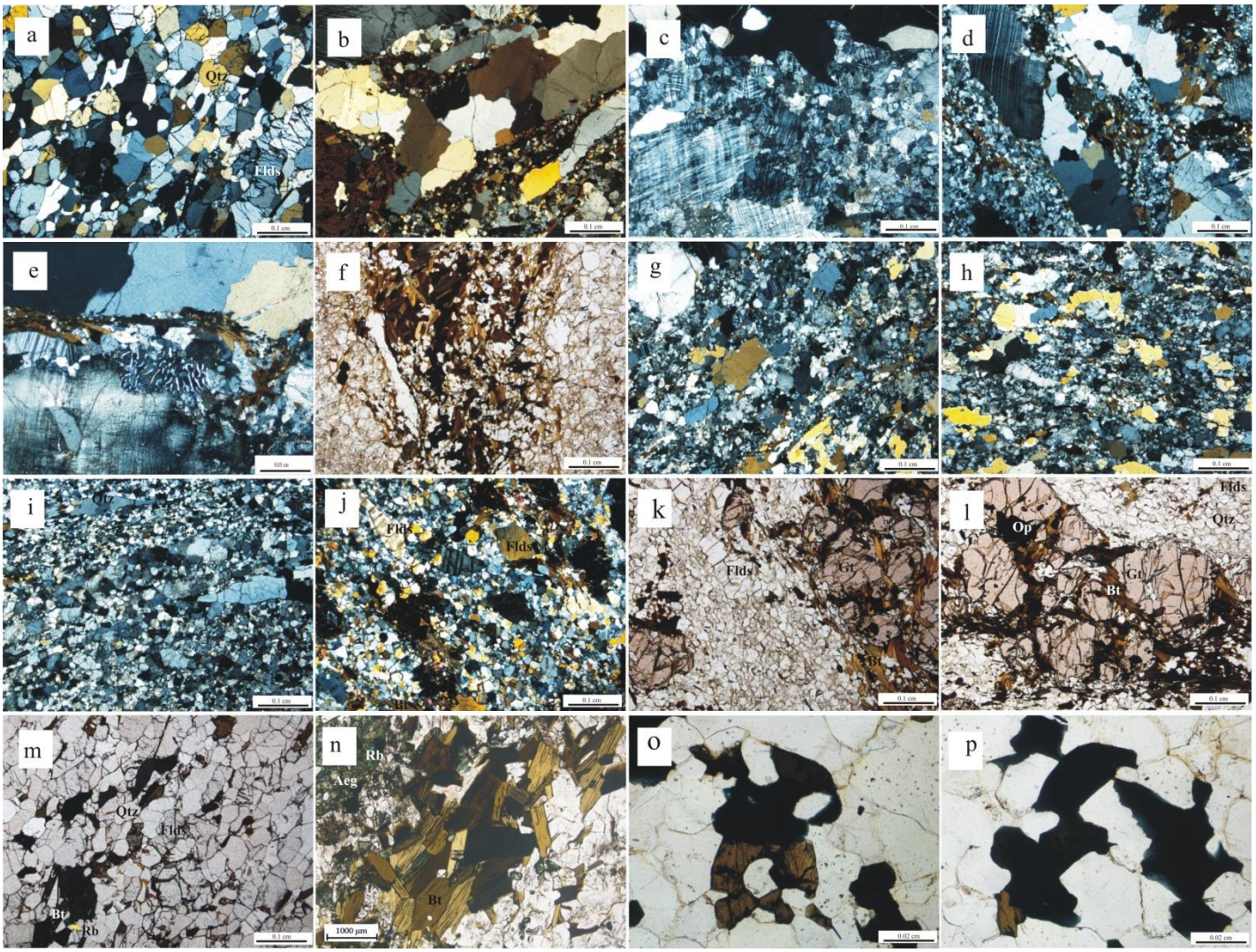

Figure 4.2. Photomicrographs of different granitoid rock types of CGGC. (a) overall texture of MGG. (b) phenocrysts of plagioclase and quartz grains within the fine groundmass of quartz-feldspar-biotite. (c) occurence of alkali feldspar grains both as phenocrysts and fine grained groundmass. (d) intergrowth of quartz and feldspar defining myrmekitic texture. (e) bending of twin lamalle in plagioclase feldspar. (f) clustering of small biotite laths defining the foliation in MGG. (g) occurence of phenocrysts of alkali feldspar and quartz within fine grained groundmass of PG. (h) overall texture of PG. (i) presence of abundant elongated ribbon quartz in PG. (j) overall texture of

GGG showing presence of phenocrysts of quartz, garnet and feldspar within fine grained groundmass. (k) occurence of biotite grains defining the foliation around larger garnet grains and as inclusions within the garnet in GGG. (l) Aggregate of garnet grains in GGG and biotite grains are present along the boundaries of garnet grains. (m) Presence of bitoite-riebeckite-quartz-feldspar assemblage in AR granites. (n) occurrence of sodic-pyroxene (aegirine) and sodic amphibole (riebeckite) as clusters alongside the biotite grains in AR granites. (o) and (p) aggregate of biotite and anhedral amphibole are found as interstitial grains between alkali feldspar and quartz in AR granites.

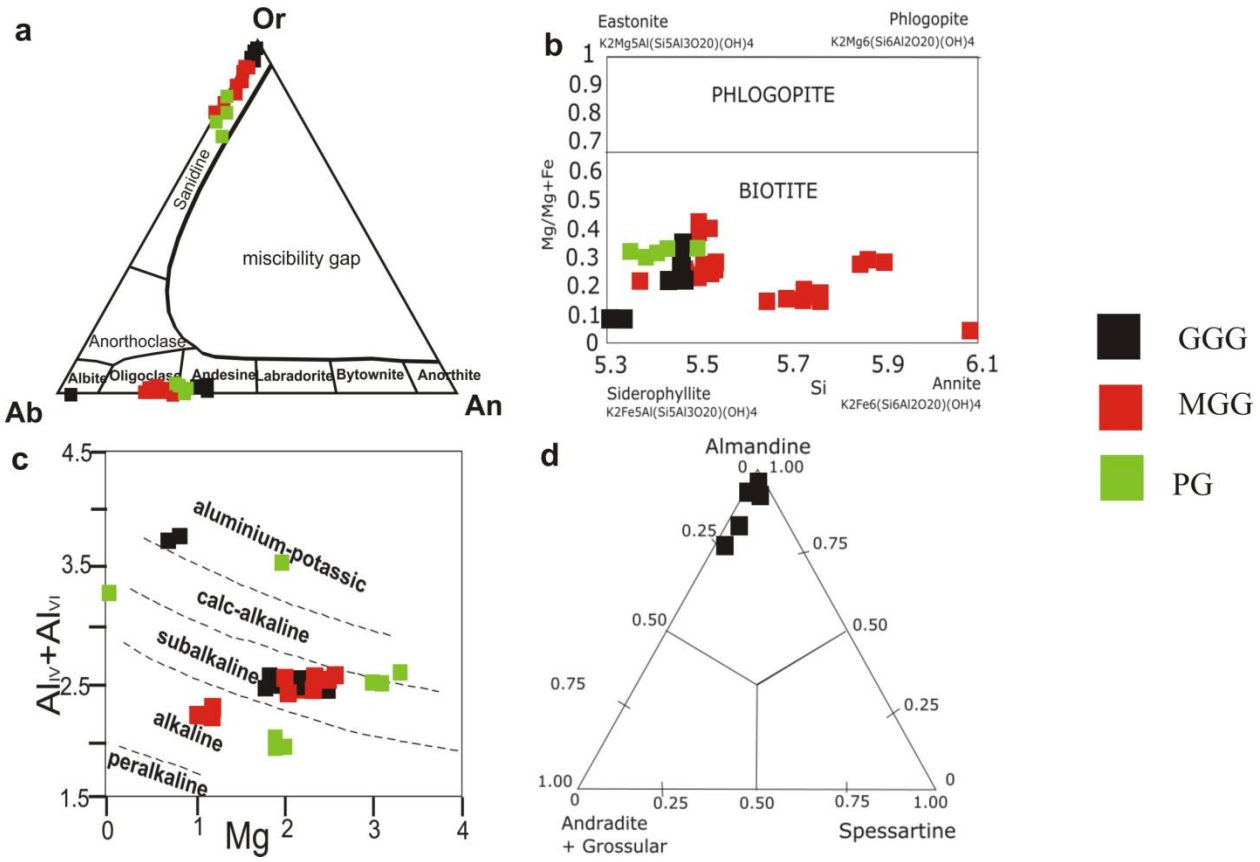

Figure 4.3 **(a)** Triangle diagram showing plots of the compositional data of Feldspar in Feldspar classification (Or-Ab-An) after Deer et. al., (1963), which shows Oligoclase-Andesine compositional range for plagioclase feldspars and Sanidine composition for alkali-feldspars in all the three varieties of Raghunathpur-Bero granitoids; (b) Classification of biotites of Raghunathpur-Bero granitoids via Si versus Mg/(Mg+Fe) diagram which shows roughly Siderophyllite nature of the biotites; (c) Plot of biotite data in discrimination diagram based on Mg and Al_{total} (Nachit 1986), which shows sub-alkaline to alkaline nature of the biotites;(d) Classification diagram of garnets of GGG based on end-member composition reflecting the Almandine nature of the garnets.

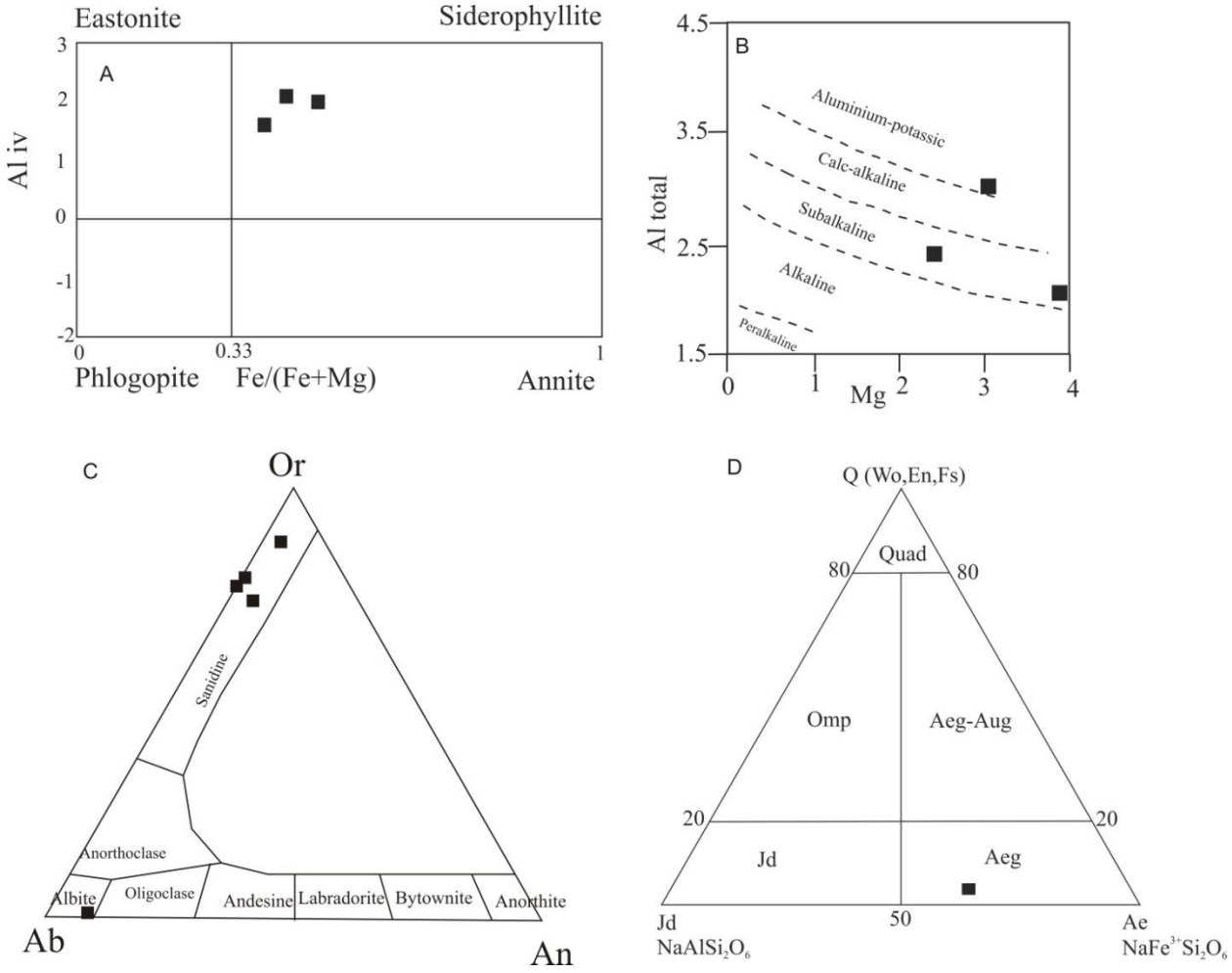

Figure 4.4 (a) Classification of biotites of alkali granites of Jhalda area via Al_{iv} versus Fe/(Mg+Fe) diagram which shows roughly Siderophyllite nature of the biotites; (b) Plot of biotite data in discrimination diagram based on Mg and Al_{total} (Nachit 1986), which shows sub-alkaline to alkaline nature of the biotites; (c) Triangle diagram showing plots of the compositional data of Feldspar in Feldspar classification (Or-Ab-An) after Deer et. al., (1963), which shows albite composition for plagioclase feldspars and Sanidine composition for alkali-feldspars in the alkali granitoids of Jhalda; (d) Classification diagram of pyroxene of alkali granites of Jhalda showing aegirine-like nature.

Table 4.1 Chemical composition of representative alkali feldspar grains including their cation and end member proportion for the granitoids of Raghunathpur-Bero area.

			PG					GGG					MGG				
Point	4 / 1	6 / 1	7 / 1	10 / 1	12/1	7 / 1	8 / 1	16 / 1	17 / 1	21 / 1	52 / 1	57 / 1	60 / 1	63 / 1	65 / 1	46 / 1	64 / 1
SiO2	64.99	64.90	64.64	64.88	65.11	64.71	64.54	64.31	63.85	64.13	64.10	63.44	64.39	64.02	64.44	64.88	64.61
TiO2	0.00	0.00	0.03	0.00	0.00	0.00	0.00	0.00	0.01	0.00	0.03	0.01	0.00	0.00	0.00	0.08	0.05
Al2O3	18.75	18.54	18.77	18.30	18.6	18.23	18.17	18.17	18.19	18.00	18.38	18.06	18.45	18.28	18.19	18.56	18.39
Cr2O3	0	0.041	0	0	0	0.011	0.035	0.037	0	0.047	0	0	0.13	0.028	0	0.025	0
Fe2O3	0	0	0	0	0	0	0	0	0	0	0	0	0	0	0	0	0
FeO	0.15	0.03	0.20	0.01	0.09	0.07	0.13	0.06	0.31	0.06	0.18	0.31	0.00	0.32	0.06	0.10	0.21
MnO	0	0	0.12	0.04	0.02	0.016	0	0.09	0.06	0	0.01	0.05	0	0	0	0	0.02
MgO	0.00	0.01	0.00	0.00	0.02	0.00	0.00	0.00	0.00	0.00	0.01	0.00	0.00	0.00	0.02	0.00	0.00
CaO	0.00	0.01	0.00	0.00	0.00	0.00	0.01	0.00	0.00	0.00	0.00	0.00	0.00	0.00	0.01	0.00	0.00
BaO	0.72	0.79	0.74	0.62	0.72	0.27	0.37	0.35	0.36	0.35	0.50	0.42	0.49	0.44	0.42	0.48	0.84
Na2O	1.82	1.75	1.15	0.83	1.24	0.66	0.67	0.47	0.38	0.34	1.05	0.82	1.42	1.46	2.40	1.15	0.94
K2O	14.22	14.40	15.28	15.47	15.1	15.83	15.86	16.21	16.03	16.18	15.25	15.77	14.86	14.64	13.55	15.24	15.33
Si	2.70	2.70	2.70	2.70	2.99	3.00	2.99	2.99	2.99	3.00	2.98	2.97	2.98	2.98	2.98	2.98	2.99
Ti	0.00	0.00	0.00	0.00	0.00	0.00	0.00	0.00	0.00	0.00	0.00	0.00	0.00	0.00	0.00	0.00	0.00
Al	1.012	1.003	1.015	0.998	1.00	0.997	0.994	0.995	1.002	0.992	1.006	0.995	1.005	1.001	0.991	1.0057	1.0011
Cr	0	0.006	0	0	0	0.00	0.001	0.001	0	0.001	0	0	0.005	0.001	0	1	0
Fe3	0	0	0	0	0	0	0	0	0	0	0	0	0	0	0	0	0
Fe2	0.006	0.001	0.007	0.000	0.003	0.003	0.005	0.002	0.012	0.002	0.007	0.012	0.000	0.013	0.002	0.004	0.008
Mn	0.000	0.000	0.005	0.002	0.001	0.001	0.000	0.004	0.003	0.000	0.000	0.002	0.000	0.000	0.000	0.000	0.001
Mg	0.000	0.001	0.000	0.000	0.001	0.000	0.000	0.000	0.000	0.000	0.000	0.000	0.000	0.000	0.001	0.000	0.000
Ca	0	0	0	0	0	0	0	0	0	0	0	0	0	0	0.000	0	0
Ba	0.013	0.014	0.013	0.011	0.013	0.005	0.007	0.006	0.007	0.006	0.009	0.008	0.009	0.008	0.008	0.009	0.015
Na	0.161	0.156	0.102	0.074	0.110	0.059	0.060	0.042	0.034	0.030	0.094	0.074	0.127	0.132	0.215	0.102	0.084
K	0.831	0.843	0.894	0.913	0.882	0.936	0.939	0.961	0.956	0.966	0.904	0.941	0.876	0.868	0.800	0.894	0.904
An	0	0.054	0	0	0	0	0.025	0.005	0	0	0	0	0	0.005	0.049	0	0
Ab	16.27	15.61	10.27	7.52	11.09	5.93	5.99	4.18	3.44	3.06	9.46	7.33	12.65	13.19	21.18	10.27	8.53
Or	83.73	84.34	89.73	92.48	88.91	94.07	93.99	95.82	96.56	96.94	90.54	92.67	87.35	86.80	78.77	89.73	91.47

Table.4.2. Chemical composition of representative plagioclase feldspar grains of Raghunathpur-Bero area and their cation composition

		PG					**GGG**					**MGG**			
Data	3 / 1	8 / 1	9 / 1	18 / 1	23 / 1	5 / 1	6 / 1	9 / 1	11 / 1	19 / 1	45 / 1	50 / 1	55 / 1	62 / 1	76 / 1
SiO2	60.27	61.57	61.35	61.3	61.02	58.97	59.64	60.04	59.04	58.84	62.58	61.53	61.42	62	61.37
Al2O3	25.15	24.72	24.54	24.59	24.99	25.63	25.24	25.36	25.24	25.2	24.1	24.39	23.94	24.1	24.2
FeO	0.05	0.06	0.11	0	0.09	0.07	0	0.35	0.02	0.05	0	0.08	0.02	0.3	0.03
MgO	0	0.009	0.000	0.005	0.011	0.000	0.022	0.000	0.000	0.000	0.000	0.003	0.000	0.000	0.000
MnO	0	0.000	0.000	0.000	0.058	0.067	0.000	0.000	0.045	0.008	0.000	0.003	0.000	0.056	0.029
CaO	6.94	6.36	6.19	6.37	6.55	7.70	7.51	7.56	7.50	7.58	5.57	6.10	5.79	5.78	5.97
Na2O	8.22	8.50	8.54	8.47	8.36	7.42	7.58	7.66	7.58	7.50	9.11	8.65	8.70	8.88	8.80
K2O	0.19	0.14	0.14	0.11	0.10	0.33	0.39	0.27	0.32	0.33	0.04	0.21	0.19	0.13	0.15
TiO2	0.05	0.00	0.00	0.01	0.01	0.00	0.01	0.00	0.00	0.00	0.00	0.04	0.02	0.00	0.00
P2O5	0.04	0.00	0.00	0.00	0.02	0.00	0.00	0.00	0.00	0.04	0.00	0.02	0.05	0.00	0.01
Si	2.71	2.71	2.70	2.70	2.70	2.62	2.65	2.64	2.64	2.64	2.73	2.70	2.72	2.71	2.71
Ti	0.00	0.00	0.00	0.00	0.00	0.00	0.00	0.00	0.00	0.00	0.00	0.00	0.00	0.00	0.00
Al	1.30	1.28	1.27	1.27	1.29	1.34	1.32	1.32	1.33	1.33	1.24	1.26	1.25	1.24	1.26
Cr	0	0	0	0	0	0	0	0	0.00	0	0.002	0	0	0	0.001
Fe3	0	0	0	0	0	0	0	0	0	0	0	0	0	0	0
Fe2	0.002	0.002	0.004	0.000	0.003	0.003	0.000	0.013	0.001	0.002	0.000	0.003	0.001	0.011	0.001
Mn	0	0	0	0	0.002	0.003	0	0	0.002	0.000	0	0.0001	0	0.002	0.001
Mg	0	0.0006	0.0000	0.0003	0.0007	0.0000	0.0015	0	0	0	0	0.0002	0	0	0
Ca	0.327	0.298	0.291	0.300	0.308	0.367	0.357	0.357	0.359	0.364	0.260	0.287	0.275	0.271	0.282
Ba	0	0	0.0007	0	0	0	0	0	0	0	0	0.001	0	0	0
Na	0.70	0.72	0.73	0.72	0.71	0.64	0.65	0.65	0.66	0.65	0.77	0.74	0.75	0.75	0.75
K	0.01	0.01	0.01	0.01	0.01	0.02	0.02	0.02	0.02	0.02	0.00	0.01	0.01	0.01	0.01
Ab	67.49	70.23	70.88	70.23	69.43	62.40	63.25	63.72	63.50	63.01	25.18	27.74	26.62	26.28	27.04
An	31.49	29.03	28.39	29.19	30.04	35.78	34.61	34.78	34.75	35.18	74.60	71.13	72.33	73.02	72.13
Or	1.02	0.74	0.74	0.57	0.53	1.83	2.15	1.49	1.75	1.80	0.22	1.13	1.05	0.70	0.83

Table.4.3. Chemical composition of representative biotite grains of Raghunathpur-Bero area and their cation composition

	PG					GGG								MGG					
Oxides	2/1	11/1	16/1	21/1	22/1	1/1	3 / 1	4/ 1	10/1	51/1	54/1	55/1	58/1	64/1	70/1	71/1	77/1	78/1	79/1
SiO2	36.59	36.91	36.42	36.29	35.17	37.03	36.99	35.15	35.39	37.87	37.81	34.77	38.04	37.65	35.36	35.49	35.38	35.43	36.4
TiO2	5.32	4.72	6.56	5.38	5.01	0.08	0.00	4.87	5.24	1.43	1.25	4.30	1.30	1.17	4.09	4.11	4.12	3.94	1.04
Al2O3	13.4	13.7	13.5	13.2	14.0	21.5	21.2	13.1	13.2	11.8	11.7	12.9	12.1	11.7	13.2	13.1	13.1	13.1	12.4
FeO	15.7	15.1	15.9	16.2	16.2	25.6	24.5	18.2	18.3	18.2	18.7	17.4	18.9	18.5	18.2	18.2	18.5	18.1	20.3
MnO	0.0	0.0	0.1	0.2	0.2	0.9	1.1	0.0	0.0	0.3	0.3	0.1	0.5	0.4	0.2	0.2	0.2	0.1	0.4
MgO	10.7	11.2	10.2	10.6	11.2	3.4	3.1	8.2	8.0	5.3	5.0	8.7	5.1	4.8	8.8	8.5	8.5	8.5	4.9
CaO	0.0	0.0	0.0	0.0	0.1	3.2	4.6	0.0	0.0	11.1	11.1	0.0	11.0	11.2	0.0	0.0	0.0	0.0	9.5
Na2O	0.04	0.01	0.01	0.02	0.05	0.01	0.01	0.04	0.00	1.65	1.57	0.06	1.58	1.61	0.03	0.02	0.04	0.05	1.36
K2O	9.52	9.06	9.39	9.43	7.48	0.02	0.00	9.52	9.60	2.28	2.29	9.54	2.24	2.23	9.49	9.48	9.30	9.55	2.02
BaO	0.47	0.32	0.43	0.42	0.30	0.04	0.03	0.28	0.31	0.01	0.00	0.33	0.02	0.03	0.16	0.33	0.32	0.30	0.01
ZnO	0.00	0.00	0.04	0.24	0.00	0.00	0.01	0.00	0.23	0.00	0.00	0.00	0.00	0.02	0.07	0.03	0.00	0.02	0.00
Si	5.73	5.78	5.66	5.70	5.60	5.70	5.71	5.75	5.74	6.07	6.10	5.77	6.06	6.10	5.77	5.80	5.78	5.82	5.99
Al iv	2.27	2.22	2.34	2.30	2.40	2.30	2.29	2.25	2.26	1.93	1.90	2.23	1.94	1.90	2.23	2.20	2.22	2.18	2.01
Al vi	0.21	0.31	0.15	0.15	0.24	1.60	1.57	0.27	0.26	0.31	0.32	0.28	0.33	0.33	0.29	0.32	0.31	0.34	0.40
Ti	0.63	0.56	0.77	0.64	0.60	0.01	0.00	0.60	0.64	0.17	0.15	0.54	0.16	0.14	0.50	0.50	0.51	0.49	0.13
Cr	0.00	0.01	0.00	0.01	0.00	0.00	0.00	0.01	0.00	0.00	0.00	0.00	0.01	0.00	0.00	0.01	0.00	0.00	0.00
Fe2+	2.06	1.97	2.06	2.13	2.16	3.30	3.16	2.49	2.48	2.45	2.52	2.41	2.52	2.51	2.49	2.49	2.53	2.48	2.79
Mn	0.00	0.01	0.01	0.02	0.02	0.12	0.15	0.00	0.00	0.04	0.04	0.02	0.06	0.05	0.03	0.03	0.03	0.02	0.06
Mg	2.51	2.62	2.37	2.49	2.66	0.79	0.72	2.01	1.93	1.26	1.21	2.15	1.21	1.16	2.14	2.07	2.08	2.07	1.20
Zn	0.00	0.00	0.00	0.03	0.00	0.00	0.00	0.00	0.03	0.00	0.00	0.00	0.00	0.00	0.01	0.00	0.00	0.00	0.00
Fe3+	0.25	0.24	0.26	0.26	0.27	0.41	0.39	0.31	0.31	0.30	0.31	0.30	0.31	0.31	0.31	0.31	0.31	0.31	0.35
Ca	0.00	0.00	0.00	0.00	0.01	0.53	0.76	0.00	0.00	1.90	1.92	0.00	1.88	1.95	0.01	0.00	0.00	0.00	1.67
Na	0.01	0.00	0.00	0.01	0.02	0.00	0.00	0.01	0.00	0.51	0.49	0.02	0.49	0.50	0.01	0.01	0.01	0.02	0.43
K	1.90	1.81	1.86	1.89	1.52	0.00	0.00	1.98	1.99	0.47	0.47	2.02	0.45	0.46	1.97	1.98	1.94	2.00	0.42
Ba	0.03	0.02	0.03	0.03	0.02	0.00	0.00	0.02	0.02	0.00	0.00	0.02	0.00	0.00	0.01	0.02	0.02	0.02	0.00
OH*	4.00	4.00	4.00	4.00	4.00	4.00	4.00	3.55	3.59	3.55	3.50	3.78	3.54	3.51	3.75	3.74	3.76	3.75	3.55
TOTAL	19.61	19.55	19.52	19.65	19.52	18.75	18.75	19.69	19.66	19.43	19.43	19.75	19.43	19.43	19.77	19.73	19.74	19.75	19.45
Al tot	2.48	2.54	2.48	2.45	2.64	3.91	3.86	2.53	2.52	2.24	2.22	2.51	2.28	2.23	2.53	2.52	2.53	2.53	2.41
Fe/(Fe+Mg)	0.45	0.43	0.47	0.46	0.45	0.81	0.81	0.55	0.56	0.66	0.68	0.53	0.68	0.68	0.54	0.55	0.55	0.54	0.70

Table.4.4. Chemical composition of representative garnet grains of Raghunathpur-Bero area and their cation composition.

Oxides	13 / 1	15 / 1	23 / 1	27 / 1	28 / 1
SiO2	27.337	34.147	27.972	37.27	36.879
TiO2	0	0.082	0	0.015	0
Al2O3	18.003	21.161	18.292	21.328	21.03
FeO	36.135	26.107	36.661	34.739	32.849
MnO	0.014	0.129	0	0.86	0.727
MgO	6.821	6.575	6.288	3.564	3.036
CaO	0.357	0.533	0.455	4.388	6.175
Na2O	0.07	0.021	0.019	0	0
K2O	0.099	0.782	0.077	0.028	0.016
ZnO	0.084	0.13	0.175	0.095	0
F	0	0.002	0	0.007	0
Cl	0.008	0.026	0.016	0	0
Si	2.531169	2.931228	2.561711	2.929483	2.938124
Al iv	0.468831	0.068772	0.438289	0.070517	0.061876
Al vi	1.530719	2.096327	1.568358	1.911684	1.918913
Ti	0	0.005294	0	0.000887	0
Cr	0	0	0	0.002734	0
Fe3+	0.417132	0	0.383776	0.075234	0.072026
Fe2+	2.381037	2.007312	2.424154	2.208389	2.116686
Mn	0.001098	0.00938	0	0.057259	0.049061
Mg	0.941473	0.841361	0.858437	0.417598	0.360564
Zn	0.005743	0.00824	0.011834	0.005514	0
Ca	0.035419	0.049025	0.044649	0.369566	0.527135
Total	8.31262	8.016938	8.291209	8.048866	8.044385
Almandine	61.36214	69.04914	64.74675	71.17501	68.11706
Andradite	1.399302	0	1.742939	3.852264	3.677164
Grossular	0	1.686405	0	8.623133	14.26406
Pyrope	37.19517	28.9418	33.51031	14.25502	12.27191
Spessartine	0.04338	0.322657	0	1.954565	1.669807
Uvarovite	0	0	0	0.140015	0

Table 4.5 Chemical composition of representative biotite grains of ARG of Jhalda area and their cation composition.

Data	**10 / 1 .**	**11 / 1 .**	**26/1**
Na2O	2.63	0.09	0.175
MgO	10.81	13.83	15.437
SiO2	42.43	42.36	39.948
Al2O3	14.16	17.84	10.708
CaO	11.29	0	2.193
P2O5	0.01	0.01	0.124
Cl	0.3	0.24	0
TiO2	0.73	4.35	0
FeO	16.46	16.55	15.572
MnO	0.24	0.19	0.111
BaO	0.04	0.75	0.097
Total	99.1	96.21	84.365
Si	5.99371	5.90554	6.39099
Al iv	2.00629	2.09446	1.60901
Al vi	0.35141	0.83711	0.41021
Ti	0.07755	0.45609	0
Cr	0	0	0
Fe	1.94459	1.92964	2.0835
Mn	0.02872	0.02244	0.01504
Mg	2.27634	2.87419	3.6815
Ca	1.70888	0	0.37593
Na	0.72038	0.02433	0.05429
K	0	0	0
Sr	0	0	0
Ba	0.00221	0.04097	0.00608
OH*	4	4	4
TOTAL	19.1101	18.1848	18.6265
Y total	4.67861	6.11946	6.19025
X total	2.43147	0.0653	0.4363
Al total	2.3577	2.93157	2.01922
Fe/Fe+Mg	0.4607	0.40169	0.3614

Table 4.6 Chemical composition of representative feldspar grains of ARG of Jhalda area and their cation composition.

Data	**4 / 1 .**	**6 / 1 .**	**8 / 1 .**	**20 / 1 .**	**9 / 1 .**
Na2O	0.858	1.691	1.809	1.716	10.408
F	0.01	0.01	0	0	0.004
MgO	0.005	0.039	0	0.013	0.004
Al2O3	19.954	20.264	19.648	19.982	21.322
SiO2	61.732	59.192	62.856	63.152	67.272
K2O	13.369	11.025	12.579	12.812	0.094
CaO	0	0.585	0	0	1.737
TiO2	0	0	0	0	0.005
Cr2O3	0	0.051	0	0.069	0
MnO	0	0.083	0	0.102	0.037
FeO	0.028	0.097	0	0.07	0.066
ZnO	0.168	0	0.11	0.144	0
Cl	0	0.016	0	0.004	0.023
P2O5	0.003	0.01	0	0.005	0.055
ZrO2	0	0	0.142	0	0
BaO	5.004	6.186	2.973	3.633	0
Total	101.131	99.25	100.117	101.701	101.026
An	3.23991	3.48785	0	0	8.39799
Ab	8.5991	18.2446	17.9363	16.913	91.0609
Or	88.161	78.2675	82.0637	83.087	0.54113

Table 4.7 Chemical composition of representative pyroxene grains of ARG of Jhalda area and their cation composition.

data	1	2	3
SiO2	50.7	52.7	50.8
TiO2	0.45	0.11	0.3
Al2O3	1.17	1.01	1.3
FeO	33.4	31.23	31.2
MnO	0.51	0.12	0.5
MgO	0.58	0.05	0.3
CaO	0.35	1.13	3.3
Na2O	6.79	12.58	11.5
K2O	1.4	0.01	0.1
Si	2.09131	2.002	1.94
Ti	0.01396		0.01
Al	0.05688	0.023	0.06
Fe+3	0.34927	0.893	0.84
Fe+2	0.80292	0.099	0.16
Mn	0.01782	0.004	0.02
Mg	0.03567	0.003	0.02
Ca	0.01547	0.046	0.13
Na	0.54303	0.926	0.85
K	0.07367	0	0.01
1- present study			
2- aegirine data of Dimra pahar, Purulia (Basak and Goswami, 2020)			
3- aegirine data of Finland (Hytonen et al 1985)			

Table 4.8 Chemical composition of representative apatite and sphene of ARG of Jhalda area.

Data			**Apatite**					**Sphene**	
Na2O	0.028	0	0.036	0.022	0.073	0.004	0.041	0.001	0.015
F	3.663	3.782	3.67	3.604	3.789	3.597	3.749	0	0
MgO	0	0.002	0	0	0	0	0	0.023	0.028
Al2O3	0	0.005	0.005	0.014	0	0	0	2.666	2.449
SiO2	0.31	0.395	0.999	0.634	0.224	0.484	0.595	29.813	29.769
K2O	0	0	0	0	0	0	0	0.011	0
CaO	55.413	55.846	54.913	55.431	55.95	55.582	55.76	27.573	26.951
TiO2	0	0	0	0	0	0	0	34.403	34.23
Cr2O3	0	0	0.038	0	0	0	0	0	0
MnO	0	0	0.075	0.057	0.011	0	0.019	0.089	0
FeO	0.022	0.095	0.017	0	0.035	0	0	1.565	1.936
ZnO	0	0	0.021	0	0	0	0	0	0
Cl	0.081	0.103	0.145	0.214	0.235	0.135	0.159	0.003	0
P2O5	40.922	41.035	39.452	40.273	41.871	39.628	40.428	0.034	0.109
ZrO2	0	0	0	0	0	0	0	0.374	0.124
BaO	0	0	0.049	0	0	0	0.026	0.342	0.347
Total	100.44	101.262	99.419	100.249	102.188	99.432	100.777	96.897	95.956

CHAPTER-5

GEOCHEMISTRY OF THE GRANITOID ROCKS OF RAGHUNATHPUR-BERO AREA AND JHALDA AREA OF CGGC

5.1. ANALYTICAL PROCEDURE

5.2. GRANITOIDS OF RAGHUNATHPUR AREA

5.2.1. MAJOR ELEMENT DATA

5.2.2. TRACE ELEMENT AND REE DATA

5.3. GRANITOIDS OF JHALDA AREA

5.3.1. MAJOR ELEMENT DATA

5.3.2. TRACE ELEMENT AND REE DATA

5.4. INTERPRETATION OF GEOCHEMICAL DATA

5.4.1. RAGHUNATHPUR AREA

5.4.2. JHALDA AREA

FIGURES

TABLES

This chapter deals with the major element and trace element geochemical data of the granitoids of both Raghunathpur and Jhalda areas. Major element geochemical datas are used in rock classification and nomenclature, in the construction of variation diagrams displaying the data as bivariate and trivariate plots and plotting the chemical composition of a rock in the phase diagram. Variation diagrams are used to show the interrelationship between the elements from which the geochemical mechanisms can be inferred. Trace elements are more capable in discriminating between petrological processes than the major element geochemical data. Geochemistry of 19 granitoid samples from Raghunathpur area and 9 samples from Jhalda area are studied in order to classify, characterize, discriminate them tectonically and assign a probable tectonic setting of their formation.

5.1. Analytical Procedure:

Bulk rock major and Trace Elements Major element analyses of twenty representative samples of Raghunathpur area of CGGC were determined in the X-ray fluorescence (XRF) instrument (SIEMENS SRS 3000) at the Wadia Institute of Himalayan Geology (WIHG), Dehra Dun, India. Samples were carefully chosen to avoid the weathered surfaces and reduced to powder form (200 mesh) with agate mortar. Major elements were determined using the X-ray Fluorescence (XRF) (SIEMENS SRS 3000) facility. Sample powders were converted into pellet form for introduction into the instrument. Analysis of major elements by XRF has over 98% accuracy. Trace element and rare earth element (REE) concentrations of the samples were also determined in WIHG with inductively coupled mass spectrometry (ICP-MS; PerkinElmer SCIEX ELANDRCe). Sample dissolution for ICP-MS analysis followed the procedure of Khanna et al., (2009). International

rock standards of granite (NIM-G) was also analysed along with the samples to check precision and accuracy.

Major and trace element analysis of nine representative samples of alkali granites from western part of CGGC (Jhalda area) were determined at the Mineral Laboratories, Bureau Veritas Commodities, Canada Ltd. The samples were analysed for 49 elements by the ICP-MS (Inductively coupled plasma-mass spectrometry) and ICP-ES (Inductively coupled plasma-emission spectrometry) analytical procedures. The following elements were analysed: Si, Ti, Al, Fe, Mn, Mg, Ca, Na, K, P, Cr, As, B, Ba, Be, Co, Cs, Cu, Ga, Hf, Mo, Nb, Ni, Pb, Rb, Sn, Sr, Ta, Th, U, V, W, Y, Zn, Zr, La, Ce, Pr, Nd, Sm, Eu, Gd, Tb, Dy, Ho, Er, Tm, Yb and Lu. Sample preparation included splitting of 0.2 g sample for $LiBO_2/Li_2B_4O_7$ fusion decomposition for ICP-ES (macro elements) and 0.2 g sample for ICP-MS (micro elements and REE (rare earth elements)). Natural rocks of known composition were used as reference standards. Rock standard for granite (STD SO-19) was also analysed to check the precision and accuracy of the analysis. The laboratory errors were below 10% which is considered very reliable.

5.2. Granitoids of Raghunathpur area:

5.2.1. Major element data:

Major element data of the three varieties of granitoid rocks are presented in Table 5.1. SiO_2 (wt %) value of the GGG, MGG and PG ranges from 55%-73%, 64%-66% and 75%-79%, respectively. Molecular ASI (Alumina saturation index, ASI = Al / (Ca-1.67P+Na+K) in molecular basis) and AI (Agpaitic index, AI = Al-(Na+K) in molecular basis) vary between 0.93 – 0.97, 0.90-1.06, 1.09 –1.13 and 1.30 –1.44, 1.09-1.20, 1.40-1.90, respectively in the MGG, PG and GGG of the CGGC granitoids. The CaO content of MGG is relatively higher (2.2-3.2 wt %)

than the other two types of granitoid (1.4-2.9 wt % in GGG and 0.6-1.9 wt % in PG).The total alkali content of MGG is slightly higher than the other two varieties. The GGG is relatively less enriched in Total Alkali (Na_2O+K_2O) content (4.9-7.1) than the other two types (8.2-9.3 in MGG and 8.06-9.2 in PG).

- **Classification diagrams:**

Bivariate oxide-oxide major element plots are the easiest way to classify igneous rocks (Rollinson 1993).

TAS diagram:

Total Alkali (TA) – Silica (S) diagram is one of the most popular classification diagrams for volcanic as well as plutonic rocks. Total alkali (Na2O + K2O) content is plotted against SiO2 content to classify the volcanic rocks. This diagram divides rocks into ultrabasic, basic, intermediate and acidic based on the SiO_2 content (Peccerrilo and Taylor, 1976). In the TAS classification diagram (Fig. 5.1.a. Cox et al., 1979 adapted by Wilson 1989), the GGG plots in the diorite-quartz diorite-granite field, whereas the MGG plots in the granite-quartz monzonite field and the PG plots in the granite field. Rocks can be sub-divided into alkaline and sub-alkaline fields based on this diagram. In this case, all the three rock types can be classified as sub-alkaline rocks.

Classification based on CIPW norm:

Norm calculation is the way of calculating the mineralogy of a rock from its chemical composition. This calculation assumes that the magma is anhydrous and based completely on the chemistry of the rocks. The calculated CIPW norm data for the three types of CGGC granitoids are presented in Table 5.2. Norm data reveals the presence of normative corundum in all the

samples except two of MGG and one of PG. Normative quartz content is highest in PG (31-67%), followed by GGG (22-36 %) and MGG (16-39%).

Classification based on Ab-Or-An diagram:

The Ab-Or-An classification diagram of granites after O'Connor (1965) can be used in felsic igneous rocks with >10% normative quartz. This diagram is mainly based on the normative feldspar composition projected in the Ab-Or-An face of the Qtz-Ab-Or-An tetrahedron. The normative feldspar composition of the three granitoid types when plotted in the Albite-Orthoclase-Anorthite diagram (O`Connor, 1965; modified by Barker, 1979, Fig. 5.1.b.) confirms the nature of the granitoid rocks of CGGC. MGG shows quartz-monzonitic composition, while the PG plots distinctly in the granitic field. The GGG plots haphazardly in the tonalite, quartz-monzonite-granodiorite field.

SiO_2 versus K_2O diagram:

Rocks of sub-alkaline series have been further subdivided into high K, medium K and low K types based on the SiO_2 and K_2O content (Le Maitre et al., 1989). In the SiO_2 versus K_2O diagram (after Peccerillo and Taylor, 1976; Le Maitre, 1989 and Rickwood, 1989, Fig. 5.1.c.), MGG, GGG and PG display a strong potassic character. The samples overlap the high K-calc-alkaline and shoshonitic fields. Precisely, the PG lies in the high K-calc-alkaline field, whereas GGG lies in the calc-alkaline-high K-calc-alkaline field and the MGG lies in the shoshonitic field.

Alumina Saturation Index (ASI):

Alumina saturation with respect to alkalis and lime is one of the most important factors recognized since long and has been most extensively and efficiently used by many workers

(Chappell, 1974; Chappell and White., 1992) for genetic classification of rocks. Rocks with ASI>1.0 are corundum normative and are termed as peraluminous (Zen, 1988). If ASI<1.0 and molecular Na+K < molecular Al then the rock is termed as metaluminous. If ASI<1.0 and molecular Na+K > molecular Al then the rock is termed as peralkaline. In the molecular Al_2O_3/ ($CaO+Na_2O+K_2O$) versus molecular Al_2O_3/(Na_2O+K_2O) diagram (Fig. 5.1.d.) after Maniar and Piccoli, (1989) and Shand,(1943); the GGG and PG with ASI>1 plot predominantly in the peraluminous field while the MGG with ASI<1 plot along the border of metalumious and peraluminous fields.

Fe number or Fe#:

Miyashiro (1974) showed that the tholeiitic and calc-alkaline trend of rocks can well be distinguished on a SiO_2 versus FeOt/(FeOt+MgO) plot. This variable is referred to as Fe-number or Fe#. The Fe# numbers (Fe# = $100Fe^{2+}$ / $Mg+Fe^{2+}$) are ≤ 0.96 for MGG and it varies between 0.73 and 0.92 for PG and GGG. In the diagram SiO_2 versus FeOt /(FeOt+ MgO) (Fig. 5.1.e.; after Frost et al., 2001), all the three types of granitoids plot in the ferroan field.

Modified Alkali Lime Index (MALI):

Peacock (1931) divided volcanic suites according to the alkali lime index that is SiO2 content at which Na2O + K2O content in a suite equals CaO. Frost et al. (2001) introduced a new variable Na2O+K2O-CaO reducing the three variables necessary for the classification. This new variable is named as Modified Alkali Lime Index (MALI). Variation in the Modified Alkali-Lime Index may be caused by either the variation in composition of source region or differentiation history of magma. In SiO_2 versus (Na_2O+K_2O-CaO) diagram (Fig. 5.1.f., after Frost, 2001), the MGG

plots in the alkalic field, while the GGG plots in the alkali-calcic to alkalic and PG plots in the alkalic field.

Classification based on multi-cationic proportion:

The most useful multi-cationic classification diagram for plutonic rocks is the R1-R2 classification plot of de La Roche et al. (1980). This classification is based upon the cation proportions expressed in mili-cations. R1 is plotted in x-axis and can be defined as:

$$R1 = [4Si – 11(Na+K) -2(Fe+Ti)]$$

R2 is plotted in the y-axis and can be defined as:

$$R2 = (Al + 2Mg + 6Ca)$$

This diagram includes the entire major element chemistry of an igneous rock and degree of silica saturation and feldspar compositions can also be plotted in this diagram. The calculated R1 and R2 parameters when plotted in this diagram (Fig. 5.2.a) it shows the following results: GGG plot in the tonalite-granite-granodiorite field, MGG plot in the quartz monzonite-granite field and PG plot in the granite field.

Chemical data obtained from granitoids of known tectonic settings, when plotted on the de la Roche R1-R2 multicationic diagram, generate definite areas which can be matched with known tectono-magmatic associations. The calculated R1-R2 parameters when plotted in the Rl-R2 diagram of Batchelor and Bowden, (1985), (Fig. 5.2.b), it shows that- GGG falls in the late-orogenic to syn-collisional field, the MGG plots in the late-orogenic field and PG plots in the post-orogenic field.

- **Variation diagrams:**

Variation diagrams are a very popular geochemical diagram in which a bivariate plot or a scatter diagram is plotted between two selected variables. Such a bivariate plot in which SiO2 is plotted in the x-axis is known as Harker diagram. SiO_2 is chosen as a parameter for majority of the igneous rocks because it is the major constituent of the rock and shows greatest variability than any other oxides in acidic igneous rocks.

Binary variation diagrams:

Major oxides of all the granitoid types have been plotted against SiO_2 wt% in the Harker variation diagram (Fig. 5.3) to evaluate trends of magmatic differentiation and element to element correlation. The bi-axial variation diagram (Fig. 5.3) of granitoids of Raghunathpur area shows good negative co-relation between SiO_2 and Al_2O_3, Fe_2O_3, CaO, TiO_2, MgO and P_2O_5 and positive co-relation with Na_2O and K_2O.Variations in the Fe_2O_3 content among the samples has been noticed. The GGG shows a relatively high amount of Fe_2O_3 (ranging from 3.2-9.3 wt %). The amount of Fe_2O_3 decreases in the MGG (3.2-4.4 wt %) and diminishes to almost nil in case of pink granite (0.22-0.68 wt. %).

Triangular variation diagrams:

Triangular variation diagrams are used when it is necessary to show simultaneous change among three variables.

AFM diagram is the most common triangular plot, named after the three parameters Alkali (Na2O+K2O) – Fe oxide (FeO+Fe2O3) – MgO. This diagram is used to differentiate between tholeiitic trend and calc-alkaline differentiation trend in sub-alkaline magma series. Alkali

content-Fe oxide-MgO contents of GGG, MGG and PG are plotted in the AFM diagram of Irvine and Baragar, (1971). All the three granitoid types show a calc-alkaline trend (Fig. 5.4.a).

Miscellaneous plots:

SiO_2 and Na_2O+K_2O values of granitoids of Raghunathpur-Bero area when plotted in the SiO_2 versus Na_2O+K_2O diagram (after Irvine and Baragar 1971; Fig.5.4.b) shows that these granitoids are of sub-alkaline nature. Similarly plots of granitoids of Raghunathpur-Bero area in the SiO_2 versus A/CNK diagram after Frost et al. (2001) (Fig.5.4.c) shows S-type nature of all the granitoid varieties.

5.2.2. Trace element data and REE data:

Trace element data of the three varieties of granitoid rocks are presented in the Table 5.3.

Normalized multi-element digrams:

Normalized multi-elemnt diagrams or spider diagrams are based upon grouping of trace elements incompatible with respect to particular mantle mineralogy. There are three popular ways of normalizing trace element datas for presentation in a spider diagram. These are primitive mantle compostion, chondritic meteorite composition and primtive MORB composition.

Primitive mantle normalized diagram:

The primitive mantle is the composition of the mantle before continental crust formed. The multi-element primitive mantle normalized spider diagram of CGGC granitoids (primitive mantle data from McDonough and Sun, 1995; Fig. 5.5.a.) reveal a strong enrichment in more incompatible elements (Cs, Ba, Rb, Th, U) compare to less incompatible elements (Ti, Y, Yb,

Lu, Sr, Nb). The diagram shows significant negative anomalies at Ba, Nb, Ta, Sr, and positive anomalies at Rb, Th, U. Negative anomalies observed for Nb and Ta support their more Nb-Ta depleted character and affinity towards arc granitoids. The granitic rocks show enrichment in large ion lithophile (LIL) elements relative to the high field strength (HFS) elements as well as negative anomalies at Ce, and Ba.

Chondrite normalized spider diagrams:

Thompson (1980) proposed that normalization with respect to chondritic values are more suitable than that of the primitive mantle values because the chondritic values are directly measured rather than estimated. REE patterns of the CGGC granitoids in the chondrite-normalized diagrams (Chondrite data from Boynton, 1984; Fig. 5.5.b.) show enrichment of light rare earth elements (LREE: La-Nd). The REE patterns reveal a relatively strong fractionation (upto 100 times) of LREE with respect to middle rare earth elements (MREE: Sm- Ho) and a slight fractionation of MREE with respect to heavy rare earth elements (HREE: Er-Lu). In the bi-variate diagrams constructed with SiO_2 against trace elements, such as Ba, Eu, Zr (Fig. 5.6), all the granitoid rocks show negative correlations, whereas Y exhibits no apparent pattern. Moderately negative Eu anomalies are shown by the granitoid rocks in the chondrite normalized REE diagram (Fig. 5.5.b.). Eu anomalies are measured by Eu/Eu* and it varies from 0.39-0.99 (in GGG), 0.57-0.89 (in MGG) and 0.29-0.59 (in PG). A single sample of PG only shows positive Eu anomaly (1.03). The values of (La/Yb) N, (La/Nd) N and (Dy/Lu)N ratios, which respectively measure fractionation of LREE over HREE, LREE over MREE and MREE over HREE, vary among granitoid samples and are given in Table 5.4.

Discrimination diagrams:

Discrimination diagrams can be used to suggest an affiliation of the former tectonic environment of the rocks by the aid of trace elements. Pearce et al. (1984) classified the tectonic setting of granites into oceanic-ridge, volcanic-arc, within-plate and collisional. Trace elements like Y, Yb, Rb, Ba, K, Nb, Ta, Ce, Sm, Zr and Hf most effectively discriminate granites of different tectonic setting. Among these, Rb, Y, Yb, Nb and Ta were selected as the most efficient discriminants to distinguish between oceanic-ridge granites (ORG), volcanic-arc granites (VAG), within-plate granite (WPG) and syn-collisional granites (syn-COLG).

In the (Y+Nb) versus Rb diagram (Fig. 5.7.a.), Y versus Nb diagram (Fig.5.7.b.), (Ta+Yb) versus Rb diagram (Fig.5.7.c.) and Ta versus Yb (Fig. 5.7.d.) all the three varieties of CGGC granitoids fall in the Volcanic Arc Granite and syn-COLG fields. In the Y versus Nb diagram (Fig.5.7.b.), the GGG plot along the Within Plate Granites and Volcanic Arc Granites boundary; MGG plot in the Within Plate Granites field and PG plot in the syn-COLG + Volcanic Arc Granites field.

5.3. Granitoid rocks of Jhalda area:

5.3.1. Major element data:

Major element data of the aegirine-riebeckite (AR) granites are given in the Table 5.5. AR granitoids are enriched in silica content (SiO_2 ranges from 75.3–76.2 wt %) and alkali content (K_2O= 4.31–4.98 wt%; Na_2O= 3.07–4.07 wt%; Na_2O+K_2O = 8.35–8.86 wt %). They show low values of CaO (0.02–0.04 wt %), Al_2O_3 (10.6–11.3 wt %), FeO_t (2.6–3.6 wt %), MgO (0.03–0.04 wt %) content, relatively higher FeO*/MgO ratios (65.7–102.5) and low Mg number. The Fe# numbers are ≥ 0.96 and ranges between 0.96 and 0.99, while molecular ASI and AI (Agpaitic Index) indices vary between 0.83-0.86 and 1.03-1.06 respectively.

Classification Diagrams:

TAS diagram:

The granitoid rocks of Jhalda area, when plotted in the Total Alkali versus Silica classification diagram (SiO_2 versus Na_2O +K_2O) after Cox et al., (1979) and adapted by Wilson (1989) show clustering of data in the granite field (Fig. 5.8.a).

Classification based on multi-cationic parameter:

AR granitoids have been classified using the R1-R2 diagram after de La Roche (1980) (Fig.5.8.b). The R1 and R2 parameters are calculated according to the expressions stated earlier. The AR granites plot in the alkali granite field.

Moreover, when the Rl-R2 parameters are plotted in the R1-R2 diagram modified by Batchelor and Bowden, (1985; Fig.5.12.), the AR granitoids cluster around the post-orogenic to anorogenic fields.

Fe number or Fe#:

The Fe number (FeOt/(FeOt+MgO) of the AR granites are calculated to be ~1.0. they can be According to the classification of Frost et al (2001), they can be classified as ferroan granites (FeOt/(FeOt+MgO) ~ 1.0) when plotted in the SiO_2 versus FeOt/(FeOt+MgO) diagram (Fig.5.8.c).

Alumina Saturation Index (ASI):

They are peralkaline in nature with ASI<1 (ASI- Alumina Saturation Index) as indicated by the molecular Al_2O_3/(CaO+Na_2O+K_2O) versus molecular Al_2O_3/(Na_2O+K_2O) diagram (Fig.5.8.d) after Maniar and Piccoli (1989) and Shand (1943).

SiO_2 versus K_2O diagram:

In the SiO_2 versus K_2O diagram (after Peccerillo and Taylor, 1976; Le Maitre, 1989 and Rickwood, 1989) the AR granitoids plot in the high K-calc-alkaline field (Fig.5.8.e). In the SiO_2 versus Na_2O+K_2O diagram (after Irvine and Baragar 1971), the AR granitoids plot in the sub-alkaline field (Fig. 5.8.f)

Classification based on CIPW norm:

The calculated CIPW norm for the AR granitoids is given in Table 5.6. Norm data reveals the presence of normative acmite in all the samples of AR granitoids.

5.3.2. Trace element data and REE data:

Trace element and REE data of the AR granites are presented in the Table 5.7.

Primitive Mantle normalized diagram:

In the multi-element primitive mantle normalized spider diagram (Fig.5.9.a. primitive mantle data from McDonough and Sun, 1995), AR granitoids show enrichment in Rb, Y, Th and U and High Field Strength Elements (HFSE) (Nb, Ta, Zr, Hf) and depletion in Sr, Ba, P and Ti which are typical of alkaline granites (Collins 1982, Whalen 1987). AR granitoids are characterized by high Zr+Nb+Ce+Y concentrations (1150–1743 ppm) and high Ga/Al ratios (10000*Ga/Al = 6.7–7.8) which is higher than the average value of 3.75 for alkaline granites as characterized by Whalen (1987). The AR granites have high abundance of Nb (120 to 160 ppm) which is higher than majority of the alkaline granites and A-type granites. AR granitoids are enriched in rare earth elements (REE) with total REE concentration ranges from 168.5–742.88 ppm.

Chondrite normalized diagram:

Chondrite normalized REE patterns (Fig. 5.9.b Chondrite data from Boynton, 1984) show strong enrichment of LREE relative to HREE with $(La/Yb)_N$ ratio of 3.72–12. Eu shows strong negative anomalies in the Chondrite normalized REE diagram (Eu/Eu*= 0.12–0.14). The values of

$(Ce/Yb)_N$, $(La/Sm)_N$ and $(Gd/Yb)_N$ ratios which respectively measure fractionation of LREE over HREE, LREE over MREE and MREE over HREE, vary among AR granitoid samples and are given in Table 5.8.

Discrimination diagrams:

In the (Y+Nb) versus Rb (Fig.5.10.a), Nb versus Y (Fig. 5.10.b), (Ta+Yb) versus Rb (Fig. 5.10.c) and Ta versus Yb (Fig. 5.10.d) (after Pearce et al., 1984), all the AR granitoids fall in the Within Plate Granite (WPG) field. In the discrimination diagrams for alkaline granites by Whalen et al. (1987), the AR granitoids fall in the A-type granite field (Fig.5.11).

5.4. **Interpretation of geochemical data:**

5.4.1. Raghunathpur area:

The granitoid rocks of GGG are mainly tonalites and quartz monzonites, whereas MGG are quartz monzonite and that of PG are granitic in composition according to the Ab–An–Or diagram by O`Connor (1965) (Fig. 5.1.b). The major elemental composition (high SiO_2, Al_2O_3, low MgO, CaO, Fe_2O_3, Ni, Cr, V), molar A/CNK > 1.1 (except for the MGG samples and one sample of PG with A/CNK<1.1) and normative corundum indicate their S-type character (Chappell, 1974, 2001) and strongly suggest derivation from a meta-sedimentary protolith. According to the classification of Frost, (2001), these granitoids are peraluminous leucogranites (except for the MGG samples and one sample of PG) owing to their strong alumina enrichment, high silica content, ferroan (Fig. 5.1.e) and calc-alkalic to alkali-calcic nature. Normative composition of the CGGC granitoids is plotted in the haplogranite Qz-Ab-Or-H_2O diagram (Johannes and Holtz, 1996, Fig. 5.13). The plot of the granitoid samples show clustering roughly around eutectic point at 5 Kbar pH_2O (Fig. 5.13). Four samples of MGG plots in the orthoclase field and one MGG sample plot in the Quartz field; whereas the PG plots in and around the Quartz-Orthoclase

cotectic join and GGG samples plot entirely in the quartz field. Fe number (≤0.96) of the three granitoid varieties indicates their ferroan nature (Fig. 5.1.e). Ferroan granitic rocks are reported to be closely associated with conditions of limited availability of H_2O and low oxygen fugacity during melting of their source rocks (Frost et al., 2001). Fe number is also strongly affected by the differentiation paths followed by the parent magma. The alkaline trends (Fig. 5.4.b) shown by the CGGC granitoids indicates more evolved nature of the magma. The CGGC granitoids are commonly characterized by enrichment of Rb, Ba, Th with respect to Ta, Nb, Zr, Y, Yb (Fig. 5.5.a), which is characteristic of calc-alkaline and shoshonitic series (Pearce et al., 1984). The GGG and MGG show negative anomalies of Sr and Eu, which implies plagioclase fractionation, whereas slight positive anomaly of Eu in PG indicate plagioclase accumulation (Fig. 5.5.b). SiO_2 enrichment associated with TiO_2 depletion indicates fractionation of low Si, high Ti phases such as Fe-Ti oxide and/or amphibole. Relative depletion of HFSE (Ti, Zr, Nb, Ta and P) has been suggested as a result of breakdown of hydrous phases in the partial melting process. The subducted oceanic crust releases volatiles which preferentially mobilize the highly water-soluble LILE into the mantle wedge of the over-riding plate (Saunders, et al.,1980; Gill, 1981), and the HFSE elements are retained in the subducting oceanic crust (Saunders, et al.,1980).Highly depleted Nb and Ta along with LILE enrichment in the granitoid samples imply a subduction related origin and their emplacement within a volcanic arc setting (Dharma Rao et al., 2013, Roberts et al.,1993). Calc-alkaline nature, geochemical signatures similar to arc granitoids along with the Volcanic Arc Granite (VAG) and syn-collisional signatures of the granitoids in tectonic discrimination diagrams, thereby, demonstrates that the CGGC granitoids might have formed in subduction zone setting. Furthermore, strong enrichment in more incompatible elements (Cs, Ba, Rb, Th, U) over less incompatible elements (Ti, Y, Yb, Lu, Sr and Nb) with significant negative anomalies at Ba, Nb, T and Sr, and positive anomalies at Rb, Th and U also indicates formation

of granitoid rocks of CGGC from orogenic/subduction zone magmas (Saunders, et al., 1980; Taylor et al., 1985). These suggests subduction zone geochemical environment in which alumina rich pelitic rocks suffered high grade metamorphism in presence of fluid phases. These fluid phases play important role in metamorphic reaction, breakdown and formation of new metamorphic minerals. A plethora of accessory mineral phases and their temperature dependent solubility control the behaviour of key tracers, such as REE, Th and U in monazite and allanite, Nb and Ta in rutile and Zr, Hf, U and HREE in zircon (Plank, 2016; Yang et al., 2008). The trace element characteristics of CGGC granite may thus be considered as the final product of subduction zone metamorphism of pre-existing alumina rich meta-pelitic rocks in presence of subduction zone fluids and their partial melting.

5.4.2. **Jhalda area**

A-type affinity:

A-type granites, abbreviated after alkaline, anorogenic and anhydrous, are characterized by high $K_2O + Na_2O$ and incompatible elements (e.g. REEs (except Eu), Zr, Y, Nb, Ce) and high $_{FeOT}/(FeO_T + MgO)$. Petrographical and geochemical characteristics of the AR granitoids strongly suggest its alkaline, post orogenic to anorogenic, within plate, A-type character. Petrographic studies of AR granitoids indicate presence of perthite, mafic minerals like sodic pyroxene (aegirine) and sodic amphibole (riebeckite) which are typical of alkaline granitoids (Bonin 2007 and references therein). Geochemically they contain higher K_2O over Na_2O (K_2O 4.3–4.98 wt % and Na_2O= 3.07–4.07 wt%), high total alkali (8.3–8.8 wt %), high Fe* (FeO_T/FeO_T+MgO = 0.985–0.994), low Al_2O_3 (10.6–11.3 wt %), low CaO (0.02–0.3 wt %), high M value (cationic ratio: (Na+K+2Ca)/ (Al*Si)). A/CNK values of the AR granitoids show peralkaline nature with (ASI <1 and NK/A >1). The AR granitoids are enriched in Nb, Zr, Hf, high HFSE (Zr+Nb+Ce+Y= 1150–1743 ppm) and depleted in Ba, Sr, Ti, Eu, P and show high

Ga/Al ratio (6.7–7.8). These geochemical characteristics are similar to those of alkaline granites worldwide (Bonin, 2007; Frost and Frost, 2011; Frost et al., 1999, 2001; King et al., 2001; Whalen et al., 1987).Y and Nb show no apparent variation trends with SiO_2, which is a characteristic of alkaline granites (King et al. 1997).The high abundance of Nb in AR granites (much higher than crustal derived A type granites and A-type granite formed from mantle derived alkali basalt by fractional crystallization) may indicate Nb enrichment in the source rock by metasomatic alteration caused by asthenospheric carbonate fluid/melt phases which are highly enriched in Nb. Similar Nb rich alkali granites (arfvedsonite granite) have also been reported by Basak and Goswami, 2020 from Dimrapahar area of Hazaribagh, Jharkhand. All of the samples from the AR granitoids plot in the A-type granite field in the different geochemical classification diagrams such as $(K_2O + Na_2O)/CaO$ versus (Zr + Nb + Ce + Y); FeO_T/MgO versus(Zr + Nb + Ce + Y); Nb versus 10,000 Ga/Al and $(K_2O + Na_2O)$ versus 10,000 Ga/Al (Whalen et al. 1987). Low P_2O_5 content (0.01–0.02 wt %) of the AR granitoids also indicates A-type granite affinity rather than S- or I-type granite. Zircon saturation temperature (T_{Zr}>900°C) of the AR granitoids indicates high temperature of primary magmas which is quite higher than that of I-type granitoids (< 800°C). Thus, AR granitoids exhibit the following charcters which typically indicate its A-type nature: i) high SiO_2 and alkali contents (high K_2O+Na_2O, K_2O/Na_2O>1), enriched HFSE elements and REE contents (except Eu) and depleted in Ba, Sr, Ti, Eu, P; ii) higher 10,000 * Ga/Al ratio (6.7-7.8), far higher than the average value for A-type granites worldwide (3.5, Whalen et al., 1984); iii) presence of characteristic minerals like Na-amphibole, Na-pyroxene, perthite, sphene etc and iv) high temperature of magmas (> 900°C).

Tectonic setting:

Loiselle and Wones (1979) defined A-type granites as anorogenic granites, but later studies suggested that they can be formed in both anorogenic and post-orogenic settings extensional

settings (Whalen et al. 1987; Eby 1992). By integrating geochemical characteristics, it can be concluded that the Ar granitoids were generated in a postorogenic extensional tectonic environment based on the following. i) On the R2 versus R1 diagram of Batchelor & Bowden (1985), all the A-type granites fall into the post-orogenic fields (Fig.). (b) In the tectonic discrimination diagrams of Pearce et al. (1984) and Pearce (1996), all the samples plot in the Within Plate Granite (WPG) (Fig). This suggests that AR granitoids may have been emplaced in an extensional tectonic regime, during a phase of cooling, relaxation and fracturing, which followed the termination of the Grenvillian orogeny.

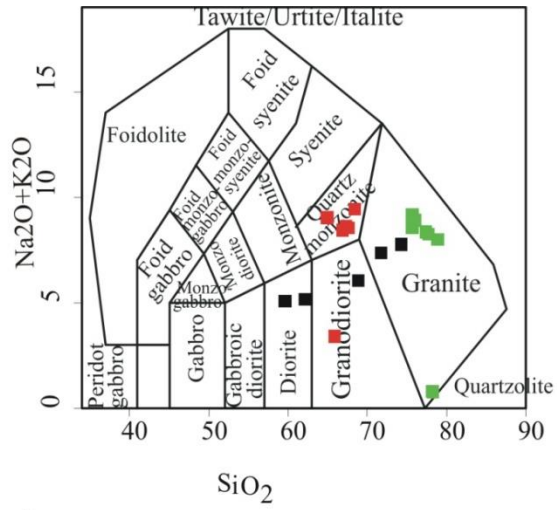
Tawite/Urtite/Italite
Foidolite
Foid syenite
Syenite
Foid monzo syenite
Foid monzo gabbro
Monzonite
Quartz monzonite
Foid gabbro
Monzo diorite
Monzo gabbro
Granodiorite
Granite
Peridot gabbro
Gabbro
Gabbroic diorite
Diorite
Quartzolite
Na2O+K2O
SiO2

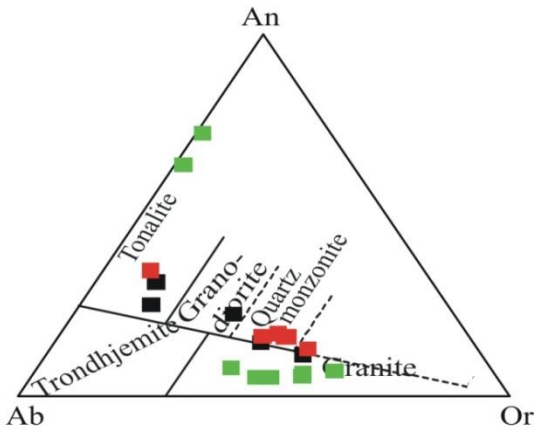
An
Tonalite
Grano-diorite
Quartz monzonite
Trondhjemite
Granite
Ab
Or

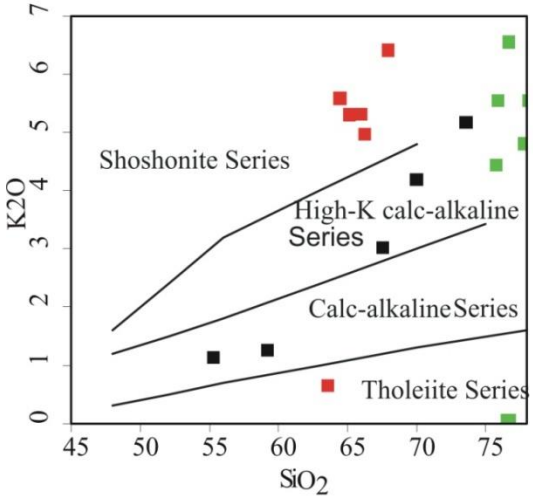
Shoshonite Series
High-K calc-alkaline Series
Calc-alkaline Series
Tholeiite Series
K2O
SiO2

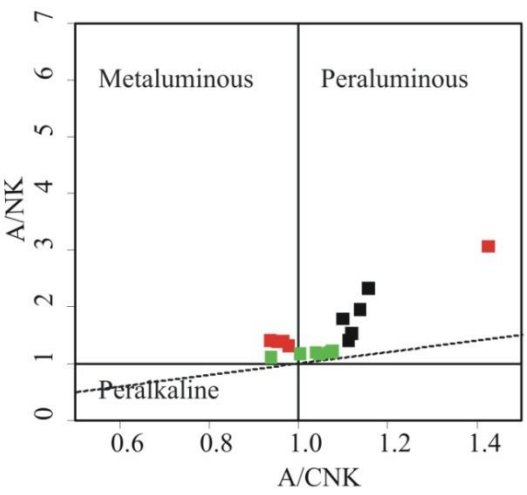
Metaluminous
Peraluminous
Peralkaline
A/NK
A/CNK

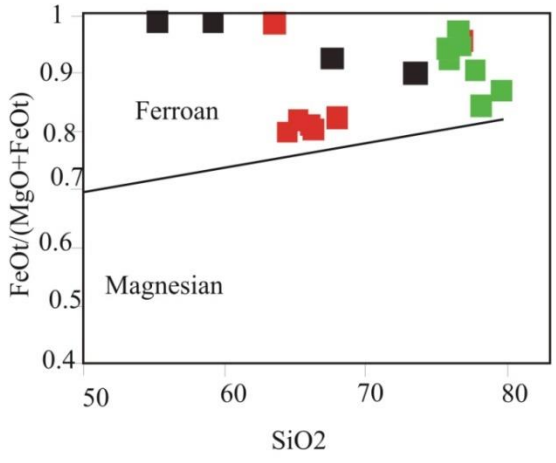
Ferroan
Magnesian
FeOt/(MgO+FeOt)
SiO2

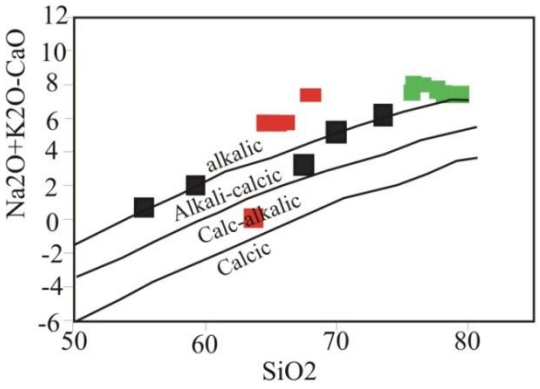
alkalic
Alkali-calcic
Calc-alkalic
Calcic
Na2O+K2O-CaO
SiO2

GGG PG MGG

Figure 5.1. (a) Diagram showing plots of granitoids of Raghunathpur-Bero area in Total alkali versus SiO_2 (TAS) diagram (after Middlemost, 1994); b) Diagram showing plots of granitoids of Raghunathpur-Bero area in the CIPW normative An-Ab-Or diagram (O'Connor, 1965) modified by Barker (1979); c) SiO_2 versus K_2O plot for granitoids of Raghunathpur-Bero area after Peccerillo and Taylor (1976), which shows calc-alkaline to high K- calc-alkaline composition for GGG and PG, while shoshonitic affinity for MGG; d) Diagram showing plots of granitoids of Raghunathpur-Bero area in the A/CNK versus A/NK diagram after Shand (1943) showing peraluminous character of GGG and PG and metaluminous character of MGG; e) Diagram showing plots of granitoids of Raghunathpur-Bero area in the SiO_2 versus Feo_t /(FeO_t+MgO) after Frost et al., (2001), which shows ferroan affinity for all the three varieties; f) Diagram showing plots of granitoids of Raghunathpur-Bero area in the SiO_2 versus (Na_2O+K_2O-CaO) diagram after Frost et al., (2001), which shows alkali nature of MGG and PG and alkali-calcic to alkali nature of GGG.

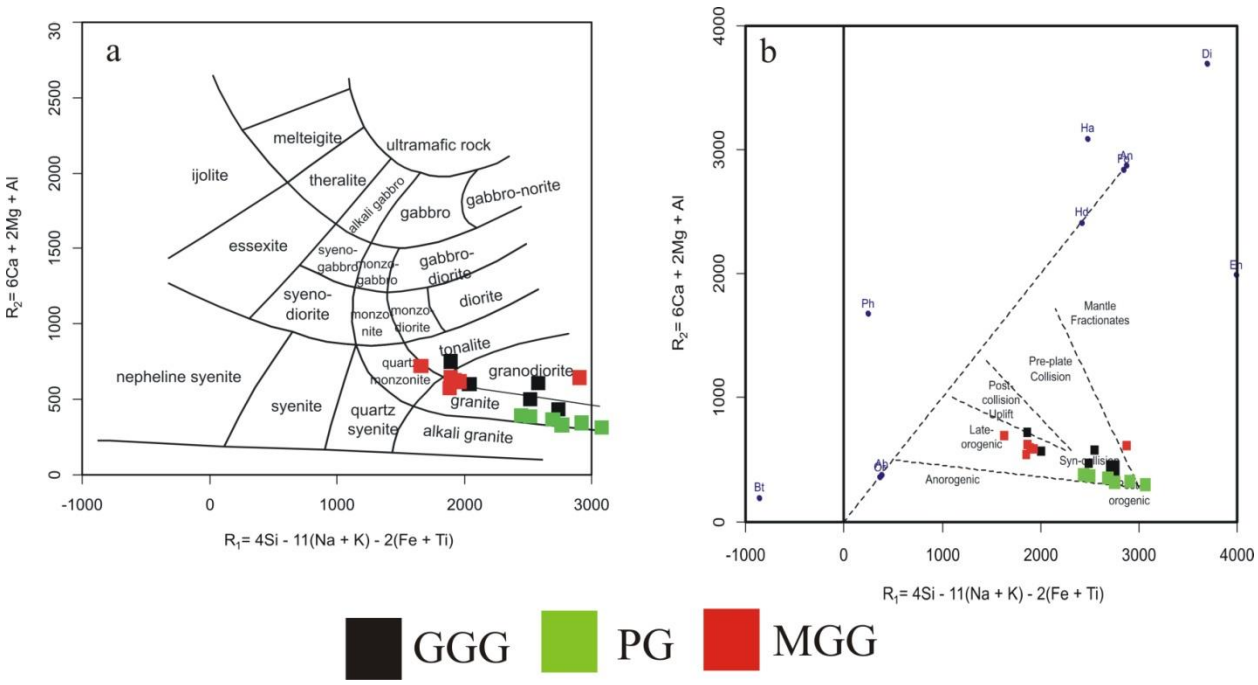

Figure 5.2. (a) R1-R2 classification diagram after De La Roche et al., (1980) showing plots of granitoids of Raghunathpur-Bero area, which shows that the three granitoids plot in the granite-granodiorite-quartzo-monzonite fields; (b) R1–R2 diagram after Batchelor and Bowden (1985) showing plots of granitoids of Raghunathpur-Bero area, which indicates syn-collisional nature of GGG and PG and late orogenic nature of MGG. (R1 = 4Si − 11(Na + K) − 2(Fe + Ti); R2 = 6Ca + 2 Mg + Al)

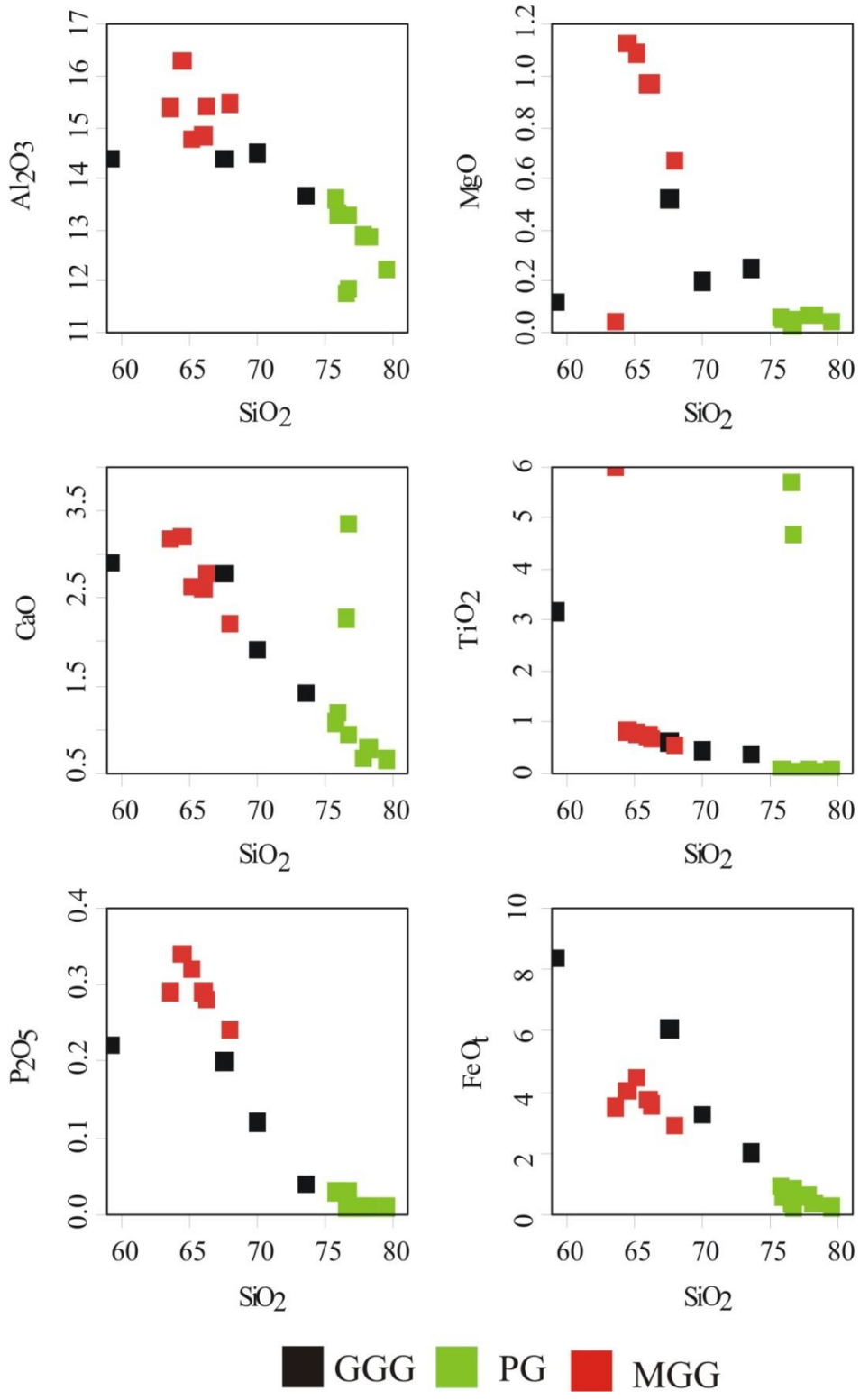

Figure 5.3. Harker variation diagram of SiO_2 versus major element oxides (Al_2O_3, MgO, Na_2O, CaO, TiO_2, K_2O, P_2O_5, and FeO_t) for the granitoids of Raghunathpur-Bero area.

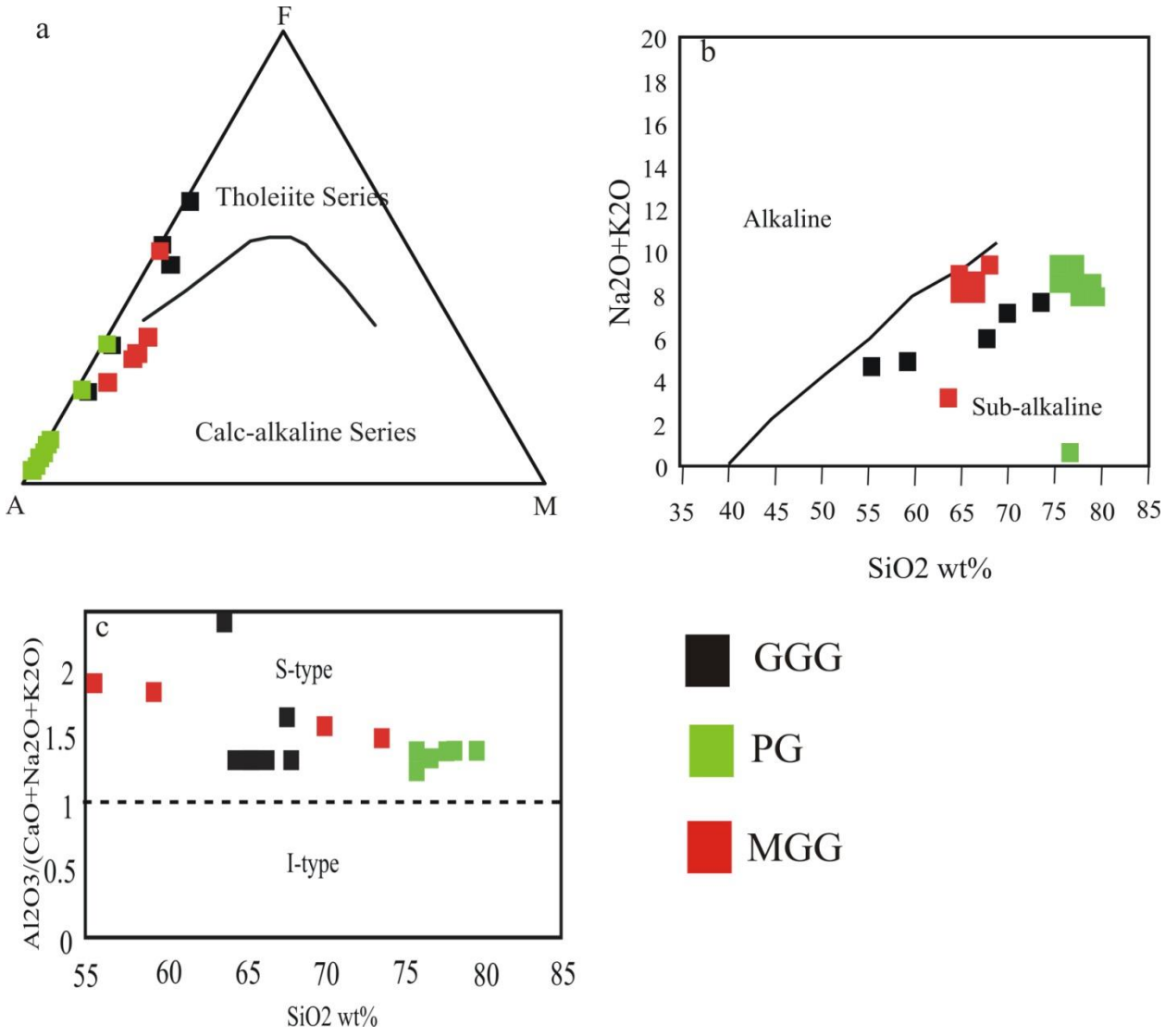

Figure 5.4 (a) Diagram showing plots of granitoids of Raghunathpur-Bero area in the AFM diagram (after Irvine and Baragar 1971) showing calc-alkaline trend of the PG, MGG and some GGG samples; (b) Diagram showing plots of granitoids of Raghunathpur-Bero area in the SiO_2 versus Na_2O+K_2O diagram (after Irvine and Baragar 1971) showing sub-alkaline nature of these granitoids; (c) Diagram showing plots of granitoids of Raghunathpur-Bero area in the SiO_2 versus A/CNK diagram after Frost et al. (2001) showing S-type nature of all the granitoid varieties.

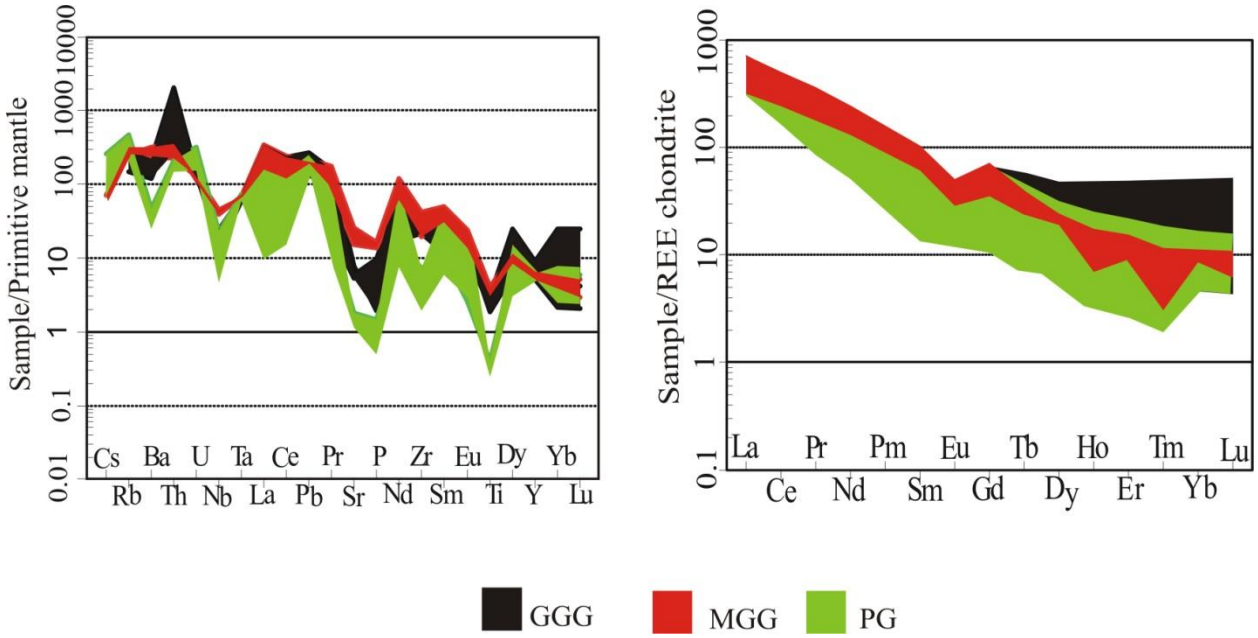

Figure 5.5. (a) Primitive-mantle-normalized multi-element diagram for the granitoids (after Sun & McDonough, 1989); (b) Chondrite normalized trace element and REE diagram after Boynton (1984) for the granitoids of Raghunathpur-Bero area.

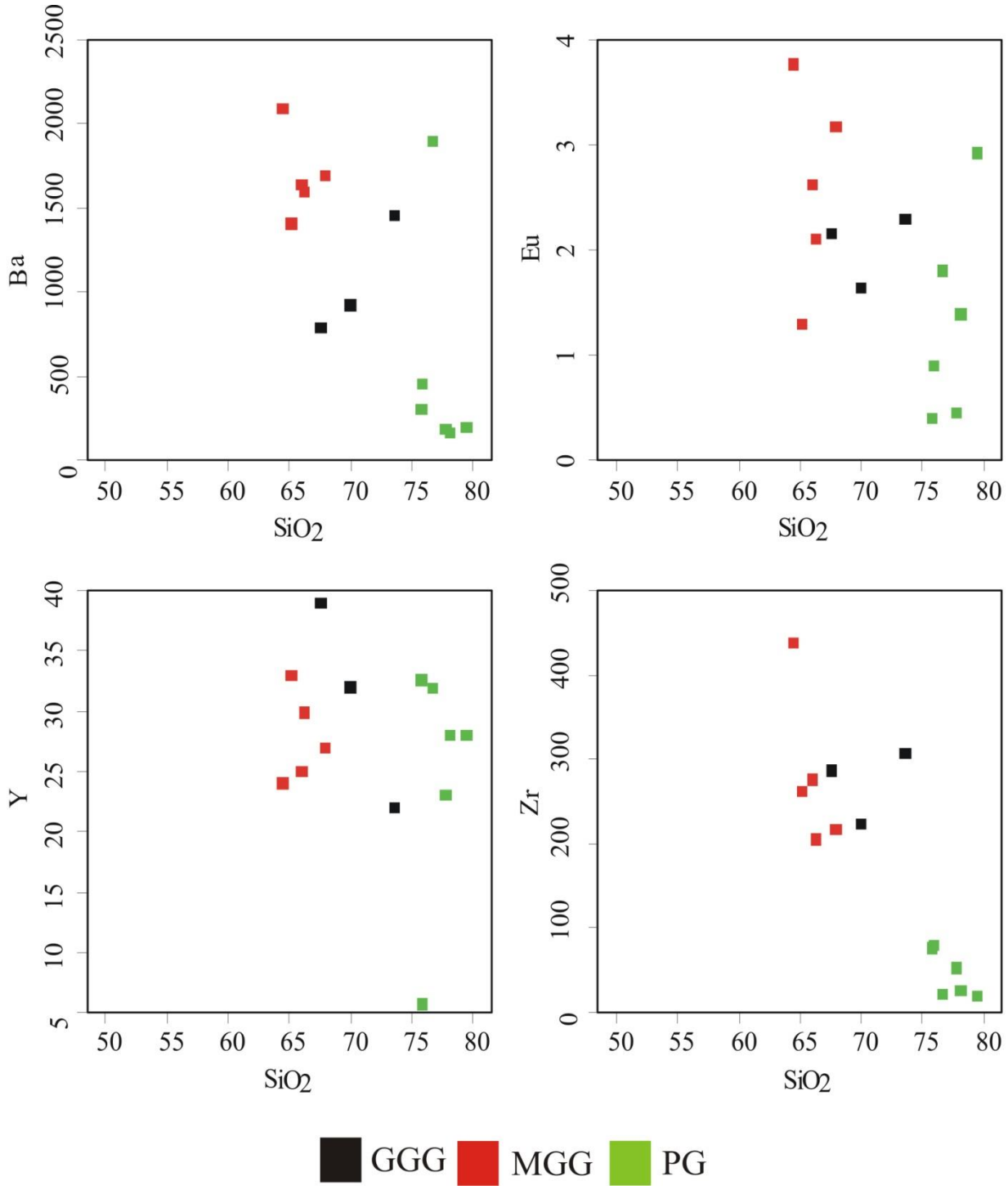

Figure 5.6 Diagram showing plots of granitoids of Raghunathpur-Bero area in the SiO_2 versus trace element diagram (Ba, Eu, Y and Zr).

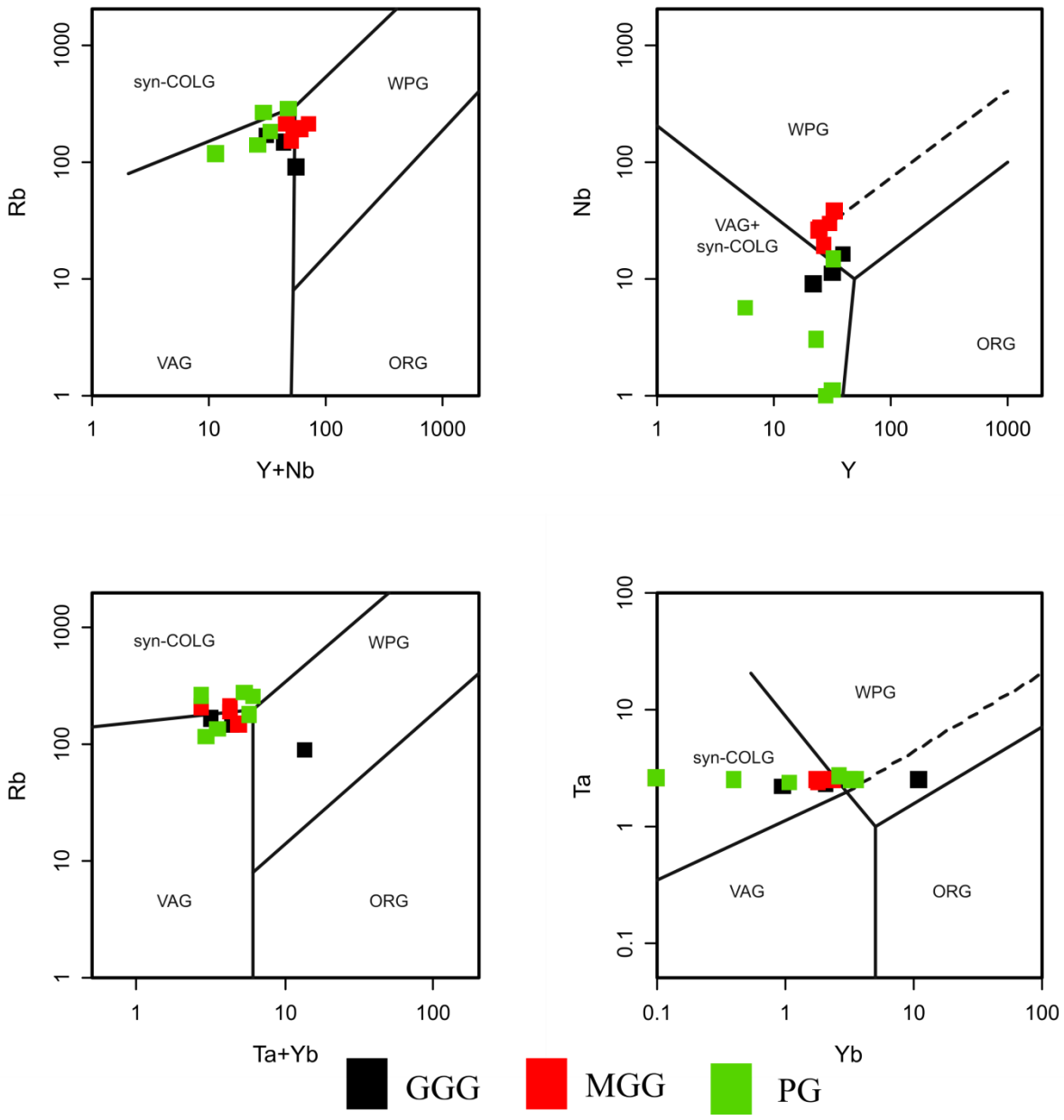

Figure 5.7. Diagram showing plot of granitoids of Raghunathpur-Bero area in the (a) (Y+Nb) versus Rb; (b) Nb versus Y; (c) (Ta +Yb) versus Rb and (d) Ta versus Yb tectonic discrimination diagram after Pearce et al. (1984). Acronyms used in the figure are: VAG- volcanic arc granite, WPG – within plate granite, Syn-COLG- syn-collisional granite and ORG- ocean ridge granite

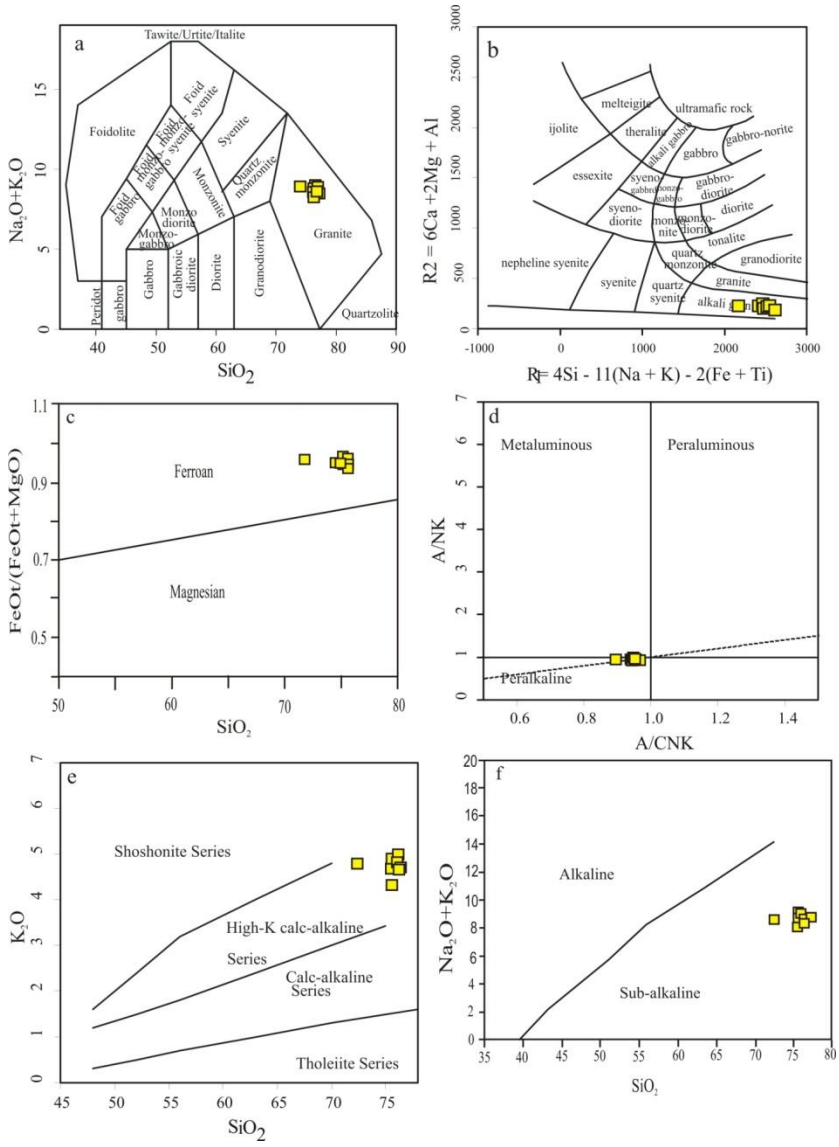

Figure 5.8 (a) Diagram showing plot of AR granitoids in the SiO_2 versus Na_2O+K_2O (TAS diagram) after Middlemost (1994); (b) Diagram showing plot of AR granitoids in the R1-R2 diagram after de La Roche (1980); (c) Diagram showing plot of AR granitoids in the SiO_2 versus FeOtot/(FeOtot+MgO) diagram after Frost et al. (2001); (d) Diagram showing plot of AR granitoids in the A/CNK versus A/NK plot after Maniar and Piccoli (1989); (e) Diagram showing plot of AR granitoids in the SiO_2 versus K_2O plot after Peccerilo and Taylor (1976); (f) Diagram showing plot of AR granite in the SiO_2 versus Na_2O+K_2O plot after Irvine and Baragar (1971). Yellow coloured filled rectangles in the diagrams indicate plots of AR granites of Jhalda.

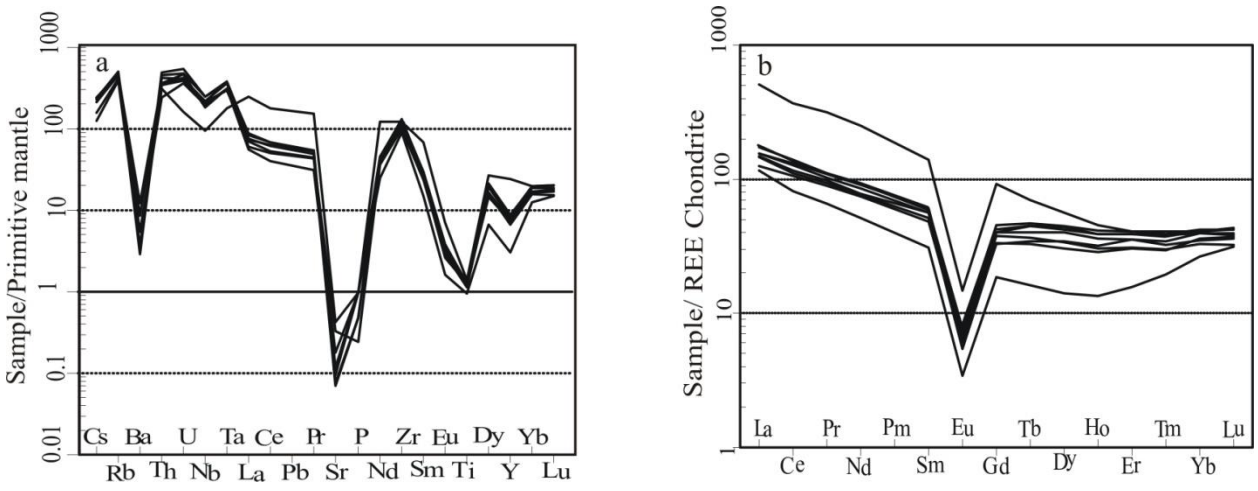

Figure 5.9 (a) Primitive – mantle normalized multi- element diagram for AR granitoids (after Sun and Mcdonnough, 1965); (b) Chondrite normalized REE diagram of AR granitoids (after Boynton 1984). Yellow coloured filled rectangles in the diagrams indicate plots of AR granites of Jhalda.

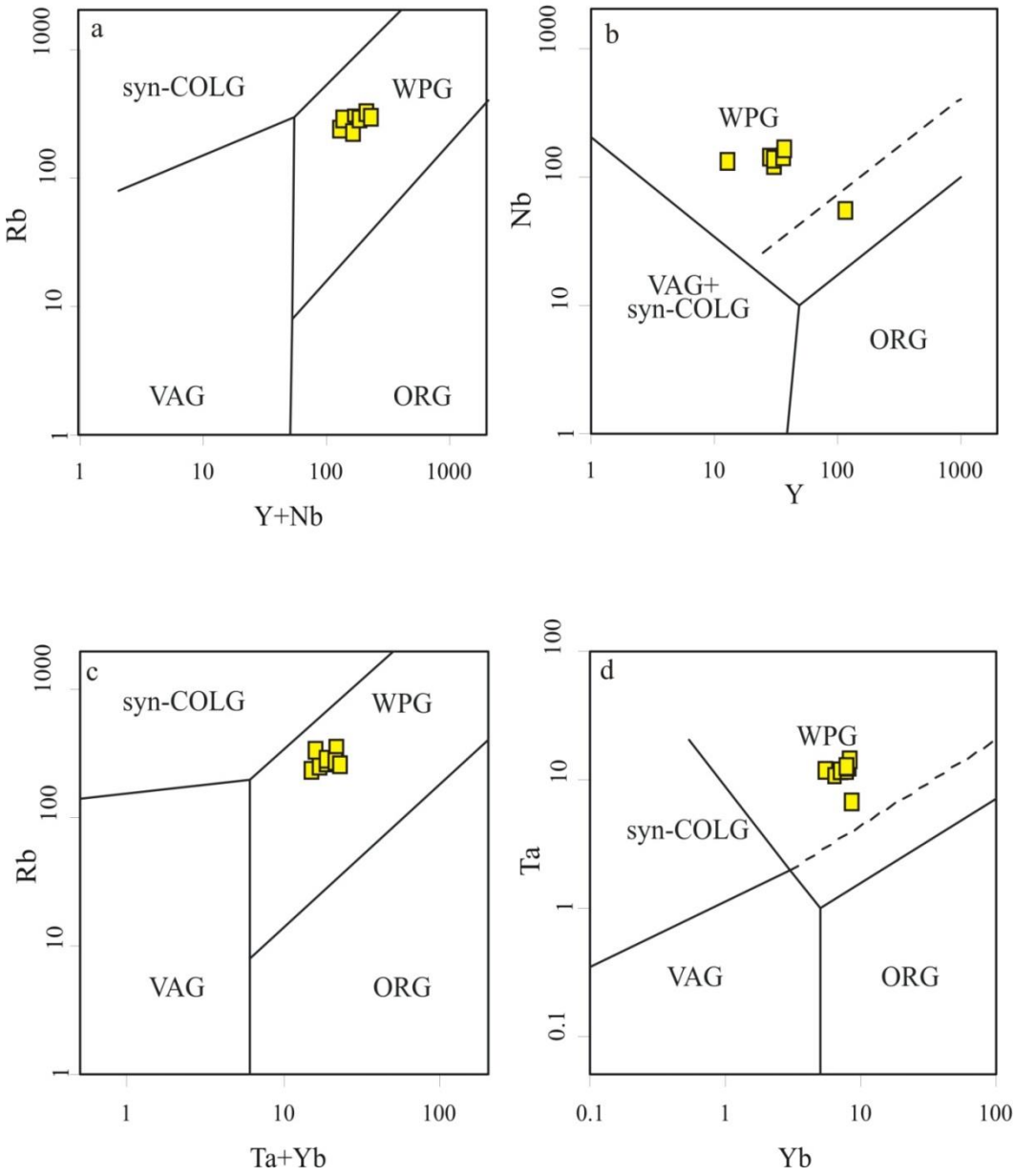

Figure 5.10 Diagram showing plot of AR granitoids in the (a) (Y+Nb) versus Rb; (b) Nb versus Y; (c) (Ta +Yb) versus Rb and (d) Ta versus Yb tectonic discrimination diagram after Pearce et al. (1984). Acronyms used in the figure are: VAG- volcanic arc granite, WPG – within plate granite, Syn-COLG- syn-collisional granite and ORG- ocean ridge granite. Yellow coloured filled rectangles in the diagrams indicate plots of AR granites of Jhalda.

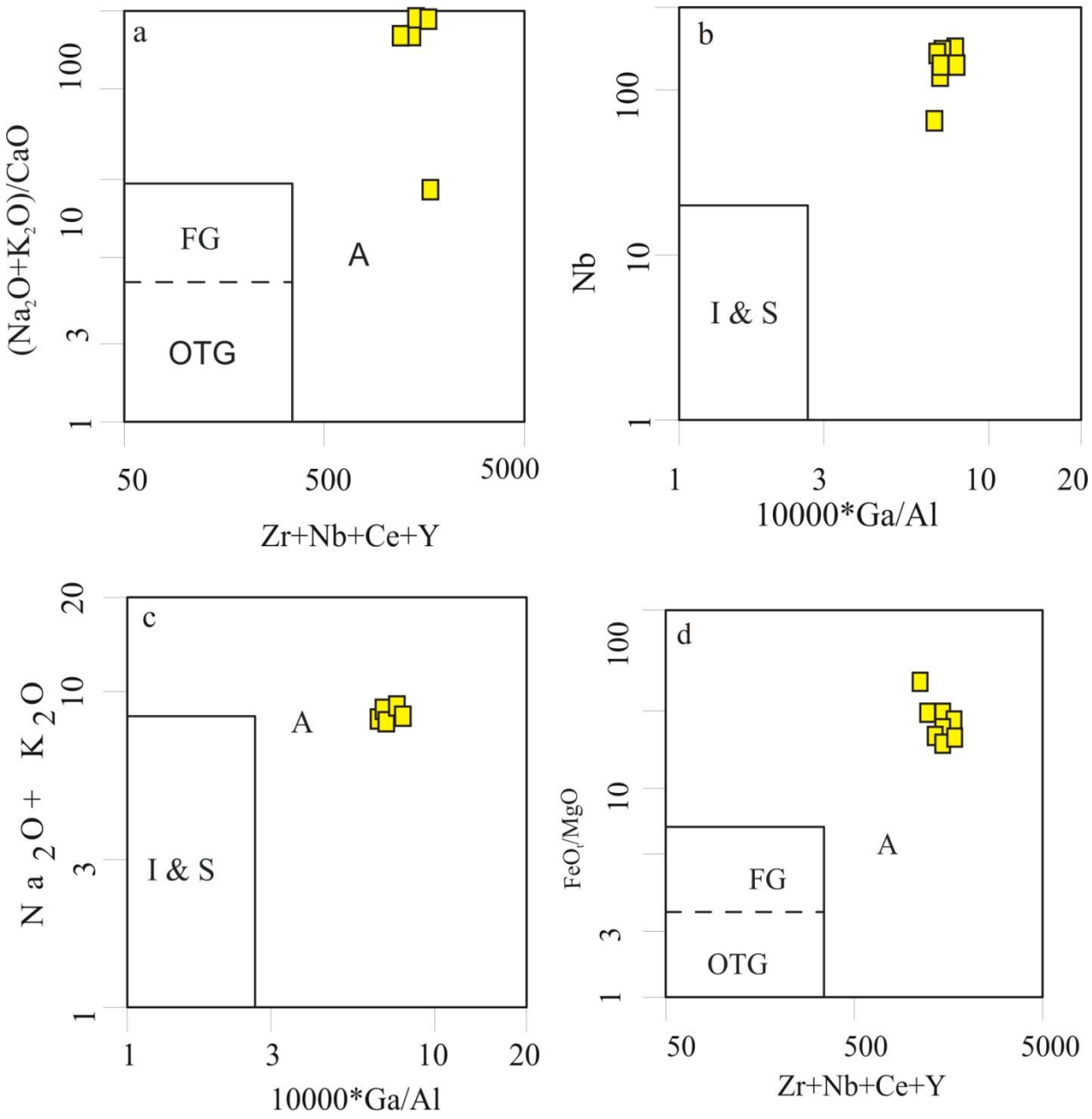

Figure 5.11 Diagram showing plot of AR granitoids in the discrimination diagram after Whalen et al. (1987). Yellow coloured filled rectangles in the diagrams indicate plots of AR granites of Jhalda.

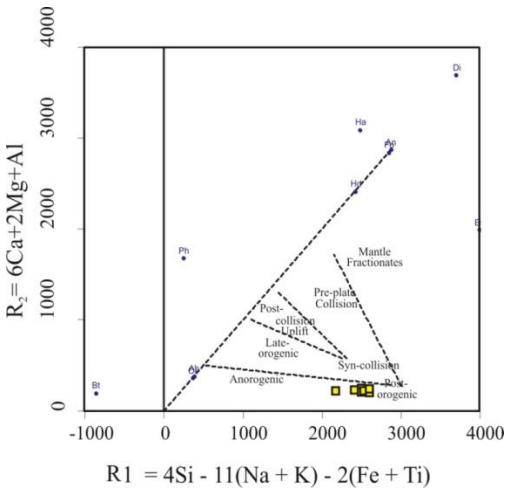

Figure 5.12 Diagram showing plot of AR granitoids in the R1-R2 diagram after Batchelor and Bowden (1985) (R1 = 4Si – 11(Na +K) – 2(Fe+Ti), R2 = 6 Ca + 2Mg + Al). Yellow coloured filled rectangles in the diagrams indicate plots of AR granites of Jhalda.

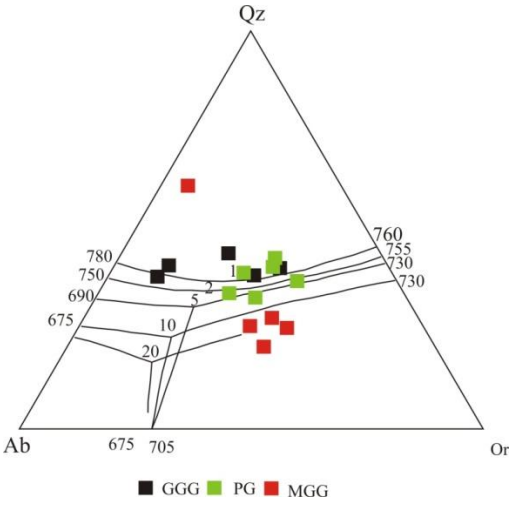

Figure 5.13 Diagram of normative Qz–Ab–Or–H_2O after Johannes and Holtz (1996) for granitoids of Raghunathpur-Bero area showing plots clustering roughly around eutectic point at 5-kbar pH_2O.

Table 5.1 Major element data of three granitoid types of Raghunathpur –Bero area.

Rock type	**Samples**	**SiO2**	**Al2O3**	**Fe2O3tot**	**MgO**	**MnO**	**Na2O**	**CaO**	**TiO2**	**K2O**	**P2O5**
		(wt %)	(wt %)	(wt %)	(wt %)	(wt %)	(wt %)	(wt %)	(wt %)	(wt %)	(wt %)
GGG	K5	73.58	13.66	2.25	0.25	0.02	2.5	1.41	0.38	5.18	0.04
GGG	K6	67.56	14.4	6.71	0.52	0.11	2.9	2.78	0.61	3.02	0.2
GGG	K7	69.99	14.49	3.61	0.2	0.04	3	1.91	0.44	4.19	0.12
GGG	L10	59.21	14.4	9.3	0.12	2.01	3.66	2.9	3.16	1.26	0.22
GGG	L1	55.29	16.54	5.91	0.05	2.24	3.58	3.95	4.28	1.13	0.39
MGG	K1	65.15	14.78	4.94	1.09	0.05	2.91	2.63	0.79	5.31	0.32
MGG	K3	67.94	15.47	3.21	0.67	0.03	2.95	2.21	0.55	6.42	0.24
MGG	K4	66	14.84	4.18	0.97	0.04	3.01	2.6	0.74	5.32	0.29
MGG	AR129A	66.25	15.41	3.98	0.97	0.03	3.5	2.78	0.68	4.97	0.28
MGG	K10	64.46	16.31	4.48	1.13	0.05	3.37	3.2	0.82	5.59	0.34
MGG	L24	63.59	15.39	3.9	0.04	1.34	2.62	3.18	5.99	0.65	0.29
PG	L22	76.71	11.84	0.22	0.01	0.47	0.7	3.35	4.67	0.05	0.01
PG	K2	77.78	12.89	0.68	0.07	0.01	3.58	0.67	0.07	4.81	0.01
PG	K8	78.13	12.87	0.38	0.07	0	2.75	0.79	0.05	5.55	0.01
PG	K9	79.49	12.23	0.27	0.04	0	2.68	0.66	0.06	5.38	0.01
PG	AR119B1	76.67	13.28	0.93	0.05	0.03	2.41	0.94	0.02	6.56	0.03
PG	AR127B	75.91	13.31	0.62	0.05	0.01	3.65	1.19	0.09	5.55	0.03
PG	ARL7	75.77	13.61	1.02	0.06	0.04	4.13	1.08	0.08	4.44	0.03
PG	L40A	76.54	11.76	0.38	0.01	0.48	0.71	2.27	5.69	0.05	0.01
NIMG	Published	75.70	12.08	2.00	0.06	-	3.36	0.78	-	4.99	-
NIMG	Analyzed	74.6	12.34	2.54	0.09	-	3.15	0.86	-	4.68	-

Table 5.2 CIPW norm data of granitoids of Raghunathpur –Bero area.

Rock type	Sample No.	Quartz	Anorthite	Diopside	Sphene	Hypersthene	Albite	Orthoclase	Wollastonite	Apatite	Ilmenite	Corundum	Rutile	Magnetite	Hematite	Total
GGG	K5	35.93	6.74	0	0	0.63	21.15	30.61	0	0.09	0.11	1.47	0.33	0	0.01	97.08
GGG	K6	32.96	12.49	0	0	1.3	24.54	17.85	0	0.47	0.53	1.79	0.33	0	0.04	92.31
GGG	K7	32.45	8.7	0	0	0.5	25.39	24.76	0	0.28	0.28	1.84	0.3	0	0.02	94.52
GGG	L10	27.32	13	0	0	0.3	30.97	7.45	0	0.51	4.64	2.27	0.72	0	0.04	87.23
GGG	L1	22.70	17.04	0	0	0.13	30.29	6.68	0	0.9	5.39	3.18	1.45	0	0.08	87.85
MGG	K1	21.54	11	0	0	2.72	24.62	31.38	0	0.74	0.6	0.23	0.48	0	0.06	93.38
MGG	K3	21.15	9.4	0	0	1.67	24.96	37.94	0	0.56	0.43	0.23	0.33	0	0.05	96.73
MGG	K4	21.93	11.01	0	0	2.42	25.47	31.44	0	0.68	0.53	0.1	0.46	0	0.06	94.1
MGG	AR129A	20.32	11.66	0	0.22	2.42	29.62	29.38	0	0.65	0.49	0	0.34	0	0.06	95.16
MGG	K10	16.05	12.9	0	0.56	2.82	28.52	33.04	0	0.79	0.62	0	0.27	0	0.07	95.64
MGG	L24	39.80	13.9	0	0	0.1	22.17	3.85	0	0.68	3.31	5.29	4.25	0	0.06	93.42
PG	L22	65.28	16.56	0	0	0.03	5.923	0.3	0	0.03	1.03	4.57	4.13	0	0	97.86
PG	K2	37.03	3.26	0	0	0.18	30.29	28.43	0	0.03	0.05	0.6	0.05	0	0	99.93
PG	K8	39.12	3.86	0	0	0.18	23.27	32.8	0	0.03	0.03	1	0.04	0	0	100.34
PG	K9	41.86	3.21	0	0	0.1	22.68	31.8	0	0.03	0.03	0.82	0.05	0	0	100.59
PG	AR119B1	35.51	4.47	0	0	0.18	20.39	38.77	0	0.07	0.04	0.58	0	0.02	0	100.04
PG	AR127B	31.36	3.54	0.27	0.14	0	30.89	32.8	0.68	0.07	0.07	0	0	0	0.01	99.83
PG	ARL7	32.43	5.16	0	0	0.15	34.95	26.24	0	0.07	0.13	0.12	0.01	0	0.01	99.28
PG	L40A	67.36	11.2	0	0	0.03	6.008	0.3	0	0.03	1.05	6.44	5.14	0	0	97.57

Table 5.3 Trace and REE abundances (in ppm) of the granitoids of Raghunathpur-Bero area

ROCK TYPE	**GGG**	**GGG**	**GGG**	**MGG**	**MGG**	**MGG**	**MGG**	**MGG**	**PG**	**PG**	**PG**	**PG**	**PG**	**PG**	**NIMG**	**NIMG**
SAMPLES	K5	K6	K7	K1	K3	K4	AR129A	K10	K2	K8	K9	AR119B1	AR127B	ARL7	Published	Analyzed
La	221.26	110.08	21.96	22.4	98.78	125.98	101.4	223.21	6.18	23.49	117.17	12.5	97.3	25.8	109	104
Ce	386.51	216.09	46.98	23.33	183.72	230.88	198.1	410.46	22.06	25.07	241.43	19.8	132.5	52.6	195	186
Pr	40.32	24.42	5.81	1.68	20.35	25.26	21.1	45.11	2.27	1.83	29.57	1.8	10.4	5.4	-	-
Nd	137.82	87.55	22.25	5.75	70.2	86.68	78.3	152.42	9.41	5.19	112.06	6.4	30.7	20.2	-	-
Sm	16.4	15.7	4.76	0.46	10.98	11.87	12.3	20.37	2.41	0.5	19.28	1.2	2.6	4.4	15.8	14.8
Eu	2.29	2.15	1.64	1.3	3.17	2.62	2.1	3.76	0.45	1.39	2.92	1.8	0.9	0.4	0.35	0.4
Gd	15.33	17.86	5.28	0.63	10.3	11.35	9.1	18.95	2.13	0.62	17.55	1.5	2.7	3.7	-	-
Tb	1.27	2.72	0.93	0.06	1.18	1.21	1.1	1.94	0.33	0.05	2.14	0.3	0.2	0.7	-	-
Dy	3.96	16.56	5.58	0.19	5.22	5.07	6.1	7.78	2.07	0.2	10.28	4.1	1	5	-	-
Ho	0.6	3.65	1.12	0.03	0.93	0.89	0.5	1.25	0.44	0.04	1.84	0.5	0	0.5	-	-
Er	1.63	10.24	2.57	0.12	2.28	2.33	1.8	3.26	1.09	0.1	4.58	2.1	0.4	1.9	-	-
Tm	0.15	1.64	0.34	0.02	0.3	0.29	0.1	0.38	0.17	0.02	0.6	0.3	0	0.2	-	-
Yb	0.96	10.93	2.07	0.1	1.8	1.76	1.8	2.32	1.07	0.1	3.5	3.2	0.4	2.6	14.2	13
Lu	0.14	1.69	0.28	0.02	0.28	0.27	0.2	0.35	0.16	0.01	0.51	0.5	0	0.4	2	1.8
Ta	2.2	2.5	2.3	2.6	2.4	2.5	2.4	2.5	2.4	2.6	2.5	2.5	2.5	2.7	-	-
Sc	3.8	12.3	4.1	9	4.9	5.8	3.8	9.2	2.3	1.1	1.5	3.3	2.2	2.8	-	-
Co	127.4	75.9	9.4	14.3	10.5	11.4	79.8	54.8	112.7	BDL	173.9	156.5	127.2	104	-	-
Ni	1	6	6	9	5	7	1.9	6	BDL	BDL	BDL	0.4	1.2	1.2	8	7
Cu	1	20	7	9	6	8	0.1	8	4	1	BDL	0.1	0.1	0.1	12	11
Zn	26	74	42	58	36	47	20.6	51	16	7	5	5.1	9.8	14	50	49.1
Ga	16	17	19	18	18	17	22.2	17	19	19	18	12.3	21.1	17.3	27	25
Pb	40	20	29	30	32	26	29.2	33	24	39	39	31.3	57	30.7	40	43
Th	163	51	24	31	21	24	17.9	28	12	1	1	2.7	30	16.8	51	48
Rb	167	90	147	210	211	192	189.8	150	138	265	262	180.5	116.8	280.9	325	322
U	3	BDL	3.2	4.3	BDL	3.1	2.6	2.3	3.1	BDL	BDL	0.3	2.8	6.3	15	-
Sr	155	116	107	363	430	401	301.5	517	23	42	38	213.6	106.4	35.8	10	12
Y	22	39	32	33	27	25	29.9	24	23	28	28	31.9	5.7	32.6	143	148
Zr	307	287	223	262	217	276	205	438	53	26	20	21.1	78.8	76.3	300	296
Nb	9	16	11	38	19	27	29.3	26	3	BDL	1	1.1	5.6	14.7	-	-
Ba	1451	788	924	1407	1691	1636	1591.4	2090	187	164	195	1893.3	454.5	306.7	120	128
Cr	9	10	71	69	54	68	5.8	12	9	61	6	5.1	4.8	5.2	12	14
V	20	45	28	58	39	51	23	55	2	3	2	2.2	5.4	5.8	2	2.3

Table 5.4 Fractionation of LREE over HREE, LREE over MREE and MREE over HREE of granitoids of Raghunathpur –Bero area

Variables	**GGG**	**MGG**	**PG**
La_N/Yb_N	7.2-7.6	39.3-69.0	4.4-174.4
La_N/Nd_N	1.94-3.16	2.8-7.6	1.2-8.9
Dy_N/Lu_N	0.9-2.8	0.95-3.05	0.82-2.01
ΣREE	2235.45	1501.695	516.123

Table 5.5 Major element data of the aegirine-riebeckite (AR) granites of Jhalda area.

Oxides	**P1**	**P2**	**P3**	**P4**	**P5**	**P6**	**P7**	**P8**	**P9**	**STD SO-19(O)**	**STD SO-19(A)**
SiO_2	76.27	72.47	76.3	76.2	75.62	75.6	75.66	75.87	76.24	60.23	60.17
Al_2O_3	10.79	11.17	10.8	10.97	10.67	11.24	11.32	11.07	11.04	14.1	14.12
Fe_2O_3 ^{tot}	3.08	5.3	3.15	2.76	3.64	3.2	2.69	2.96	2.63	7.48	7.48
FeO	1.848	3.18	1.89	1.656	2.184	1.92	1.614	1.776	1.578	4.488	4.488
Fe_2O_3	1.37	2.35	1.4	1.23	1.61	1.42	1.19	1.31	1.16	3.32	3.32
MgO	0.03	0.03	0.03	0.04	0.04	0.04	0.04	0.04	0.04	2.94	2.96
CaO	0.03	0.02	0.04	0.03	0.34	0.03	0.03	0.04	0.03	5.99	6.01
Na_2O	3.75	3.95	3.71	3.82	4.04	4.07	3.98	3.85	3.71	4.03	4.04
K_2O	4.66	4.77	4.73	4.8	4.31	4.66	4.88	4.83	4.98	1.3	1.31
TiO_2	0.25	0.19	0.23	0.26	0.28	0.25	0.25	0.24	0.23	0.7	0.71
P_2O_5	0.02	0.02	0	0.01	0.02	0.01	0.02	0.01	0	0.32	0.32
MnO	0.04	0.02	0.04	0.04	0.05	0.04	0.04	0.04	0.04	0.13	0.13
Cr_2O_3	<0.002	<0.002	<0.002	<0.002	<0.002	<0.002	<0.002	<0.002	<0.002	0.501	0.5
Ba	57	36	81	22	24	20	23	19	20	477	481
Ni	<20	<20	<20	<20	<20	<20	<20	<20	<20	468	467
Sc	<1	<1	<1	<1	<1	<1	<1	1	<1	26	26
LOI	0.6	1.7	0.5	0.6	0.5	0.4	0.6	0.6	0.6	1.9	1.9
Sum	99.55	99.63	99.57	99.51	99.5	99.55	99.5	99.54	99.55	99.78	99.79
Fe#	0.990354	0.994371	0.990566	0.985714	0.98913	0.987654	0.985348	0.986667	0.985019	0.7178503	0.7164751
ASI	0.859645	0.859825	0.852145	0.850594	0.831682	0.862777	0.856332	0.851569	0.845816	0.9175298	0.91544673
Fe#	$FeO^{tot}/(FeO^{tot}+MgO)$			(O)	Original						
ASI	Al/(Ca – 1.67P + Na + K)			(A)	Analysed						
FeO	$0.6*Fe_2O_3^{tot}$										
Fe2O3	$Fe_2O_3^{tot}$*****0.4*****1.11										

Table 5.6 Calculated CIPW norm data for the AR granitoids of Jhalda area.

Minerals	**P1**	**P2**	**P3**	**P4**	**P5**	**P6**	**P7**	**P8**	**P9**
Quartz	35.95	29.83	35.86	35.07	34.56	33.39	33.33	34.34	35.03
Acmite	1.918	2.226	1.918	2.311	2.907	2.264	2.31	2.228	2.056
Diopside	0.016	0	0.176	0.074	1.381	0.074	0.016	0.118	0.132
Hypersthene	2.541	4.332	2.538	2.398	2.494	2.721	2.386	2.538	2.247
Albite	29.55	30.9	29.22	29.7	30.89	31.87	31.06	30.05	29.06
Orthoclase	27.54	28.19	27.95	28.37	25.47	27.54	28.84	28.54	29.43
Apatite	0.046	0.046	0	0.023	0.046	0.023	0.046	0.023	0
Ilmenite	0.475	0.361	0.437	0.494	0.532	0.475	0.475	0.456	0.437
Magnetite	1.025	2.291	1.069	0.625	0.892	0.924	0.568	0.783	0.666
Total	99.06	98.18	99.17	99.06	99.17	99.28	99.02	99.08	99.06

Table 5.7 Trace element and REE data of the AR granites of Jhalda area.

Samples	**P1**	**P2**	**P3**	**P4**	**P5**	**P6**	**P7**	**P8**	**P9**	**STD SO-19**	**STD SO-19**
Be	14	12	7	17	4	11	8	8	11	21	19
Co	145	120	149	149	141	134.1	166.7	151.2	143.7	22.7	21.4
Cs	5.1	3.3	5	4.5	2.6	4.8	4.9	4.5	4.7	4.2	4.4
Ga	45	41.5	41.4	42.1	38.4	42.5	45.8	41.5	42.1	16.6	15.1
Hf	32.9	25	30.2	39.9	35.8	34	38.1	31.2	33.5	3.3	3.3
Nb	138	129	121	164	63	134.9	161.4	144.1	159.3	73.7	69.6
Rb	283	246	273	280	236	284.6	299.5	271.5	293.4	20.1	20.2
Sn	13	11	12	15	14	15	16	14	16	18	17
Sr	2.3	3.6	6.6	1.4	8.4	1.4	1.9	1.5	1.2	309.4	288.8
Ta	10.8	11.6	11.4	14	6.6	11.3	13.5	13.2	12.5	5.3	5.3
Th	27.7	19.2	28.8	38.7	24.8	28.6	36.1	33.8	32.3	13.6	13.1
U	7.8	7.3	9.2	10.8	3.2	8.4	9.5	8.2	8.7	20.8	20.4
V	<8	<8	<8	<8	<8	<8	<8	<8	<8	169	166
W	1140	1001	1228	1179	1189	1152	1331	1337	1069	11.8	11.9
Zr	1229	942	1046	1389	1278	1267	1352	1121	1232	118.6	113.4
Y	28.7	13.2	31.3	37.7	104	31.6	36.4	34.2	37.6	36.3	35.3
La	47.9	35.9	39	53.7	158	45.4	56.6	48.2	46.2	67.9	69.3
Ce	107	66.2	85.1	113	298	89.6	112.9	102.1	93.6	154.8	153.1
Pr	13.3	7.96	10.8	13.4	38.6	11.33	13.73	12.6	11.99	18.81	18.76
Nd	54.7	30.6	44.7	55.7	151	45.8	56.8	51.5	46.9	73.9	76.4
Sm	11.9	6.05	9.46	11.5	27.4	10.03	12.14	10.91	11.02	12.92	12.57
Eu	0.48	0.25	0.44	0.57	1.09	0.4	0.58	0.52	0.48	3.68	3.66
Gd	9.75	4.84	8.56	11.8	23.7	8.67	11.02	10.36	10.31	10.69	10.55
Tb	1.73	0.76	1.63	2.2	3.3	1.55	2.14	1.89	2.11	1.42	1.33
Dy	11	4.53	11	14.5	18.2	9.82	13.76	12.86	14.14	7.63	6.97
Ho	2.17	0.97	2.28	2.98	3.25	2.06	2.83	2.59	2.8	1.48	1.37
Er	6.44	3.31	7.45	8.49	8.61	6.37	8.27	7.45	8.14	3.96	3.63
Tm	0.97	0.63	1.04	1.31	1.25	0.96	1.22	1.11	1.24	0.52	0.52
Yb	6.85	5.5	7.28	8.45	8.78	7.54	8.62	8.21	8.26	3.5	3.53
Lu	1.04	1.01	1.16	1.39	1.36	1.2	1.37	1.28	1.23	0.53	0.5
ΣREE	275	169	230	299	743	240.7	302	271.6	258.4	361.7	362.2

Table 5.8 Fractionation of LREE over HREE, LREE over MREE and MREE over HREE of AR granitoids of Jhalda area.

Sample	(Ce/Yb)N	(La/Sm)N	(Gd/Yb)N
P1	4.085677	2.507328	1.138686
P2	3.157079	3.708678	0.704
P3	3.066114	2.576638	0.940659
P4	3.498302	2.913411	1.112426
P5	8.91146	3.611568	2.162187
P6	3.116928	2.829013	0.919894
P7	3.435396	2.913921	1.022738
P8	3.261916	2.761228	1.009501
P9	2.972254	2.620236	0.998547

CHAPTER-6

GEOCHRONOLOGY OF THE GRANITOID ROCKS OF RAGHUNATHPUR-BERO AREA AND JHALDA AREA OF CGGC

6.1. ANALYTICAL PROCEDURE

6.1.1. RAGHUNATHPUR AREA

6.1.2. JHALDA AREA

6.2. SAMPLE DESCRIPTION

6.2.1. RAGHUNATHPUR AREA

6.2.2. JHALDA AREA

6.3. GEOCHRONOLOGICAL ANALYSIS

6.3.1. RAGHUNATHPUR AREA

6.3.2. JHALDA AREA

FIGURES

TABLES

Geochronology deals with the age of the rocks delineating its position in the stratigraphic sequence. Absolute geochronology can be carried out proficiently by radioactive isotopes. Uranium-lead dating method is very common in every variety of rock type because of the abundance of zircons ($ZrSio_4$) in all rock types as accessory phase. Monazite geochronology is another example of U–Pb dating, employed for dating metamorphism. Zircon is extremely resistant to chemical weathering and metamorphism. They can survive a number of geologic events, which can be recorded as rings in zircon that grow around the original crystal. However, the core of the zircon remains unchanged, and preserves the chemical characteristics of the rock in which it originally crystallized. Zircons ability to retain its chemical and isotopic information helps to unravel the evolutionary history of earth's crust and mantle (Hanchar et al. 1994; Vervoort et al. 1996). Zircon acts as a robust geochronometer to unravel the chronology of rocks in space and time (Gibson and Ireland 1995; Bowring et al. 1998; Solar et al. 1998). Zircon acts as a tracer to pinpoint the isotopic character of the source rock (Scherer, Whitehouse and Munker 2007). In addition, it is the major host of Hf (radiogenic isotopic tracer) and is used to determine oxygen isotopic composition, REE and other trace elemental abundances, which can be used as a valuable clue indicating the history of the host rock. Zircon ranges in size from 20-200 micrometer (Silver and Deutsch 1963). Zircon is tetragonal and prismatic in shape with elongation (length-to-width) ratios ranging from 1 to 5. This ratio indicates crystallization velocity. For example, needle-shaped acicular zircon crystals indicate rapidly crystallized, porphyritic, sub-volcanic intrusions, high-level granites, and gabbros etc. Skeletal zircon crystals are the best example of rapid growth. Such zircons are observed in mafic and undersaturated alkaline rocks. Zircon crystals with metamorphic origin are characterized generally by subrounded and highly resorbed faces. However, euhedral shapes in metamorphic origin is also

possible in cases with very fluid-rich systems such as in amphibolite facies, mica schists and migmatites. Pupin (1980) suggested that the prismatic faces of zircon develops as a result of temperature of crystallization whereas the development of the pyramidal faces can be linked to the chemical factors, and suggested that this parameters can be used to describe the evolution of a magma system. Benisek and Finger (1993) also showed that chemical composition have a significant influence on the development of prism faces in zircon. In some magmas with very low Zr contents, or high Zr solubility or both (Hanchar et al., 1994), zircons exhibit partially developed crystal faces (e.g., Poldervaart 1956, Scoates and Chamberlain 1995). This phenomenon is common for gabbroic rocks.

This chapter deals with the age data of the granitoid varieties of Raghunathpur area and Jhalda. The age dating is carried out by the aid of U-Pb zircon geochronoly by LA-ICP-MS and U-Th-total Pb monazite dating by EPMA.

6.1. Analytical Procedure:

6.1.1. Raghunathpur area

U-Pb zircon geochronology by LA-ICP-MS:

Zircon U-Pb isotope analysis was performed using 213 nm Nd-YAG Laser (New Wave ResearchUP-213) combined with Agilent 7500 ICP-MS at the Department of Earth and Planetary Systems Science, Hiroshima University. The detailed analytical method was adopted from Das et al., (2017) and Saha et al., (2016). The selected samples were crushed using a handheld mortar-pestle. The zircons were separated using density and magnetic separation followed by handpicking under a binocular microscope. All the samples yielded variable number

of zircon grains of different size population with variable shapes. Zircon grains were mounted on glass slide in epoxy resin together with the zircon age standard FC-1 (207Pb/206Pb age of 1.09 ± 0.06 Ga; Paces and Miller, 1993) for LA-ICP-MS analysis. NIST610 glass standard was used for Th/U data calibration. Zircon grains were studied in detail in terms of internal structure, zoning pattern, fracture distribution and mineral inclusion(s) by scanning electron microscope (JEOL JSM6390A) installed at Hiroshima University, Japan. SEM-CL technique revealed internal structure of the individual zircon grains, whereas compositional zoning, fracture distribution and mineral inclusion(s) were determined by the SEM-BSI method. Analytical points for dating were, thus, predetermined from the observation of such internal structure, compositional zoning, fracture distribution and mineral inclusion(s). Pepi-AGE (Dunkl et al., 2008), a data reduction program, was used to process the raw data. Conventional geochronological and statistical plots were constructed using the processed data by the Isoplot/Ex (Version 4.15; Ludwig, 2012). The isotopic ratios and age data were quoted at 2σ, while the weighted average age was given at the 95% confidence level. To obtain reasonable age peaks from the analysed zircon grains, only near-concordant (≤10% discordance) data points were considered for the probability density plots.

U-Th-total Pb monazite dating by EPMA:

U-Th-total Pb monazite dating were carried out at Natural Science Center for Basic Research and Development, Hiroshima University using EPMA (JEOL JXA 8200 Superprobe). Alike U-Pb zircon dating, the analytical spots were carefully predetermined by observing the compositional zoning pattern and fracture distribution as revealed by the SEM-BSI technique. The detailed method described by Suzuki and Adachi (1991) was followed for the monazite dating.

Namaqualand monazite (1.03 Ga; Hokada and Motoyoshi 2006) was used as the age standard. The beam current was fixed at 200 nA, whereas the acceleration voltage was 15 kV throughout the analysis. Fifteen characteristic X-ray lines were measured for each element (Si-K α, Sm-M β, Gd-M β, Dy-M β, Th-M α, U-M β, Ca-K α, La-L α, Ce-L α, Y-L α, P-K α, S-K α, Pr-β1, Nd-Lβ1, Pb-M β). The raw data were first revised by using the recalculation methods developed by (Fujii, et al., 2008). The revised data were further processed, and then used for various statistical age plots using the Isoplot/Ex version 4.15 (Ludwig, 2012). The age data were quoted at 2σ.

6.1.2. Jhalda area:

Among the collected samples, sample P6 was chosen for geochronological study. Zircons were separated, mounted on thin-sections and polished for analysis in the Department of Earth and Planetary Systems Science, Hiroshima University. The electron back-scattered images (BSI) and cathodoluminescence (CL) images of the separated zircon grains were taken using the scanning electron microscope (SEM) facility of Hiroshima University (Model: JEOL JSM 7500F). These images were used to get an idea about the size and internal structure (zoning, inclusions etc.) of the zircon grains. The zircons were analyzed for U-Pb isotopes using 213 nm Nd-YAG Laser (New Wave Research UP-213) coupled with ICP-MS (Thermo Fisher X-Series-II) at the Department of Earth and Planetary Systems Science, Hiroshima University. The detailed analytical methodology is described by Katsube et al. (2012). The apparatus contains a mixed He-N_2-Ar carrier gas system equipped with small volume ablation cell, sample aerosol stabilizer (buffering chamber) and charcoal filter attachment. Spot size of the laser was 25 μm, and the zircon grains were measured in a mixed sequential order to avoid the influences of time-depending changes in the instrumental condition. Raw data were processed using the PepiAGE

(Dunkl et al., 2008) program, and plotted using Isoplot/Ex (Version 3; Ludwig, 2003). The isotopic ratios and age data are quoted at the estimation error of 2σ level, whilst, the weighted mean is given at the 95% confidence level. Zircon standard of FC1 ($^{206}Pb/^{238}U$ age of 1099.0 ± 0.6 Ma; Paces and Miller, 1993) was used for correction of U-Pb ratio, and glass standard of NIST SRM 610 was used for correction of Th/U ratio. In this study, $^{206}Pb/^{238}U$ ages are used for the zircon younger than 1000 Ma and $^{207}Pb/^{206}Pb$ ages are used for the zircon older than 1000 Ma, on the basis of their reproducibility in our measurement system (Katsube et al., 2012).

6.2. Sample Description:

6.2.1. Raghunathpur area:

GGG:

The main constituent minerals are quartz, alkali-feldspar, plagioclase feldspar, garnet and biotite and accessory phases are monazites and opaque minerals.

Monazite grains are sub-rounded in nature with the diameter ranged between ~50 and ~30 μm. The BSI imageries show that the majority of the grains are homogenously zoned. However, few grains are patchy zoned core, which graded outward in to brighter mantle and darker core.

MGG:

The main constituent minerals of this highly porphyritic/megacrystic granite variety are alkali feldspar, quartz, plagioclase feldspar with minor biotite, amphibole and opaque.

Zircon grains are subhedral and elongated in shape, with length to width ratio ~4:1. CL imagery exhibit a homogenous dark core surrounded by an oscillatory zoned brighter mantle which grades to a thin darker rim.

PG:

This granite variety is leucocratic, equigranular, medium grained rock consisting of alkali feldspar, quartz, plagioclase feldspar, biotite as major mineral constituents and apatite and opaques as minor constituents.

Zircon grains of this variety are subhedral and elongated in nature with an aspect ratio of ~3:1. Most of the grains contain a darker-CL core, which graded outward in to a brighter-CL rim. Some grains have a patchy zoned core, surrounded by a relatively brighter mantle and rim.

Monazite grains are subhedral to anhedral in nature. The tabular grains had an aspect ratio of ~2:1. Occasionally, irregular-shaped grains are also present. In BSI imagery shows that all the grains exhibited a well-developed (rarely patchy) brighter core surrounded by a darker rim.

6.2.2. Jhalda area:

AR granites

The major constituent minerals are quartz, alkali feldspar, alkali pyroxene (aegirine), alkali amphibole (riebeckite, arfvedsonite) and biotite. The accessory minerals are zircon, plagioclase, sphene, ilmenite, and allanite.

Zircon grains are relatively elongated and subhedral in nature. They are relatively smaller (100–250 μm) and contain significantly less inclusions. They show oscillatory zoning as well, and some grains show oscillatory to patchy-zoned core.

6.3. Geochronological Analyses

6.3.1. Raghunathpur area:

Geochronological analyses were carried out using LA-ICP-MS for bulk separated zircon grains (sample L22 and L24 by U-Pb isotopic technique) and EPMA for monazite grains (sample L22 and L10 by U-Th-total Pb method). The analytical data of geochronological analyses are presented in Table 6.1. and Table 6.2.

U-Pb zircon dating by LA-ICP-MS

PG (Sample L22): Total twenty points were measured from eighteen extracted zircon grains from the powdered bulk rock. The majority of the grains were subhedral and elongated in shape with an aspect ratio of ~3:1 (length ~150μm and breadth ~50 μm). Most of the grains contain a homogenous darker-CL core, which graded outward in to a brighter-CL rim (Fig. 6.1.a). Rarely grains had a patchy zoned core, which was surrounded by a relatively brighter mantle and rim. Th/U ratio of these zircon grains ranged between 0.34 and 0.06. Out of twenty measured point from both core and rim, only five data points acquired as near concordant. All the analysed data points, when plotted on the Tera-Wasserburg concordia diagram, did not construct a concordia line due to variable discordancy of the discordant data points. However, all the near-concordant data cluster at ~1.05 Ga (Fig. 6.1.b). Five near concordant age data yielded a single-population

weighted mean age as 1.06 ± 0.03 Ga ($^{207}Pb/^{206}Pb$ age with MSWD = 1.3 and probability = 0.25; Fig. 6.1.c).

MGG (Sample L24): Out of sixteen separated zircon grains, total nineteen points were measured from both the core and rim. Zircon grains were subhedral and elongated in shape, but of variable sizes (length ~200-80 µm and breadth ~50-20 µm). In response to CL, the zircon grains exhibit a homogenous dark core, which was surrounded by an oscillatory zoned brighter mantle, and then graded in to a thin darker rim (Fig. 6.1.d). Th/U ratio varied from1.81 to 0.17. Tera-Wasserburg plot constitute of all data points yielded a single population age cluster on concordia line at ~1.0 Ga (Fig. 6.1.e). Due to occurrence of single age cluster on concordia diagram, discordia line could not be drawn. Eighteen near-concordant age data defined a single-population weighted average 207Pb/206Pb age as 9.98±0.01 Ga [n=17 (one data has been rejected during statistical data plotting) with MSWD = 2.3 and probability = 0.003; Fig. 6.1.f)

U-Th-total Pb monazite dating by EPMA

PG (Sample L22): Total six grains were selected for geochronological analysis. The majority of the grains are subhedral to anhedral with various shapes and sizes. The diameter of subrounded grains varied between ~100 and ~50 µm, while the tabular grains had an aspect ratio of ~2:1.Occasionally, irregular-shaped grains were also reported. In BSI response, almost all the grains exhibited a well-developed (rarely patchy) brighter core which was surrounded by a darker rim (Fig. 6.2.a). The spot ages of total thirty-seven analysed points were ranging in between 0.92±0.01 Ga and 1.05±0.01 Ga, irrespective of the zoning pattern. All age data, when plotted on a probability density diagram, revealed two major peaks at ~0.99 Ga and ~1.01 Ga

with two minor peaks at ~0.94 Ga and ~0.96 Ga (Fig. 6.2.b). A meaningful weighted average of the data-points could not be obtained due to presence of multiple age peaks.

GGG (Sample L10): Out of six monazite grains, total twenty-seven points were measured. Almost all the grains are sub-rounded with the diameter ranged between ~50 and ~30 μm. The BSI imageries revealed that the majority of the grains exhibited homogenously zoned CL response. However, few grains contained patchy zoned core, which graded outward in to brighter mantle and darker core (Fig. 6.2.c). The oldest spot age recorded from this rock as 1.03±0.02 Ga, whereas the youngest spot date recorded as 0.94±0.03 Ga. Probability density plot of all data points yielded two very closely-spaced peaks at ~0.98 Ga and ~1.01 Ga (Fig. 6.2.d).

6.3.2. Jhalda area:

The zircon grains separated from a specimen of AR granite are relatively elongated and subhedral in nature with rounded outlines. The analysed zircon grains are relatively smaller (100–250 μm) and contain significantly less inclusions (Fig.6.3). Almost all of these grains display oscillatory zoning as well, and some grains show oscillatory to patchy-zoned core. The oscillatory zoning is parallel to the external crystal faces of the euhedral-sub-hedral grains. The oscillatory zoning in zircons is generally attributed to growth during magma crystallization (Corfu et al., 2003). On the other hand, patchy zoning reflects strain experienced by zircon during final magmatic emplacement. Length to width ratio is ~ 4:1 indicating relatively high crystallization rate.

The zircon grains from P4 are relatively large (150-350 μm) and contain numerous inclusions and complex zoning (Fig. 10a). Zircon grains show dark homogeneous core, oscillatory mantle

and bright rim in the CL images. A total of 21 points were measure from 15 selected zircon grains from P4. Analyzed data of 16 points out of 21 lie on the concordia line within their analytical error, which have discordance <2%. $^{207}Pb/^{206}Pb$ ages that from dark homogeneous core and oscillatory zoned mantle parts range from ca. 1298 to 1361 Ma, and their weighted average yields an age of 1328 ± 13 Ma (2σ, MSWD = 0.42). Th/U ratio ranges between 0.34 and 0.77. On the other hand, the data from bright rim part are almost discordant except only one concordant data that shows the spot $^{207}Pb/^{206}Pb$ age of 1103 ± 97 Ma and Th/U ratio of 0.27.

A total of 21 points were analyzed from 19 selected zircon grains and all the datas are plotted in the Terra-Wasserburg diagram (Fig. 6.4.a). Analyzed data of 18 points out of 21 lie on the concordia line within their analytical error, which have discordance <3%. $^{206}Pb/^{238}U$ ages from oscillatory mantle parts, range from ca. 951 to 990 Ma, and their weighted average yields an age of 966.7 ± 7.0 Ma (2σ, MSWD = 0.73), except one data that measured not only oscillatory mantle but also patchy zoned core and shows $^{206}Pb/^{238}U$ age of ca. 1009 ± 35 Ma (Fig. 6.4.b). Th/U ratio ranges between 0.68 and 1.35 (Table 6.3) indicating its igneous origin. One data from oscillatory core part is discordant.

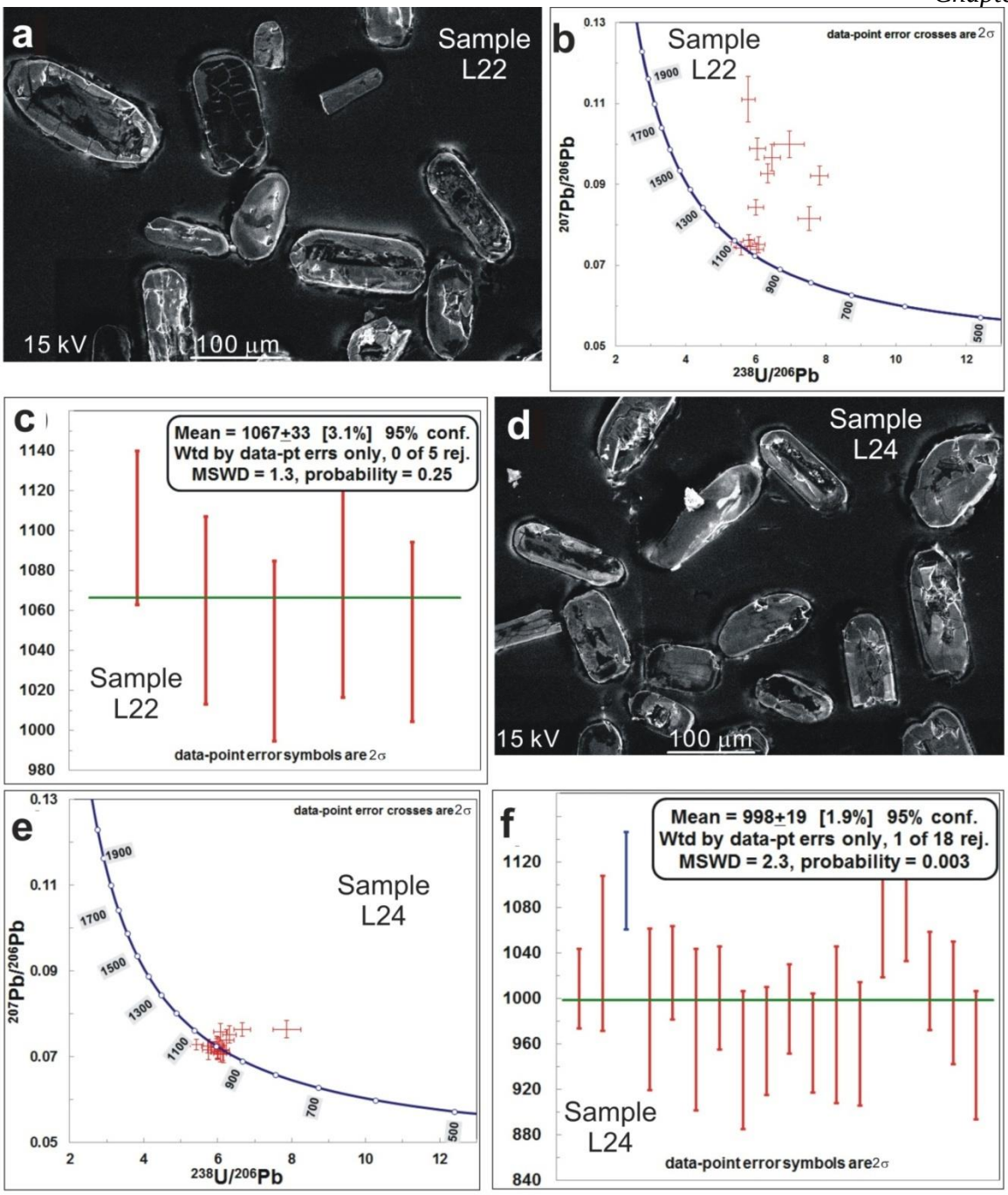

Figure. 6.1. a) Cathodluminescence (CL) images of zircon grains of PG showing homogenous darker-CL core, which grades outward into a brighter-CL rim; b) Plot of 238U/206Pb versus 207Pb/206Pb for the sample L22 (PG) in the Tera-Wasserburg diagram; c) Probability density diagram showing mean age of 1.06±0.03 Ga obtained from zircons of L22 (PG); d) Cathodluminescence (CL) images of zircon grains of MGG showing homogenous dark core

surrounded by an oscillatory zoned brighter mantle which grades to a thin darker rim; e) Plot of 238U/206Pb versus 207Pb/206Pb for the sample L24 (MGG) in the Tera-Wasserburg diagram; f) Probability density diagram showing mean age of 0.99±0.01 Ga obtained from zircons of L24 (MGG).

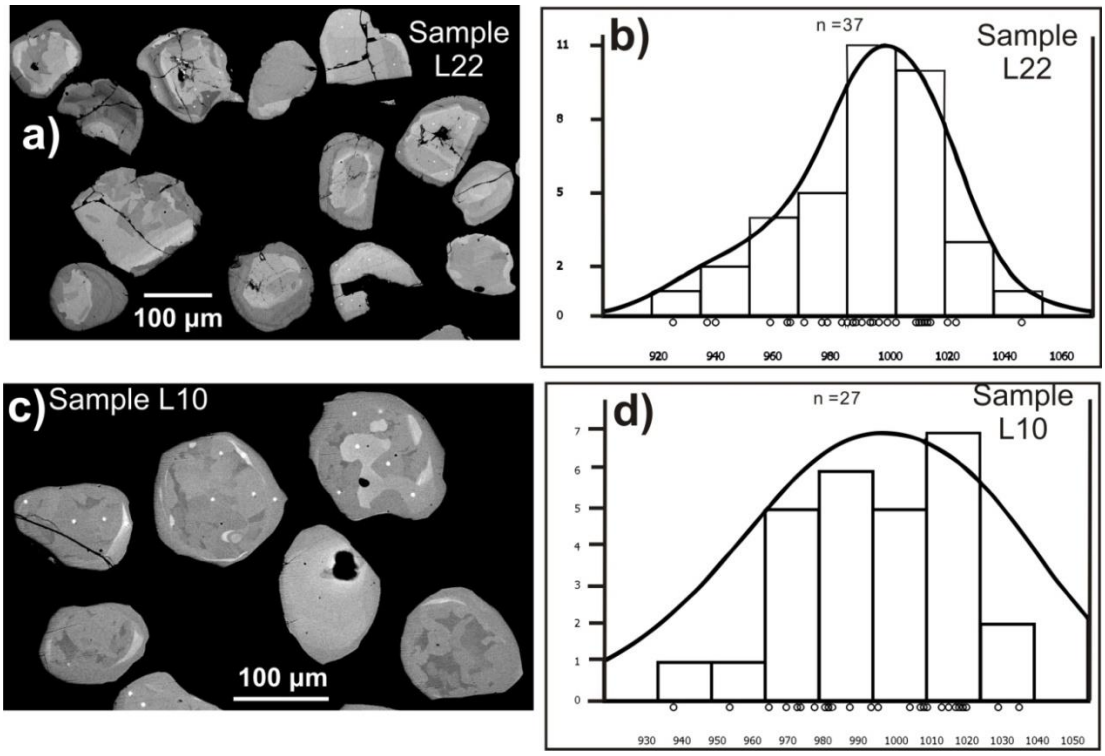

Figure. 6.2. a) Back Scattered Images (BSI) of monazite grains of PG showing well-developed (rarely patchy) brighter core surrounded by a darker rim; b) Probability density plot of all monazite data points of L22 (PG) showing two major peaks at ~0.99 Ga and ~1.01 Ga with two minor peaks at ~0.9 Ga and ~0.9 Ga; c) Back Scattered Images (BSI) of monazite grains of L10 (GGG) showing homogenously zoned CL response with few grains containing patchy zoned core which grades outward in to brighter mantle and darker core; d) Probability density plot of all

monazite data points of L10(GGG) yielding two very closely-spaced peaks at ~0.98 Ga and ~1.01 Ga.

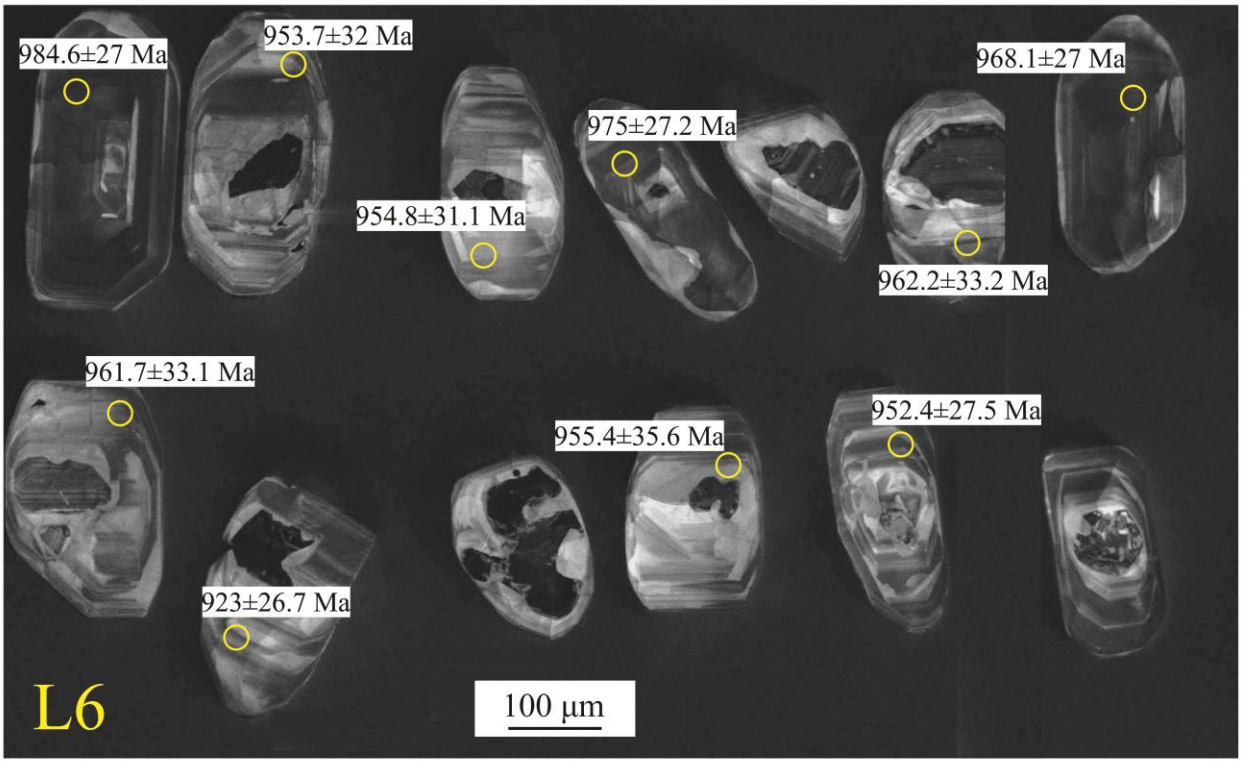

Figure. 6.3. Cathodoluminescence (CL) images of selected zircon grains from one sample (L6) of AR granitoids exhibiting complex zoning and spongy texture. The analytical points have been marked with their respective calculated ages.

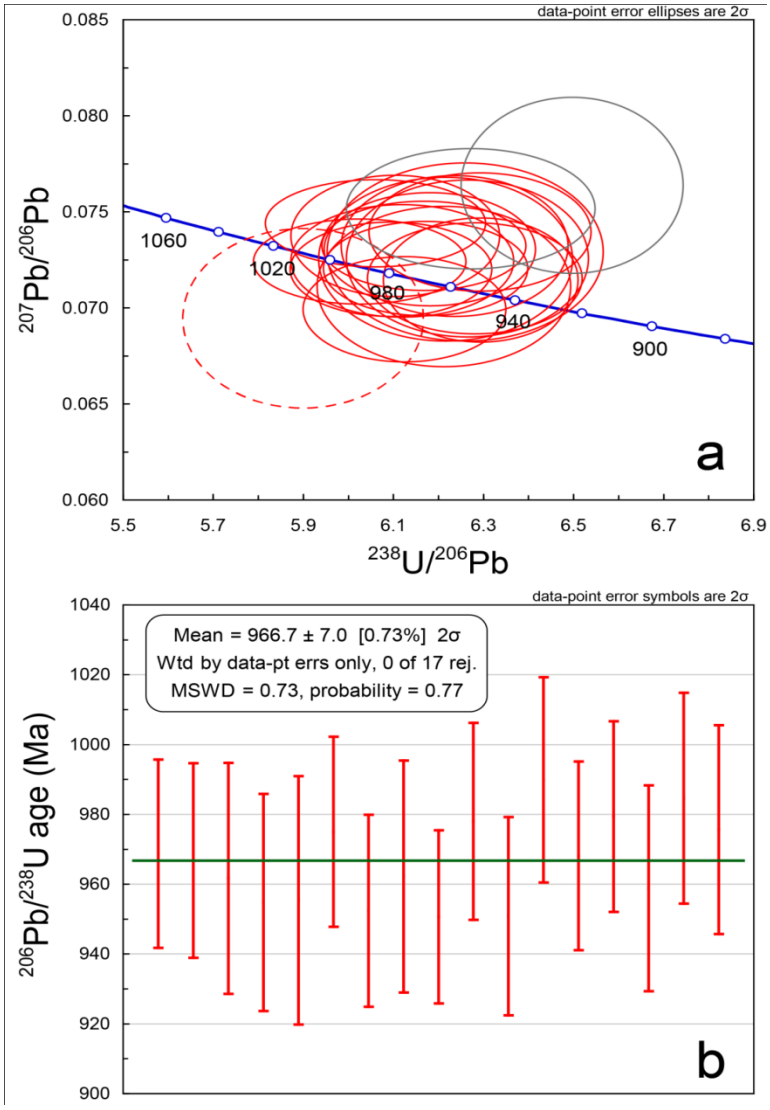

Figure. 6.4. a) Tera-Wasserburg concordia diagram of zircons of L6 of AR granitoids of Jhalda area. Red solid ellipses represent concordant data; gray ellipses represent discordant data, and red dashed ellipse represents that measured both oscillatory mantle and patchy zoned core. (b) Probability density diagram showing mean age of 966.7 ± 7.0 Ma obtained from zircons of L6.

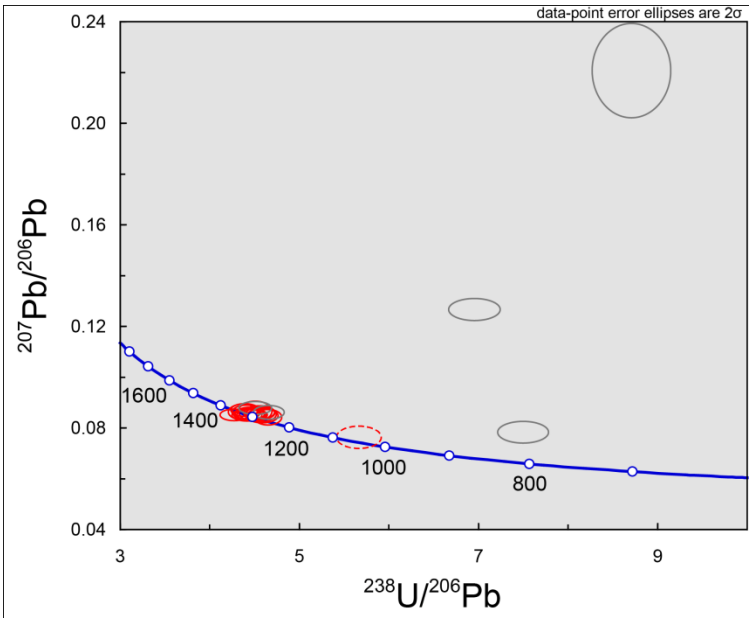

Figure 6.5. Terra-Wasserburg concordia diagram of zircons of P4 of AR granitoid of Jhalda area.

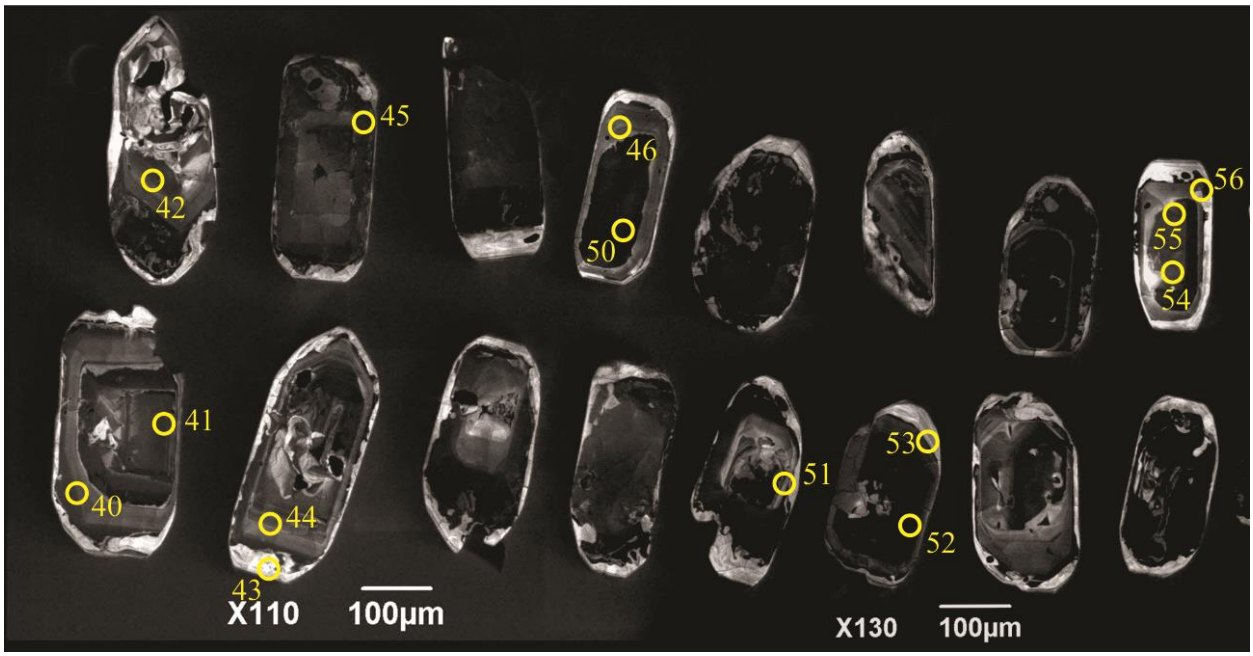

Figure 6.6. Cathodoluminescence (CL) images of selected zircon grains from one sample (P4) of AR granitoids exhibiting complex zoning and spongy texture.

Table 6.1. LA-ICP-MS Zircon U-Pb isotopic age data obtained from the samples of (MGG) L24 and (PG) L22.

L24															
		Isotopic ratios[*1]							Isotopic ages[*2]						
Points*	$^{238}U/^{206}Pb$	± (%)	$^{207}Pb/^{235}U$	± (%)	$^{207}Pb/^{206}Pb$	± (%)	$^{206}Pb/^{238}U$	±	$^{207}Pb/^{235}U$	±	$^{207}Pb/^{206}Pb$	±	Th/U	discordance[3]	discordance[4]
L24_1	5.428	3.2	1.849	3.6	0.0728	1.7	1090	32	1063	24	1009	35	0.19	-2.5%	-8.1%
L24_2	6.247	3.2	1.632	4.6	0.0739	3.3	957	29	982	29	1039	68	0.63	2.6%	7.9%
L24_2C	6.670	3.3	1.578	3.9	0.0763	2.1	901	28	961	25	1103	43	0.65	6.8%	18.4%
L24_3	6.019	3.0	1.653	4.5	0.0722	3.4	991	28	991	29	990	71	1.04	0.0%	-0.1%
L24_4	5.965	3.0	1.694	3.6	0.0733	2.0	999	28	1006	23	1022	41	1.81	0.7%	2.3%
L24_4R	7.870	4.7	1.338	5.4	0.0764	2.7	771	34	863	32	1106	55	0.78	11.9%	30.2%
L24_5	6.139	2.8	1.607	4.4	0.0715	3.4	973	25	973	28	973	71	0.75	0.0%	0.0%
L24_5R	5.727	2.9	1.745	3.6	0.0725	2.2	1037	28	1026	24	1000	45	0.50	-1.1%	-3.7%
L24_6C	6.161	2.8	1.580	4.0	0.0706	2.9	970	25	962	25	946	61	1.03	-0.8%	-2.5%
L24_6R	5.988	2.8	1.639	3.6	0.0712	2.3	996	26	985	23	963	48	0.76	-1.0%	-3.4%
L24_7	5.912	3.2	1.683	3.7	0.0722	1.9	1008	30	1002	24	991	39	0.17	-0.5%	-1.7%
L24_8	5.994	3.0	1.636	3.7	0.0711	2.1	995	28	984	24	961	44	0.25	-1.1%	-3.6%
L24_9	5.757	3.1	1.716	4.5	0.0717	3.3	1033	30	1015	29	977	69	0.71	-1.7%	-5.7%
L24_10	6.001	2.8	1.633	3.8	0.0711	2.6	994	26	983	24	960	54	0.60	-1.0%	-3.5%
L24_11	6.320	3.0	1.641	4.0	0.0752	2.7	947	27	986	26	1074	55	0.98	4.1%	11.8%
L24_12	6.073	3.1	1.719	4.1	0.0757	2.7	983	28	1016	27	1088	55	1.05	3.4%	9.7%
L24_13	6.008	2.9	1.676	3.6	0.0730	2.1	993	27	1000	23	1015	43	0.65	0.7%	2.2%
L24_14	5.981	2.9	1.668	3.9	0.0724	2.6	997	27	996	25	996	54	0.57	0.0%	-0.1%
L24_16	6.069	2.8	1.607	3.9	0.0707	2.7	983	26	973	25	950	56	0.90	-1.0%	-3.5%
L22															
L22_1C	5.305	2.7	1.935	3.4	0.0745	2.0	1113	28	1093	23	1054	41	0.13	-1.8%	-5.6%
L22_1R	10.820	4.3	2.126	4.9	0.1668	2.3	570	24	1157	34	2526	39	0.14	103.1%	77.4%

L22_2	5.794	3.4	2.644	6.1	0.1111	5.1	1026	32	1313	46	1818	96	0.27	27.9%	43.5%
L22_3	5.807	2.8	1.810	3.4	0.0762	1.9	1024	27	1049	23	1101	39	0.09	2.4%	7.0%
L22_4	6.052	3.8	2.252	4.7	0.0988	2.7	986	35	1197	34	1602	51	0.16	21.5%	38.5%
L22_5R	12.814	6.0	3.299	6.5	0.3066	2.5	484	28	1481	52	3504	39	0.23	205.7%	86.2%
L22_6	5.853	3.0	1.759	3.8	0.0747	2.3	1017	28	1031	25	1060	47	0.09	1.4%	4.1%
L22_8	6.031	3.1	1.690	3.8	0.0739	2.2	989	29	1005	25	1040	45	0.30	1.6%	4.9%
L22_9	6.334	3.0	2.019	4.0	0.0928	2.6	945	26	1122	28	1483	50	0.16	18.7%	36.3%
L22_10	11.732	3.4	1.263	4.5	0.1075	2.9	527	17	829	26	1757	54	0.17	57.3%	70.0%
L22_11	6.010	3.6	1.935	4.2	0.0843	2.2	992	33	1093	29	1301	43	0.14	10.2%	23.7%
L22_12	7.523	4.2	1.497	5.5	0.0817	3.6	805	32	929	34	1237	72	0.21	15.5%	35.0%
L22_13	6.086	3.0	1.702	4.0	0.0751	2.7	981	27	1009	26	1072	55	0.34	2.9%	8.5%
L22_13	8.302	3.9	3.328	5.4	0.2004	3.7	733	27	1488	43	2829	62	0.17	102.9%	74.1%
L22_14	7.814	3.2	1.627	4.1	0.0922	2.5	776	23	981	26	1472	48	0.13	26.3%	47.3%
L22_15	5.578	3.4	1.836	4.0	0.0743	2.2	1063	33	1059	27	1049	45	0.24	-0.4%	-1.3%
L22_16	6.954	6.1	1.980	6.9	0.0999	3.3	866	50	1109	48	1622	63	0.06	28.0%	46.6%
L22_17	6.471	3.6	2.058	5.0	0.0966	3.4	926	31	1135	35	1560	65	0.12	22.5%	40.6%
L22_18	6.870	5.3	2.945	6.9	0.1468	4.4	876	44	1394	54	2309	78	0.09	59.1%	62.1%
*** C = core of the grain, R = rim of the grain**															
***1, *2 = All data are corrected for common Pb**															
Discordance[3]: Calculated from $^{206}Pb/^{238}U$ age and $^{207}Pb/^{235}U$ age															
Discordance[4]: Calculated from $^{206}Pb/^{238}U$ age and $^{207}Pb/^{206}Pb$ age															

Table 6.2. EPMA Monazite U-Th- total Pb age data obtained from the samples (PG) L22 and (GGG) L10.

Spot	**ThO_2**	**UO_2**	**PbO**	**CaO**	**P_2O_5**	**Y_2O_3**	**La_2O_3**	**Ce_2O_3**	**Pr_2O_3**	**Nd_2O_3**	**Sm_2O_3**	**Gd_2O_3**	**Dy_2O_3**	**SO_3**	**Total**	**Age**	**± 2 σ**
number																(Ma)	(Ma)
L-10-1-1	9.393	0.084	0.411	0.843	28.49	0.165	14.37	30.388	2.979	10.374	2.8557	0.4244	0.0291	0.003	102.4	976	23
L-10-1-2	6.056	0.073	0.271	0.615	29.1	0.083	15.63	31.814	3.071	10.432	3.3659	0.5712	0	0	102.1	983	33
L-10-1-3	7.307	0.132	0.342	0.676	28.26	0.153	14.76	31.444	3.091	10.734	2.7693	0.316	0	0	101.3	1011	29
L-10-1-4	5.955	0.145	0.264	0.592	30.07	0.288	15.2	31.913	3.097	11.238	3.3939	0.5438	0	0.003	103.7	940	33
L-10-1-5	6.21	0.089	0.279	0.659	29.91	0.106	15.19	31.913	3.049	11.089	3.4781	0.7149	0	0.009	103.7	980	32
L-10-2-1	6.297	0.12	0.288	0.676	29.56	0.309	15.13	31.185	3.097	11.336	3.464	0.7368	0.0285	0.003	103.3	985	32
L-10-2-2	7.08	0.045	0.321	0.713	29.15	0.273	15.19	31.336	3.008	10.682	3.055	0.4125	0	0	102.4	1016	29
L-10-2-3	7.241	0.05	0.318	0.718	29.8	0.281	15.37	31.464	3.043	10.707	2.9905	0.4604	0.0629	0	103.7	984	28
L-10-2-4	6.13	0.132	0.294	0.547	28.86	0.344	16	31.831	2.928	10.178	2.9333	0.5202	0.0682	0.014	101.9	1021	34
L-10-2-5	12.49	0.139	0.554	0.941	26.93	0.215	13.21	28.609	2.865	10.045	2.5499	0.3534	0	0	101.2	985	18
L-10-3-1	6.293	0.192	0.3	0.79	29.47	0.536	14.94	30.714	2.968	10.692	3.6832	0.9565	0.1294	0.006	102.6	990	32
L-10-3-2	5.77	0.093	0.268	0.615	29.74	0.242	15.17	31.683	3.137	11.266	3.286	0.7437	0	0.017	103	1007	35
L-10-3-3	12.22	0.142	0.57	0.957	26.66	0.222	13.18	28.454	2.88	10.147	2.5224	0.4058	0.0258	0.007	100.5	1032	19
L-10-3-4	6.774	0.077	0.293	0.66	30.35	0.173	15.38	31.882	3.062	11.048	3.305	0.5003	0	0	104.6	956	30
L-10-4-1	5.935	0.158	0.275	0.679	28.82	0.275	14.79	30.677	3.042	10.879	3.612	0.9526	0.0217	0.003	101.1	975	34
L-10-4-2	6.09	0.154	0.288	0.725	29.18	0.445	14.61	30.612	3.074	11.092	3.7277	1.066	0.0477	0.014	102.1	998	33
L-10-4-3	6.308	0.122	0.284	0.65	29.4	0.165	15.32	31.196	3.013	10.591	3.4285	0.8112	0.0178	0	102.4	967	32
L-10-4-4	6.287	0.126	0.285	0.651	29.89	0.163	15.24	31.598	3.023	10.872	3.6985	0.8151	0	0	103.7	972	32
L-10-4-5	5.678	0.422	0.317	0.931	29.97	1.493	14.2	29.428	2.883	10.569	3.7954	1.4284	0.5625	0	102.4	1022	33
L-10-5-1	5.735	0.245	0.292	0.738	29.01	1.287	14.88	30.183	2.922	10.125	3.3593	1.0223	0.3727	0.009	101	1018	35
L-10-5-2	10.36	0.037	0.461	0.511	27.01	0.609	16.32	29.757	2.683	8.3204	2.5607	0.3538	0.0818	0.002	101.3	1010	21

L-10-5-3	10.3	0.032	0.463	0.496	26.73	0.599	16.15	29.826	2.623	8.2778	2.458	0.3313	0.1009	0	100.6	1023	21
L-10-5-4	5.577	0.173	0.268	0.96	30.13	1.197	14.53	30.368	2.929	10.359	3.5828	1.1719	0.3743	0.009	102.2	996	36
L-10-5-5	6.44	0.139	0.308	0.559	28.26	0.359	15.96	31.625	2.881	9.7397	2.821	0.4457	0.028	0	100.7	1020	32
L-10-5-6	7.828	0.043	0.361	0.543	27.78	0.617	16.58	30.998	2.685	8.6752	2.8355	0.4336	0.051	0.013	101	1038	27
L-10-6-1	6.461	0.122	0.304	0.711	29.11	0.332	14.75	30.665	3.016	10.591	3.4558	0.9462	0.092	0.002	101.6	1012	32
L-10-6-2	6.248	0.1	0.29	0.69	29.01	0.322	14.92	30.716	3.024	10.745	3.3534	0.91	0.0631	6E-04	101.4	1010	33
L-22-1-1	17.78	0.163	0.809	0.348	23.57	0.2	16.89	27.704	2.157	5.4097	2.0707	0.0782	0.0211	0.004	101.6	1018	14
L-22-1-2	11.94	0.39	0.585	0.843	25.93	1.065	16.72	28.515	2.337	6.1683	2.6525	0.3349	0.153	0.005	99.99	1016	19
L-22-1-3	13.62	0.531	0.678	0.476	24.93	0.768	16.91	28.145	2.366	5.9875	2.5617	0.2803	0.1564	0.005	100.7	1013	17
L-22-1-4	18.63	0.735	0.885	0.522	24.11	0.962	15.21	26.175	2.173	5.6557	2.4013	0.2928	0.2051	0.006	102.6	968	13
L-22-1-5	18.71	1.113	0.99	0.509	23.01	1.156	14.58	25.556	2.187	5.6154	2.107	0.2219	0.2001	0.016	100.6	1015	13
L-22-1-6	16.4	1.105	0.891	0.468	23.47	1.314	15.09	26.312	2.197	5.7239	2.0899	0.2335	0.1823	0.006	99.48	1018	15
L-22-2-1	18.93	0.206	0.849	0.323	23.26	0.206	16.43	26.811	2.147	5.1582	2.144	0.0722	0.032	0.004	101.3	998	13
L-22-2-2	20.32	0.226	0.905	0.337	22.91	0.234	15.89	26.479	2.174	5.3143	2.1104	0.0597	0	0.008	102	991	13
L-22-2-3	20.56	0.226	0.917	0.348	22.97	0.24	15.77	26.435	2.245	5.2949	2.0486	0.0764	0.0141	0	102.2	992	13
L-22-2-4	16.56	0.143	0.758	0.357	24.05	0.199	17.5	28.134	2.205	5.2165	2.2786	0.0851	0	0.005	101.6	1024	15
L-22-2-5	20.78	0.587	1	0.434	22.58	0.864	14.58	25.24	2.043	5.5748	2.0437	0.1735	0.0841	0.009	100.9	1013	13
L-22-3-1	19.26	0.215	0.855	0.338	23.13	0.248	16.41	26.843	2.128	5.244	2.1449	0.0975	0	0	101.7	987	13
L-22-3-2	18.18	0.177	0.828	0.333	23.28	0.217	16.68	27.517	2.229	5.4118	2.2944	0.1127	0.0208	0.003	101.8	1017	14
L-22-3-3	20.17	0.232	0.932	0.35	22.2	0.281	15.81	26.013	2.16	5.3363	2.0481	0.1572	0.0791	0	100.8	1027	13
L-22-3-4	17.21	0.187	0.773	0.362	23.99	0.277	17.02	27.945	2.232	5.4376	2.2131	0.0901	0	0.012	102.1	1000	14
L-22-3-5	19.7	0.416	0.921	0.338	22.53	0.428	15.27	26.396	2.293	5.7392	2.1357	0.1383	0.0763	0.01	101.4	1006	13
L-22-3-6	14.83	0.94	0.733	0.445	25.63	1.375	16.36	27.814	2.264	5.8453	2.5621	0.3209	0.2066	0.007	103.1	940	15
L-22-3-7	15.2	0.658	0.767	0.552	24.76	1.06	16.05	27.354	2.192	5.8881	2.3597	0.2703	0.1621	0.006	100.8	1014	16
L-22-4-1	19.59	0.224	0.871	0.315	23.5	0.274	16.14	27.059	2.202	5.6008	2.0871	0.0699	0	0	102.8	989	13
L-22-4-2	20.05	0.218	0.903	0.329	22.85	0.258	16.02	26.692	2.191	5.4474	2.1377	0.0954	0.0094	0.001	102.2	1003	13
L-22-4-3	18.88	0.205	0.845	0.34	23.7	0.232	16.57	27.531	2.173	5.5302	2.1263	0.0402	0	0	102.9	997	13
L-22-4-3	18.28	1.01	0.886	0.518	24.76	1.37	15.53	26.302	2.186	5.631	2.303	0.2741	0.2554	0.008	103.9	943	13

L-22-4-4	17.46	0.96	0.863	0.395	24.25	1.445	15.65	26.663	2.252	5.6189	2.385	0.3197	0.1635	0.013	103	962	14
L-22-5-1	18.44	0.2	0.823	0.339	23.34	0.206	16.79	27.469	2.237	5.2772	2.1659	0.0974	0	0.004	101.9	994	14
L-22-5-2	18.86	0.196	0.839	0.335	23.63	0.219	16.61	27.239	2.199	5.2489	2.2565	0.0741	0.0091	0.011	102.4	992	13
L-22-5-3	14.85	0.521	0.708	0.409	25.11	0.534	16.85	28.177	2.306	5.9326	2.4342	0.2182	0.0953	0.009	101.9	982	16
L-22-5-4	14.92	0.523	0.738	0.418	24.9	0.568	16.64	28.329	2.307	5.9127	2.4046	0.2215	0.1274	0.007	101.6	1018	16
L-22-5-5	11.65	0.343	0.545	0.695	27.27	0.942	17.43	29.636	2.478	6.2225	2.5118	0.323	0.1582	8E-04	102.6	980	20
L-22-5-6	11.61	0.361	0.54	0.668	27.12	0.968	17.59	29.447	2.421	6.2793	2.6401	0.3593	0.2015	0.013	102.7	969	19
L-22-5-6	14.63	0.806	0.698	0.381	25.83	1.317	16.75	28.364	2.272	5.9037	2.594	0.2384	0.1916	0.018	103.8	928	15
L-22-6-1	18.41	0.197	0.819	0.343	23.7	0.232	16.88	27.611	2.161	5.3024	2.1837	0.1082	0	0.011	102.4	991	14
L-22-6-2	18.34	0.205	0.827	0.331	23.55	0.233	16.69	27.445	2.173	5.3261	2.0723	0.1027	0.0272	0	101.8	1003	14
L-22-6-3	20.22	0.274	0.933	0.353	22.25	0.37	15.2	26.249	2.149	5.4779	2.0149	0.11	0.0334	0.006	100.6	1017	13
L-22-6-4	15.45	0.553	0.732	0.446	24.66	0.609	16.54	27.919	2.374	5.9606	2.587	0.2694	0.1238	0.001	102.1	974	15
L-22-6-5	15.5	0.59	0.729	0.426	25.35	0.606	16.59	28.236	2.301	6.0596	2.5546	0.213	0.0544	0.01	103.1	962	15
L-22-6-6	12.95	1.037	0.733	0.597	24.86	1.72	16	27.278	2.263	5.8318	2.3437	0.3145	0.3026	0.022	99.41	1024	17
L-22-6-7	12.71	0.884	0.717	0.6	24.19	1.452	16.22	27.55	2.237	5.8639	2.1709	0.3281	0.2577	0.02	98.15	1050	18

All ages are in Ma and all errors are quoted as 2σ

Table 6.3. LA-ICPMS data obtained from zircon grains of P4 and L6 samples of AR granitoids of Jhalda area.

Spot name	$^{238}U/^{206}Pb^* \pm 2\sigma$			$^{207}Pb^*/^{206}Pb^* \pm 2\sigma$			$^{206}Pb^*/^{238}U$ age ± 2σ (Ma)			$^{207}Pb^*/^{235}U$ age ± 2σ (Ma)			$^{207}Pb^*/^{206}Pb^*$ age ± 2σ (Ma)			Th/U	Disc. %
P4																	
040P4	4.57	±	0.13	0.0861	±	0.0021	1276.1	±	32.5	1300.4	±	27.5	1340.8	±	47.1	0.42	1.9
041P4	4.45	±	0.13	0.0855	±	0.0021	1307.1	±	35.6	1314.4	±	29.2	1326.3	±	49.2	0.47	0.6
042P4	4.59	±	0.14	0.0848	±	0.0023	1271.0	±	35.9	1285.7	±	30.3	1310.5	±	53.3	0.37	1.2
043P4	7.50	±	0.23	0.0783	±	0.0035	807.1	±	23.6	905.5	±	33.5	1154.1	±	92.0	0.32	12.2
044P4	4.38	±	0.14	0.0863	±	0.0026	1325.4	±	38.5	1332.6	±	33.2	1344.1	±	59.1	0.34	0.5
045P4	4.46	±	0.15	0.0851	±	0.0019	1303.5	±	39.1	1309.3	±	29.9	1318.7	±	43.2	0.48	0.4
046P4	4.65	±	0.13	0.0842	±	0.0025	1255.6	±	30.9	1271.2	±	29.4	1297.8	±	59.4	0.39	1.2
050P4	4.39	±	0.13	0.0870	±	0.0021	1322.0	±	34.8	1336.9	±	28.6	1361.0	±	46.9	0.56	1.1
051P4	4.41	±	0.13	0.0863	±	0.0022	1317.4	±	34.6	1327.6	±	29.3	1344.3	±	51.1	0.47	0.8
052P4	4.46	±	0.12	0.0852	±	0.0017	1304.8	±	33.2	1310.6	±	25.3	1320.3	±	39.2	0.54	0.4
053P4	5.67	±	0.20	0.0763	±	0.0036	1047.8	±	34.9	1065.8	±	39.7	1103.0	±	97.0	0.27	1.7
054P4	4.66	±	0.14	0.0862	±	0.0022	1253.1	±	34.3	1286.1	±	29.6	1341.6	±	51.0	0.48	2.6
055P4	4.51	±	0.15	0.0866	±	0.0033	1291.3	±	39.9	1314.0	±	38.3	1351.3	±	75.1	0.36	1.8
056P4	8.71	±	0.36	0.2207	±	0.0152	700.8	±	27.3	1526.1	±	65.2	2986.0	±	115.6	0.72	117.8
060P4	4.51	±	0.15	0.0879	±	0.0021	1291.5	±	38.7	1325.1	±	30.8	1379.9	±	46.8	0.48	2.6
061P4	4.45	±	0.15	0.0853	±	0.0019	1307.3	±	39.2	1313.0	±	29.9	1322.3	±	43.2	0.45	0.4
062P4	4.57	±	0.14	0.0853	±	0.0024	1275.6	±	36.0	1292.7	±	31.2	1321.3	±	55.3	0.38	1.3
063P4	4.55	±	0.14	0.0860	±	0.0022	1279.8	±	36.1	1301.6	±	29.8	1337.6	±	51.1	0.51	1.7
064P4	4.42	±	0.14	0.0851	±	0.0020	1315.9	±	37.0	1316.6	±	29.2	1317.6	±	45.2	0.58	0.1
065P4	4.27	±	0.13	0.0851	±	0.0019	1355.9	±	36.8	1340.9	±	27.9	1317.2	±	43.2	0.76	-1.1
066P4	6.95	±	0.24	0.1266	±	0.0035	866.1	±	27.6	1274.9	±	32.5	2051.2	±	50.3	0.40	47.2
L6																	
006L6	6.17	±	0.19	0.0732	±	0.0019	968.7	±	27.0	984.6	±	25.5	1020.4	±	53.6	1.07	1.6
007L6	6.18	±	0.19	0.0731	±	0.0024	966.8	±	27.9	981.8	±	28.7	1015.4	±	68.3	0.76	1.6
009L6	4.28	±	0.14	0.1743	±	0.0049	1353.2	±	40.4	1918.4	±	37.8	2599.8	±	47.5	0.59	41.8
010L6	6.22	±	0.23	0.0725	±	0.0035	961.7	±	33.1	973.7	±	38.9	1001.1	±	100.6	0.81	1.2
011L6	6.27	±	0.23	0.0752	±	0.0026	953.7	±	32.0	990.4	±	32.1	1072.7	±	69.8	1.34	3.8
012L6	6.50	±	0.20	0.0764	±	0.0037	923.0	±	26.7	978.4	±	37.1	1105.0	±	101.2	0.87	6.0
013L6	6.26	±	0.22	0.0726	±	0.0033	954.8	±	31.1	969.3	±	36.9	1002.4	±	96.3	0.74	1.5

017L6	6.26	±	0.25	0.0729	±	0.0038	955.4	±	35.6	972.6	±	42.2	1011.5	±	109.2	0.68	1.8
018L6	6.12	±	0.18	0.0699	±	0.0022	975.0	±	27.2	960.1	±	27.7	926.2	±	67.1	0.97	-1.5
019L6	6.28	±	0.19	0.0715	±	0.0024	952.4	±	27.5	958.6	±	28.3	972.8	±	68.8	0.95	0.7
020L6	6.21	±	0.23	0.0711	±	0.0034	962.2	±	33.2	961.7	±	38.6	960.6	±	101.3	0.70	-0.1
021L6	6.29	±	0.18	0.0715	±	0.0026	950.6	±	24.8	956.5	±	28.9	970.3	±	77.3	0.85	0.6
022L6	6.10	±	0.19	0.0737	±	0.0026	978.0	±	28.2	995.5	±	30.3	1034.4	±	72.4	0.91	1.8
023L6	6.29	±	0.20	0.0740	±	0.0025	950.8	±	28.4	978.2	±	29.9	1040.2	±	70.2	1.08	2.9
027L6	6.03	±	0.19	0.0724	±	0.0018	989.9	±	29.4	992.2	±	26.3	997.5	±	51.6	1.35	0.2
028L6	6.17	±	0.19	0.0721	±	0.0020	968.1	±	27.0	974.0	±	26.0	987.4	±	58.0	1.07	0.6
029L6	6.09	±	0.18	0.0720	±	0.0020	979.4	±	27.3	981.6	±	26.1	986.4	±	58.1	0.88	0.2
030L6	6.24	±	0.21	0.0732	±	0.0030	958.8	±	29.5	977.7	±	33.8	1020.2	±	85.3	0.98	2.0
031L6	6.06	±	0.20	0.0744	±	0.0019	984.6	±	30.2	1005.9	±	26.5	1052.8	±	51.2	1.22	2.2
032L6	6.12	±	0.20	0.0725	±	0.0024	975.6	±	29.9	982.7	±	30.0	998.6	±	68.5	1.00	0.7
033L6	5.90	±	0.22	0.0695	±	0.0038	1009.4	±	34.7	979.3	±	42.3	912.5	±	117.5	0.77	-3.0
The degree of discordance (Disc. %) is defined as [(^{207}Pb*/^{235}U age) / (^{206}Pb*/^{238}U age) -1] × 100 (%)																	

CHAPTER- 7

PETROGENESIS OF THE GRANITOID ROCKS OF RAGHUNATHPUR-BERO AREA AND JHALDA AREA OF CGGC

7.1. GRANITOIDS OF RAGHUNATHPUR AREA

7.1.1. PROBABLE SOURCE ROCK

7.1.2. MECHANISM

7.2. GRANITOIDS OF JHALDA AREA

7.2.1. PROBABLE SOURCE ROCK

7.2.2. MECHANISM

7.3. CRYSTALLIZATION TEMPERATURE

FIGURES

Origin of granites remained a debatable topic over years among the workers. In the light of observations based on field relations, the petrologists became polarized into two thoughts, one believed in magmatic crystallization of granites which was designated as magmatists and the other school believed in metasomatic transformation which was designated as transformists.

According to Bowen (1928) and Tuttle and Bowen (1958), laboratory evidences indicated that fractionation of basaltic magma may give rise to a series of magma compositions including intermediate magmas and ultimately culminate into an acidic magma.

But according to Read (1957), extensive metasomatic transformation in pre-existing rocks may give rise to granites. Granitisation can be defined as a 'solid state metasomatic transformation of pre-existing rocks to produce granites'. The mechanism of granitisation process includes diffusion of elements through pre-existing rocks along a chemical potential gradient. These elements include K, Na, and H_2O which tends to transform the pre-existing parent rock to granites in solid state. They considered that diffusion of elements have taken place along the grain boundaries, mineral cleaveges, microfractures etc. Granitisation process can only interpret certain field relations but is not proved experimentally to be the dominant petrogenetic process for the formation of granites. Moreover, experimental evidences suggest that, diffusion in solid state is a very slow process to produce such large scale granitic bodies.

Bowen (1928), Osborne (1962) demonstrated that differentiation of mafic magmas like tholeiitic basalts fractionating in presence of water can produce granitic magmas. Mafic layered complexes give clear evidences of formation of granites from fractionation of mafic magmas. Tuttle and Bowen (1958) demonstrated that the product of the fractionating magmas comes down through the low temperature trough in Qtz-Ab-Or system to produce the granitic melt. But

large granitic batholiths would need voluminous basaltic parent magma for its formation through this process. But in most cases examples of such voluminous parent basalt magma is lacking. Another problem of this hypothesis is the room problem.

Based on the flaws of the two earlier believed hypotheses regarding the origin of granites, it appears that granites are likely to form in different ways apart from following any strict process. Apparently it is a result of partial melting of deeper source rock followed by melt segregation and emplacement at shallower levels.

Source material of granitic rocks also plays an important role in granite petrogenesis. Magmatists attempted to group the granites based on their source material. Based on the origin of the source melt from upper mantle and lower crust granites can be classified as I- and S- type respectively. I- type granites indicates its origin from igneous lineage. They are emplaced along the continental margins or in closed ocean basins along convergent plate margins. They have comparatively lower Al_2O_3 / (Na_2O+K_2O+CaO) ratio. $^{87}Sr/^{86}Sr$ ratio is variable which suggests that they are derived from mantle followed by assimilation of lower crustal rocks. They are poor in quartz and high in biotite content leading to higher Fe_2O_3 / FeO ratio with magnetite as the common oxide phase.

On the other hand, S- type granites indicate its origin from older meta-sedimentary rocks of lower crust. They are considered to form in the low-mid crustal zones. They are peraluminous in nature with garnet, sillimanite, cordierite etc derived from older metamorphic assemblages. $^{87}Sr/^{86}Sr$ ratio in S- type granites indicates its origin from crustal sources with little or no contribution of mantle derived melt.

Based on the emplacement of granites with respect to time and orogenesis, granites can be classified as A- type and M- type. Post-orogenic or anorogenic granites are designated as A- type granites. High $^{87}Sr/^{86}Sr$ ratio indicates its residence and evolution within the crust. M-type granites are localized in oceanic island arc and represents volcanic arc granites. Low $^{87}Sr/^{86}Sr$ ratio indicates initial mantle source.

This chapter deals with the probable source rock of the granitoids of both Rahgunathpur area and Jhalda area. An attempt has been made to identify the probable mechanism of their formation whether partial melting or fractional crystallization. Quantification of this process has been made by trace element modeling.

7.1. Granitoids of Raghunathpur area:

7.1.1. Probable source rock

The granitoid rocks of the Raghunathpur area of CGGC are ferroan, peraluminous and S-type in nature, which have chemical affinity towards arc granitoid. They are rich in biotite and among them GGG is rich in garnet. Parent magmas of S-type granitic rocks are usually produced by partial melting of metasedimentary host rocks, namely metapellite and metagreywacke, under water-unsaturated conditions (e.g., Vielzeuf and Holloway, 1988; Patino Douce and Harris, 1998; Zhang et al., 2004; Guo and Wilson, 2012; Wang et al., 2012). The origin of the biotite-garnet-bearing granites is attributed to the anatectic melting of khondalite metamorphic sediments during high-grade regional metamorphism reported from the cratons of northern China (Lu et al., 1996). In the current study area, khondalite has been found near the Ramchandrapur-Ledason area, with well-preserved bedding (characterized by alternating layers of quartz feldspar and garnet-sillimanite) with bedding parallel schistosity with east-west strike and northerly dip.

In the area north of Ledason, khondalite has been found metamorphosed to migmatite, well exposed on the quarry faces. Khondalite was the only high-grade metasedimentary rock found in abundance in the study area. All other high-grade metamorphic protoliths present in the study area (e.g., charnokites, pyroxene granulites, amphibolites) were meta-igneous rocks in nature. Therefore, partial melting of khondalite can be considered as a possible mechanism for the formation of S-type granites in CGGCs.

7.1.2. Mechanism:

Quantification of partial melting processes is considered an important aspect in petrogenetic studies. This can be done using robust petrogenetic modeling/trace elemental modeling. In such modeling, the modal mineral composition and chemical composition of putative sources are the main requirements, along with the elemental mineral-melt partition coefficients (KD) (Table 7.1) and varying degrees of partial melting (F). The chemical composition of the obtained melt is compared with that of the studied GGG. For petrogenetic modeling, REEs are considered as a potentially and efficient group of elements that remain highly incompatible and immobile during weathering, metamorphism and hydrothermal alteration. Rare earth elements are also very sensitive to magmatic processes such as partial melting and fractional crystallization. Four khondalite samples from the Ramchandrapur area were analysed from Bureau Veritus Canada Commodities Ltd. They were analyzed to determine the abundance of major and trace elements. This chemical data was used to gain ideas about petrogenetic processes The modal mineralogy of these four khondalite samples was also measured and the modal data are as follows: 50% quartz, 8% plagioclase feldspar, 15% alkali feldspar, 10% biotite, 2% garnet and 15% ilmenite. There are two types of partial melting: equilibrium batch melting and Rayleigh melting. In Rayleigh melting, the melt fraction is removed as soon as it is formed, which is unrealistic for silicate

melts owing to their higher viscosity. In equilibrium batch melting, the melt fraction starts moving upwards only after reaching a certain volume. This is more realistic for silicate melts. A viscous silicate melt can only move beyond a certain volume. Therefore, equilibrium batch melting is considered as a possible process of magma generation. The batch melting equation of Shaw, (1970) which has been used is as follows-

$C_i^L / C_i^O = 1/ D_i^{O/L}(1-F) +F$

Where, C_i^L = concentration of element i in the melt C_i^O = concentration of element i in original rock $D_i^{O/L}$ = bulk rock/ melt distribution coefficient of element i, and F= fraction of melt produced. To calculate the bulk distribution coefficients of the REEs in different constituent minerals of khondalite, standard density data (Index of /data : http://www.webmineral.com/data/) and mineral/melt partition coefficients (GERM Partition Coefficient (K D) Database -- https://earthref.org/KDD/) are utilized. The REE of the resulting melts were modelled for F= 0.1, 0.2, 0.3 and 0.5. The REE abundances of the calculated melt were compared with the REE plots of the GGG granitoids in the chondrite-normalized REE diagram. The possibility of equilibrium batch melting of 10% of the source rock was ruled out after field observations, as only 10% melting cannot produce such extensive granitoid plutons. However, at F=0.25 and 0.30, the inferred melting showed patterns and levels of rare earth enrichment similar to those of the GGG granitoids (Fig. 7.1). Thus 25-30% equilibrium batch melting of khondalites have the potential to produce GGG parent magma.

7.2. Granitoids of Jhalda area:

The petrogenesis of alkaline granite is still a controversial topic in igneous petrology because of their diverse geochemical compositions. The main petrological models proposed by various

researchers include: (a) partial melting of quartzo-feldspathic crustal rocks; (b) differentiation of alkaline basaltic magmas and (c) a combination of the two models in which differentiated basaltic magmas assimilate crustal rocks.

Fractional crystallization of a mafic magma would result in a melt with a wide range of SiO_2wt % (40–75 wt%). The mafic and felsic variants thus formed are generally spatially associated with the main granitoid body. But the AR granitoids have high and restricted silica content (72–76 wt%). The restricted nature of SiO_2 content and absence of nearby mafic and intermediate felsic rock variants goes against fractional crystallization of a basaltic magma as a probable mechanism of petrogenesis (Martin, 2006). As shown by the bi-axial variation diagram with major oxides (Harker diagrams) do not show very clear linear trends of variation for the AR granitoids, indicating that fractional crystallization does not plays a dominant role in the evolution of the AR granitoids (Cai et al., 2017). Felsic magmas formed by fractionation of mafic magmas are generally deficient in zirconium content. But the high Zr content of AR granitoids (941–1389 ppm) possibly rules out the possibility of formation of AR granite of present study through fractional crystallization of alkali basalt magma and strongly supports its crustal origin. Low MgO and Ni content of AR granitoids possibly reflect partial melting of crustal rocks as a possible mechanism of formation of alkaline granitic melt. AR granitoids do not contain any xenoliths and xenocrysts which are commonly found in A-type granites which may be attributed to the high viscosities (due to high SiO_2 content) of the parent magma of AR granitoids rather than as evidence against crustal contamination (Martin, 2006).The A-type granites formed from mantle derived alkali basalt magma through crystal fractionation are rich in Nb than A-type granites formed from crustal source (Eby, 1990). The AR granites have much higher

concentration of Nb than mantle derived A-type granites and it has all other evidences in support of crustal origin.

7.2.1. Probable source rock:

Various petrogenetic schemes have been proposed about the source rocks of alkaline granitoids (Martin, 2006; Bonin, 2007; Zhang et al., 2007). In 1979, Loiselle and Wones suggested that alkaline granitoids formed by fractionation of mantle derived alkali basalt with or without crustal interaction. They proposed granulite facies lower crustal rocks as the crustal component which suffered a partial melting episode as studied by Barker et al. (1975). The residual model of Collins et al. (1982) suggested a residual felsic granulite as the source which remained after extraction of an I-type granite melt and such residual granulite source may alone produce alkaline granites along with its major features. But Creaser et al. (1991) suggested that previously partially melted crust could not yield the major element geochemical characteristics of alkaline granitoids. Thus the possibility of its generation from differentiation from I-type magma can be ruled out. Eby (1990) showed that alkaline granitoids can be formed from mixed sources. The high temperature nature of AR granitoids (>900°C) also suggest that they must have been generated in the lower crust with some additional heat supplied possibly by asthenospheric mantle upwelling and mafic magma underplating.

The AR granitoids are ferroan, alkalic, and peralkaline in nature. Mineralogical and geochemical features suggest that AR granitoids crystallized at a high temperature from relatively anhydrous magma. It has already been proposed from field and geochemical studies that AR granites of present study did not form from mantle derived alkali basalt magma and it has many similarities with crustally derived A-type granites. Field investigation showed that older lower crustal high grade metamorphic rocks which occur in the vicinity of Jhalda AR granite are khondalite,

charnockite and granite gneiss (frequently migmatitic). These lower crustal rocks yielded Paleoproterozoic ages (Sanyal and Sengupta, 2012) and might act as source rocks of AR granites. Crustal sources for the AR granitoids might be only a single variety of older lower crustal rock but could also be a mixture of different crustal rocks.

7.2.2. Mechanism:

In the following part an attempt has been made to identify the possible crustal source rocks of the AR granitoids through finite element trace element model. So in order to discern which of the aforementioned rock/rocks is/are more likely to represent the source material of the AR granitoid magma, selected trace element concentrations of partial melts were modelled using the batch melting equations of Shaw (1970):

$$C_i^L / C_i^O = 1/ D_i^{O/L}(1-F) +F$$

Where C_i^L= concentration of element i in the melt; C_i^O= concentration of element i in original rock; $D_i^{O/L}$= bulk rock/melt distribution coefficient of element i; and F = fraction of melt produced. Moreover, it is discussed earlier that the AR granitoids are the result of partial melting process. The lower crustal rocks which constitute the country rocks of alkaline granites of Jhalda area are garnetiferous granite gneiss (GGG), charnockite and khondalite. These are possible crustal source rocks of alkaline granites.

The trace element modelling started with charnockite singularly as the possible source for the parent melt of AR granitoids. The REE data of the melt is modelled for F= 5%, 10%, 15% and 20% (F= degree of partial melting). The REE values of the resulting melt shows a significantly lower REE concentration and relatively flat Eu trough with serrated HREE pattern when compared to that of the observed REE pattern of AR granitoids (Fig. 7.2a). In the second

attempt, khondalite is taken singularly as the possible source and the REE data of the melt is modelled for F= 5%, 10%, 15% and 20%. REE diagram shows relatively similar concentration of LREE but shows flat Eu trough along with a deep trough at Dy (Fig. 7.2b). REE data of modelled melt taking garnetiferous granite gneiss as source rock for F= 5%, 10%, 15% and 20% shows deepened Eu trough and high LREE concentration (Fig. 7.2c). It is concluded that no single crustal rock act as source for parent magma of AR granite. A combination of charnockite and GGG (mixed in varying proportions like 50%-50% or 40%-60% or 30%-70%) as the two components of the crustal source rock is considered. The calculated melt (5% to 20% partial melting) shows higher concentrations of REE and wider Eu trough than that of the AR granitoids (Fig. 7.2d). A combination of khondalite and GGG (mixed in varying proportion) is attempted then as possible source rock. The REE pattern of the calculated melt (5% to 20% partial melting) shows clear mismatch with the observed REE pattern of AR granitoids (Fig. 7.2e). In the next step the charnockite and khondalite together is considered as a combined source (two components are mixed in varying proportion). The REE pattern yields best result when the charnockite and khondalite are taken in 70%-30% proportions. The REE plot of the resulting melt shows good match with REE pattern of AR granitoids but with higher values for Eu and a trough at Dy (Fig. 7.2f). Also, the pattern of HREE in modelled melt is slightly different from that of the AR granitoids. Europium anomaly reflects the role of plagioclase feldspar in the melt. Lower amount of Eu in the AR granitoid than the modelled melt indicates possibility of fractionation of plagioclase feldspar after the partial melting process. This is also evident from the petrography of the rock; i.e. AR granitoids are devoid of plagioclase feldspar. Thus fractionation of plagioclase feldspar was carried out using the following equation:

$C_i^L / C_i^O = F^{\wedge} (D_i^{O/L}-1)$

Where C_i^L = concentration of trace element i in melt, C_i^O = concentration of trace element i in initial stage, F= fraction of melt remaining and $D_i^{O/L}$ = solid/melt partition coefficient. Fractionation of about 30% plagioclase feldspar has led to a more or less good matching of the REE pattern of modelled melt with that of the AR granitoids (Fig. 2f). So it may be concluded that both khondalite and charnockite constitute the source rock which underwent intermediate degree (5% to 20%) of partial melting followed by 30% fractionation of plagioclase feldspar to produce the parent melt of AR granitoids.

7.3. Crystallization Temperature:

A good estimate of the magmatic crystallization temperature in silica-rich systems can be gauged by employing zircon saturation thermometry (Tzr). The temperatures were calculated using zircon saturation thermometry (Tzr) of (Watson and Harrison, 1983) with the following solubility equation: $\ln D_{zircon}^{zircon/melt} = [- 3.80 – \{0.85(M-1)\}] + 12,900/T$

where $\ln D_{zircon}^{zircon/melt}$ is the zircon concentration ratio of Zr concentration (in ppm) in zircon (~496,000 ppm, Miller, Mcdowell and Mapes 2003) to zircon in saturated melt; M is a compositional factor that accounts for dependence of zircon solubility on SiO_2 and peraluminosity of the melt [measured by a factor (Na + K + 2*Ca)/(Al *Si) all in cation fraction] and T is temperature (in Kelvin). The crystallization temperatures of the granitoids of both Raghunathpur and Jhalda areas obtained using the above equations are given in a tabular form (Table 7.2).

The GGG records the highest crystallization temperature of 800-850 °C among the granitoids of Raghunathpur area. The higher crystallization temperature of GGG with S-type characters indicates its generation from meta-sedimentary protolith under water under-saturated condition through the process of partial melting (anatexis) during the peak high grade metamorphic event

at granulite facies condition (750– 850 °C and 4–6 kbar, Maji et al., 2008; > 900 °C and ~ 5–8 kbar, Sanyal and Sengupta, 2012). Low LOI data (0.59 wt %) of the GGG also supports the fact that the GGG was derived through nearly anhydrous melting of meta-sedimentary protolith at a significant depth of ~20- 30km. The second variety of granitoid, MGG, records a relatively lower crystallization temperature ~ 770-830°C. From the low crystallization temperature of MGG, it is assumed that MGG was formed by partial melting of a meta-sedimentary protolith under slightly more water saturated condition than GGG. PG shows a still lower temperature of crystallization around 639-725°C, indicating partial melting and subsequent crystallization under more water-saturated condition (high LOI: 1.04 wt %) of meta-sedimentary protolith. Thus, the condition of partial melting of meta-sedimentary protolith might have changed in terms of degree of water-saturation in these rocks.

Zircon saturation thermometry of the AR granitoids of Jhalda suggests relatively high crystallization temperature (>900°C). Higher crystallization temperature indicates its generation at water under-saturated to anhydrous condition. This is further supported by the low LOI (~0.5) of the studied granitoids.

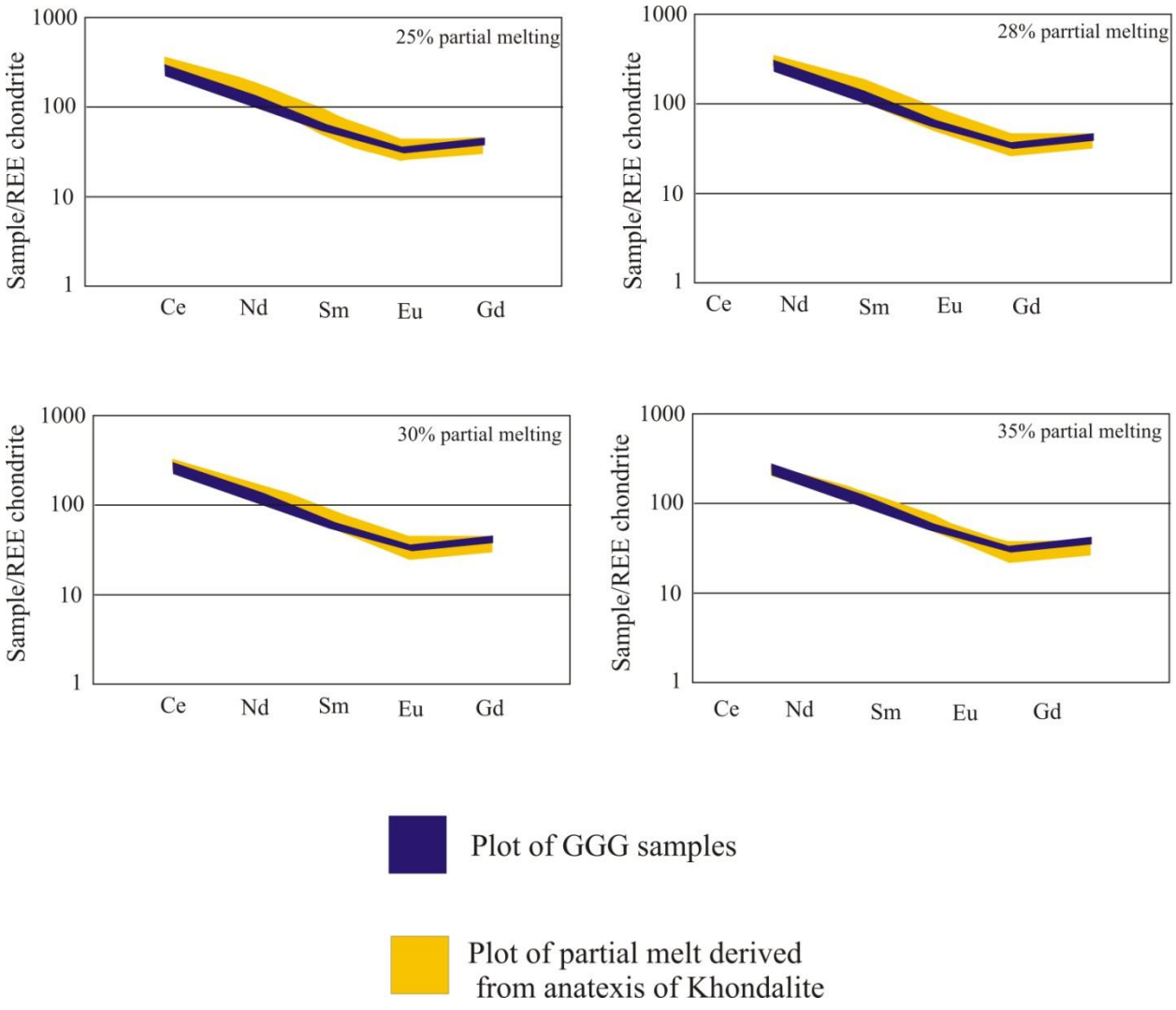

Figure.7.1. Diagram showing matching of REE pattern of granitoid rocks (GGG) with model granitic melt produced by varying degree of partial melting of khondalite.

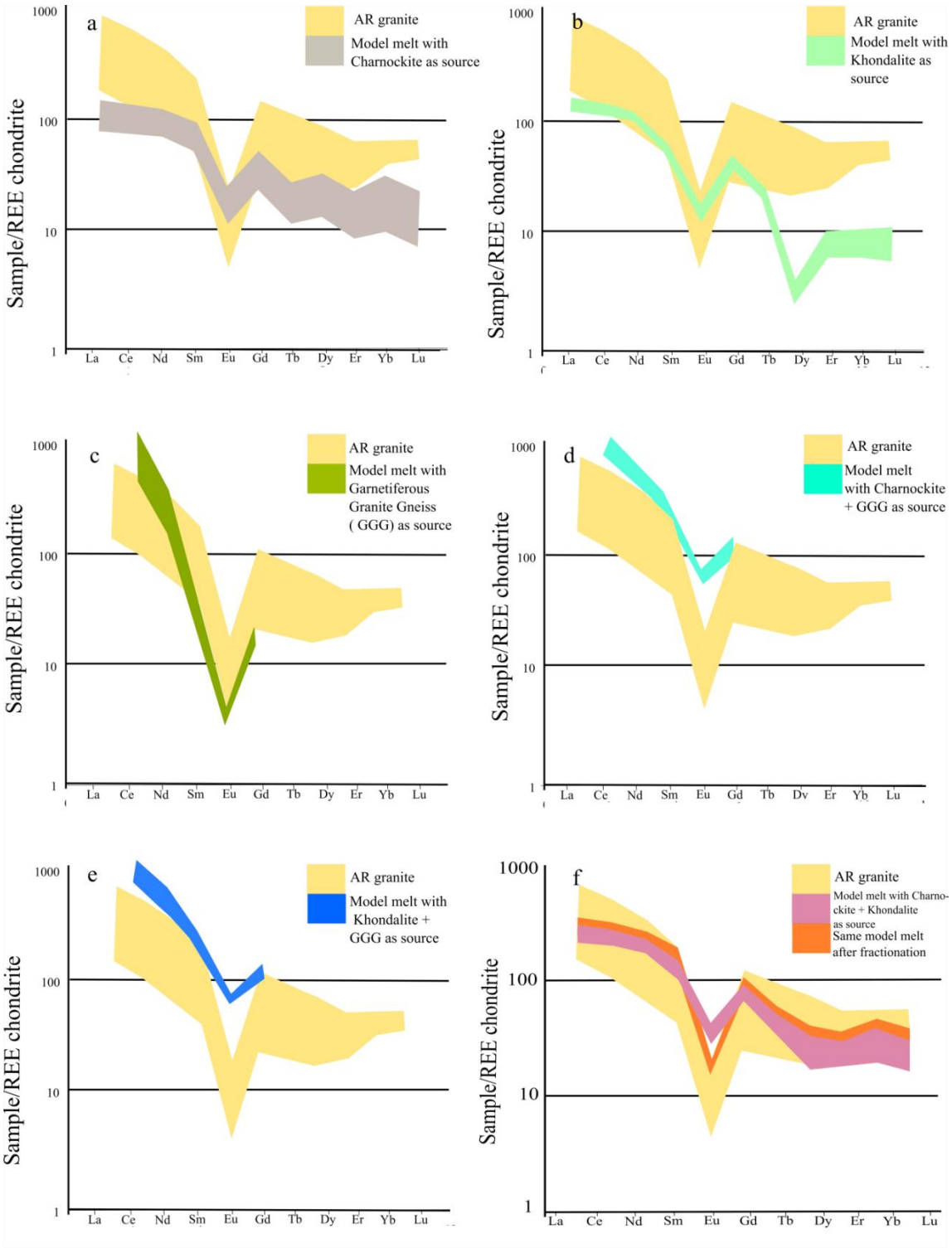

Figure.7.2. Diagram showing matching of REE pattern of the AR granitoids with that of the following modelled melts (a) 5-10% partial melting of charnockitic melt; (b)5-10% partial

melting of khondalitic melt; (c) 5-10% partial melting of garnetiferous granite gneissic melt; (d) 5-10% partial melting of charnockite + GGG melt; (e) 5-10% partial melting of khondalite + GGG melt and (f) 5-10% partial melting of charnockite + khondalite melt followed by 30% fractional crystallization of plagioclase feldspar.

Table 7.1 KD values of each element used in the REE modeling and their rock types

Elements	KD value	Element and rock type	Reference
La	4.61	plagioclase feldspar in peraluminous granite	Bea et al. 1994
La	0.06	biotite in peraluminous granite	Bea et al. 1994
La	1.01	alkali feldspar in peraluminous granite	Bea et al. 1994
La	0.27	hornblende	Winter 2010
La	0.1	garnet	Winter 2010
Ce	3.87	plagioclase feldspar in peraluminous granite	Bea et al. 1994
Ce	0.05	biotite in peraluminous granite	Bea et al. 1995
Ce	0.86	alkali feldspar in peraluminous granite	Bea et al. 1995
Ce	0.34	hornblende	Winter 2010
Ce	0.51	garnet in Rhyolite-dacite	Irving and Frey 1978
Nd	2.56	plagioclase feldspar in peraluminous granite	Bea et al. 1994
Nd	0.08	biotite in peraluminous granite	Bea et al. 1994
Nd	0.51	alkali feldspar in peraluminous granite	Bea et al. 1994
Nd	0	hornblende	Winter 2010
Nd	0.4	garnet in rhyolite	Sisson and Bacon 1992
Sm	1.45	plagioclase feldspar in peraluminous granite	Bea et al. 1994
Sm	0.392	biotite in peraluminous granite	Bea et al. 1994
Sm	0.42	alkali feldspar in peraluminous granite	Bea et al. 1994
Sm	0.91	hornblende	Winter 2010
Sm	6.4	garnet in rhyolite	Sisson and Bacon 1992
Eu	2.99	plagioclase feldspar in peraluminous granite	Bea et al. 1994
Eu	0.05	biotite in peraluminous granite	Bea et al. 1994
Eu	2.32	alkali feldspar in peraluminous granite	Bea et al. 1994
Eu	1.01	hbl	Winter 2010
Eu	1.52	garnet in dacite	Schnetzler and Philpotts 1970
Gd	2.05	plagioclase feldspar in peraluminous granite	Bea et al. 1994
Gd	0.1	biotite in peraluminous granite	Bea et al. 1994
Gd	0.6	alkali feldspar in peraluminous granite	Bea et al. 1994
Gd	1.1	hornblende	Winter 2010

Gd	3.8	garnet in dacite	Irving and Frey 1978
Tb	2.93	plagioclase feldspar in peraluminous granite	Bea et al. 1994
Tb	0.18	biotite in peraluminous granite	Bea et al. 1994
Tb	0.92	alkali feldspar in peraluminous granite	Bea et al. 1994
Tb	1.4	hornblende	Winter 2010
Tb	7.2	garnet in rhyolite	Irving and Frey 1978
Dy	0.07	plagioclase feldspar in peraluminous granite	Bea et al. 1994
Dy	0.17	biotite in peraluminous granite	Bea et al. 1994
Dy	0.77	alkali feldspar in peraluminous granite	Bea et al. 1994
Dy	0	hornblende	Winter 2010
Dy	116	garnet in rhyolite	Irving and Frey 1978
Er	1.94	plagioclase feldspar in peraluminous granite	Bea et al. 1994
Er	0.22	biotite in peraluminous granite	Bea et al. 1994
Er	1.14	alkali feldspar in peraluminous granite	Bea et al. 1994
Er	0	hornblende	Winter 2010
Er	42.8	garnet in dacite	Schnetzler and Philpotts 1970
Yb	0.82	plagioclase feldspar in peraluminous granite	Bea et al. 1994
Yb	0.12	biotite in peraluminous granite	Bea et al. 1994
Yb	0.64	alkali feldspar in peraluminous granite	Bea et al. 1994
Yb	0.97	hornblende	Winter 2010
Yb	53	garnet in andesite	Irving and Frey 1978
Lu	1.32	plagioclase feldspar in peraluminous granite	Bea et al. 1994
Lu	0.2	biotite in peraluminous granite	Bea et al. 1994
Lu	0.96	alkali feldspar in peraluminous granite	Bea et al. 1994
Lu	0.89	hornblende	Winter 2010
Lu	23.8	garnet in dacite	Irving and Frey 1978

Table 7.2 Crystallization temperatures of the granitoids of both Raghunathpur and Jhalda areas by Zircon Saturation Thermometer

Rock type	Sample number	T (degree celsius)	Thermometer used
GGG	K5	850.35	Zircon saturation thermometry (T_{zr})*
GGG	K6	816.81	Zircon saturation thermometry (T_{zr})*
GGG	K7	811.9	Zircon saturation thermometry (T_{zr})*
MGG	K1	795.23	Zircon saturation thermometry (T_{zr})*
MGG	K3	790.09	Zircon saturation thermometry (T_{zr})*
MGG	K4	801.56	Zircon saturation thermometry (T_{zr})*
MGG	AR129A	772.9	Zircon saturation thermometry (T_{zr})*
MGG	K10	831.71	Zircon saturation thermometry (T_{zr})*
PG	K2	706.9	Zircon saturation thermometry (T_{zr})*
PG	K8	657.59	Zircon saturation thermometry (T_{zr})*
PG	K9	641.64	Zircon saturation thermometry (T_{zr})*
PG	AR119B1	639.45	Zircon saturation thermometry (T_{zr})*
PG	AR127B	721.43	Zircon saturation thermometry (T_{zr})*
PG	ARL7	725.7	Zircon saturation thermometry (T_{zr})*
AR	P1	1026.27	Zircon saturation thermometry (T_{zr})*
AR	P2	986.36	Zircon saturation thermometry (T_{zr})*

AR	P3	1006.57	Zircon saturation thermometry (T_{zr})*
AR	P4	1042.37	Zircon saturation thermometry (T_{zr})*
AR	P5	1004.06	Zircon saturation thermometry (T_{zr})*
AR	P6	1023.53	Zircon saturation thermometry (T_{zr})*
AR	P7	1036.76	Zircon saturation thermometry (T_{zr})*
AR	P8	1013.42	Zircon saturation thermometry (T_{zr})*
AR	P9	1031.23	Zircon saturation thermometry (T_{zr})*

CHAPTER-8

DISCUSSION AND CONCLUSION

8.1. COMPARATIVE STUDY OF GRANITOID ROCKS OF RAGHUNATHPUR-BERO AREA AND JHALDA AREA

8.2. GRANITOID ROCKS OF RAGHUNATHPUR-BERO AREA AND JHALDA AREA IN RELATION TO RODINIA SUPERCONTINENT CYCLES

8.3. PETROTECTONIC MODEL ON EVOLUTION OF GRANITOIDS OF RAGHUNATHPUR-BERO AREA AND JHALDA AREA ALONG NPSZ

FIGURES

TABLES

8.1. Comparative study of granitoid types of Raghunathpur area and Jhalda area:

The granitic rocks of the two study areas show contrasting characters in terms of petrography, mineralogy, geochemistry, geochronology and tectonic setting. The comparisons of the granitoid varieties are summed up in Table. 8.1.

Among the three varieties of granites of Raghunathpur-Bero area, Megacrystalline granite gneiss (MGG) was the most abundant variety in the areathat was found intrusive in to the garnet granite gneiss (GGG). Garnet-bearing granite gneiss (GGG) was found in close association with migmatite. Extensive outcrops of the MGG have been observed along the western part of the migmatite quarry. At places, MGGs occurred as intrusive veins within migmatite bodies. They were generally exposed as a series of low lying mounds forming bald-headed mounds to low lying chattans. Megacrystic granites and pink granites (PGs) are oriented east-west parallel to the NPSZ, showing evidence of intense shearing. Pink granite (PG) appeared as thin (2–5 mm) to thick (~24 cm) lenses.

The aegirine-riebeckite-arfvedsonite granite of Jhalda, occurs as E-W elongated isolated lensoid mounds within the migmatitic country rock in the Dimra region and Perehandopahar region of Jhalda. Perehando Pahar is composed totally of the aegirine-riebeckite granite gneiss and is flanked by mica schists to the northwest, calc-silicate gneiss to the east, and brecciated-limonitised-silicified quartzite to the south. In the western and central part of the Dimra peralkaline body which typically strikes NE-SW, enclaves of mica schist and quartz schists can be observed.

MGG is strongly porphyritic/megacrystic and consists of alkali feldspar, quartz, plagioclase feldspar with minor amount of biotite, amphibole and opaque. Gneissosity of the

rock is mainly defined by the clusters of biotite laths. Alkali feldspar occurred both as phenocryst/megacryst and as groundmass. Large, rectangular, elliptical, rounded (sometimes altered) phenocrysts of alkali feldspar along with plagioclase feldspar and quartz occurred within the fine-medium grained groundmass consisting of quartz, alkali feldspar, plagioclase feldspar, biotite, amphibole and opaque minerals. Foliation was defined by alignment of biotite and also by alignment of extremely stretched alkali feldspar grains. Quartz occurs as elongate, lenticular grains and deformed or warped crystals around microcline grains. Amphibole (yellowish green to brownish green to dark green) was relatively rare and occurred as small, subhedral grains associated with biotite forming clusters. The accessory minerals like Sphene (weakly pleochroic from pale brown to reddish brown), apatite, opaque (commonly ilmenite), epidote, allanite, zircon, rutile, muscovite and chlorite are intimately associated with biotite-hornblende-rich layers. Zircon when present, occur in trace amount as subidiomorphic to idiomorphic grains within the quartzo-feldspathic mass. Pink granites are leucocratic, equigranular, medium grained rock which consists of alkali feldspar, quartz, plagioclase feldspar, biotite as major mineral constituents and apatite and opaques as minor constituents. Alkali feldspar grains occurred mainly as phenocrysts and were also present in the fine-medium grained groundmass. The alkali feldspar grains in the groundmass were very fine, rounded and subhedral. The abundance of the alkali feldspar grains in the groundmass was typically high. Quartz occurred less in abundance than alkali feldspar. They were typically elongated – lenticular in shape (ribbon like) due to shearing, had subhedral appearance and were present as coarse flattened grains. Biotite grains were small, elongated, subhedral to euhedral in nature. Apatite grains were rounded, somewhat drop like appearance and were present in a significant amount. GGG is leuco-mesocratic in nature; medium grained which composed of quartz, alkali-feldspar, plagioclase feldspar, garnet

and biotite as major minerals and opaque minerals and zircons as accessory phases. Quartz grains occurred as medium to coarse grained subhedral phenocrysts. At places they occur as small, anhedral grains in the groundmass. Alkali feldspar grains occurred mostly as large, subhedral grains (phenocrysts) and as small, anhedral grains in the groundmass. Plagioclase feldspar grains of GGG were medium sized, anhedral and relatively rounded. At places, bending in the twin lamellae of plagioclase feldspars was noticed. Garnet occurred as medium to large sized, subhedral, rounded, fractured grains within the groundmass made up of small sized quartz grains, alkali feldspar, plagioclase feldspar, biotite and opaques.

The peralkaline granitoids (AR granitoids) of Jhalda area show a general hypidiomorphic granular texture and the primary minerals present are quartz, alkali feldspar, alkali pyroxene (aegirine), alkali amphibole (riebeckite, arfvedsonite) and biotite. The accessory minerals are zircon, plagioclase, sphene, ilmenite, and allanite. Quartz occur as medium sized, irregular, lensoidal, unaltered grains and appear at some places next to perthite grains. Undulose extinctions are common. Alkali feldspar (modal value varies from 42% to 44%) occurs as elongated, medium sized subhedral grains present in association with quartz and other mafic minerals. Plagioclase (modal value up to 3%) occurs as occasional phases in this granitoid variety. Pyroxene grains (modal value up to 4%) occur as large elongated prismatic grains showing pleochroism in shades of green and pinkish brown and identified as aegirine. The amphiboles (modal value up to 2%) are typically long prismatic and occasionally occur as thin laths with euhedral boundaries. Pyroxene, amphibole grains are intimately associated and strongly oriented defining a weak gneissosity. Biotites (modal value up to 2%) are characterized by green to brown pleochroism. The gneissic texture of the peralkaline granites of the Jhalda area

is defined by alternate bands of thinner ferro-magnesian minerals and relatively thicker quartzo-feldspathic minerals.

SiO_2 (wt %) content of GGG, MGG and PG ranges from 55%-73%, 64%-66% and 75%-79%, respectively. Molecular ASI (Alumina saturation index, ASI = Al / (Ca-1.67P+Na+K) in molecular basis) and AI (Agpaitic index, AI = Al-(Na+K) in molecular basis) vary between 0.93 – 0.97, 0.90-1.06, 1.09 –1.13 and 1.30 –1.44, 1.09-1.20, 1.40-1.90, respectively in the MGG, PG and GGG of the CGGC granitoids. The CaO content of MGG is relatively higher (2.2-3.2 wt %) than the other two types of granitoid (1.4-2.9 wt % in GGG and 0.6-1.9 wt % in PG). The GGG is relatively less enriched in Total Alkali (Na_2O+K_2O) content (4.9-7.1) than the other two types (8.2-9.3 in MGG and 8.06-9.2 in PG). They can be classified as ferroan, peraluminous, sub-alkaline, high - K calc-alkaline to shoshonitic and syn-collisional in nature. The multi-element primitive mantle normalized spider diagram of CGGC granitoids (primitive mantle data from McDonough and Sun, 1995) reveal a strong enrichment in more incompatible elements (Cs, Ba, Rb, Th, U) compared to less incompatible elements (Ti, Y, Yb, Lu, Sr, Nb). They show significant negative anomalies at Ba, Nb, Ta, Sr, and positive anomalies at Rb, Th, U. REE patterns of the CGGC granitoids in the chondrite-normalized diagrams (Chondrite data from Boynton, 1984) show enrichment of light rare earth elements (LREE: La-Nd). Moderately negative Eu anomalies are shown by the granitoid rocks in the chondrite normalized REE diagram. Eu anomalies are measured by Eu/Eu* and it varies from 0.39-0.99 (in GGG), 0.57-0.89 (in MGG) and 0.29-0.59 (in PG). They plot in the Volcanic Arc Granite and Syn-COLG fields when plotted in the (Y+Nb) versus Rb diagram, Y versus Nb diagram, (Ta+Yb) versus Rb diagram and Ta versus Yb.

AR granitoids are enriched in silica content (SiO_2 ranges from 75.3–76.2 wt %) and alkali content (K_2O= 4.31–4.98 wt%; Na_2O= 3.07–4.07 wt%; Na_2O+K_2O = 8.35–8.86 wt %). They show low values of CaO (0.02–0.04 wt %), Al_2O_3 (10.6–11.3 wt %), FeO_t (2.6–3.6 wt %), MgO (0.03–0.04 wt %) content, relatively higher FeO*/MgO ratios (65.7–102.5) and low Mg number. The Fe# numbers are ≥ 0.96 and ranges between 0.96 and 0.99, while molecular ASI and AI (Agpaitic Index) indices vary between 0.83-0.86 and 1.03-1.06 respectively. They can be classified as ferroan, peralkaline, post-orogenic-late-orogenic alkali granites. In the multi-element primitive mantle normalized spider diagram (primitive mantle data from McDonough and Sun, 1995), AR granitoids show enrichment in Rb, Y, Th and U and High Field Strength Elements (HFSE) (Nb, Ta, Zr, Hf) and depletion in Sr, Ba, P and Ti which are typical of alkaline granites (Collins 1982, Whalen 1987). AR granitoids are characterized by high Zr+Nb+Ce+Y concentrations (1150–1743 ppm) and high Ga/Al ratios (10000*Ga/Al = 6.7–7.8). Chondrite normalized REE patterns (Chondrite data from Boynton, 1984) show strong enrichment of LREE relative to HREE with $(La/Yb)_N$ ratio of 3.72–12. Eu shows strong negative anomalies in the Chondrite normalized REE diagram (Eu/Eu*= 0.12–0.14). They plot as within-plate granite according to the (Y+Nb) versus Rb, Nb versus Y, (Ta+Yb) versus Rb and Ta versus Yb diagrams (after Pearce et al. 1984). In the discrimination diagrams for alkaline granites by Whalen et al. (1987), the AR granitoids fall in the A-type granite field.

Geochronological analysis of the zircon grains of PG shows that the majority of the grains was subhedral and elongated in shape with an aspect ratio of ~3:1 (length ~150µm and breadth ~50 µm). Most of the grains contain a homogenous darker-CL core, which graded outward in to a brighter-CL rim. Th/U ratio of these zircon grains ranged between 0.34 and 0.06. Five near concordant age data yielded a single-population weighted mean age as 1.06 ± 0.03 Ga

($^{207}Pb/^{206}Pb$ age with MSWD = 1.3 and probability = 0.25).Zircon grains of MGG were subhedral and elongated in shape, but of variable sizes (length ~200-80 µm and breadth ~50-20 µm). Th/U ratio varied from1.81 to 0.17. Eighteen near-concordant isotopic data defined a single-population weighted average 207Pb/206Pb age as 9.98±0.01 Ga [n=17 (one data has been rejected during statistical data plotting) with MSWD = 2.3 and probability = 0.003). Monazite grains of GGG shows that they are sub-rounded with the diameter ranged between ~50 and ~30 µm. The oldest spot age recorded from this rock as 1.03±0.02 Ga, whereas the youngest spot date recorded as 0.94±0.03 Ga. Probability density plot of all data points yielded two very closely-spaced peaks at ~0.98 Ga and ~1.01 Ga.

The zircon grains of alkali granites are relatively elongated and subhedral in nature with rounded outlines. Almost all of these grains display oscillatory zoning as well, and some grains show oscillatory to patchy-zoned core. Length to width ratio is ~ 4:1 indicating relatively high crystallization rate. $^{207}Pb/^{206}Pb$ ages that from dark homogeneous core and oscillatory zoned mantle parts range from ca. 1298 to 1361 Ma, and their weighted average yields an age of 1328 ± 13 Ma (2σ, MSWD = 0.42). Th/U ratio ranges between 0.34 and 0.77. On the other hand, the data from bright rim part are almost discordant except only one concordant data that shows the spot $^{207}Pb/^{206}Pb$ age of 1103 ± 97 Ma and Th/U ratio of 0.27.$^{206}Pb/^{238}U$ ages from oscillatory mantle parts, range from ca. 951 to 990 Ma, and their weighted average yields an age of 966.7 ± 7.0 Ma (2σ, MSWD = 0.73).

8.2. Granitoid rocks of Raghunathpur-Bero area and Jhalda area in relation to Rodinia supercontinent cycle:

During the Earth's evolution, continents were assembled into supercontinents, broken apart and re -assembled several times to form supercontinents like Columbia (2.1 –1.8 Ga), Rodinia (1100 –750 Ma) and Pangaea (350 –165 Ma) (Hoffman, 1991; Moores, 1991; Dalziel, 1995; Park et al., 1995; Rogers and Santosh, 2004; Li et al., 1999, 2004, 2008 a; Nance et al., 2014; Meert and Santosh, 2017). Rodinia was a Neoproterozoic supercontinent that has been considered to have assembled 1.1–0.9 billion years ago and broke up 750–633 million years ago. It was renamed 'Rodinia' by McMenamin & McMenamin 1990 who first proposed a temporal framework for Rodinia. Rodinia formed at about 1.23 Ga by accretion and collision of parts produced by breakup of an older supercontinent, Columbia, known to be assembled during 2.0–1.8 Ga collisional events. The Grenville belt of eastern North America, long recognized as a collisional orogen (Dewey and Burke, 1973), and its age-correlatives in the Amazon (Sunsas belt), Congo (Irumide and Kibaran belts) and Kalahari (Namaqua–Natal belt) cratons, were interpreted to reflect the amalgamation of Rodinia, whereas the Neoproterozoic passive margin sequences that surrounded Laurentia reflected its breakup and dispersal (Hoffman, 1991). According to Evans (2009), the pattern of supercontinental transition involved large-scale dextral motion of West Africa and Amazonia, and sinistral motion plus rotation of Kalahari, Australia, India and South China.

Many alternative reconstructions have been proposed for the configuration of the cratons in this supercontinent. Mostly these reconstructions are based on the correlation of different orogens on the constituting cratons. Most reconstructions shows that the core of the Rodinia supercontinent was formed by the North American craton (the

later paleocontinent of Laurentia), surrounded in the southeast with the East European craton (the later paleocontinent of Baltica), the Amazonian craton ("Amazonia") and the West African craton; in the south with the Río de la Plata and São Francisco cratons; in the southwest with the Congo and Kalahari cratons; and in the northeast with Australia, India and eastern Antarctica. The positions of Siberia and North and South China, north of the North American craton differ strongly depending on the reconstruction (Li et al., 2008; Torsvik 2003; Weil 1998):

- SWEAT-Configuration (Southwest US-East Antarctica craton): Antarctica is on the Southwest of Laurentia and Australia is at the North of Antarctica (Moores et al., 1991).
- AUSWUS-Configuration (Australia-western US): Australia is at the West of Laurentia.
- AUSMEX-Configuration (Australia-Mexico): Australia is at the location of current day Mexico relative to Laurentia.
- The "Missing-link" model by Li et al. 2008 which has South China between Australia and the west coast of Laurentia (Li et al., 2008). A revised "Missing-link" model is proposed in which Tarim Block serves as an extended or alternative missing-link between Australia and Laurentia (Wen et al., 2017)
- Siberia attached to the western US (via the Belt Supergroup)
- Rodinia of Scotese (Schotese 2009; Torsvik et al., 2008)

In 2009 UNESCO's IGCP project 440, named 'Rodinia Assembly and Breakup', concluded that Rodinia broke up in four stages between 825 and 550 Ma (Bogdanova et al., 2009):

- The breakup was initiated by a superplume around 825–800 Ma whose influence—such as crustal arching, intense bimodal magmatism, and accumulation of thick rift-type sedimentary successions—have been recorded in South Australia, South China, Tarim, Kalahari, India, and the Arabian-Nubian Craton.

- Rifting progressed in the same cratons 800–750 Ma and spread into Laurentia and perhaps Siberia. India (including Madagascar) and the Congo-Säo Francisco Craton were either detached from Rodinia during this period or simply never were part of the supercontinent.

- As the central part of Rodinia reached the Equator around 750–700 Ma, a new pulse of magmatism and rifting continued the disassembly in western Kalahari, West Australia, South China, Tarim, and most margins of Laurentia.

- 650–550 Ma several events coincided: the opening of the Iapetus Ocean; the closure of the Braziliano, Adamastor, and Mozambique oceans; and the Pan-African orogeny. The result was the formation of Gondwana.

Rodinia Supercontinent cycle is marked by evolution of varied types of magmatic rocks from India, Australia, Antarctica, South China, and South Africa (Table.8.2.). Magmatic rocks have both alkaline-anorogenic and calc-alkaline-orogenic affinity. Imprints of Rodinia tectonics are well documented from the CITZ (Lippolt and Hautmann, 1995), ADFB (Buick et al., 2006; Bhowmik et al., 2010; Deb et al., 2001), EGMB (Chatterjee et al., 2010), CGGC (Maji et al., 2008; Sanyal and Sengupta, 2012; Chatterjee et al., 2010; present study) and SMGC (Chatterjee, et al., 2007) of India; Albany-Fraser hills of Australia; Bunger Hills of East Antarctica (both referred in Harris 1995); Yangtze block of South China (Zhou et al., 2002); Grenville province

of Laurentia (Kalsbeek, et al., 2008); Sunsas Orogen and Putumayo orogen of Amazonia (Rizzotto et al., 2014; Fig. 8.1.). The granulite gneiss complexes of the CITZ, CGGC, SPGC and EGMB preserve key evidences of tectonic activity/movement during late Mesoproterozoic-early Neoproterozoic time period. Subsequent high-grade Grenvillian metamorphism recorded in monazite grains at 1.04±0.01 Ga in the garnet-cordierite migmatite of northern Sausar belt, xenotime growth at 0.97 ± 0.06 Ga in northwestern CGGC granite gneiss, zircon growth at 0.94 ± 0.02 Ma in Bengal Anorthosite, and monazite growth at 0.99-0.95 Ga in northeastern CGGC metapelite granulite indicate an Early Neoproterozoic terminal collision between the south Indian and north Indian block. This event is coeval with the collision between the EGMB and Rayner Complex of East Antarctica, and emplacement of the Chilka Lake Anorthosite in northeastern EGMB at 0.98 Ga. All these Early Neoproterozoic (0.98-0.94 Ga) events may be temporally correlated with the assembly of Rodinia (Chatterjee et al., 2010 and references therein). In the present study, we obtained monazite ages of 1.0 Ga for the high grade metamorphism (M3) of CGGC metapelites and 1.0 Ga age of S-type granitoids from Raghunathpur-Bero area of CGGC. S-type granites are considered as a definite evidence of existence of collisional orogen (Frost and Frost 2013).

Occurrences of alkaline rocks of Proterozoic age in India are well reported from the works of Santosh et al., 1989; Natarajan et al., 1994; Kumar et al., 1998; Upadhyay et al., 2006a, b; Upadhyay 2008; Renjith et al., 2014; Chakraborty et al., 2016; Hippe et al., 2016; Ackerman et al., 2017; Das et al., 2018; Ranjan et al., 2018; Paul et al., 2020 etc. Alkaline rocks are mainly reported from the western part (Rajasthan), eastern part (West Bengal and Odisha) and southern part (Tamil Nadu and Kerala) in India (Table. 8.3; Fig.8.2). The alkaline granites of Siwana, (Rajasthan) Malani Igneous suite yields emplacement age of 750 Ma. Splitting of Rodinia

Supercontinent at 750 Ma caused anorogenic rift magmatism which give rise to Siwana-Jalore alkaline granites. The alkaline rocks of Odisha evolved during Rodinia (950-930 Ma) age are mainly reported from Rairakhol and Koraput areas of Odisha. The Neoproterozoic alkaline rocks and carbonatites of Tamil Nadu comprises mainly of nepheline syenite, ijolite, alkali gabbro, pyroxenite, alkali granites and carbonatite. Elagiri alkaline complex contains syenite, monzonite and pyroxenite with minor carbonatite (Miyazaki et al., 2000; Renjith 2014).

Reports on the alkaline magmatism from different parts of the world during Neoproterozoic age are well documented by the works of Li et al., (2002); Upadhyay et al., (2008); Wang et al., (2003a) etc. The alkaline rocks of Neoproterozoic age from India can be correlated with that of the alkaline rocks of Australia, Lauretia, Madagascar, South Africa, South China etc (Table.8.4; Fig. 8.3.). The giant plume driven mafic magmatism in the world during 825-760 Ma (Li et al., 2008) can be well documented by Amata dolerite dyke swarm, Gairdner dyke swarm, Little Broken Hill in Australia. Post 825 Ma magmatism is represented in Australia by the Mundine Well dyke swarm in Western Australia (Wingate and Giddings, 2000). Little Dal quartz diorite in Mackenzie mountain (after Jefferson and Parrish, 1989) records the post 800 Ma magmatism in western Lauretia which matches the 780 Ma magmatism event in Australia and South China. A relatively similar alkali granite sample (both in age and composition) is reported from Sor Rondane Mountains, Antarctica. This A-type granite of Antarctica comprises a part of the post-subduction magmatic activity (960-925 Ma, Elburg et al., 2014). The alkaline A-type granite of Jhalda area (966.7 ± 7.0 Ma) of NPSZ which evolved during late/post orogenic stage in CGGC and is associated with orogenic calc-alkaline granitoids might have a link with Rodinia break up because all along NPSZ fesic magmatic rocks and a few mafic intrusives have been

reported in the time span of 1.0 to 0.9 Ga (Das et al., 2018, Chakraborty et al., 2018) have possible connection with Rodinia Supercontinent cycle.

8.3. Petrotectonic Model on evolution of granitoid rocks of Raghunathpur-Bero area and Jhalda area along NPSZ:

Geochemistries of basalts, granitoids are used as effective indicators of tectonic setting. This indicator along with other indicators like sedimentary rock association, nature of deformation provides valuable clues to identify ancient unknown tectonic setting. Geochemistry of magmatic rocks become especially important paleotectonic study for the older terrains where weathering, erosion obliterated sedimentary rock records. There are many areas, where granitoid rocks are the only exposed plutonic rocks present as products of a magmatic event. Granites received less attention as tectonic indicators than basalts because of the following: difficulty of sampling granites of known setting because evidence for the tectonic setting at the time of intrusion is often difficult to obtain by the time they are exposed at the surface; complicated petrogenetic history of granites, which can make their chemical compositions difficult to interpret: crystal accumulation, involvement of continental crust, redistribution and loss of elements by volatile fluxing and crystallization of trace element-rich minor phases are generally of little relevance to basalt genesis yet can obscure the important geochemical features of granites (Hanson, 1978).

With the advent of modern geochemical methods, it was recognized that there is a relationship between the composition of granite and tectonic setting (Pearce et al., 1984; Maniar and Piccoli, 1989; Bonin, 1990; Barbarin, 1999). Consequently, nomenclature of granitic rocks rapidly expanded and no fewer than 30 classification schemes have been developed (e.g., Streckeisen, 1976; Pearce et al., 1984; Maniar and Piccoli, 1989; Barbarin, 1999; Frost et al., 2001).

Classification of granites is based on a number of factors including mineralogy, petrology, and geochemistry, leading to the creation of the widely used but petrogenetically linked 'letter based' (e.g., I-type granites (I = igneous); S-type granites (S = sedimentary); M-type granites products of mantle melts (M = mantle) and A-type (A = anorogenic) (Chappell et al., 1974) A type granites were referred as alkaline or anorogenic granites (Loiselle and Wones 1979) classification scheme (Chappell and White, 1974; Loiselle and Wones, 1979; White, 1979). Non-genetic classification schemes based on major element geochemistry are also used, and have the advantage of not being interpretive (Frost et al., 2001; Frost and Frost, 2011). The scientific benefits of granite classification are clear, but the debate around their application continues and new methods of classification are frequently proposed (c.f, Glazner et al., 2019; Bonin et al., 2020). Nevertheless, the discovery that there is a distinct correlation between the type of granite and tectonic setting presents an opportunity to extrapolate the possible geodynamic processes that operated in the past, even in regions where a complete geological record is not preserved. There is a tectono-magmatic connection, where each granite type is related to definite tectonic settings, and all magmatism is tectonically motivated, so that such a division is simply a matter of emphasis (Pitcher 1997).

Granites formed in a variety of tectonic settings around the world, either at plate margins or intraplate. They are subdivided according to their tectonic environments into four main groups—ocean ridge granites (ORG), volcanic arc granites (VAG), within plate granites (WPG) and collision granites (COLG) using trace element Y-Nb, Yb-Ta, Rb-(Y + Nb) and Rb— (Yb + Ta) diagrams (Pearce et al., 1974). Harris et al. (1986) recognized four groups of collisional zone granites: (1) Pre-collision calc-alkaline (volcanic-arc) intrusions which are mostly derived from mantle modified by a subduction component; (2) Syn-collision peraluminous intrusions

(leucogranites) which may be derived from the hydrated bases of continental thrust sheets; and (3) Late or post-collision calc-alkaline intrusions which may be derived from a mantle source but undergo extensive crustal contamination and (4) A fourth category, distinguished by Sylvester (1989), consists of Alkaline granites in post - orogenic continental settings and fall within the A - type or anorogenic category of granitoids.

Sources of magma include two proposed processes: (i) fractional crystallization of mantle - derived basic magma; and (ii) partial melting of old sialic continental crust, leading either to the formation of anatectic plutons or to the contamination of mantle - derived magmas. The Cordilleran-type granites form in arc environments are characterized by magnesian compositions dictated by early crystallization of magnetite (Frost et al., 2001). In contrast, ferroan granites are characteristic of extensional environments, where they form by partial melting or extreme differentiation of basaltic magma. Island arc granitoids (I-type granites) are produced above subduction zones, which characterized by large masses of batholiths made of diorites, quartz diorites, tonalites, granodiorites and minor granites. They are calc alkaline with small to high K contents and their initial Sr ratio $(Sr^{87}/Sr^{86})_i$ are in the range 0.704–0.705 (Nedelec et al., 2015). S-type granites in continental collision span in compositions from granodiorites to granite, peraluminous granites without magnetite. Collision - related leucogranites of the High Himalayan have high (^{87}Sr / ^{86}Sr) ratios in the range 0.743–0.762) and enriched in Rb and K but are depleted in Sr, Zr and LREE compared to Cordilleran granitoids (Harris et al., 1995). Intraplate (within plate) granites can be subdivided based on tectonic criteria into intraoceanic, intracontinental and attenuated continental lithosphere. A-type granites are commonly alkali feldspar granites or syenogranites and often associated with syenites; these granites were defined by Loiselle and Wones (1979) as alkaline or anorogenic granites. They are rich in silica and

having high contents of LILE, HFSE (Zr, Ce, Nb, Hf, Ta, etc.), REE, K and Zr, but low in trace elements compatible in mafic silicates (Co, Sc, Cr, Ni) and feldspars (Ba, Sr., Eu) relative to the I-type ones. Intraplate A-type granitoids have significantly higher Fe/Mg ratios (Fe – number) than typical Cordilleran granitoids and accordingly fall in the "ferroan" granitoid category. Eby (1990) divided A-type granites into two categories according to their Y/Nb ratios: a group have low Y/Nb ratios and generally low $(Sr^{87}/Sr^{86})_I$ ratios that formed by differentiation of basaltic magmas of OIB – like (plume) mantle sources; the second group of A-type granitoids characterized by higher Y/Nb ratios (1.2–7) and highly variable $(Sr^{87}/Sr^{86})_I$. This group shows a complex petrogenetic history as having a significant mantle component or may be totally of crustal origin. M-type granites (plagiogranites) can be subdivided tectonically into subduction-related and subduction-unrelated on the basis of the chemistry of their associated basalts. Plagiogranites are characterized by normalized and REE patterns with a notable depletion in the most highly incompatible large-ion lithophile (LIL) elements Rb, Ba and K, greater enrichment in Th, Nb and prominent negative anomalies in P and Ti.

The granitoids of the present study shows differences in geochemistry and petrology. The granitoids of the Raghunathpur-Bero area shows high SiO_2, Al_2O_3, and low MgO, CaO, Fe_2O_3, Ni, Cr, V elemental composition. They are peraluminous leucogranites, with molar A/CNK > 1.1 and showing calc-alkalic to alkali-calcic and ferroan nature. They are characterized by enrichment of Rb, Ba, Th with respect to Ta, Nb, Zr, Y, Yb which is characteristic of Calc-alkaline and Shoshonitic series (Pearce et al., 1984). Highly depleted Nb and Ta along with LILE enrichment in the granitoid samples imply a subduction related origin and their emplacement within a volcanic arc setting (Dharma Rao et al., 2013, Roberts et al.,1993). Calc-alkaline nature, geochemical signatures similar to arc granitoids along with the Volcanic Arc Granite

(VAG) and syn-collisional signatures of the granitoids in tectonic discrimination diagrams, thereby, demonstrates that the CGGC granitoids might have formed in subduction zone setting. Furthermore, strong enrichment in more incompatible elements (Cs, Ba, Rb, Th, U) over less incompatible elements (Ti, Y, Yb, Lu, Sr and Nb) with significant negative anomalies at Ba, Nb, T and Sr, and positive anomalies at Rb, Th and U also indicates formation of granitoid rocks of CGGC from orogenic/subduction zone magmas (Saunders, et al., 1980; Taylor et al., 1985).

The granitoids of the Jhalda area are enriched in silica content (SiO_2 ranges from 75.3–76.2 wt %) and alkali content (K_2O= 4.31–4.98 wt%; Na_2O= 3.07–4.07 wt%; Na_2O+K_2O = 8.35–8.86 wt %). They show low values of CaO (0.02–0.04 wt %), Al_2O_3 (10.6–11.3 wt %), FeO_t (2.6–3.6 wt %), MgO (0.03–0.04 wt %) content, higher FeO^{tot}/MgO ratios (65.7–102.5).They can be classified as ferroan, peralkaline granites and plots in the high K-calc-alkaline field. They show enrichment in Large Lithophile elements (LILEs: Rb, Th and U) and High Field Strength Elements (HFSE) (Nb, Ta, Zr),high Zr+Nb+Ce+Y concentrations (1150–1743 ppm) (as compared to 430-646 ppm, Xiao et al. 2019; 389-655 ppm, Whalen et al. 1987),high Ga/Al ratio (6.7–7.8) and depletion in Sr, Ba, P and Ti,which are typical of alkaline granites (Collins 1982, Whalen 1987).The AR granites have high abundance of Nb (120 to 160 ppm) which is higher than majority of the alkaline granites and A-type granites. In the tectonic discrimination diagrams (after Pearce et al., 1984), all the AR granitoids fall in the Within Plate Granite (WPG) field. In the Rl-R2 diagram (Batchelor and Bowden, 1985), the AR granitoids fall in the post-orogenic to anorogenic field. Zircon saturation temperature (T_{Zr}>900°C) of the AR granitoids indicates high temperature of primary magmas which is quite higher than that of I-type granitoids (< 800°C). Though they show differences in geochemistry and petrology but they show similar ages around 970 to 1000Ma. 1000Ma is marked as an important age in the history

of the tectonic events of CGGC. Grenvillian orogeny is reported to play an important role in shaping the continents of the Earth during this 1000Ma time.

Deformation in continental interiors far away from plate boundaries is enigmatic and not yet fully understood due to the lack of broad consensus on the underlying mechanisms responsible for it. Deformation in the plate boundaries are solely related to the divergence or convergence of those tectonic plates whereas movement of the plates is not solely responsible for the deformation of those plates in intraplate setting (e.g., Gorczyk et al., 2013).Crust-mantle interactions are probably necessary to explain the origin and evolution of intra-continental deformation since tectonic plates do not exist in isolation but are dynamically pushed by and connected to mantle convection. Surface uplift caused by crustal thickening by mafic magmatic underplating is supposed to occur in a variety of tectonic settings (e.g., McKenzie, 1984; Thybo & Artemieva, 2013). It has been hypothesized that small-scale asthenospheric upwelling caused by the removal of isolated lithospheric parts can cause localized regions of surface deformation and upheaval (e.g. Bird, 1979; Kay & Kay, 1993). Volcanic activities may be also associated spatially and temporally with such an event (e.g., Kay & Kay, 1993). Lithospheric removal can occur in various ways. One of them is Rayleigh-Taylor instability, or drip (e.g., Conrad & Molnar, 1997; Houseman et al., 1981; Magni & Király, 2019; Molnar et al., 1998). This gravitational instability forms as a small disturbance in the thermal boundary layer when convective thinning of the lithosphere is present. Another mechanism proposes that, the negatively buoyant lithosphere peels away laterally and sinks as the asthenosphere buoyantly rises to replace it (e.g., Bird, 1978, 1979; Magni & Király, 2019; Meissner & Mooney, 1998). Here we adopt the term delamination to refer to this mechanism, although, definitions vary and the mechanism can take several distinct forms (Magni & Király, 2019) that are much broader

than that originally described by Bird (1979). Although many studies consider dripping and delamination to be separate removal mechanisms, some studies have explored hybrid styles that combine components of both mechanisms (e.g., Beall et al., 2017). The controlling driving force of delamination is the negative buoyancy, and several other causes have been proposed. One of them is the phase change in the lower continental crust from mafic granulite facies to eclogite, which is significantly denser and is possibly due to a thickening crust (Krystopowicz & Currie, 2013; Meissner & Mooney, 1998). According to the numerical models, a lithospheric removal event causes the upwelling of buoyant asthenosphere which results in and supports surface uplift (e.g., Meissner & Mooney, 1998). Numerical modeling studies shows that a weak lower crust is a crucial requirement for decoupling a portion of the lithosphere and triggering a delamination event (e.g., Krysto-powicz & Currie, 2013; Meissner & Mooney, 1998). According to Jull & Kele-men, (2001); Morency & Doin, (2004), the prerequisites for triggering a lithospheric removal event are thick, dense crust and a high-temperature crust-mantle boundary in addition to a moderate continental convergence rate (e.g., Krysto-powicz & Currie, 2013). Lithospheric removal by delamination has been proposed in many diverse orogenic settings worldwide, including: the Tibetan Plateau, the Andean Plateau, the Sierra Nevada ranges, the Colorado Plateau, the Anatolian Plateau, and Central Australia (e.g., Demidjuk et al., 2007; Jimenez-Munt et al., 2008; Krystopowicz & Currie, 2013; Le Pourhiet et al., 2006; Levander et al., 2011; Şengör et al., 2003).

In the present study field relations show no evidences of post-collisional rifting process. Thus slab delamination process may be assumed as the probable process for the generation of A-type granites in an orogenic belt during post collisional extension. Based on the earlier considerations and observations, a schematic model may be proposed for the generation of S-type granites of

Raghunathpur-Bero area and A-type granites of Jhalda area showing contrasting chemistry but originating in near about same age. During 1.2-1.0 Ga, partial melting of crustal sediments of the subducted slab, under high pressure might have given rise to the S-type granites of the Raghunathpur-Bero area (Fig.8.4b). With increasing subduction, the subducted oceanic plate transformed to eclogite and henceforth a sharp increase in density along with a moderate to high temperature at the crust-mantle boundary and a moderate convergence rate promotes delamination of the subducting slab. A pre-existing weak zone, interpreted to be the local shear zone, might have been found to promote and facilitate the delamination process by focusing deformation and creating an initiation point for detachment. As the slab broke off, the asthenosphere rose rapidly into the lithosphere break as it developed and impinged upon the thickened mantle lithosphere of the overlying mantle wedge. The first likely consequence of the break off was the juxtaposition of hot asthenosphere against the thickened mantle lithosphere of the overriding plate. As the suducting slab fell away, more of the overlying mantle is exposed to hot asthenosphere. This active situation should maintain a fairly active flow near the base of the overriding mantle lithosphere near the breakoff point. The heating up of the overriding lithosphere by conduction as a result of the upwelling asthenosphere arriving at its base following breakoff led to melting of the metasomatised and hydrated layers. We would expect various chemical compositions, ranging from alkaline to ultrapotassic melts from the smallest degree melting of enriched layers, up to calc-alkaline melts for slightly higher degree melting of the more fertile or hydrated peridotite layers. Here in our case alkaline granitoids were supposed to be produced by small degree melting of the metasomatised mantle layer (Fig. 8.4d).

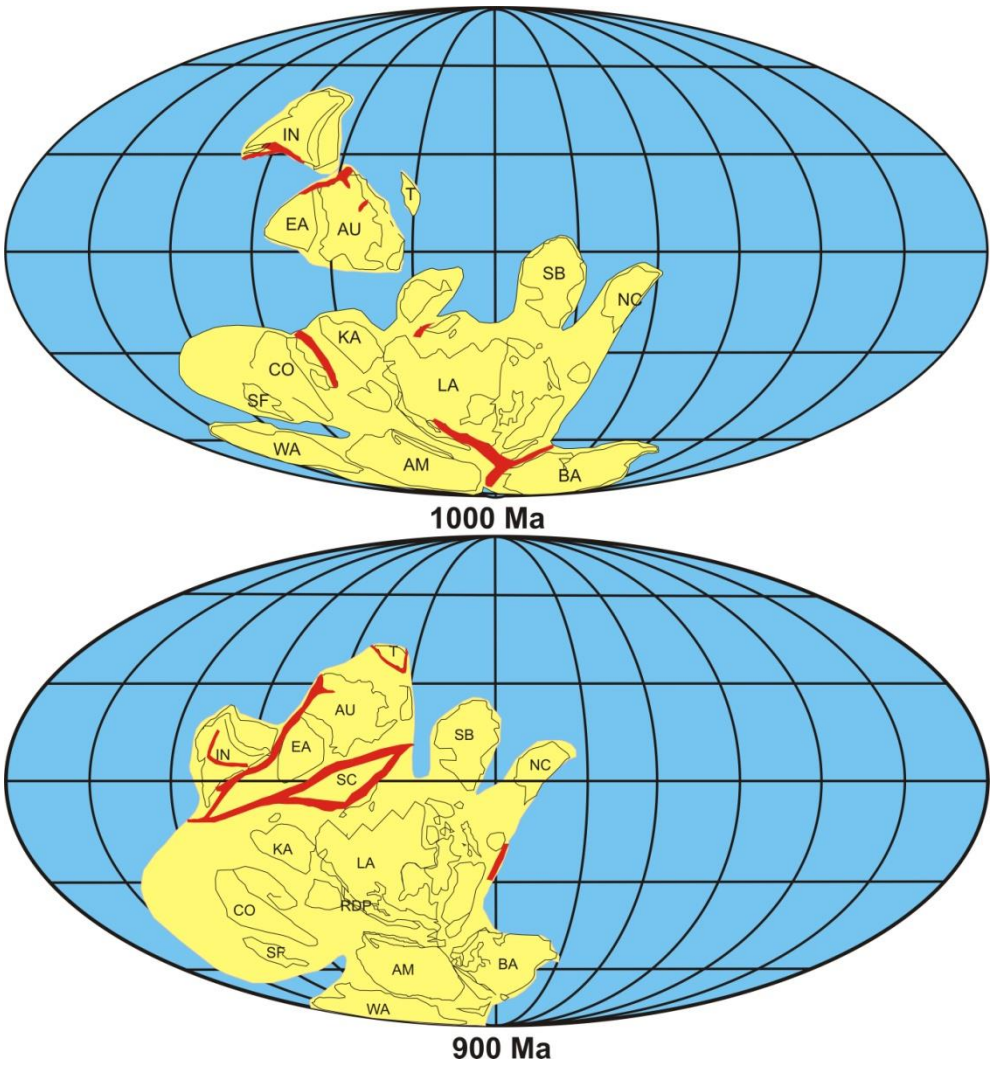

Figure.8.1.Schematic diagram showing relative position of different continents during the assembly of Rodinia supercontinent (1.0-0.9 Ga) modified after Li et al., (2008). Acronyms used in the figures are: IN: India, EA: East Antarctica, T: Tarim, AU: Australia, KA: Kalahari, CO: Congo, SF: Sao Francisco, SB: Siberia, NC: North China, BA: Baltica, AM: Amazonia, WA: West Africa, SC: South China.

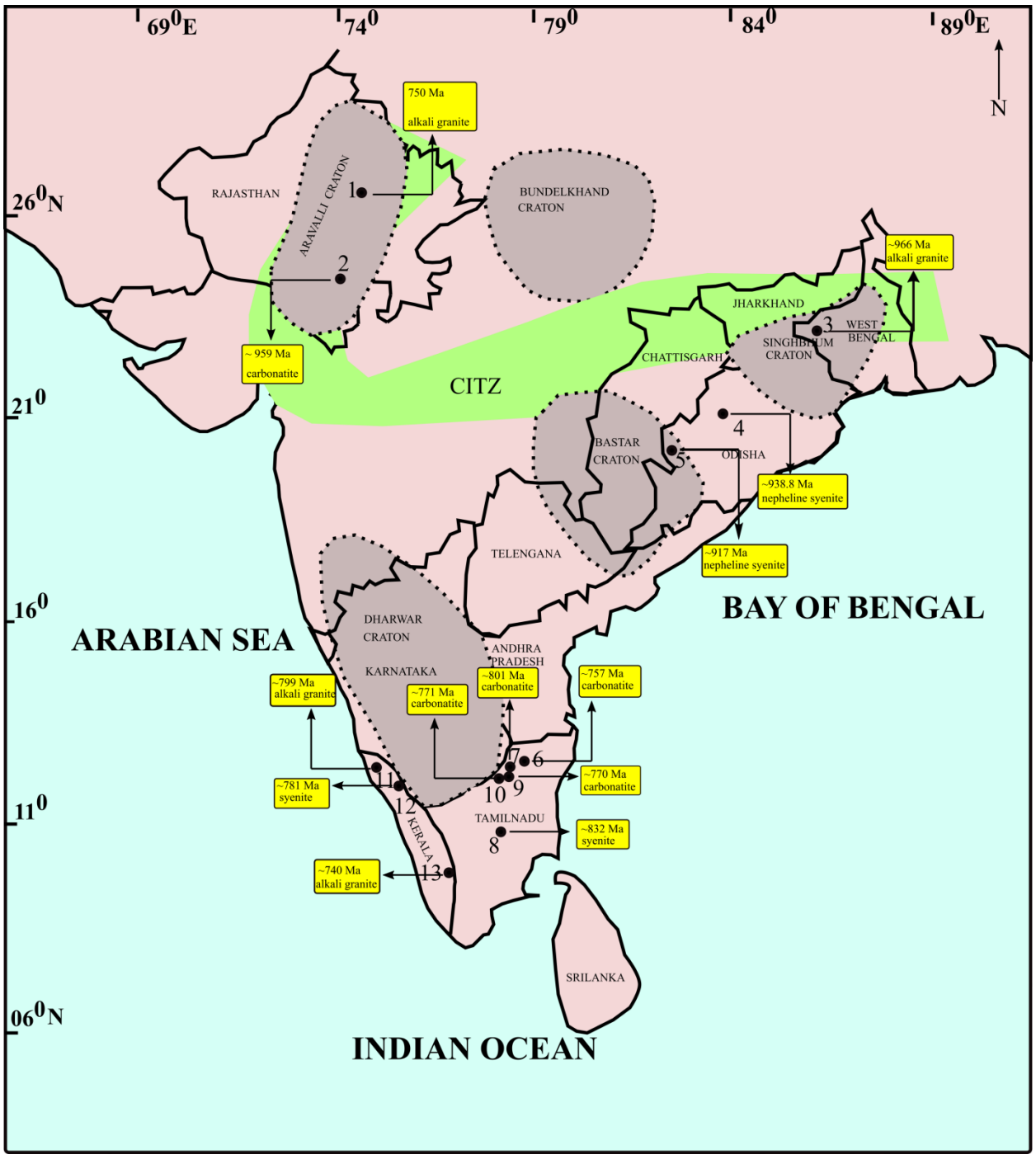

Figure.8.2.Geological map of India showing occurrences of Proterozoic alkaline rocks (after Leelanandam *et al*., 2006) along with their rock type and age. Major Precambrian cratons are also indicated in the map (after Naqvi and Rogers, 1987).

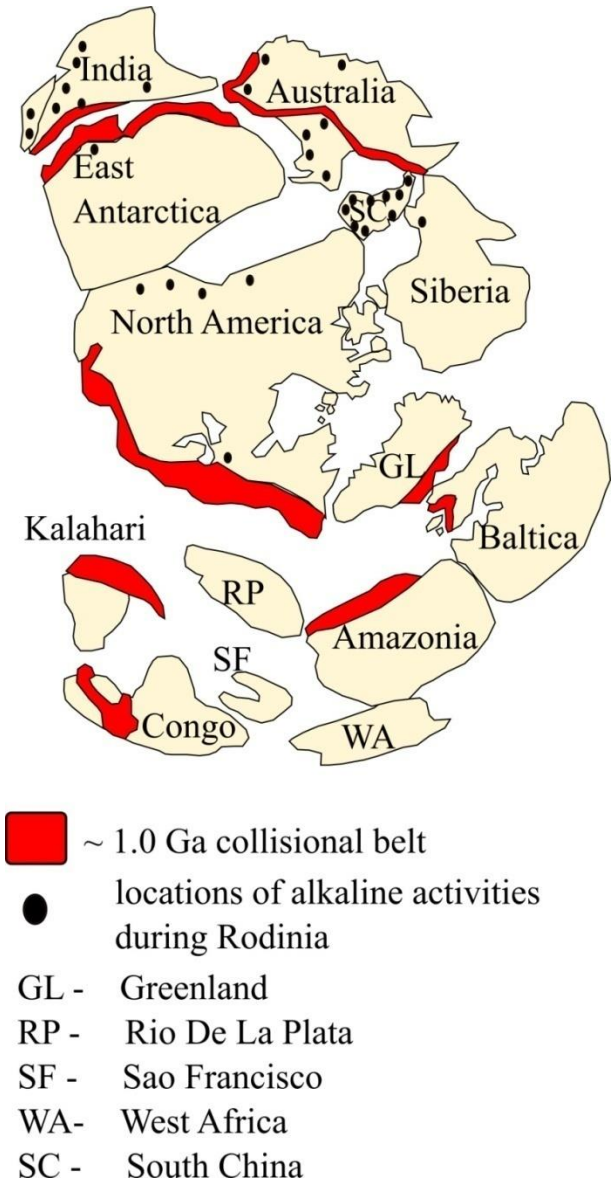

Figure.8.3.Configuration of the supercontinent Rodinia during 1000Ma (after Zhao *et al*., 2004). (Abbreviations: GL – Greenland, RP – Rio de la Plata, SF – Sao Francisco, WA – West Africa, SC – South China).

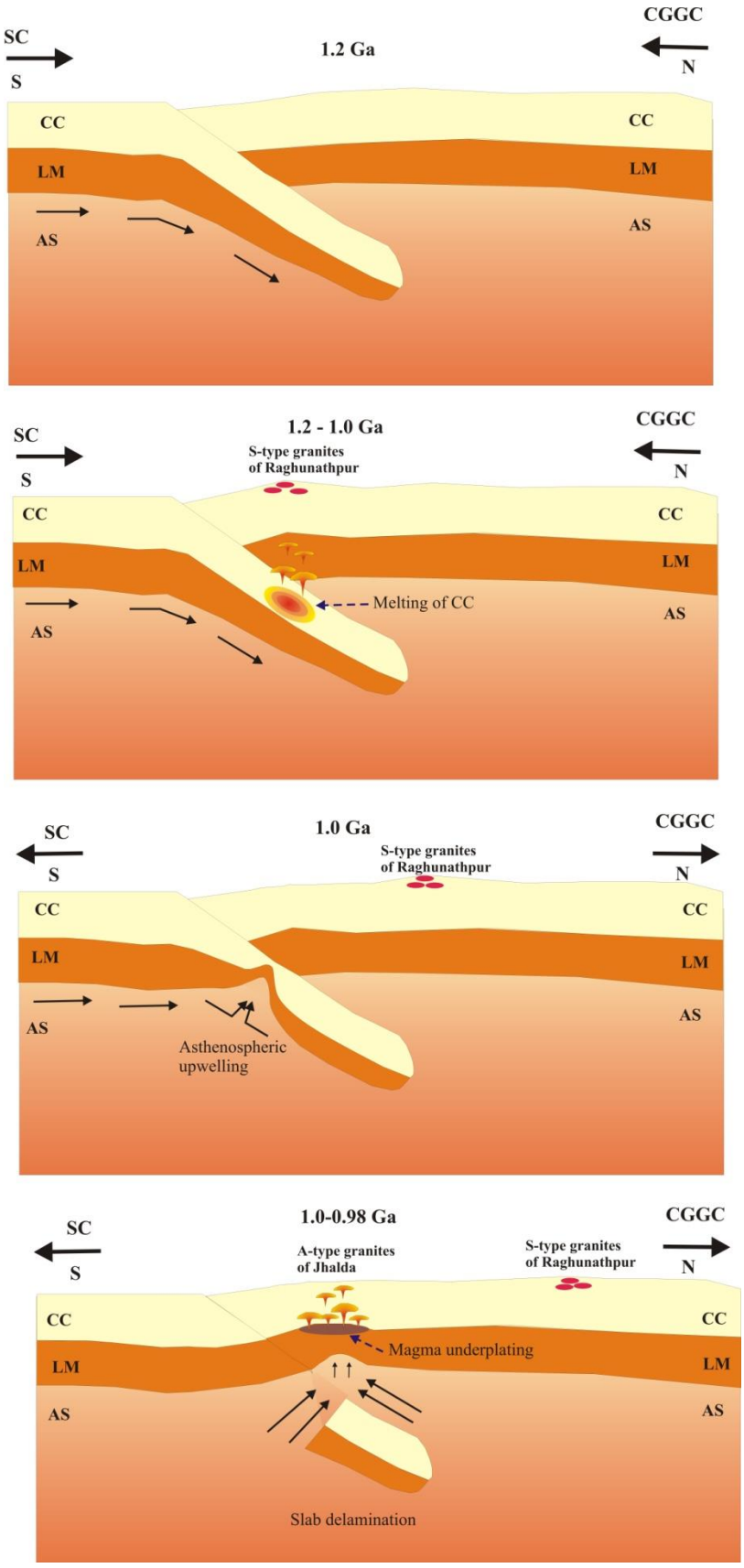
SC
S
1.2 Ga
CGGC
N
CC
LM
AS
CC
LM
AS
SC
S
1.2 - 1.0 Ga
S-type granites
of Raghunathpur
CGGC
N
CC
LM
AS
Melting of CC
CC
LM
AS
SC
S
1.0 Ga
S-type granites
of Raghunathpur
CGGC
N
CC
LM
AS
Asthenospheric
upwelling
CC
LM
AS
SC
S
1.0-0.98 Ga
A-type granites
of Jhalda
S-type granites
of Raghunathpur
CGGC
N
CC
LM
AS
Magma underplating
CC
LM
AS
Slab delamination

Figure. 8.4. Schematic geodynamic model to explain the generation of the A-type granites of the study area. (a) subduction of the oceanic lithosphere during 1.2 Ga (b) generation of S-type granites by slab-dehydration during 1.2-1.0 Ga (c) slab delamination and asthenospheric upwelling during 1.0 Ga (d) slab break-off, upwelling of asthenosphere, mafic magma underplating, melting of asthenosphere and generation of A-type granite during 1.0 to 0.95 Ga

Table.8.1. Comparison between the different types of granitoids of the study area.

Parameter	**GGG**	**MGG**	**PG**	**ARG**
Petrography	Major phases: Quartz, alkali-feldspar, plagioclase feldspar, garnet and biotite accessory phases: opaque minerals and zircons as accessory phases.	Major phases: alkali feldspar, quartz, plagioclase feldspar accessory phases: biotite, amphibole and opaque	Major phases: alkali feldspar, quartz, plagioclase feldspar, biotite accessory phases: apatite and opaques	Major phases: quartz, alkali feldspar, aegirine,riebeckite, and biotite accessory phases: zircon, plagioclase, sphene, ilmenite, and allanite as
SiO2	55-73	63-67	75-79	72-76
Al2O3	13.6-16.5	14.7-16.3	11.7-13.3	10.6-11.3
ASI index	>1, peraluminous	>1, peraluminous	<1, Na+K < Al, metaluminous	<1, Na+K>Al, peralkaline
Fe#	0.92	<0.96	0.73	0.96-0.99
Na2O+K2O	4.7-7.6	8.3-9.3	8.0-9.2	8.35–8.86
Norm	Normative quartz present	Normative quartz present	Normative quartz present	Normative acmite presen
Eu anomaly	negative	negative	Slight positive	negative
Temperature	800-850°C	770-830°C	639-725°C	>900°C
Tectonic setting	Volcanic Arc Granite and syn-COLG fields.	Volcanic Arc Granite and syn-COLG fields.	Volcanic Arc Granite and syn-COLG fields.	Within plate granite

Table. 8.2. Report of Grenvillian ages from different parts of India and Rodinian cratons.

	Age of metamorphism	**Dating method**	**Reference**
Eastern Ghats mobile Belt			
Domain 2	911±7	Monazite U-Pb	Bose et al. (2011)
	913±7		
Rengali Province	805±13	Monazite- U-Pb	Chattopadhyay et al. (2015)
	827±7		
Domain 2	902±17	Zircon U-Pb	Das et al. (2011)
Domain 2	921±15	Monazite U-Pb	Korhonen et al. (2013)
	855±15		
	822±31	Zircon U-Pb	
	874±20		
Eastern Ghats Province	830±44	Monazite U-Pb	Simmat and Raith (2008)
	836±43		
	845±26		
Eastern Ghats province	921±19	Monazite U-Pb	Dobmeier & Simmat, (2002)
East Indian Shield			
North CGGC	910±9	Monazite U-Pb	Rekha et al., (2011)
North CGGC	904±5	Zircon U-Pb	Mukherjee et al., (2017)
North CGGC	827±45	Monazite	Chatterjee et al. (2010)
	876±13		
North Singhbhum Fold Belt	848±63	Monazite U-Pb	Chatterjee et al. (2010)
	843±110		
South CGGC	825±26	Monazite	Maji et al. (2008)
	818±11		
South CGGC	861±53	Monazite U-Pb	Karmakar et al. (2011)
	856±49		
	903±40		
Eastern margin-South CGGC	937±30	Monazite U-Pb	Chatterjee et al. (2010)
Central Indian Tectonic Zone			
Mahakosal Belt	882±6	Monazite U-Pb	Deshmukh et al., (2017)
	868±130	Monazite U-Pb	
Betul Belt	850±50	Whole rock-Rb-Sr	Roy & Prasad, (2001)

Gavilgarh-Tan Shear zone	953±75	Zircon U-Pb	Chattopadhyay et al. (2017)
Aravalli-Delhi Mobile belt			
Mangalwar complex	946±6	Monazite U-Pb	Bhowmik et al., (2010)
	909±9		
	865±10		
Post-Delhi Granites (Erinpura Granites)	800±50	Whole rock-Rb-Sr	Choudhary, Gopalan, & Sastry, (1984)
Migmatitic country rock in contact with Sandmata Complex	949±11	Zircon U-Pb	Buick et al. (2006)
Eastern Indian Tectonic Zone			
Eastern margin of NSMB	848±63	Zircon U-Pb	Chatterjee et al.(2010)
East Antarctica			
Stillwell hills	913±8	Zircon U-Pb	Kelly et al., (2002)
Oygarden Group	904±6	Zircon U-Pb	
	884±24		
North Mawson Escarpment	928±29	Zircon U-Pb	Corvino et al., (2008)
Northern prince Charles mountains	900 ± 28	Zircon U-Pb	Boger, (2000)
	915 ± 12	Zircon U-Pb	Liu et al., (2014)
	914 ± 5		
	921 ± 19		
	915 ± 13		
	920 ± 7	Zircon U-Pb	Morrissey et al., (2015)
	902 ± 7		
Grove mountains, Pyrdz Bay	927 ± 29	Zircon U-Pb	Liu et al., (2009)
	900 ± 14		
	898 ± 18		
	907 ± 22		
Pyrydz bay	930	Zircon U-Pb	Liu et al. (2013)
SouthwesternPyrdz Bay	922± 10	Zircon U-Pb	Liu et al. (2014)
Bolingen Islands, Pyrydz Bay	915 ±10	Monazite U-Pb	Kelsey et al., (2007)
	901 ± 11		
Rayner complex	906 ± 6	Monazite U-Pb	Halpin et al., (2007)
	915 ± 13		
Yangzte Block, South China			

Southern Yangtze Block	1007±14	Zircon U-Pb	Li et al. (2014)
Dulanterrane, North Qaidam	932 ± 18	Zircon U-Pb	
East Greenland			
Southern part of Caledonian Orogen	950	Zircon U-Pb	Kalsbeek et al.(2000)
Amazonia craton			
SunsasOrogen	984±13	Zircon U-Pb	Rizzotto et al.(2014)

Table.8.3. Details of Proterozoic alkaline complexes in India including rock type and age.

	Location	Province	Rock type	Age	Reference
1.	Siwana, Rajasthan	Malani Igneous Province	Alkaline granites	750 Ma	Sharma (2005)
2.	Puruliya, West Bengal (Jhalda)	Chotanagpur Granite Gneissic Complex	Alkali Granite	966+7 Ma (U-Pb)	Present study
3.	Rairakhol, Odisha	Rengali Province	Nepheline syenite	938.8+3.1 Ma (U-Pb)	Bhattacharya and Basei (2010)
4.	Koraput , Odisha	Jeypore Province, EGMB	Nepheline syenite, syenite, syenodiorite, alkali gabbro	917 Ma (U-Pb, 4); 869+11 Ma (u-Pb, 5); 856+18 Ma (Rb-Sr, 1)	Sarkar et al., (1989) Nanda et al., (2008) Upadhyay (2008) Bhattacharya and Basei (2010) Hippe et al., (2016)
5.	Elagiri, Tamil Nadu	Southern Granulite terrain	Syenite, monzonite, pyroxenite, gabbronorite, dunite, lamprophyre, carbonatite	757+32 Ma (Rb-Sr)	Miyazaki et al., (2000) Mukhopadhyay et al., (2011b) Renjith et al., (2014)
6.	Sevattur, Tamil Nadu	Southern Peninsular Gneiss, Salem Block, SGT	Carbonatite, pyroxenite, aplite, pegmatite and syenite	720+30 Ma (K-Ar, 10; 770+18 Ma (Rb-Sr, 3); 767+8 (Rb-Sr, 6); 756+11 Ma (Rb-Sr, 8); 770+18 Ma, 773+18 Ma (Rb-Sr, 3); 801+11 Ma (Pb-Pb, 7)	Deans and Powell (1968) Udas and Krishnamurthy (1970) Kumar and Gopalan (1991) Peucat et al., (1993) Viladkar and Subramaniam (1995) Kumar et al., (1998) Schleicher et al., (1997) Miyazaki et al., (2000)

					Ackerman et al., (2017)
7.	Sundamalai, TamilNadu	Salem Block, Southern Granulite Terrain	Syenite	832.6+3.2 Ma (U-Pb)	Renjith et al., (2016a)
8.	Samalpatti, Tamil Nadu	Salem Block, Southern Granulite Terrain	Syenite, Carbonatite, pyroxenite, alkali gabbro, serpentinized dunite	700+30 Ma (K-Ar, 1); 770 Ma (4)	Moralev et al. (1975) Subramaniam et al., (1978) Viladkar and Subramaniam (1995) Srivastava (1998) Schleicher et al., (1998) Pandit et al., (2002) Ackerman et al., (2017)
9.	Pakkanadu-Mulakkadu, Tamil Nadu	Madurai block, SGT	Calciocarbonatite, pyroxenite, syenite	771+2 Ma (K-Ar, 1); 750 +2 Ma, 759 +3 Ma (monazite date, 4,5)	Moralev et al., (1975) Ravindran (1986) Schleicher et al., (1998) Moller et al., (2001) Pandit et al., (2002)
10.	Peralimala, Kerala	Coorg Block, SGT	Alkali granite	797.5+3.7 Ma; 799+6.2 Ma (U-Pb, 1); 750 +40 Ma (Rb-Sr, 1)	Santosh et al (2014)
11.	Angadimogar, Kerala	Coorg Block, SGT	Syenite	781.8+3.8 Ma (U-Pb, 2); 638 +28 Ma (Rb-Sr,1)	Santosh et al., (1989) Santosh et al (2014)
12.	Munnar, Kerala	Madurai Block, SGT	Alkali granite-syenite carbonatite	740+30 Ma	Odom (1982) Nair et al., (1984) Catlos et al (2008)

Table.8.4. Details of the Proterozoic alkaline provinces of the world

Location	Rock type	Age (Ma)	Reference
Australia			
Amata Dyke swarm, central Australia	dolerite	824±4	Sun and Seraton 1996
Gairdener Dyke Swarm, Southeastern Australia	dolerite	827±6	Wingate et al. 1998
Little Broken Hill, southeastern Australia	gabbro	837±9	Wingate et al. 1998
Kimberley, northwestern Australia	lamprophyre, kimberlite	815-800	Pidgeon et al., 1989
Mundine Well Dyke swarm, western ralia	dolerite	755±3	Wingate and Giddings, 2000
northwestern Tasmania	granitoid	777±7	Turner et al., 1998
King Island, north of Tasmania	granitoid	760±12, 748±2	Turner et al., 1998, Black et al., 1997
Alaska			
Sadlerochit-Shublik Mountain, Alaska	basalt	810±20	Rainbird et al., 1996
Lauretia			
Little Dal, Mackenzie Mountains, western Lauretia	quartz diorite	780	Jefferson and Parrish, 1989
Gunbarrel mafic magmatic event, western Lauretia		780±1	Harlan et al., 2003
Mount Copeland, western Lauretia	syenite gneiss	740±36	Parrish and Scammell, 1988
Franklin dyke swarm, northern Lauretia		723±4	Heaman et al., 1992
Malton, southern Rocky mountain	gneissic granite	741±22	Evenchick et al., 1984
Mount Harper group, northwest Canada	rhyolite	751±26	Roots and Parrish, 1988
Blue range Province, southern Appalachians	alkali granites	765±7	Fetter and Goldberg,1995
South Africa			
southwest Africa	syenite gneiss	770	Li et al.,
Richtersveld Igneous complex, eastern South Africa		833±2	Frimmel et al., 2000
Seychelles			
Seychelles	granitoids	808.8±1.9	Tucker et al., 2001

Mahe Island, Seychelles	granitoids	750.2±2.5	Torsvik et al., 2001a
Madagascar			
west-central Madagascar	granitoids	791	Handke et al., 1999
North of Ranotsara shear zone, Madagascar	granitoids	788.6±0.7	Kroner et al 1999
Antananarivo Block, central Madagascar	granitoids	824	Kroner et al 2000
Siberia			
Yenisei ridge, Siberian craton	A -type leucogranite, carbonatite	710-690	Romanova et al., 2012
South Korea			
Gyeonggi massif, South Korea	Alkaline granite, syenite	742±13	Lee et al., 2002
Antarctica			
Sor Rondane mountain, Antarctica	A -type granite	960-925	Elburg et al., 2014
South China			
Kangding Complex, Sinchuan	granitoids	755, 768, 751, 797, 795 (1)	Li et al., 2002 Zhou et al., 2002 (1)
Shaanxi, South China	Leuco-granite	762	Xue et al., 1996
Daxiangling, Sinchuan	granitoids	809	Ma et al., 1989
Tongde diorite, Sinchuan	diorite	813	Sinclair et al 2001
Sanfang mafic intrusive, South China		828±7	Li et al., 1999
Cathaysia block, southeastern South China	Alkaline rhyolite	818±9	Li et al., 2004

REFERENCES

1. Acharyya, S. K. (2003). A plate tectonic model for Proterozoic Crustal evolution of Central Indian Tectonic Zone. *Gondwana Geological Magazine*, 9–31.
2. Ackerman L, Magna T, Rapprich V, Upadhyay D, Krátký O, Čejková B, Erban V, Kochergina YV, Hrstka T (2017). Contrasting petrogenesis of spatially related carbonatites from Samalpatti and Sevattur, Tamil Nadu, India. *Lithos*, (284–285) 257–275.
3. Anderson, J. L., Barth, A. P., Wooden, J. L., & Mazdab, F. (2008). Thermometers and Thermobarometers in Granitic Systems. *Reviews in Mineralogy and Geochemistry*, *69*(1), 121–142. https://doi.org/10.2138/RMG.2008.69.4
4. Arndt, N. T., Coltice, N., Helmstaedt, H., & Gregoire, M. (2009). Origin of Archean subcontinental lithospheric mantle: Some petrological constraints. *Lithos*, *109*(1-2), 61-71.
5. Baidya T. K. (1992). Apatite-magnetite deposit in the Chhotanagpur Gneissic Complex, Panrkidih area, Purulia district, West Bengal. *Indian Journal of Geology*, *64*(1), 88–95.
6. Baidya, T. K. (1981). Tin-Tungsten Mineralization in and Around Jabarban-Belamu, Purulia District, West Bengal. *Geological Society of India*, *22*(8), 403–404. http://www.geosocindia.org/index.php/jgsi/article/view/64953
7. Baidya, T. K., Chakravorty, P. S., Drubetskoy, E., & Khiltova, V. J. (1987). New geochronologic data on some granitic phases of the Chhotanagpur granite gneiss complex in the north-western Purulia district, West Bengal. *Indian Journal of Earth Sciences*, *14*(2), 136–141.

8. Baidya, T. K., Maity, N. & Biswas, P. (1989). Tectonic phases and crustal evolution in a part of the Eastern Chotanagpur Gneissic Complex. *Journal of the Geological Society of India*, 34, 318–324.

9. Baidya, T.K. and Chakravarty, P.S. (1988). Mineralization in the Belamu-Jaipur sector of northwestern Purulia district, West Bengal. *Geological Society of India, Memoir 8*, 147-165.

10. Ball, V. (1881). Geology of Manbhum and Singhbhum. *Memoir of Geological Survey of India*, *18*, 61–90.

11. Banerjee, A. K. (1991). Geology of the Chhotanagpur region. *Indian Journal of Geology*, *63*(4), 275–282.

12. Barker, F. (1979). Trondhjemite: Definition, *Environment and Hypotheses of Origin,* 1–12. https://doi.org/10.1016/B978-0-444-41765-7.50006-X

13. Barker, F., Wones, D. R., Sharp, W. N., & Desborough, G. A. (1975). The Pikes Peak batholith, Colorado Front Range, and a model for the origin of the gabbro—anorthosite—syenite—potassic granite suite. *Precambrian Research*, *2*(2), 97–160. https://doi.org/10.1016/0301-9268(75)90001-7

14. Basak, A., & Goswami, B. (2020). The physico-chemical conditions of crystallization of the Grenvillian arfvedsonite granite of Dimra Pahar, Hazaribagh, India: constraints on possible source regions. *Mineralogy and Petrology 2020*, *114*(4), 329–356. https://doi.org/10.1007/S00710-020-00708-W

15. Batchelor, R. A., & Bowden, P. (1985). Petrogenetic interpretation of granitoid rock series using multi-cationic parameters. *Chemical Geology*, *48*(1–4), 43–55. https://doi.org/10.1016/0009-2541(85)90034-8

16. Beall, A. P., Moresi, L., & Cooper, C. M. (2017). Formation of cratonic lithosphere during the initiation of plate tectonics. *Geology*, *46*(6), 487-490.
17. Bekker, A., Holland, H. D., Wang, P. L., Rumble, D., Stein, H. J., Hannah, J. L., Coetzee, L. L., & Beukes, N. J. (2004). Dating the rise of atmospheric oxygen. *Nature*, *427*(6970), 117–120. https://doi.org/10.1038/NATURE02260
18. Benisek, A., & Finger, F. (1993). Factors controlling the development of prism face in granite zircons: a microprobe study. *Contributions to Mineralogy and Petrology 1993*, *114*(4), 441–451. https://doi.org/10.1007/BF00321749
19. Bhattacharya, A., Krishnakumar, K., Raith, M. & Sen, S.K. (1991). An improved set of a-X parameters for Fe-Mg-Ca garnets and refinements of the orthopyroxene-garnet thermometer and the orthopyroxene-garnet-plagioclase quartz barometer. *Journal of Petrology*, *32,* 629-656.
20. Bhattacharya, B. P. (1976). Metamorphism of the Precambrian rocks of the central part of Santhal Parganas district, Bihar. *Quarternary Journal of the Geology, Mining and Metallurgical Society of India*, *48,* 183–196.
21. Bhattacharyya, B. P. (1975). Structural evolution in the central part of Santhal Parganas district, Bihar. *Geological, Mining, and Metallurgical Society of India*, *48* (1), 41-47.
22. Bhattacharyya, D. S., & Dasgupta, D. (1982). Metamorphism of the Dalma Mafic Rocks. *Geological Society of India*, *23*(2), 90–98.
23. Bhattacharyya, P.K., Mukherjee, S. (1987). Granulites in and around the Bengal anorthosite, eastern India: genesis of coronal garnet and evolution of the granulite– anorthosite complex. *Geological Magazine 124*, 21–32.

24. Bhaumik, T, Mukherjee, S and Bose, S. (1990). Petrology of nepheline syenites from Santuri, Puruliya District, West Bengal. *Geological Society of India 36,* 589–606.
25. Bhowmik, S.K., Bernhardt, H.J., & Dasgupta, S., (2010). Grenvillian age high-pressure upper amphibolite–granulite metamorphism in the Aravalli–Delhi Mobile Belt, North-western India: new evidence from monazite chemical age and its implication. *Precambrian Research,* 178 168–184.
26. Bird, P. (1979). Continental delamination and the Colorado Plateau. *Journal of Geophysical Research: Solid Earth*, *84*(B13), 7561–7571.
27. Bogdanova, S. V., Pisarevsky, S. A., & Li, Z. X. (2009). "Assembly and Breakup of Rodinia (Some Results of IGCP Project 440)". *Stratigraphy and Geological Correlation.* 17 (3): 259–274.
28. Bonin, B. (1990). From orogenic to anorogenic settings: evolution of granitoid suites after a major orogenesis. *Geological Journal* 25, 261–270. doi:10.1002/gj.3350250309
29. Bonin, B. (2004). Do coeval mafic and felsic magmas in post-collisional to within-plate regimes necessarily imply two contrasting, mantle and crustal, sources? A review. *Lithos*, *78*(1–2), 1–24. https://doi.org/10.1016/j.lithos.2004.04.042
30. Bonin, B. (2007) A-Type Granites and Related Rocks: Evolution of Concept, Problems and Prospects. *Lithos, 97,* 1-29.
31. Bonin, B., Janoušek, V., & Moyen, J.-F. (2020). "Chemical variation, modal compositional and classification of granitoids," in *Post-archean granitic rocks: petrogenetic processes and tectonic environments*. Editors V. Janoušek, B. Bonin, W. J. Collins, F. Farina, and P. Bowden (Bath, UK: Geological Society of London Special Publication).

32. Bourne, J. H., & L'Heureux, M. (1991). The petrography and geochemistry of the Clericy Pluton: an ultrapotassic pyroxenite-syenite suite of late Archaean age from the Abitibi region, Quebec. *Precambrian Research, 52*(1–2), 37–51. https://doi.org/10.1016/0301-9268(91)90012-Y
33. Bowen N. L. (1928). The Evolution of the Igneous Rocks: Princeton, New Jersey, *Princeton University Press, 332*
34. Bowring, S. A., Erwin, D. H., Jin, Y. G., Martin, M. W., Davidek, K., & Wang, W. (1998). U/Pb zircon geochronology and tempo of the end-Permian mass extinction. *Science*, *280*(5366), 1039–1045. https://doi.org/10.1126/SCIENCE.280.5366.1039
35. Boynton, W.V. (1984). Cosmochemistry of the rare earth elements; meteorite studies. In: Rare earth element geochemistry. Henderson, P. (Editors), *Elsevier Science Publishing Co.*, Amsterdam. 63-114
36. Brown M. (2013). Granite: From genesis to emplacement. *GSA Bulletin* .125 (7-8): 1079–1113. doi: https://doi.org/10.1130/B30877.1
37. Buick, I.S., Allen, C., Pandit, M., Rubatto, D., & Herman, J., (2006). The Proterozoic magmatic and metamorphic history of the banded gneissic complex, central Rajasthan, India: LA-ICP-MS U–Pb zircon constraints. *Precambrian Research 151*, 119–142
38. Cai, J., Liu, F., & Liu, P. (2017). Paleoproterozoic multistage metamorphic events in Jining metapelitic rocks from the Khondalite Belt in the North China Craton: Evidence from petrology, phase equilibria modelling and U–Pb geochronology. *Journal of Asian Earth Sciences, 138,* 515–534. https://doi.org/10.1016/j.jseaes.2017.02.034
39. Campbell, I. H. & Davies, D. R. (2017). Raising the continental crust. *Earth and Planetary Science Letters 460,* 112–122

40. Canfield, D.E., Habicht, K.S., & Thamdrup, B., (2000). The Archean sulfur cycle and the early history of atmospheric oxygen. *Science 288,* 658–661

41. Catling, D. C., & Claire, M. W. (2005). How Earth's atmosphere evolved to an oxic state: a status report. *Earth and Planetary Science Letters*, *237*(1-2), 1-20.

42. Chakrabarty, A., Mitchell, R. H., Ren, M., Saha, P. K., Pal, S., Pruseth, K.L. & Sen, A.K., (2016). Magmatic, hydrothermal and subsolidus evolution of the agpaitic nepheline syenites of the Sushina Hill Complex, India: implications for the metamorphism of peralkaline syenites. *Mineralogical Magazine*, *80*(7), 1161-1193

43. Chakraborty, K., Ray, A., Chatterjee, A., Deb, G. K., & Das, K. (2019). Neoproterozoic granitic activity in syn-collisional setting: Insight from petrology, geochemistry, and zircon–monazite geochronology of S-type granites of the Chotanagpur Granite Gneissic Complex, eastern India. *Geological Journal*, *54*(5), 3112–3147. https://doi.org/10.1002/gj.3555

44. Champion, D. C., & Sheraton, J. W. (1997). Geochemistry and Nd isotope systematics of Archaean granites of the Eastern Goldfields, Yilgarn Craton, Australia: implications for crustal growth processes. *Precambrian Research*, *83*(1-3), 109-132.\

45. Champion, D.C. & Smithies, R.H., (2001). Archaean granites of the Yilgarn and Pilbara cratons, Western Australia. In K.F. Cassidy, J.M. Dunphy & M.J. Van Kranendonk (editors), 4th International Archaean Symposium 2002, Extended abstracts. AGSO-Geoscience Australia, Record 2001/37, 134-136

46. Champion, D.C. and Smithies, R.H. (1999) Archaean granites of the Yilgarn and Pilbara cratons, Western Australia: secular changes in the origin of granites and related rocks. *In:* Proc. Fourth Hutton Symp. (Abstracts), 137.

47. Chappell, B. W. and White, A. J. R., (1974). Two contrasting granite types. *Pacific Geology 8*, 173-174

48. Chappell, B. W., & White, A. J. R. (1992). I- and S-type granites in the Lachlan Fold Belt. *Transactions of the Royal Society of Edinburgh: Earth Sciences*, *83*(1–2), 1–26. https://doi.org/10.1017/S0263593300007720

49. Chappell, B. W., & White, A. J. R. (2001). Two contrasting granite types: 25 years later. *Australian Journal of Earth Sciences*, *48*(4), 489–499. https://doi.org/10.1046/J.1440-0952.2001.00882.X

50. Chatterjee, N., and Ghose, N. C. (2011). Extensive early neoproterozoic high-grade metamorphism in north Chotanagpur gneissic complex of the central Indian tectonic zone. *Gondwana Research, 20* 362–379.

51. Chatterjee, N., Banerjee, M., Bhattacharya, A., & Maji, A. K. (2010). Monazite chronology, metamorphism-anatexis and tectonic relevance of the mid- Neoproterozoic Eastern Indian Tectonic Zone. *Precambrian Research*, *179*, 99–120.

52. Chatterjee, N., Crowley, J. L., & Ghose, N. C. (2008). Geochronology of the 1.55 Ga Bengal anorthosite and Grenvillian metamorphism in the Chotanagpur gneissic complex, eastern India. *Precambrian Research*. https://doi.org/10.1016/j.precamres.2007.09.005

53. Chatterjee, N., Mazumdar, A. C., Bhattacharya, A., & Saikia, R. R. (2007). Mesoproterozoic granulites of the Shillong–Meghalaya Plateau: Evidence of westward continuation of the Prydz Bay Pan-African suture into Northeastern India. *Precambrian Research, 152*(1–2), 1–26. https://doi.org/10.1016/J.PRECAMRES.2006.08.011

54. Chatterjee, S. R., & SenGupta, D. K. (1980). Structural and Petrological Evolution of the Rocks around Jamua-Kakwara-Bhatia of Satpura Orogeny, Bhagalpur District, Bihar. *Geological Society of India, 21*(4), 171–183.
55. Chattopadhyay, B., and Saha, A. K., (1974). The Neropahar Pluton in Eastern India—A Model of Precambrian Diapiric Intrusion: *Neues Jahrbuch für Mineralogie (Abhandlungen) 121*, 103–126.
56. Clarke, D. B. (1992). Granitoid Rocks. Topics in the Earth Sciences 7. London, Glasgow, New York, Tokyo, Melbourne, Madras: Chapman & Hall. ISBN 0 412 29170 3.
57. Clemens, J. D., & Stevens, G. (2012). What controls chemical variation in granitic magmas? *Lithos, 134–135*, 317–329. https://doi.org/10.1016/j.lithos.2012.01.001
58. Collins, L.S., (1993). Neogene paleo-environments of the Bocas del Toro Basin, Panama: *Journal of Paleontology, 67*, 699-710.
59. Collins, W. J., Beams, S. D., White, A. R. J., & Chappell, B. W. (1982). Nature and origin of A-type granites with Particular Reference to Southeastern Australia. *Contribution to Mineralogy and Petrology, 80*, 189–200.
60. Condie, K. C. (1981). Archean greenstone belts. *Elsevier.*
61. Condie, K. C. (1989). Geochemical changes in baslts and andesites across the Archean-Proterozoic boundary: Identification and significance. *Lithos, 23*(1-2), 1-18.
62. Condie, K. C. (Ed.). (1994). Archean crustal evolution. *Elsevier.*
63. Condie, K. C., & O'Neill, C. (2010). The Archean-Proterozoic boundary: 500 My of tectonic transition in Earth history. *American Journal of Science, 310*(9), 775-790.

64. Conrad, C. P., & Molnar, P. (1997). The growth of Rayleigh—Taylor-type instabilities in the lithosphere for various rheological and density structures. *Geophysical Journal International*, *129*(1), 95-112.

65. Corfu, F., Hanchar, J. M., Hoskin, P. W. O., & Kinny, P. (2003). Atlas of Zircon Textures. *Reviews in Mineralogy and Geochemistry*, *53*(1), 469–500. https://doi.org/10.2113/0530469

66. Cox, K. G., Bell, J. D., & Pankhurst, R. J. (1979). The Interpretation of Igneous Rocks. Springer Netherlands. https://doi.org/10.1007/978-94-017-3373-1

67. Creaser, Robert. A., Price, Richard. C., & Wormard, Richard. J. (1991). A-type granites revisited: assessment of a residual- source model. *The Geological Society of America*, *19*, 163–166.

68. Dalziel, I. W. D. (1995). Earth before Pangea. *Scientific American*, *272*(1), 58–63. http://www.jstor.org/stable/24980139

69. Das D K, (1977). A review on sulphide zone around Belamu hill, Purulia, West Bengal. *Journal of Mines Metals Fuels*, Purulia Seminar, special number, 75-77.

70. Das, A., & Bhattacharyya, C. (2007). Alkaline granitoids from the Northern Shear Zone of Puruliya District, West Bengal. In *Journal of the Geological Society of India* 69.

71. Das, B. & Nandi, M. (1995). Preliminary exploration for apatite and REE, Northern Shear Zone, Purulia district. West Bengal. *Record of Geological Survey of India*, *28* (3), 69.

72. Das, K., Bose, S., & Ghosh, G. (2017). The Neoarchean-Paleoproterozoic basin development and growth of the Singhbhum Craton, eastern India and its global implications: Insights from detrital zircon U-Pb data. In *Precambrian Research 298*.

73. Das, S., Nasipuri, P., Bhattacharya, A., & Swaminathan, S. (2008). The thrust-contact between the Eastern Ghats Belt and the adjoining Bastar craton (Eastern India): Evidence

from mafic granulites and tectonic implications. *Precambrian Research*, *162*(1–2), 70–85. https://doi.org/10.1016/J.PRECAMRES.2007.07.013

74. Das, S., Sanyal, S., Karmakar, S., Sengupta, S., & Sengupta, P. (2019). Do the deformed alkaline rocks always serve as a marker of continental suture zone? A case study from parts of the Chotanagpur Granite Gneissic complex, India. *Journal of Geodynamics*, *129*, 59–79. https://doi.org/10.1016/J.JOG.2018.10.001
75. Dasgupta, S., & Others. (2000). Seismotectonic Atlas of India and Its Environs, *Geological Survey of India.*
76. De la Roche, H., Leterrier, J., Grandclaude, P. and Marchal, M. (1980). A Classification of Volcanic and Plutonic Rocks Using R1-R2 Diagrams and Major Element Analyses—Its Relationships with Current Nomenclature. *Chemical Geology, 29*, 183-210. http://dx.doi.org/10.1016/0009-2541(80)90020-0
77. Deb, M., Thorpe, R.I., Krstic, D., Corfu, F., & Davis, D.W., (2001). Zircon U-Pb and galena Pb isotope evidence for an approximate 1.0 Ga terrane constituting the western margin of the Aravalli Delhi orogenic belt, northwestern India: *Precambrian Research, 108*, 195–213.
78. Deer, W. A., Howie, R. A., & Zussman, J. (1963). "Rock-Forming Minerals. Vol. 2, Chain Silicates". Longmans, Green, London. 379
79. Demidjuk, Z., Turner, S., Sandiford, M., George, R., Foden, J., & Etheridge, M. (2007). U-series isotope and geodynamic constraints on mantle melting processes beneath the Newer Volcanic Province in South Australia. *Earth and Planetary Science Letters*, *261*(3–4), 517–533. https://doi.org/10.1016/J.EPSL.2007.07.006

80. Dewey, J.F. and Burke, K.C. (1973). Tibetan, Variscan, and Precambrian Basement Reactivation: Products of Continental Collision. *The Journal of Geology*, *81*, 683-692. https://doi.org/10.1086/627920

81. Dey, A., Choudhury, S. R., Mukherjee, S., Sanyal, S., & Sengupta, P. (2019). Origin of vesuvianite-garnet veins in calc-silicate rocks from part of the Chotanagpur Granite Gneiss Complex, East Indian Shield: The quantitative P-T-XCO2 topology in parts of the system CaO-MgO-Al2O3-SiO2-H2O-CO2 (+Fe2O3, F). *American Mineralogist*, *104*(5), 744–760. https://doi.org/10.2138/am-2019-6811

82. Dey, A., Mukherjee, S., Sanyal, S., Ibanez-Mejia, M., & Sengupta, P. (2017). Deciphering Sedimentary Provenance and Timing of Sedimentation from a Suite of Metapelites From the Chotanagpur Granite Gneissic Complex, India. In *Sediment Provenance*. Elsevier. p.453-486. doi:10.1016/b978-0-12-803386-9.00016-2

83. Dharma Rao, C. V., Kim, S. W., & Li, S. (2013). Arc magmatism in the Delhi Fold Belt: SHRIMP U–Pb zircon ages of granitoids and implications for Neoproterozoic convergent margin tectonics in NW India. *Journal of Asian Earth Sciences*, *78*, 83–99. https://doi.org/10.1016/J.JSEAES.2012.09.007

84. Dhuime, B., Hawkesworth, C. J., Cawood, P. A., & Storey, C. D. (2012). A change in the geodynamics of continental growth 3 billion years ago. *Science*, *335*(6074), 1334-1336.

85. Dunkl, I., Mikes, T., Simon, K. & von Eynatten, H. (2008). Brief introduction to the Windows program Pepita: data visualization, and reduction, outlier rejection, calculation of trace element ratios and concentrations from LA-ICP-MS data. In *Laser ablation ICP-MS in the Earth Sciences: Current practices and outstanding issues: Vol. Short Course 40* (334–340).

86. Dunn J A, (1929). Geology of North Singhbhum including parts of Ranchi and Manbhum districts. *Memoir of Geological Survey of India, 54*(1).

87. Eby, G. N. (1990). The A-type granitoids: A review of their occurence and chemical characteristics and speculations on their petrogenesis. *Lithos, 26*, 115–134.

88. Eby, G. N. (1992). Chemical sub-division of the A-type granitoids: Petrogenetic and tectonic implications. *The Geological Society of America*, *20*, 641–644.

89. Elburg, M. A., Smet, I., & De Pelsmaeker, E. (2014). Influence of source materials and fractionating assemblage on magmatism along the Aegean Arc, and implications for crustal growth (Vol. 385(1), pp. 137–160). London: *Geological Society*, Special Publications. https://doi. org/10.1007/s10570-017-1384-910.1144/sp385.1

90. Evans, D. A. D. (2009). The palaeo-magnetically viable, long-lived and all-inclusive Rodinia supercontinent reconstruction. *Geological Society Special Publication*, *327*, 371–404. https://doi.org/10.1144/SP327.16

91. Flament, N., Coltice, N., & Rey, P. F. (2008). A case for late-Archaean continental emergence from thermal evolution models and hypsometry. *Earth and Planetary Science Letters*, *275*(3-4), 326-336.

92. Foster, M.D. (1960). Interpretation of the composition of lithium micas. *U.S. Geological Survey*.

93. Frost, B., & Frost, C. (2013). Essentials of Igneous and Metamorphic Petrology (1st ed.). Cambridge: Cambridge University Press.

94. Frost, B.R, Barnes, C.G, Collins, W.J, Arculus, R.J, Ellis D.J, & Frost C.D. (2001). A geochemical classification for granitic rocks. *Journal of Petrology 42*, 2033-2048

95. Frost, C. D., & Frost, B. R. (2011). On Ferroan (A-type) Granitoids: their Compositional Variability and Modes of Origin. *Journal of Petrology*, *52*(1), 39–53. https://doi.org/10.1093/petrology/egq070

96. Frost, C. D., Bell, J. M., Frost, B. R., & Chamberlain, K. R. (2001). Crustal growth by magmatic underplating: isotopic evidence from the northern Sherman batholith. *Geology*, *29*(6), 515–518.

97. Frost, C. D., Frost, B. R., Chamberlain, K. R. & Edwards, B. R. (1999). Petrogenesis of the 1·43 Ga Sherman batholith, SE Wyoming: reduced rapakivi-type anorogenic granite. *Journal of Petrology 40*, 1771-1802

98. Frost, C. D., Frost, B. R., Chamberlain, K. R., & Hulsebosch, T. P. (1998). The Late Archean history of the Wyoming province as recorded by granitic magmatism in the Wind River Range, Wyoming. *Precambrian Research*, *89*(3-4), 145-173.

99. Fujii, M., Hayasaka, Y., & Terada, K. (2008). SHRIMP zircon and EPMA monazite dating of granitic rocks from the Maizuru terrane, southwest Japan: Correlation with East Asian Paleozoic terranes and geological implications. *Island Arc*, *17*(3), 322–341. https://doi.org/10.1111/J.1440-1738.2008.00623.X

100. Ghose, N. C. (1971). Chemical composition of Biotite in the metamorphic and granitic rocks of Richughuta , Dist. Palamau, Bihar. *Chemical Geology*, *7*, 107–121.

101. Ghose, N. C. (1983). Geology, tectonics and evolution of the Chhotanagpur Granite - Gneiss Complex, eastern India. *Recent Researches in Geology*, *10*, 211–247.

102. Ghose, N. C. (1992). Chhotanagpur gneiss-granulite complex, Eastern India: Present status and future prospect. *Indian Journal of Geology, 64*(1), 100–121.

103. Ghose, N. C., Shmakin, B. M., & Smirnov, V. N. (1973). Some geochronological observations on the Precambrians of Chotanagpur, Bihar, India. *Geological Magazine*, *110*(5), 477–482.

104. Ghosh N C, (1974). Experimental study of the melting relationships between palcosome and leucosome of a migmatite from Dypvag, South Norway, and its bearing on granite magma genesis. *Proc. 4lh Int. Cong, on Pressure Research*, Kyoto, 488-494;

105. Ghosh, N. C., and Chatterjee, N. (2008). Petrology, Tectonic setting and Source of Dykes and Related magmatic bodies in the Chotanagpur Gniessic Complex, Eastern India. In: *INDIAN DYKES: Geochemistry, Geophysics and Geochronology.*

106. Ghosh, S. K. & Sengupta, S. (1999). Boudinage and composite boudinage in superposed deformations and syntectonic migmatization. *Journal of Structural Geology, 21*, 97–110

107. Gibson G. M. and Ireland T. R. (1995). Granulite formation during continental extension in Fiordland, New Zealand. *Nature 375*, 479-482.

108. Gill, J.B. (1981). Orogenic andesites and plate tectonics. *Springer Verlag, Berlin, 358*.

109. Glazner, A. F., Bartley, J. M., & Coleman, D. S. (2019). A more informative way to name plutonic rocks. GSA Today. 29, 4-10.

110. Gorczyk, W., Hobbs, B., Gessner, K., & Gerya, T. (2013). Intracratonic geodynamics. *Gondwana Research*, *24*(3-4), 838-848.

111. Goswami, B. (2015). Petrography and geochemistry of Aegirine-Arfvedsonite bearing granite gneiss from Dimra Pahar, Hazaribagh District, Jharkhand, Eastern India: Implication for petrogenetic evolution. Conference: International Conference on Research Development in Environment, Social Sciences and Humanities At: University of Delhi (DU), Conference centre, New Delhi (India)

112. Goswami, B., & Bhattacharyya, C. (2008). Metamorphism of nepheline syenite gneisses from Chhotanagpur granite gneiss complex, Northeastern Puruliya district, Eastern India. In *Journal of the Geological Society of India 71*.

113. Goswami, B., & Bhattacharyya, C. (2010). Tectonothermal evolution of Chhotanagpur Granite Gneiss complex from northeastern part of Puruliya district, West Bengal, eastern India. *Indian Journal of Geology*, *80*(1-4), 41-54.

114. Goswami, B., & Bhattacharyya, C.R. (2014). Petrogenesis of shoshonitic granitoids, eastern India: Implications for the late Grenvillian post-collisional magmatism. *Geoscience frontiers*, *5*, 821-843.

115. Gumsley, A. P., Chamberlain, K. R., Bleeker, W., Söderlund, U., De Kock, M. O., Larsson, E. R., & Bekker, A. (2017). Timing and tempo of the Great Oxidation Event. *Proceedings of the National Academy of Sciences*, *114*(8), 1811-1816.

116. Guo, Q., Strauss, H., Kaufman, A. J., Schröder, S., Gutzmer, J., Wing, B., & Farquhar, J. (2009). Reconstructing Earth's surface oxidation across the Archean-Proterozoic transition. *Geology*, *37*(5), 399-402.

117. Guo, Z., & Wilson, M. (2012). The Himalayan leucogranites: Constraints on the nature of their crustal source region and geodynamic setting. *Gondwana Research*, *22*(2), 360–376. https://doi.org/10.1016/J.GR.2011.07.027

118. Halla J., Whitehouse M. J., Ahmad T., Bagai Z. (2017). Archaean granitoids: an overview and significance from a tectonic perspective. In: Betterton J., Craig J., Mendum J. R., Neller R., Tanner J. (eds) Aspects of the Life and Works of Archibald Geikie. *Geological Society, London, Special Publications* 449, 1–18.

119. Hanchar J. M., Miller C. F., Wooden J. L., Bennett V. C., & Staude J-MG (1994). Evidence from xenoliths for a dynamic lower crust, eastern Mojave desert, California. *Journal of Petrology 35,* 1377-1415

120. Hanson, G. N. (1978). The application of trace elements to the petrogenesis of igneous rocks of granitic composition. *Earth and Planetary Science Letters*, *38*(1), 26–43.

121. Harris, N. B. W., Pearce, J. A., & Tindle, A. G. (1986). Geochemical characteristics of collision-zone magmatism. *Geological Society, London, Special Publications*. https://doi.org/10.1144/GSL.SP.1986.019.01.04

122. Harris, N., Ayres, M. and Massey, J. (1995). Geochemistry of granitic melts produced during the incongruent melting of muscovite – implications for the extraction of Himalayan leucogranite magmas, *Journal of Geophysical Research, 100*, 15767-15777

123. Hazen R. M., Sverjensky D. A., Azzolini D., Bish D. L., Elmore S. C., Hinnov L., Milliken R. E. (2013). Clay mineral evolution. *American Mineralogist, 98*, 2007–2029.

124. Hazen, R. M., Papineau, D., Bleeker, W., Downs, R. T., Ferry, J. M., McCoy, T. J. ... & Yang, H. (2008). Mineral evolution. *American Mineralogist*, *93*(11-12), 1693-1720.

125. Hill R. I., Chappell B. W., Campbell I. H. (1992). Late Archaean granites of the southeastern Yilgarn Block, Western Australia: age, geochemistry, and origin. *Earth and Environmental Science Transactions of the Royal Society of Edinburgh, 83*, 211–226.

126. Hippe K., Miller A., von Quadt A., Peytcheva I., & Hammerschmidt K. (2016) Zircon geochronology of theKoraput alkaline complex: Insights from combinedgeochemical and U-Pb-Hf isotope analyses, andimplications for the timing of alkaline magmatism in the Eastern Ghats Belt, India. *Gondwana Research, 34,* 205-220

127. Hoffman, P. F. (1991). Did the breakout of Laurentia turn Gondwanaland inside-out? *Science, 252*(5011), 1409-1412.

128. Hokada T., Motoyoshi Y (2006). Electron microprobe technique for U–Th–Pb and REE chemistry of monazite, and its implications for pre-, peak- and post-metamorphic events of the Lützow-Holm Complex and the Napier Complex, East Antarctica. *Polar Geoscience, 19*, 118-151

129. Holland H. D. (2002). Volcanic gases, black smokers, and the great oxidation event. *Geochimica et Cosmochimica Acta, 66*, 3811–3826.

130. Holland H. D. (2006). The oxygenation of the atmosphere and oceans. *Philosophical Transactions of the Royal Society of Londo*n, *B 361*, 903–915.

131. Holland, H. D. (1985). The Chemical Evolution of the Atmosphere and Oceans. Princeton, N.J.: Princeton University Press. ISBN 0 691 08348 7 (hard covers), 0 691 02381 6 (paperback). *Geological Magazine*, *122*(4), 404–405.

132. Holmes, A., (1950). Age of uraninite from a pegmatite near Singar, Gaya district, India. *American Mineralogist, 35*, 19.

133. Holmes, A., (1955). Dating the Precambrian of Peninsular India and Ceylon. *Proceedings of Geological Association of Canada, 7*, 81–106.

134. Hossain, I., Tsunogae, T., Rajesh, H.M., Chen, B. & Arakawa, Y., (2007). Palaeoproterozoic U–Pb SHRIMP zircon age from basement rocks in Bangladesh: a possible remnant of Columbia supercontinent. *Comptes Rendus Geoscience 339*, 979–986

135. Hou, G., Santosh, M., Qian, X., Lister, G. S., & Li, J. (2008). Tectonic constraints on 1.3~ 1.2 Ga final breakup of Columbia supercontinent from a giant radiating dyke swarm. *Gondwana Research, 14*(3), 561-566.

136. Houseman, G. A., McKenzie, D. P., & Molnar, P. (1981). Convective instability of a thickened boundary layer and its relevance for the thermal evolution of continental convergent belts. *Journal of Geophysical Research: Solid Earth*, *86*(B7), 6115–6132. https://doi.org/10.1029/JB086IB07P06115

137. Hyndman, D. W. (1985). Petrology of igneous and metamorphic rocks (Second Edition) McGraw-Hill Book Co., New York

138. Hytönen, K., & Hautala, T. U. U. L. A. (1985). Aegirine and riebeckite of the alkali gneiss of Pikkukallio in the Honkamäki-Otanmäki region, Finland. Bulletin *of the Geological Society of Finland*, *57*, 169-180.

139. Irvine, T. N., & Baragar, W. R. A. (1971). A Guide to the Chemical Classification of the Common Volcanic Rocks. *Canadian Journal of Earth Sciences*, *8*(5), 523–548. https://doi.org/10.1139/e71-05

140. Jahn, B. M. (1988). Pb–Pb dating of young marbles from Taiwan. *Nature*, *332*(6163), 429-432.

141. Jayananda, M., Moyen, J. F., Martin, H., Peucat, J. J., Auvray, B., & Mahabaleswar, B. (2000). Late Archaean (2550–2520 Ma) juvenile magmatism in the Eastern Dharwar craton, southern India: constraints from geochronology, Nd–Sr isotopes and whole rock geochemistry. *Precambrian Research*, *99*(3–4), 225–254. https://doi.org/10.1016/S0301-9268(99)00063-7

142. Jefferson, C.W., & Parrish, R. (1989). Late Proterozoic stratigraphy, U–Pb zircon ages, and rift tectonics, Mackenzie Mountains, northwestern Canada. *Canadian Journal of Earth Sciences*, *26*, 1784-1801.

143. Jiménez-Munt, I., Fernàndez, M., Vergés, J., & Platt, J. P. (2008). Lithosphere structure underneath the Tibetan Plateau inferred from elevation, gravity and geoid anomalies. *Earth and Planetary Science Letters*, *267*(1–2), 276–289.

144. Johannes, W., & Holtz, F. (1996). Petrogenesis and experimental petrology of granitic rocks. *Springer*.

145. Joshi, B. K., Bhattacharjee, J., Rai, G., Halla, J., Ahmad, T., Kurhila, M., & Choudhary, A. K. (2017). The diversification of granitoids and plate tectonic implications at the Archaean–Proterozoic boundary in the Bundelkhand Craton, Central India. *Geological Society, London, Special Publications*, *449*(1), 123-157.

146. Jull, M., & Kelemen, P. Á. (2001). On the conditions for lower crustal convective instability. *Journal of Geophysical Research: Solid Earth*, *106*(B4), 6423-6446.

147. Kalsbeek, F., Higgins, A. K., Jepsen, H. F., Frei, R., Nutman, A. P., Gilotti, J. A., & Smith, M. P. (2008). Granites and granites in the East Greenland Caledonides. *The Greenland Caledonides: Evolution of the Northeast Margin of Laurentia. Geological Society of America, Memoirs*, *202*, 227-249.

148. Karmakar, S., Bose, S., Sarbadhikari, A. B., & Das, K. (2011). Evolution of granulite enclaves and associated gneisses from Purulia, Chhotanagpur Granite Gneiss Complex, India: Evidence for 990-940Ma tectonothermal event(s) at the eastern India cratonic fringe zone. *Journal of Asian Earth Sciences*.

149. Kasting J. F. (2001). The rise of atmospheric oxygen. *Science, 293*, 819–820

150. Katsube, A., Hayasaka, Y., Sakaguchi, A., & Takahashi, Y. (2012). U-Pb zircon dating using Nd-YAG (213 nm) Laser ablation-ICP-MS, and evaluating the consistency with SHRIMP dating. In *The Journal of the Geological Society of Japan 118*.

151. Kay R. W. & Kay S. M. (1993). Delamination and delamination magmatism. *Tectonophys.*219: 177-189

152. Keller B., Schoene B. (2018). Plate tectonics and continental basaltic geochemistry throughout Earth history. *Earth and Planetary Science Letters, 481*, 290–304.

153. Keller C. B., Schoene B. (2012). Statistical geochemistry reveals disruption in secular lithospheric evolution about 2·5 Ga ago. *Nature 485*, 490–493.

154. Khanna, P. P., Saini, N. K., Mukherjee, P., & Purohit, K. K. (2009). An appraisal of ICP-MS technique for determination of REEs: Long term QC assessment of silicate rock analysis. *Himalayan Geology*, *30*, 95–99.

155. King, P. L., Chappell, B. W., Allen, C. M., & White, A. J. R. (2001). Are A-type granites the high-temperature felsic granites? Evidence from fractionated granites of the Wangrah Suite. *Australian Journal of Earth Sciences*, *48*(4), 501–514.

156. King, P. L., Chappell, B. W., White, A. J. R., & Williams, I. S. (1992). A-type granites from the Lachlan Fold Belt, eastern Australia. *EOS, Transactions, American Geophysical Union*, *73*, 346.

157. King, P. L., White, A. J. R., Chappell, B. W., & Allen, C. M. (1997). Characterization and Origin of Aluminous A-type Granites from the Lachlan Fold Belt, Southeastern Australia. *Journal of Petrology*, *38*(3), 371–391. https://doi.org/10.1093/PETROJ/38.3.371

158. Krishna V, Sastry D, Pandey BK, Sinha RP (2003). U-Pb and Pb-Pb ages on columbite-tantalite minerals from pegmatites of Bihar Mica Belt, Jharkhand, India. In: ISMAS silver jubilee symposium on mass spectrometry. V. 2: contributed papers

159. Krishnan, M. S. (1953). The structural and tectonic history of India. *Memoir of Geological Survey of India*, *81*, 137

160. Krystopowicz, N. J., & Currie, C. A. (2013). Crustal eclogitization and lithosphere delamination in orogens. *Earth and Planetary Science Letters*, *361*, 195–207. https://doi.org/10.1016/J.EPSL.2012.09.056

161. Kumar, A., Charan, S.N., Gopalan, K. & Macdougall, J.D., (1998). Along-lived enriched mantle source for two Proterozoic carbonatite complexes from Tamil Nadu, southern India. *Geochimica et Cosmochimica Acta, 62*(3), 515-523

162. Kump L. R., Barley M. E. (2007). Increased subaerial volcanism and the rise of atmospheric oxygen 2·5 billion years ago. *Nature*, *448*, 1033–1036.

163. Kump L. R., Kasting J. F., Barley M. E. (2001). Rise of atmospheric oxygen and the 'upside-down' Archean mantle. *Geochemistry Geophysics. Geosystems, 2*, 1025.

164. Laflèche, M. R., Dupuy, C., & Dostal, J. (1991). Archaean orogenic ultrapotassic magmatism: an example from the southern Abitibi greenstone belt. *Precambrian Research*, *52*(1–2), 71–96.

165. Lal, N., Saini, H. S., Nagpaul, K. K., & Sharma, K. K. (1976). Tectonic and cooling history of the Bihar Mica Belt, India, as revealed by fission-track analysis. *Tectonophysics*, *34*(3–4), 163–180. https://doi.org/10.1016/0040-1951(76)90094-9

166. Laurent, A., Janousek, V., Magna, T., Schulmann, K., Mikova, J., Laurent, A., Janousek, V., Magna, T., Schulmann, K., & Mikova, J. (2014). Petrogenesis and geochronology of a post-orogenic calc-alkaline magmatic association: the Zulova Pluton, Bohemian Massif. *Journal of Geosciences, 59*(4), 415–440. https://doi.org/10.3190/JGEOSCI.176

167. Le Maitre R.W., Bateman P., Dudek A., Keller J., Lameyre J., Le Bas M.J., Sabine P.A., Schmid R., Sorensen H., Streckeisen A., Woolley A.R. & Zanettin B. (1989). A classification of igneous rocks and glossary of terms: Recommendations of the International Union of

Geological Sciences Subcommission on the Systematics of Igneous Rocks. Blackwell Scientific Publications, Oxford, U.K.

168. Le Pourhiet, L., Gurnis, M., & Saleeby, J. (2006). Mantle instability beneath the Sierra Nevada mountains in California and Death Valley extension. *Earth and Planetary Science Letters*, *251*(1-2), 104-119.

169. Lee, H.Y., & Ganguly, J. (1988). Equilibrium compositions of coexisting garnet and orthopyroxene: Reversed experimental determinations in the system FeO-MgO-Al2O3- SiO2, and applications: *Journal of Petrology, 29*, 93-113

170. Levander, A., Schmandt, B., Miller, M. S., Liu, K., Karlstrom, K. E., Crow, R. S., & Humphreys, E. D. (2011). Continuing Colorado plateau uplift by delamination-style convective lithospheric downwelling. *Nature*, *472*(7344), 461-465.

171. Li, Z. X., Evans, D. A. D., & Zhang, S. (2004). A 90 spin on Rodinia: possible causal links between the Neoproterozoic supercontinent, superplume, true polar wander and low-latitude glaciation. *Earth and Planetary Science Letters*, *220*(3-4), 409-421.

172. Li, Z. X., Li, X. H., Kinny, P. D., & Wang, J. (1999). The breakup of Rodinia: did it start with a mantle plume beneath South China? *Earth and Planetary Science Letters*, *173*(3), 171-181.

173. Li, Z. X., Li, X. H., Zhou, H., & Kinny, P. D. (2002). Grenvillian continental collision in south China: New SHRIMP U-Pb zircon results and implications for the configuration of Rodinia. *Geology*, *30*(2), 163-166.

174. Li, Z. X.; Bogdanova, S. V.; Collins, A. S.; Davidson, A.; De Waele, B.; Ernst, R. E.; Fitzsimons, I. C. W.; Fuck, R. A.; Gladkochub, D. P.; Jacobs, J.; Karlstrom, K. E.; Lul, S.; Natapov, L. M.; Pease, V.; Pisarevsky, S. A.; Thrane, K.; Vernikovsky, V. (2008). Assembly,

configuration, and break-up history of Rodinia: a synthesis. *Precambrian research*, *160*(1-2), 179-210.

175. Liegeois, J. P., Navez, J., Hertogen, J., & Black, R. (1998). Contrasting origin of post-collisional high-K calc-alkaline and shoshonitic versus alkaline and peralkaline granitoids. The use of sliding normalization. *Lithos*, *45*(1-4), 1-28.

176. Lippolt, H. J., & Hautmann, S. (1995). 40Ar/39Ar ages of Precambrian manganese ore minerals from Sweden, India and Morocco. *Mineralium Deposita*, *30*(3), 246-256.

177. Litvinovsky, B. A., Tsygankov, A. A., Jahn, B. M., Katzir, Y., & Be'eri-Shlevin, Y. (2011). Origin and evolution of overlapping calc-alkaline and alkaline magmas: The Late Palaeozoic post-collisional igneous province of Transbaikalia (Russia). *Lithos*, *125*(3-4), 845-874.

178. Loiselle, M. C., & Wones, D. R. (1979). Characteristics of Anorogenic Granites. *Geological Society of America, 11*, 468.

179. Lu, L. Z., Xu, X. C., and Liu, F.L. (1996). Early Cambrian khondalite series in northern China: Changchun, China, *Changchun Publishing House, 276* (in Chinese).

180. Ludwig KR (2003). User's Manual for Isoplot 3.6 (April 2008 revision).Berkeley Geochronology Center Special Publication 4.

181. Ludwig, K. (2012). User's Manual for Isoplot 3.75 A Geochronological Toolkit for Microsoft Excel, Berkeley, CA, Berkeley Geochronological Center Special Publication No. 5

182. Lyons T. W., Reinhard C. T., Planavsky N. J. (2014). The rise of oxygen in Earth's early ocean and atmosphere. Nature 506, 307–315.

183. Magni, V., & Király, Á. (2019). Delamination. *Reference Module in Earth Systems and Environmental Sciences*. https://doi.org/10.1016/B978-0-12-409548-9.09515-4

184. Mahadevan, T. M. (2002). Geology of Bihar and Jharkhand. *Geological Society of India*, *60*(1), 66–66.

185. Mahmoud, M. Y., Mitra, A. K., Dhar, R., Sarkar, S. & Mandal, N. (2008). Repeated emplacement of syntectonic pegmatites in Precambrian granite gneisses: indication of pulsating brittle–ductile rheological transitions. In: Srivastava, R. K. (ed.) Indian Dykes: Geochemistry, Geophysics, and Geochronology. Narosa, New Delhi.

186. Maji, A. K., Goon, S., Bhattacharya, A., Mishra, B., Mahato, S., & Bernhardt, H. J. (2008). Proterozoic polyphase metamorphism in the Chhotanagpur Gneissic Complex (India), and implication for trans-continental Gondwanaland correlation. *Precambrian Research*. https://doi.org/10.1016/j.precamres.2007.10.002

187. Mallik A. K., Gupta S.N., & Barman Ray T. (1991) Dating of early Precambrian granite-greenstone complex of the eastern Indian Precambrian shield with special reference to the Chotanagpur granite gneiss complex. *Record of Geological Survey of India*, *125*, 20–21

188. Maniar, P. D., & Piccoli, P. M. (1989). Tectonic discrimination of granitoids. *Geological Society of America Bulletin*, *101*(5), 635–643.

189. Manna, S. S., & Sen, S. K. (1974). Origin of garnet in the basic granulites around Saltora, W. Bengal, India. *Contributions to Mineralogy and Petrology*, *44*(3), 195–218.

190. Martin H., Moyen J. F., Rapp R. (2009). The sanukitoid series: magmatism at the Archaean–Proterozoic transition. *Earth and Environmental Science Transactions of the Royal Society of Edinburgh*, *100*, 15–33.

191. Martin, H. (1986). Effect of steeper Archean geothermal gradient on geochemistry of subduction-zone magmas. *Geology*, *14*(9), 753-756.

192. Martin, H. (1987). Petrogenesis of Archaean Trondhjemites, Tonalites, and Granodiorites from Eastern Finland: Major and Trace Element Geochemistry. *Journal of Petrology*, *28*(5), 921–953. https://doi.org/10.1093/PETROLOGY/28.5.921

193. Martin, H. (1994). Chapter 6 The Archean Grey Gneisses and the Genesis of Continental Crust. *Developments in Precambrian Geology*, *11*(C), 205–259.

194. Martin, R.F. (2006): A-type granites of crustal origin ultimately result from open-system fenitization-type reactions in an extensional environment. *Lithos 91*, 125-136

195. Mazumdar, S. K. (1988): Crustal evolution of the Chhotanagpur Gneissic Complex and the Mica belt of Bihar. In Precambrian of Eastern Indian shield (Ed. D. Mukhopadhyay), *Memoir of Geological Society of India, 8*, 49-83.

196. Mazumder, S.K. (1979). Precambrian geology of eastern India between the Ganga and Mahanadi— a review. *Record of Geological Survey of India, 110*, 60–116.

197. Mazumder, S.K. (1996) Precambrian geology of Peninsular eastern India -a perspective review. *Indian Mineralogist, 50*, 139-174

198. McDonough, W. F., & Sun, S. -s. (1995). The composition of the Earth. *Chemical Geology*, *120*(3–4), 223–253. https://doi.org/10.1016/0009-2541(94)00140-4

199. McKenzie, D. (1984). The Generation and Compaction of Partially Molten Rock. *Journal of Petrology, 25* (3), 713-765.

200. McMenamin, M. A., & McMenamin, D. L. S. (1990). The Emergence of Animals the Cambrian Breakthrough. In *The Emergence of Animals the Cambrian Breakthrough*. Columbia University Press.

201. Meert, J. G., & Santosh, M. (2017). The Columbia supercontinent revisited. *Gondwana Research, 50*, 67–83. https://doi.org/10.1016/J.GR.2017.04.011

202. Meissner R and Mooney WD (1998) Weakness of the lower continental crust: A condition for delamination, uplift, and escape. *Tectonophysics* 296: 47–60.

203. Melnikova, G., (1964). Geochronology of India (Precambrian). Proc. 22nd Intern. Geol.

204. Miller, C.F., McDowell, S. M., & Mapes, R. W (2003). Hot and cold granites? Implications of zircon saturation temperatures and preservation of inheritance. *Geology*, *31* (6): 529–532. doi: https://doi.org/10.1130/0091-7613(2003)031<0529:HACGIO>2.0.CO;2

205. Miyashiro, A. (1974). Volcanic Rock Series in Island Arcs and Active Continental Margins. *American Journal of Science, 274*, 321-355.https://doi.org/10.2475/ajs.274.4.321

206. Molnar, P., Houseman, G. A., & Conrad, C. P. (1998). Rayleigh—Taylor instability and convective thinning of mechanically thickened lithosphere: effects of non-linear viscosity decreasing exponentially with depth and of horizontal shortening of the layer. *Geophysical Journal International*, *133*(3), 568-584.

207. Moores, E. M. (1991). "Southwest US-East Antarctic (SWEAT) connection: a hypothesis". *Geology*. 19 (5): 425–428.

208. Morency, C., & Doin, M. P. (2004). Numerical simulations of the mantle lithosphere delamination. *Journal of Geophysical Research: Solid Earth*, *109*(B3).

209. Moyen J. F., Martin H., Jayananda M., Auvray B. (2003). Late Archaean granites; a typology based on the Dharwar Craton, India. Precambrian Research 127, 103–123.

210. Mukherjee, D., Ghose, N. C. & Chatterjee, N. (2005). Crystallization history of a massif anorthosite in the eastern Indian shield margin based on borehole lithology. *Journal of Asian Earth Sciences, 25*, 77–94.

211. Mukherjee, S., Dey, A., Ibanez-Mejia, M., Sanyal, S., & Sengupta, P. (2018). Geochemistry, U-Pb geochronology and Lu-Hf isotope systematics of a suite of ferroan (A-type) granitoids

from the CGGC: Evidence for Mesoproterozoic crustal extension in the east Indian shield. *Precambrian Research, 305,* 40–63. https://doi.org/10.1016/j.precamres.2017.11.018

212. Mukherjee, S., Dey, A., Sanyal, S., & Sengupta, P. (2019) Proterozoic Crustal Evolution of the Chotanagpur Granite Gneissic Complex, Jharkhand-Bihar-West Bengal, India: Current Status and Future Prospect. In *Tectonics and Structural Geology: Indian Context*. Springer International Publishing. 7-54. doi:10.1007/978-3-319-99341-6_2

213. Mukherjee, S., Dey, A., Sanyal, S., Ibanez-Mejia, M., Dutta, U., & Sengupta, P. (2017). Petrology and U-Pb geochronology of zircon in a suite of charnockitic gneisses from parts of the Chotanagpur Granite Gneiss Complex (CGGC): Evidence for the reworking of a Mesoproterozoic basement during the formation of the Rodinia supercontinent. *Geological Society Special Publication, 457*(1), 197–231. https://doi.org/10.1144/SP457.6

214. Mukhopadhyay, S. (2022). Petrology, Geochemistry and U-Pb zircon geochronology of Alkali granites of Jhalda, Eastern India and their possible linkage to Rodinia Supercontinent. *Journal of Earth System Science* (in press).

215. Mukhopadhyay, S., Ray, J., Chattopadhyay, B., Sengupta, S., Ghosh,B. and Mukhopadhyay, S., (2011a). Significance of mineral chemistry of syenites and associated rocks of Elagiri Complex, Southern Granulite Terrane of the Indian Shield. *Journal of the Geological Society of India, 77*(2), .113-129

216. Myers, J S. (1997). Geology of granite. Journal of the Royal Society of Western *Australia, 80,* 87-100.

217. Nachit, H. (1985). Composition chimique des biotites et typologie magmatique des granitoids. *Comptes Rendus de l'Académie des Sciences. Paris, 301*, 813–818.

218. Nance R.D., Murphy J.B. & Santosh M. (2014). The supercontinent cycle: a retrospective essay. *Gondwana Research*, 25, 4–29.

219. Natarajan, M., Bhaskara Rao, B., Parthasarathy, R., Anil Kumar and Gopalan, K. (1994) 2.0Ga. old pyroxenite – carbonatite complex of Hogenakal, Tamil Nadu, South India, Precambrian. Research, 65, 167-181.

220. Nedelec, A. and Bouchez, J.L. (2015). Granites: petrology, structure, geological setting, and metallurgy. Oxford, Ltd, Croydon, ISBN 978-0-19-870561-1, 335

221. Nisbet E. G. (1987). The Young Earth: an Introduction to Archaean Geology. Boston and London (Unwin Hyman Ltd.).

222. Nockolds, S. R. (1947). The relation between chemical composition and paragenesis in the biotite micas of igneous rocks. *American Journal of Science. 245*(7), 401-420

223. O`Connor, J.T. (1965). A classification of quartz rich igneous rock based on feldspar ratios. *US Geological Survey*, 525B, B79-B84

224. Osborn, E. F. (1962). Reaction series for subalkaline igneous rocks based on different oxygen pressure conditions. *American Mineralogist 47*, 211-26.

225. Paces, J. B., & Miller, J. D. (1993). Precise U-Pb ages of Duluth Complex and related mafic intrusions, northeastern Minnesota: Geochronological insights to physical, petrogenetic, paleomagnetic, and tectonomagmatic processes associated with the 1.1 Ga Midcontinent Rift System. *Journal of Geophysical Research: Solid Earth*, *98(*B8), 13997–14013. https://doi.org/10.1029/93JB01159

226. Pandey, B. K., Gupta, J. N., Lall, Y., & Mahadevan, T. M. (1986). Rb− Sr isochron and Sm− Nd model ages for soda granites from Singhbhum Shear Zone, Bihar and their bearing on crustal evolution. *Indian Journal of Earth Sciences*, *13*(2–3), 117–128.

227. Park, J. K., Buchan, K. L., and Harlan, S. S. (1995). A proposed giant radiating dyke swarm fragmented by the separation of Laurentia and Australia based on paleomagnetism of ca. 780 Ma mafic intrusions in western North America. *Earth and Planetary Science Letters, 132*, 129–139.

228. Patel, S. C. (2007). Vesuvianite–wollastonite–grossularbearing calc-silicate rock near Tatapani, Surguja district, Chhattisgarh. *Journal of Earth System Science, 116*, 143–147.

229. Patel, S. C., Sundararaman, S., Dey, R., Thakur, S. S. & Kumar, M. (2007). Deformation pattern in a Proterozoic low pressure metamorphic belt near Ramanujganj, western Chotanagpur terrane. *Journal of the Geological Society of India, 70*, 207–216

230. Patino Douce, A. E., & Harris, N. (1998). Experimental Constraints on Himalayan Anatexis. *Journal of Petrology*, *39*(4), 689–710. https://doi.org/10.1093/petroj/39.4.689

231. Paul, D., Chandra, J., & Halder, M. (2020). Proterozoic Alkaline rocks and Carbonatites of Peninsular India: A review. *Episodes Journal of International Geoscience*, *43*(1), 249–277. https://doi.org/10.18814/EPIIUGS/2020/020015

232. Peacock, M. A. (1931). Classification of igneous rock series. *Journal of Geology, 39*, 54–67.

233. Pearce, J. (1983). Role of the sub-continental lithosphere in magma genesis at active continental margin. *Continental Basalts and Mantle Xenoliths.* 230-249.

234. Pearce, J. A., Harris, N. B. W., & Tindle, A. G. (1984). Trace Element Discrimination Diagrams for the Tectonic Interpretation of Granitic Rocks. *Journal of Petrology*, *25*(4), 956–983. http://dx.doi.org/10.1093/petrology/25.4.956

235. Pearce, J.A. (1996). A User's Guide to Basalt Discrimination Diagrams. In: Wyman, D.A., Ed., Trace Element Geochemistry of Volcanic Rocks: Applications for Massive Sulphide Exploration, *Geological Association of Canada*, Short Course Notes, 12, 79-113.

236. Peccerillo, A. and Taylor, S.R. (1976). Geochemistry of Eocene Calc-Alkaline Volcanic Rocks from the Kastamonu Area, Northern Turkey. Contributions to Mineralogy and *Petrology, 58*, 63-81. http://dx.doi.org/10.1007/BF00384745

237. Pitcher, W. S. (1997). The Nature and Origin of Granite. Chapman & Hall, 2nd edition. 10.1007/978-94-011-5832-9, 387

238. Pitcher, W.S. (1993). The Nature and origin of granite,. Blackie Academic & Professional, London. 321

239. Planavsky N. J., Asael D., Hofmann A., Reinhard C. T., Lalonde S. V., Knudsen A., Wang X., Ossa Ossa F., Pecoits E., Smith A. J. B., Beukes N. J., Bekker A., Johnson T. M., Konhauser K. O., Lyons T. W., & Rouxel O. J. (2014). Evidence for oxygenic photosynthesis half a billion years before the Great Oxidation Event. *Nature Geoscience 7*, 283.

240. Plank, T. (2016). Subduction zone geochemistry. Springer International Publishing Switzerland. W. M. White (editor). *Encyclopedia of Geochemistry, 213*(2004), 1384–1393. https://doi.org/10.1007/978-3-319-39193-9_268-1

241. Poldervaart, A. (1956). Zircon in rocks. Igneous rocks: *American Journal of Science, 254*, 521-554.

242. Prasad, U. (1975). Andalusite deposit near Nagar Untari, Palamau district, Bihar. *Indian Mineralogist 29*, 32-38.

243. Prasad, U. (1976). Geology and petrochemistry of a part of Hesatu-Belbathan polymetallic mineralised belt, Eastern Bihar. *Memoir of Geological Survey of India 107*, 130

244. Pupin, J.P., (1980). Zircon and granite petrology. Contribution to *Mineralogy and. Petrology 110*, 463–472

245. Querré, G. (1985). Palingogenesis of continental crust in the Archean: the late granitoids (2.5–2.4 Ga) of eastern Finland. Petrology and geochemistry. Memoirs and Documents of the Armorican Center for Structural Study of Bases. No. 2. University of Rennes.

246. Ranjan, S., Upadhyay, D., Abhinay, K., Pruseth, K. L., & Nanda, J. K. (2018). Zircon geochronology of deformed alkaline rocks along the Eastern Ghats Belt margin: India–Antarctica connection and the Enderbia continent. *Precambrian Research, 310*, 407–424. https://doi.org/10.1016/J.PRECAMRES.2018.04.005

247. Rasmussen B., & Buick R. (1999). Redox state of the Archean atmosphere: evidence from detrital heavy minerals in ca. 3250–2750 Ma sandstones from the Pilbara Craton, Australia. *Geology 27*, 115–118.

248. Ray Barman, T., Bishui, P.K., Mukhopadhyay, K., Ray, J. N. (1994). Rb–Sr geochronology of the high-grade rocks from Purulia, West Bengal and Jamua-Dumka sector, Bihar. *Indian Minerals*, *48*, 45–60.

249. Ray, A. (2008). Tectonic control of North Purulia Shear Zone on emplacement of ultramafic and associated rocks. In: *International Conference on Geology Indian Scenario and Global Perspective*.

250. Ray, J. S. (2008). Radiogenic isotopic ratio variations in carbonatites and associated alkaline silicate rocks: role of crustal assimilation. *Journal of Petrology*, *50*(10), 1955-1971.

251. Ray, J., Saha, A., Ganguly, S., Balaram, V., Keshav Krishna, A., & Hazra, S. (2011). Geochemistry and petrogenesis of Neoproterozoic Mylliem granitoids, Meghalaya Plateau, northeastern India. *Journal of Earth System Science, 120,* 459–473.

252. Ray, S., & Gangopadhyay, P. K. (1971). Metamorphic belt of Singhbhum, Manbhum and Chottanagpur. *Journal of Geological Society of India 12*, 286–294

253. Ray, S., Sanyal, S., & Sengupta, P. (2011). Mineralogical Control on Rheological Inversion of a Suite of Deformed Mafic Dykes from Parts of the Chottanagpur Granite Gneiss Complex of Eastern India. *Dyke Swarms: Keys for Geodynamic Interpretation*, 263–276. https://doi.org/10.1007/978-3-642-12496-9_15

254. Read, H. H. (1957). The granite controversy. *Geologiska Föreningen i Stockholm Förhandlingar*, *79*(3), 591-593.

255. Reddy, S.M. & Evans, D. A. D. (2009). Palaeoproterozoic supercontinents and global evolution: correlations from core to atmosphere. In: Reddy, S.M., Mazumder, R., Evans, D.A.D, & Collins, A.S. (eds) Palaeoproterozoic Supercontinents and Global Evolution.

256. Rehman, H.U., Khan, T., Jan, M.Q., Lee, H-Y.,Chung, S-L., & Murata, M. (2018). Timing and span of the continental crustal growth in SE Pakistan: Evidence from LA-ICP-MS U–Pb zircon ages from granites of the Nagar Parkar Igneous Complex. *Gondwana Research, 61*, 172-186.

257. Reinhard C. T., Lalonde S. V., Lyons T. W. (2013). Oxidative sulfide dissolution on the early Earth. *Chemical Geology, 362*, 44–55

258. Rekha, S., Upadhyay, D., Bhattacharya, A., Kooijman, E., Goon, S., Mahato, S., & Pant, N. C. (2011). Lithostructural and chronological constraints for tectonic restoration of Proterozoic accretion in the Eastern Indian Precambrian shield. *Precambrian Research*, *187*(3–4), 313–333. https://doi.org/10.1016/j.precamres.2011.03.015

259. Renjith, M. L., Charan, S. N., Subbarao, D. v., Babu, E. V. S. S. K., & Rajashekhar, V. B. (2014). Grain to outcrop-scale frozen moments of dynamic magma mixing in the syenite magma chamber, Yelagiri Alkaline Complex, South India. *Geoscience Frontiers*, *5*(6), 801–820. https://doi.org/10.1016/J.GSF.2013.08.006

260. Rickwood, P. C. (1989). Boundary lines within petrologic diagrams which use oxides of major and minor elements. *Lithos, 22* (1989) 247-263

261. Rizzotto, G. J., Hartmann, L. A., Santos, J. O., & McNaughton, N. J. (2014). Tectonic evolution of the southern margin of the Amazonian craton in the late Mesoproterozoic based on field relationships and zircon U-Pb geochronology. *Anais da Academia Brasileira de Ciências*, *86*, 57-84.

262. Roberts, M P., Clemens, J D. (1993). Origin of high-potassium, calc-alkaline, I-type granitoids. *Geology*, *21* (9): 825–828.

263. Rogers, J. J., & Santosh, M. (2002). Configuration of Columbia, a Mesoproterozoic supercontinent. *Gondwana Research*, *5*(1), 5-22.

264. Rogers, J. J., & Santosh, M. (2003). Supercontinents in Earth history. *Gondwana Research*, *6*(3), 357-368.

265. Rogers, John & Santosh, M.. (2004). Continents and Supercontinents. *Gondwana Research, 7*, 653-653. 10.1016/S1342-937X(05)70827-3.

266. Rollinson, H. R. (1993). Using Geochemical Data : Evaluation, Presentation, and Interpretation. Routledge. https://doi.org/10.4324/9781315845548

267. Roy, A. K. (1977). Structure and metamorphic evolution of the Bengal anorthosite and associated rocks. *Journal of the Geological Society of India*, *18*, 203–223.

268. Roy, A., Devarajan, M. K. & Prasad, H. (2002). Ductile shearing and syntectonic granite emplacement along the southern margin of the Palaeoproterozoic Mahakoshal supracrustal belt: evidence from Singrauli Area, Madhya Pradesh. *Journal of the Geological Society of India*, *59*, 9–21.

269. Saha A K, (1994). Crustal evolution of Singbhum - North Orissa, Eastern India. *Geological Society of India, Memoir 27.*

270. Saha, S., Das, K., Hidaka, H., Kimura, K., Chakraborty, P. P., & Hayasaka, Y. (2016). Detrital zircon geochronology (U–Pb SHRIMP and LA-ICPMS) from the Ampani Basin, Central India: Implication for provenance and Mesoproterozoic tectonics at East Indian cratonic margin. *Precambrian Research*, *281*, 363–383.

271. Saikia, A., Gogoi, B., Kaulina, T., Lialina, L., Bayanova, T., & Ahmad, M. (2017). Geochemical and U-Pb zircon age characterization of granites of the Bathani Volcano Sedimentary sequence, Chotanagpur Granite Gneiss Complex, eastern India: Vestiges of the Nuna supercontinent in the Central Indian Tectonic Zone. *Geological Society Special Publication*, *457*(1), 233–252. https://doi.org/10.1144/SP457.11

272. Santosh, M., Iyer, S. S., Vasconcellos, M. B. A., & Enzweiler, J. (1989). Late Precambrian alkaline plutons in southwest India: Geochronological and rare-earth element constraints on Pan-African magmatism. *Lithos*, *24*, 65–79.

273. Sanyal, S., & Sengupta, P. (2012). Metamorphic evolution of the Chotanagpur Granite Gneiss Complex of the East Indian Shield: current status. *Geological Society, London, Special Publications*, *365*(1), 117–145. https://doi.org/10.1144/SP365.7

274. Sanyal, S., Sengupta, P. & Goswami, R. (2007). Evidence of Mesoproterozoic ultra-high temperature metamorphism from parts of CGGC, Jharkhand, India. Abstract Volume of the International Conference on Precambrian Sedimentation and Tectonics and Second GPSS Meeting. Indian Institute of Technology, 62–63.

275. Sarkar, A. N., (1988). Tectonic evolution of the Chhotanagpur plateau and Gondwana basins in Eastern India: An interpretation based .on supra-subduction geological processes. In

Precambrian of the Eastern Indian Shield, D Mukhopadhyay (ed.), Memoir 8, *Geological Society of India,* 127-146.

276. Sarkar, A.N. and Jha, B. N. (1985). Structure, metamorphism and granite evolution of the Chhotanagpur granite gneiss complex around Ranchi. *Record of Geological Survey of India, 113*(3), 1–12.

277. Sarkar, D. N, (1977). Occurrences of arseniferous minerals in. pegmatite veins of Belamu, P.S. Jhalida, Dist. Purulia — a preliminary report. *Journal of Mines Metals Fuels, 26*, 263-264

278. Sarkar, P. & Bandyopadhyay, K.C. & Singh, B. & Sarkar, S. (2001). On the rare-metal-bearing pegmatite bodies within the Chotanagpur Gneissic Complex and its geological environ in Purulia District, West Bengal. *Indian Minerals. 55*. 55-66.

279. Sarkar, P., & Bandyopadhyay, K. C., (1993). Study of Chhotanagpur Gneissic Complex. *Record of Geological Survey of India, 126*(3), 81-84

280. Sarkar, S. C., Bhattacharyya, P. K., & Mukherjee, A. D. (1980). Evolution of the sulfide ores of Saladipura, Rajasthan, India. *Economic Geology*, *75*(8), 1152–1167.

281. Sarkar, S. N., (1968). Precambrian stratigraphy and geochronology of peninsular India. Dhanbad Publishers, Dhanbad, 33

282. Saunders, A. D., Tarney, J. & Weaver, S. D. (1980). Transverse geochemical variations across the Antarctic Peninsula: implications for the genesis of calc-alkaline magmas. *Earth planetary Science Letters 46*, 344-360

283. Scherer, E. E., Whitehouse, M. J., & Münker, C. (2007). Zircon as a Monitor of Crustal Growth. *Elements*, *3*(1), 19–24. https://doi.org/10.2113/GSELEMENTS.3.1.19

284. Schotese, C. R. (2009). "Late Proterozoic plate tectonics and palaeogeography: a tale of two supercontinents, Rodinia and Pannotia". *Geological Society of London, Special Publications. 326* (1), 67–83.

285. Scoates, J. S., & Chamberlain, K. R. (1995). Baddeleyite (ZrO2) and zircon (ZrSiO4) from anorthositic rocks of the Laramie anorthosite complex, Wyoming: Petrologic consequences and U-Pb ages. *American Mineralogist, 80*(11–12), 1317–1327. https://doi.org/10.2138/AM-1995-11-1222

286. Scott C., Lyons T. W., Bekker A., Shen Y., Poulton S. W., Chu X., Anbar A. D. (2008). Tracing the stepwise oxygenation of the Proterozoic ocean. *Nature 452*, 456–458.

287. Sen, S. (1956). Structures of porphyritic granite and associated rocks in east Manbhum, Bihar, India. *Bulletin of the Geological Society of America 67*,647-670

288. Sen, S. (1959). Mineralogic trends in the evolution of metamorphic rocks and origin of granites of East Manbhum, India. Proceedings: National Institute of Science of India 25A, No.2.

289. Sen, S. K. & Manna, S. S., (1976). Patterns of cation fractionation among pyroxenes, hornblende and garnet in the basic granulites of Saltora, West Bengal. *Indian Journal of Earth science, 3,* 117-128.

290. Sen, S.K. & Bhattacharya, A. (1993). Post-peak pressure temperature fluidhistory of the granulites around Saltora, West Bengal. *Proceedings of the National Academy of Sciences of India*, 282–306.

291. Sen, S.K. and Bhattacharya, A. (1985). Fluid induced metamorphic changes in the Bengal anorthosite around Saltora, West Bengal, India. *Indian Journal of Earth science, 13*, 45-64.

292. Şengör, A. M. C., Özeren, S., Genç, T., & Zor, E. (2003). East Anatolian high plateau as a mantle-supported, north-south shortened domal structure. *Geophysical Research Letters*, *30*(24).

293. Sengupta, D.K. & Sarkar, S.N. (1964). Structure of the granitic rock and associated metamorphites of the area around Muri-Silli-Jhalida, Ranchi and Purulia Districts, India. Proceedings, *22nd International Geological Congress 4*, 374-389.

294. Sengupta, D.K. & Sarkar, S.N. (1968). Structure of granitic rocks and associated metamorphites of the area around Muri-Silli-Jhalida, Ranchi and Purulia Districts, India. *Transactions Geological Metallurgical Institute of India 65*, 1-18.

295. Shand, S.J. (1927). Eruptive Rocks, Their Genesis, Composition Classification and Their Reaction to Ore-Deposits, with a Chapter on Meteorites. Murby, London.

296. Shand, S.J. (1943). The eruptive rocks: 2nd edition, John Wiley, New York, 444 p

297. Sharma, N. L., & Agrawal, Y. K. (1950). A note on the rapakivi structure in the epidiorite and injection gneiss of Dhanbad area. *Quarterly Journal of Geological, Mining and Metallurgical Society of India*, *22*, 11-13.

298. Sharma, R. (2009). Cratons and Fold Belts of India. Springer, Berlin, 304.

299. Shaw, D.M., (1970). Trace element fractionation during anatexis. *Geochimica et Cosmochimica Acta, 34*, p. 237–243

300. Silver, L. T., & Deutsch, S. (1963). Uranium-Lead Isotopic Variations in Zircons: A Case Study. *The Journal of Geology*, *71*(6), 721–758. https://doi.org/10.1086/626951

301. Singh, R. N., Thorpe, R. & Kristic, D. (2001). Galena Pb isotope date of base metal occurrences in the Hesatu– Belbathan belt, eastern Precambrian shield, Bihar. *Journal of the Geological Society of India, 57*, 535–538

302. Singh, S. P. (1998). Precambrian stratigraphy of Bihar – an overview. In: Paliwal, B. S. (ed.) The Indian Precambrian. Scientific Publishers (India), Jodhpur, 376–408.

303. Singh, Y. & Krishna, V. (2009). Rb–Sr geochronology and petrogenesis of granitoids from the Chotanagpur Granite Gneiss Complex of Raikera–Kunkuri region, Central India. *Journal of the Geological Society of India, 74,* 200–208

304. Smithies R. H., & Champion D. C. (2000). The Archaean high-Mg diorite suite: links to tonalite–trondhjemite–granodiorite magmatism and implications for early Archaean crustal growth. *Journal of Petrology, 41,* 1653–1671.

305. Solar, G. S., Pressley, R. A., Brown, M., & Tucker, R. D. (1998). Granite ascent in convergent orogenic belts: Testing a model. *Geology,* 711.

306. Som, S. K., & Joshi, R. (2002). Chemical Weathering of serpentinite and Ni enrichment in Fe oxide at Sukinda area, Jaipur District, Orissa, India *Economic Geology*, *97*(1), 165–172. https://doi.org/10.2113/GSECONGEO.97.1.165

307. Spencer C. J., Cawood P. A., Hawkesworth C. J., Raub T. D., Prave A. R., & Roberts N. M. (2014). Proterozoic onset of crustal reworking and collisional tectonics: Reappraisal of the zircon oxygen isotope record. *Geology 42,* 451–454.

308. Spencer C. J., Partin C. A., Kirkland C. L., Raub T. D., Liebmann J., & Stern R. A. (2019). Paleoproterozoic increase in zircon δ18O driven by rapid emergence of continental crust. *Geochimica et Cosmochimica Acta 257*, 16–25.

309. Suzuki, K., & Adachi, M. (1991). Precambrian provenance and Silurian metamorphism of the Tsunosawa paragneiss in the South Kitakami terrane, Northeast Japan, revealed by the chemical Th-U-total Pb isochron ages of monazite, zircon and xenotime. *Geochemical Journal, 25*, 357–376.

310. Sverjensky D. A., & Lee N. (2010). The great oxidation event and mineral diversification. *Elements 6*, 31–36.

311. Sylvester, P. J., (1989). Post - collisional alkaline granites. *Journal of Geology, 97,* 261-280.

312. Taylor, R. S. & McClennan, M. S. (1985). The continental crust: Its composition and evolution. Blackwell Scientific Publications, Oxford.

313. Thompson, G., Bryan, W.B. and Melson, W.G. (1980). Geological and geophysical investigation of the mid-Cayman rise spreading center: geochemical variations and petrogenesis of basalt glasses. *Journal of Geology, 88,* 41-55.

314. Thurston P. C. (1990). Early Precambrian basic rocks of the Canadian shield. In: Hall R. P., Hughes E. J. (ed.) Early Precambrian Basic Magmatism. Glasgow: Blackie, 221–247.

315. Thybo, H., & Artemieva, I. M. (2013). Moho and magmatic underplating in continental lithosphere. *Tectonophysics*, *609*, 605–619. https://doi.org/10.1016/J.TECTO.2013.05.032

316. Torsvik, T. H. (2003). "The Rodinia Jigsaw Puzzle". Science. 300 (5624): 1379–1381. doi:10.1126/science.1083469

317. Torsvik, T. H., Gaina, C., & Redfield, T. F. (2008). "Antarctica and Global Paleogeography: From Rodinia, through Gondwanaland and Pangea, to the birth of the Southern Ocean and the opening of gateways" . In Cooper, A. K.; Barrett, P. J.; Stagg, H.; Storey, B.; Stump, E.; Wise, W.; the 10th ISAES editorial team (eds.). Antarctica: A Keystone in a Changing World. Proceedings of the 10th International Symposium on Antarctic Earth Sciences. Washington, DC: The National Academies Press. pp. 125–140. doi:10.3133/of2007-1047.kp11

318. Tuttle, O. F., & Bowen, N. L. (1958). Origin of Granite in the Light of Experimental Studies in the System NaAlSi3O8–KAlSi3O8–SiO2–H2O. 74.

319. Upadhyay, D. (2008). Alkaline magmatism along the southeastern margin of the Indian shield: Implications for regional geodynamics and constraints on craton–Eastern Ghats Belt suturing. *Precambrian Research, 162*, 59-69

320. Upadhyay, D., & Raith, M.M., (2006b). Petrogenesis of the Kunavaram alkaline complex and the tectonothermal evolution of the neighboring Eastern Ghats Belt granulites, SE India. *Precambrian Research, 150*, 73-94

321. Upadhyay, Dewashish & Jahn-Awe, Silke & Pin, Christian & Paquette, J.L. & Braun, I.. (2006a). Neoproterozoic alkaline magmatism at Sivamalai, southern India. *Gondwana Research, 10*. 156-166. 10.1016/j.gr.2005.11.020.

322. Valley J. W., Lackey J. S., Cavosie A. J., Clechenko C. C., Spicuzza M. J., Basei M. A. S., Bindeman I. N., Ferreira V. P., Sial A. N., King E. M., Peck W. H., Sinha A. K., Wei C. S. (2005). 4·4 billion years of crustal maturation: oxygen isotope ratios of magmatic zircon. *Contributions to Mineralogy and Petrology, 150*, 561–580.

323. Vervoort, J. D., Patchett, P. J., Gehrels, G. E., & Nutman, A. P. (1996). Constraints on early Earth differentiation from hafnium and neodymium isotopes. *Nature, 379*(6566), 624–627. https://doi.org/10.1038/379624a0

324. Vielzeuf, D., & Holloway, J.R., (1988). Experimental determination of the fluid-absent melt relations in the pelitic system. *Contributions to Mineralogy and Petrology, 98*, 257-276

325. Vinogradov, A., Tugarinov, A., Zhykov, C., Stapnikova, N., Bibikova, E., & Khorre, K.G. (1964) Geochronology of Indian Precambrian, XXII *International Geological Congress Report X*, 553-567

326. Wang, F., Xu, W.-L., Meng, E., Cao, H.-H., & Gao, F.-H. (2012). Early Paleozoic amalgamation of the Songnen–Zhangguangcai Range and Jiamusi massifs in the eastern

segment of the Central Asian Orogenic Belt: Geochronological and geochemical evidence from granitoids and rhyolites. *Journal of Asian Earth Sciences*, *49*, 234–248. https://doi.org/10.1016/J.JSEAES.2011.09.022

327. Wang, R. C., Fontan, F., Chen, X. M., Hu, H., Liu, C. S., Xu, S. J. and De Parseval, P. (2003a) Accessory minerals in the Xihuashan Y-enriched granitic complex, southern China: a record of magmatic and hydrothermal stages of evolution. *Canadian Mineralogist*, *41*, 727– 748.
328. Wanjari, N. R., Chaturvedi, R. & Mahanta, D. N. (2012). Specialised thematic mapping in Munger–Rajgir Group of rocks to examine structural and stratigraphic set up in and around Gaya–Rajgir areas in parts of Gaya, Nawada and Jahanabad districts of Bihar; Unpublished report, GSI (F.S.: 2008-09, 2009-10).
329. Watson, E. B., & Harrison, T. M. (1983). Zircon saturation revisited: temperature and composition effects in a variety of crustal magma types. *Earth and Planetary Science Letters*, *64*(2), 295–304. https://doi.org/10.1016/0012-821X(83)90211-X
330. Weil, A. B., Van der Voo, R., Mac Niocaill, C., Meert, J. G. (1998). "The Proterozoic supercontinent Rodinia: paleomagnetically derived reconstructions for 1100 to 800 Ma". *Earth and Planetary Science Letters. 154* (1), 13–24.
331. Wen, Bin; Evans, David A. D.; Li, Yong-Xiang (2017). "Neoproterozoic paleogeography of the Tarim Block: An extended or alternative "missing-link" model for Rodinia?" *Earth and Planetary Science Letters. 458*, 92–106.
332. Whalen, J. B., Curie, K. L., & Chappell, B. W. (1987). A-type granites: geochemical characteristics, discrimination and petrogenesis. *Contribution to Mineralogy and Petrology*, *95*, 407–419.

333. Wilson, M. (1989). Igneous Petrogenesis: A Global Tectonic Approach. Unwin Hyman, London, 466.https://doi.org/10.1007/978-1-4020-6788-4

334. Windley B. F. (1977). Timing of continental growth and emergence. *Nature, 270,* 426

335. Wingate, M.T.D., & Giddings, J.W., (2000), Age and palaeomagnetism of the Mundine Well dyke swarm, Western Australia: Implications for an Australia-Laurentia connection at 755 Ma: *Precambrian Research, 100,* 335–357, doi: 10.1016/S0301-9268(99)00080-7

336. Yang, J., Qi, X., Xu, Z., Wu, C., Liu, F., & Zeng, L. (2008). A New Caledonian Khondalite Series in West Kunlun, China: Age Constraints and Tectonic Significance. *International Geology Review, 47*(9), 986–998. https://doi.org/10.2747/0020-6814.47.9.986

337. Yang, X. M. (2017). Estimation of crystallization pressure of granite intrusions. *Lithos*. https://doi.org/10.1016/j.lithos.2017.06.018

338. Zen, E-an, (1988). Bedrock geology of the Vipond Park 15-minute, Stine Mountain 7-1/2-minute, and Maurice Mountain 7-1/2-minute quadrangles, Pioneer Mountains, Beaverhead County, Montana. USGS Numbered Series 1625. https://doi.org/10.3133/b1625

339. Zhang, H., Harris, N., Parrish, R., Kelley, S., Zhang, L., Rogers, N., Argles, T., & King, J. (2004). Causes and consequences of protracted melting of the mid-crust exposed in the North Himalayan antiform. *Earth and Planetary Science Letters*, *228*(1–2), 195–212. https://doi.org/10.1016/J.EPSL.2004.09.031

340. Zhang, H.-F., Parrish, R., Zhang, L., Xu, W.-C., Yuan, H.-L., Gao, S., & Crowley, Q. G. (2007). A-type granite and adakitic magmatism association in Songpan–Garze fold belt, eastern Tibetan Plateau: Implication for lithospheric delamination. *Lithos, 97*(3–4), 323–335. https://doi.org/10.1016/j.lithos.2007.01.002

341. Zhao, G. C., Sun, M., Wilde, S. A. & Li, S. Z. (2004). A Paleo-Mesoproterozoic supercontinent: Assembly, growth and breakup. *Earth-Science Reviews, 67*, 91–123.

342. Zhou, M. F., Yan, D. P., Kennedy, A. K., Li, Y., & Ding, J. (2002). SHRIMP U–Pb zircon geochronological and geochemical evidence for Neoproterozoic arc-magmatism along the western margin of the Yangtze Block, South China. *Earth and Planetary Science Letters*, *196*(1–2), 51–67. https://doi.org/10.1016/S0012-821X(01)00595-7

LIST OF PUBLICATIONS

1. Chakraborty, K., Ray, A., Chatterjee, A., Deb, G.K., Das, K., 2019. Neoproterozoic granitic activity in syn-collisional setting: Insight from petrology, geochemistry, and zircon–monazite geochronology of S-type granites of the Chotanagpur Granite Gneissic Complex, eastern India. Geological Journal, 1–36. doi:10.1002/gj.3555
2. Chakraborty, K., Ray, A., Chakraborti T.M., Deb, G.K., Mandal, A., Kimura, K., Mukhopadhyay, S., 2022. Petrology, Geochemistry and U-Pb zircon geochronology of Alkali granites of Jhalda, Eastern India and their possible linkage to Rodinia Supercontinent. Journal of Earth System Science. (Accepted)